Thesis for the Degree of Doctor

Measurements of Masses and Decay Widths of the $\mathbf{\Sigma_c(2455)^{0/++}}$ and $\mathbf{\Sigma_c(2520)^{0/++}}$ Baryons

by

Soohyung Lee

Department of Physics

Graduate School

Korea University

July, 2014

元 殷 溢 教 授 指 導

博 士 學 位 論 文

Measurements of Masses and Decay Widths of the $\Sigma_c(2455)^{0/++}$ and $\Sigma_c(2520)^{0/++}$ Baryons

이 論文을 理學 博士學位 論文으로 提出함.

2014 年 7 月

高 麗 大 學 校 大 學 院

物 理 學 科

李 秀 炯 (印)

李 秀 炯의 理學 博士學位論文 審査를 完了함.

2014 年 6 月

委員長 (印)

委 員 (印)

委 員 (印)

委 員 (印)

委 員 (印)

When one door closes, another door opens.

- Alexander Graham Bell

Abstract

Hadrons that contain b or c quark are a good testbed for the quantum chromodynamics. However, the masses and decay widths of those hadrons cannot be calculated within the framework of perturbative quantum chromodynamics. To describe the hadrons, many theoretical models are introduced but the experimental results have large uncertainty to validate the models. Therefore, precise measurements of the masses and decay widths of the hadrons are necessary to test the models.

In this dissertation, the measurements of the masses and decay widths of the $\Sigma_c(2455)^{0/++}$ and $\Sigma_c(2520)^{0/++}$ baryons using the mass differences, $m(\Sigma_c(2455)^{0/++}) - m(\Lambda_c^+)$ and $m(\Sigma_c(2520)^{0/++}) - m(\Lambda_c^+)$, are presented. Furthermore, the mass splittings, $m(\Sigma_c(2455)^{++}) - m(\Sigma_c(2455)^0)$ and $m(\Sigma_c(2520)^{++}) - m(\Sigma_c(2520)^0)$, are presented as well.

By exploiting the large data sample corresponding to the integrated luminosity of 711 fb^{-1} collected at the $\Upsilon(4S)$ with the Belle detector at the KEKB e^+e^- asymmetric-energy collider, the mass differences of the $\Sigma_c(2455)^{0/++}$ and $\Sigma_c(2520)^{0/++}$ baryons with respect to the Λ_c^+ baryons are measured as

$$\begin{aligned} m(\Sigma_c(2455)^0) - m(\Lambda_c^+) &= 167.29 \pm 0.01 \pm 0.02 \text{ MeV}/c^2, \\ m(\Sigma_c(2455)^{++}) - m(\Lambda_c^+) &= 167.51 \pm 0.01 \pm 0.02 \text{ MeV}/c^2, \\ m(\Sigma_c(2520)^0) - m(\Lambda_c^+) &= 231.98 \pm 0.11 \pm 0.04 \text{ MeV}/c^2, \\ m(\Sigma_c(2520)^{++}) - m(\Lambda_c^+) &= 231.99 \pm 0.10 \pm 0.02 \text{ MeV}/c^2, \end{aligned}$$

and the invariant masses of the $\Sigma_c(2455)^{0/++}$ and $\Sigma_c(2520)^{0/++}$ baryons using the measured mass differences are measured as

$$\begin{aligned} m(\Sigma_c(2455)^0) &= 2453.75 \pm 0.01 \pm 0.02 \pm 0.14 \text{ MeV}/c^2, \\ m(\Sigma_c(2455)^{++}) &= 2453.97 \pm 0.01 \pm 0.02 \pm 0.14 \text{ MeV}/c^2, \\ m(\Sigma_c(2520)^0) &= 2518.44 \pm 0.11 \pm 0.04 \pm 0.14 \text{ MeV}/c^2, \\ m(\Sigma_c(2520)^{++}) &= 2518.45 \pm 0.10 \pm 0.02 \pm 0.14 \text{ MeV}/c^2, \end{aligned}$$

where the first uncertainties are statistical, the second are systematic, and the third are the total uncertainty of the world average of Λ_c^+ mass.

The decay widths of the $\Sigma_c(2455)^{0/++}$ and $\Sigma_c(2520)^{0/++}$ baryons are also measured to be

$$\begin{aligned}
\Gamma(\Sigma_c(2455)^0) &= 1.76 \pm 0.04^{+0.09}_{-0.21}\ \mathrm{MeV}/c^2, \\
\Gamma(\Sigma_c(2455)^{++}) &= 1.84 \pm 0.04^{+0.07}_{-0.20}\ \mathrm{MeV}/c^2, \\
\Gamma(\Sigma_c(2520)^0) &= 15.41 \pm 0.41^{+0.20}_{-0.32}\ \mathrm{MeV}/c^2, \\
\Gamma(\Sigma_c(2455)^{++}) &= 14.77 \pm 0.25^{+0.18}_{-0.30}\ \mathrm{MeV}/c^2,
\end{aligned}$$

where the first uncertainties are statistical, and the second are systematic. From the results of the mass measurements, the mass splittings, $m(\Sigma_c(2455)^{++}) - m(\Sigma_c(2455)^0)$ and $m(\Sigma_c(2520)^{++}) - m(\Sigma_c(2520)^0)$, are also calculated and they are $m(\Sigma_c(2455)^{++}) - m(\Sigma_c(2455)^0) = 0.22 \pm 0.01 \pm 0.01\ \mathrm{MeV}/c^2$ and $m(\Sigma_c(2520)^{++}) - m(\Sigma_c(2520)^0) = 0.01 \pm 0.15 \pm 0.03\ \mathrm{MeV}/c^2$.

The measurements are the most precise to date.

국문초록

b 또는 c 쿼크를 포함하는 강입자들은 양자색소역학을 시험하는데 좋은 환경을 제공한다. 하지만, 이러한 강입자들의 질량과 붕괴폭의 계산은 미동적 양자색소역학으로는 불가능하다. 이러한 강입자들을 설명하기 위해서, 많은 이론적인 모형들이 소개되었지만 이러한 모형들을 검증하기에는 실험적인 결과의 불확정성이 크다. 따라서, 이론적인 모형들을 시험하기 위해 이 강입자들의 질량과 붕괴폭의 정밀한 측정이 필요하다.

이 학위 논문을 통해, $\Sigma_c(2455)^{0/++}$ 와 $\Sigma_c(2520)^{0/++}$ 중입자들의 질량과 붕괴폭을 질량 차 $m(\Sigma_c(2455)^{0/++}) - m(\Lambda_c^+)$ 와 $m(\Sigma_c(2520)^{0/++}) - m(\Lambda_c^+)$를 이용하여 측정한 결과를 발표한다. 또한 질량 갈라짐 $m(\Sigma_c(2455)^{++}) - m(\Sigma_c(2455)^0)$ 와 $m(\Sigma_c(2520)^{++}) - m(\Sigma_c(2520)^0)$ 또한 발표한다.

비대칭 에너지의 전자-반전자 가속기인 KEKB에서 Belle 검출기를 이용하여 $\Upsilon(4S)$ 공명 상태에서 축적한 711 fb^{-1} 누적 광도의 큰 데이터를 사용하여, Λ_c^+에 대한 $\Sigma_c(2455)^{0/++}$ 와 $\Sigma_c(2520)^{0/++}$의 질량 차는

$$
\begin{aligned}
m(\Sigma_c(2455)^0) - m(\Lambda_c^+) &= 167.29 \pm 0.01 \pm 0.02 \text{ MeV}/c^2, \\
m(\Sigma_c(2455)^{++}) - m(\Lambda_c^+) &= 167.51 \pm 0.01 \pm 0.02 \text{ MeV}/c^2, \\
m(\Sigma_c(2520)^0) - m(\Lambda_c^+) &= 231.98 \pm 0.11 \pm 0.04 \text{ MeV}/c^2, \\
m(\Sigma_c(2520)^{++}) - m(\Lambda_c^+) &= 231.99 \pm 0.10 \pm 0.02 \text{ MeV}/c^2,
\end{aligned}
$$

로 측정되었고, 이 측정된 질량 차를 이용하여 $\Sigma_c(2455)^{0/++}$ 와 $\Sigma_c(2520)^{0/++}$의 불변질량은

$$
\begin{aligned}
m(\Sigma_c(2455)^0) &= 2453.75 \pm 0.01 \pm 0.02 \pm 0.14 \text{ MeV}/c^2, \\
m(\Sigma_c(2455)^{++}) &= 2453.97 \pm 0.01 \pm 0.02 \pm 0.14 \text{ MeV}/c^2, \\
m(\Sigma_c(2520)^0) &= 2518.44 \pm 0.11 \pm 0.04 \pm 0.14 \text{ MeV}/c^2, \\
m(\Sigma_c(2520)^{++}) &= 2518.45 \pm 0.10 \pm 0.02 \pm 0.14 \text{ MeV}/c^2,
\end{aligned}
$$

로 측정되었는데, 첫번째 불확정도는 통계적 오차, 두번째 불확정도는 계통적 오차이고 세번째 불확정도는 Λ_c^+ 중입자의 세계 평균 질량의 총 불확정도이다.

$\Sigma_c(2455)^{0/++}$ 와 $\Sigma_c(2520)^{0/++}$ 중입자의 붕괴폭은,

$$\begin{aligned}
\Gamma(\Sigma_c(2455)^0) &= 1.76 \pm 0.04^{+0.09}_{-0.21}\ \mathrm{MeV}/c^2 \\
\Gamma(\Sigma_c(2455)^{++}) &= 1.84 \pm 0.04^{+0.07}_{-0.20}\ \mathrm{MeV}/c^2 \\
\Gamma(\Sigma_c(2520)^0) &= 15.41 \pm 0.41^{+0.20}_{-0.32}\ \mathrm{MeV}/c^2 \\
\Gamma(\Sigma_c(2455)^{++}) &= 14.77 \pm 0.25^{+0.18}_{-0.30}\ \mathrm{MeV}/c^2
\end{aligned}$$

로 측정되었고, 첫번째 불확정도는 통계적 오차, 두번째 불확정도는 계통적 오차이다. 측정된 질량 차를 이용하여 질량 갈라짐 $m(\Sigma_c(2455)^{++}) - m(\Sigma_c(2455)^0)$ 와 $m(\Sigma_c(2520)^{++}) - m(\Sigma_c(2520)^0)$ 역시 계산되었고 그 결과는 각각 $m(\Sigma_c(2455)^{++}) - m(\Sigma_c(2455)^0) = 0.22 \pm 0.01 \pm 0.01\ \mathrm{MeV}/c^2$ 와 $m(\Sigma_c(2520)^{++}) - m(\Sigma_c(2520)^0) = 0.01 \pm 0.15 \pm 0.03\ \mathrm{MeV}/c^2$ 이다.

이 측정 결과는 오늘날 가장 정밀한 결과이다.

Acknowledgements

Particle physics is a big challenge to reveal the mysteries of the universe. It is my great honor to get involved in this most advanced science and challenge to expand the boundary of human knowledge. There are many people whom I have to appreciate during my journey.

First of all, I have no words to express my gratitude enough to my thesis advisor, Professor Eunil Won (Korea University, Korea). His passions and professions for physics encourages and inspires me, and he has been always supportive to my researches. As a role model and a mentor, he demonstrates the way how I would live as a physicist in my future career.

I would like to appreciate Dr. Byeong Rok Ko (Korea University, Korea) as well. Without his deep knowledge on physics, and abundant experience, this study would be painful. His enthusiasm for physics always motivates me. Whenever I encountered difficulties even including technical ones, he saved me with brilliant solutions.

The referees of this study in the Belle collaboration, Dr. Anze Zupanc (Jožef Stefan Institute, Slovenia), Dr. Yuji Kato (Nagoya University, Japan), and Dr. Anton Poluektov (Budker Institute of Nuclear Physics, Russia), showed their interests in my study and faithfully advised through the entire authorship process. Professor Yoshihide Sakai (KEK, Japan), Professor James Libby (Indian Institute of Technology Madras, India), Professor Yasushi Watanabe (Kanagawa University, Japan), Dr. Bansal Vikas (Pacific Northwest National Laboratory, USA), and Dr. Olivier Schneider (Ecole Polytechnique Federale de Lausanne, Switzerland) gave lots of helps to perfect this study as well. They all deserve to take my gratitude.

I also express my gratitude to the committee members, Professor Byeonggu Cheon (Hanyang University, Korea), Professor Un-ki Yang (Seoul National University, Korea), and Professor Jung Keun Ahn (Korea University) for their service to evaluate this dissertation.

During my Ph. D. course, I was involved in a development of a high level trigger software for the Belle II experiment. I have learned lots of valuable knowledges and experiences from my co-worker, Professor Ryosuke Itoh (KEK, Japan) who is the leader of data acquisition group of the Belle and Belle II experiment. His enthusiasm and diligence are the greatest lessons that I have ever learned.

I also appreciate for the support from my family. There is always no word to thank to my father, who has been persistently self-sacrificing.

Dr. Hyuncheong Ha (Samsung Electronics, Korea), my university senior as well as the former lab senior, introduced the particle physics to me at the first place. He willingly shared his knowledge and experiences. Without his help, it would be much harder to settle in this field.

I also thank to my lab colleagues, Jihoon Choi, Kyungtae Kim, Jaebak, Kim, Kyungmin Lee, Donghyun Lee, Hyunki Moon, Woodo Lee, Hoyong Jung, and Andrea Maria Kim (Korea University, Korea) and to a former lab member, Minju Lee.

I would like to deeply thank to Korean Belle members; Professor Youngjoon Kwon (Yonsei University, Korea) and Dr. Yuji Unno (Hanyang University, Korea) showed their persistent interests in my physics analysis. Oksu Seon (Nagoya University, Japan) who is a former Korean Belle member, Dr. Soo Ryu (Seoul National University, Korea) and Sunghyun Kim (Hanyang University, Korea) shared the difficulties as a graduate student. I would also appreciate Professor Sunkee Kim (Seoul National University, Korea), Professor Soo Kyung Choi (Gyeongsang National University, Korea), Dr. Doris Yangsoo Kim (Soongsil University, Korea), Dr. Kihyeon Cho, Dr. Young Jin Kim, Dr. Jung Hyun Kim (Korea Institute of Science and Technology Information, Korea), Dr. Myungjae Lee (Lawrence Berkeley National Laboratory, USA), Dr. Hyo Jung Hyun (Kyungpook National University, Korea), Dr. Bong Ho Kim (Seoul National University, Korea), Insoo Lee, and Youngmoon Goh (Hanyang University, Korea).

I also thank to my university friends, Minho Cho, Sangyoung Seo, Wonthaek Oh, Guntae Park, and Minyoung Choi as well as my oldest friends, Junhyup Kim, Yongkwan Jang, Heonchang Jung, Ho Sin Han, and Jeong-hoon Heo.

Finally, I express my gratitude to my love, Sungeun Kim.

At the another open door,
Soohyung Lee

Contents

List of Figures

List of Tables

Chapter 1

Introduction

1.1 Standard Model

The standard model has been the most successful theory to describe the elementary particles that are constituents of the universe, and the interactions among them. In the standard model, there are six quarks, six leptons, four interaction mediators involved in the interactions among the particles, and the Higgs boson which gives masses to massive elementary particles. The elementary particles in the standard model are summarized in Fig. 1.1.

1.1.1 Quarks

Quarks are basic blocks of hadrons, and there are six different types known as flavors: up (u), down (d), charm (c), strange (s), top (t), and bottom (b). Quarks have spin $\frac{1}{2}$, therefore, they are fermions, and u, c, and t quarks have $+\frac{2}{3}$ of the magnitude of the electron charge while d, s, and b quarks have $-\frac{1}{3}$ of the magnitude of the electron charge. These quarks are classified into three generations: $\binom{u}{d}$, $\binom{c}{s}$, and $\binom{t}{b}$. For example, u and d quarks have similar masses ($m_u = 2.3^{+0.7}_{-0.5}$ MeV/c^2 and $m_d = 4.8^{+0.7}_{-0.3}$ MeV/c^2 [3]) while c and s quarks have the masses away from them ($m_c = 1275 \pm 25$ MeV/c^2 and $m_s = 95 \pm 5$ MeV/c^2 [3]). The known properties of quarks are summarized in Table 1.1.

In addition to the flavors, quarks have another quantum number called color charge. The color charge is introduced in quantum chromodynamics (QCD) and consists of three colors: red, green, and blue. A quark is an eigenstate of a color charge, and the strong interaction among quarks can be explained by exchanging the colors.

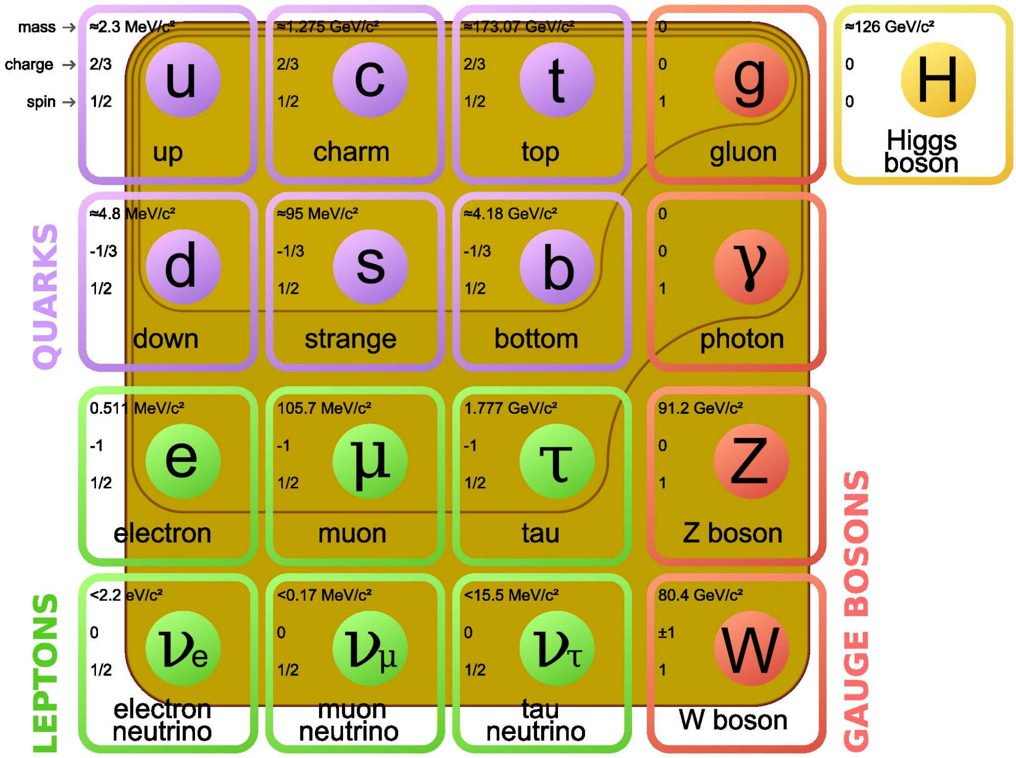

Figure 1.1: Elementary particles in the standard model. Anti-particles are not listed. Image is taken from Ref. [2].

Particles made of the quarks by the strong interaction are called hadrons. From the constituent quark numbers, the hadrons are classified into two types: baryons and mesons. The baryons contain three quarks, namely, qqq, and the mesons contain a quark and an anti-quark, that is, $q\overline{q}$ where $q = \{u, d, c, s, b\}$. For example, a proton consists of two u and a d quarks (uud), therefore, it is a baryon. On the other hand, a positively charged pion (π^+) consists of an u and a $\overline{d}$ quarks ($u\overline{d}$), therefore, it is a meson. Since the quarks are fermions, the baryons are fermions that have half-integer spin while the mesons are bosons that have integer spin.

1.1.2 Leptons

Leptons are another kind of the elementary particles in the standard model. Leptons can exist as free particles while quarks usually cannot. There are six leptons with different flavors in the standard model: electron (e^-), electron neutrino (ν_e), muon (μ^-), muon neutrino (ν_μ), tau (τ^-), and tau neutrino (ν_τ). Electrons, muons, and taus are negatively charged leptons[1] while the neutrinos are electrically neutral.

[1] Positively charged leptons also exist as their corresponding anti-particles, for example, the anti-particle of the electron is positron (e^+).

Generation	Quark	Q	U	D	C	S	T	B	Mass
First generation	u	$+\frac{2}{3}e$	1	0	0	0	0	0	$2.3^{+0.7}_{-0.5}$ MeV/c^2
	d	$-\frac{1}{3}e$	0	-1	0	0	0	0	$4.8^{+0.7}_{-0.3}$ MeV/c^2
Second generation	c	$+\frac{2}{3}e$	0	0	1	0	0	0	1275 ± 25 MeV/c^2
	s	$-\frac{1}{3}e$	0	0	0	-1	0	0	95 ± 5 MeV/c^2
Third generation	t	$+\frac{2}{3}e$	0	0	0	0	1	0	173.5 ± 1.0 GeV/c^2
	b	$-\frac{1}{3}e$	0	0	0	0	0	-1	4.18 ± 0.03 GeV/c^2

Table 1.1: Quarks and their properties in the standard model. Q, U, D, C, S, T, and B denote the charge in terms of the magnitude of the electron charge e, upness, downness, charm, strangeness, truth, and beauty of the quark [1]. The masses are the current world average [3].

Generation	Quark	Q	L_e	L_μ	L_τ	Mass
First generation	e^-	$-1e$	1	0	0	0.51 MeV/c^2
	ν_e	0	1	0	0	< 2 eV/c^2
Second generation	μ^-	$-1e$	0	1	0	105.66 MeV/c^2
	ν_μ	0	0	1	0	< 2 eV/c^2
Third generation	τ^-	$-1e$	0	0	1	1776.82 ± 0.16 MeV/c^2
	ν_τ	0	0	0	1	< 2 eV/c^2

Table 1.2: Leptons and their properties in the standard model. Q, L_e, L_μ, and L_τ denote the charge, electron number, muon number, and tau number of the lepton [1]. The masses are the current world average [3].

Leptons have spin $\frac{1}{2}$, therefore, they are fermions as quarks are. Similar to the quarks, the leptons can be classified into three generations by their flavors [4]: $\binom{e^-}{\nu_e}$, $\binom{\mu^-}{\nu_\mu}$, and $\binom{\tau^-}{\nu_\tau}$. The known properties of leptons are summarized in Table 1.2.

1.1.3 Interactions and Interaction Mediators

There are four fundamental interactions among the elementary particles: gravitational[2], electromagnetic, strong, and weak interactions. These interactions take place by exchanging the corresponding mediators. Photon (γ) is involved in the electromagnetic interaction, gluon (g) in strong interaction, and $W^\pm$ and Z^0 in the weak interaction. These particles have spin 1, therefore, they are bosons.

[2]The gravitational interaction is not included in the standard model [1].

The electromagnetic interaction mediated by photon is a binding force in atoms, molecules, and crystals. Maxwell formulated the electromagnetic interaction in his theory, also known as Maxwell's equation. Tomonaga [5], Schwinger [6, 7], and Feynman [8, 9, 10] perfected the theory of electromagnetic interaction with relativistic quantum theory known as quantum electrodynamics (QED), and it successfully describes the quantum mechanical electromagnetic interaction. The electromagnetic interaction affects to charged particles, and the range of the electromagnetic interaction is infinite.

The strong interaction mediated by gluon is a binding force in nucleons and atomic nuclei. Quantum chromodynamics (QCD) [11, 12, 13, 14] is the theory of the strong interaction. The gluon is an eigenstate of two color charges while a quark is an eigenstate of a color charge. Therefore, there can be nine species of the gluons: $r\overline{r}$, $r\overline{b}$, $r\overline{g}$, $b\overline{r}$, $b\overline{b}$, $b\overline{g}$, $g\overline{r}$, $g\overline{b}$, and $g\overline{g}$, and they form nine states which consist of a color octet,

$$\begin{aligned}
\frac{1}{\sqrt{2}}(r\overline{b}+b\overline{r}), &\qquad -\frac{i}{\sqrt{2}}(r\overline{g}-g\overline{r}),\\
-\frac{1}{\sqrt{2}}(r\overline{b}+b\overline{r}), &\qquad \frac{1}{\sqrt{2}}(b\overline{g}+g\overline{b}),\\
\frac{1}{\sqrt{2}}(r\overline{r}-b\overline{b}), &\qquad -\frac{i}{\sqrt{2}}(b\overline{g}-g\overline{b}),\\
\frac{1}{\sqrt{2}}(r\overline{g}+g\overline{r}), &\qquad \frac{1}{\sqrt{6}}(r\overline{r}+b\overline{b}-2g\overline{g}),
\end{aligned}$$

and a color singlet,

$$\frac{1}{\sqrt{3}}(r\overline{r}+b\overline{b}+g\overline{g}).$$

Since the color singlet leads the gluon to be a free particle, it is excluded in QCD, therefore, there are only eight eigenstates of the gluons [1]. The strong interaction affects in short distance and to quarks that have color charges, and the range of the strong interaction is roughly 10^{-15} m.

The weak interaction [15, 16, 17] mediated by $W^{\pm}$ and Z^0 bosons accounts for nuclear beta decay. Similar to the way that electron charge produces the electromagnetic interaction, and color charge produces the strong interaction, weak isospin produces the weak interaction, and all quarks and leptons carry the weak isospin. The weak interaction is the only interaction that is able to change the flavor of a quark and violates parity symmetry (P) [18, 19] as well as charge conjugation parity symmetry (CP) [20, 21, 22, 23, 24, 25]. There are two kinds of weak interactions: charged and neutral. The charged weak interaction is mediated by $W^{\pm}$ bosons and affects to charged leptons and quarks while the neutral weak interaction is mediated by Z^0 boson and affects to neutrinos. The range of the weak interaction is about 10^{-18} m.

1.1.4 Mesons and Baryons

Hadrons consisting of a quark and an anti-quark ($q\overline{q}$) are called mesons. Since the quarks are spin $\frac{1}{2}$ particles, the mesons can have spin 0 with anti-parallel configuration and spin 1 with parallel configuration of two spins. Without any orbital excitation, which means that the quantum number of the orbital angular momentum is zero ($l = 0$), spin 0 mesons are referred as pseudoscalar meson while spin 1 mesons are referred as vector mesons. Since the parity of a meson follows [26]

$$P = (-1)^{l+1},$$

the quantum numbers of pseudoscalar and vector mesons are $J^P = 0^-$ and $J^P = 1^-$, respectively. With the lightest two quarks, u and d, possible combinations are

$$\begin{aligned}
|1,1\rangle &= (\uparrow\uparrow) \\
|1,0\rangle &= \frac{1}{\sqrt{2}}(\uparrow\downarrow + \downarrow\uparrow) \\
|1,-1\rangle &= (\downarrow\downarrow) \\
|0,0\rangle &= \frac{1}{\sqrt{2}}(\uparrow\downarrow - \downarrow\uparrow)
\end{aligned}$$

where the first and second in ket states are the spin and the third component of isospin (I_3), and the upward and downward arrows denote spin up ($\frac{1}{2}$) and down ($-\frac{1}{2}$) states. In terms of $SU(2)$ group where SU stands for special unitary [1, 26], it can be written as

$$2 \otimes \overline{2} = 3 \oplus 1,$$

in other words, a combination of a triplet and a singlet where the triplet is spin 1 states, and the singlet is spin 0 state. If it extends to include an s quark, mesons belong to $SU(3)$ group, and

$$3 \otimes \overline{3} = 8 \oplus 1,$$

therefore, it consists of an $SU(3)$ octet and a singlet. Furthermore, $SU(4)$ group is expressed to be

$$4 \otimes \overline{4} = 15 \oplus 1$$

by including a c quark.

Hadrons consisting of three quarks (qqq) are referred as baryons. Since there are three quarks in baryons, the baryons can have spin $\frac{1}{2}$ and $\frac{3}{2}$. Assuming no orbital excitation, the quantum numbers of baryons are $J^P = \frac{1}{2}^+$ and $J^P = \frac{3}{2}^+$ because their parity follows[3] [27]

$$P = (-1)^l.$$

With the lightest two quarks, u, and d, possible combinations of baryons are

$$\begin{aligned}
\left|\frac{3}{2},\frac{3}{2}\right\rangle &= (\uparrow\uparrow\uparrow) \\
\left|\frac{3}{2},\frac{1}{2}\right\rangle &= \frac{1}{\sqrt{3}}(\uparrow\uparrow\downarrow + \uparrow\downarrow\uparrow + \downarrow\uparrow\uparrow) \\
\left|\frac{3}{2},-\frac{1}{2}\right\rangle &= \frac{1}{\sqrt{3}}(\downarrow\downarrow\uparrow + \downarrow\uparrow\downarrow + \uparrow\downarrow\downarrow) \\
\left|\frac{3}{2},-\frac{3}{2}\right\rangle &= (\downarrow\downarrow\downarrow) \\
\left|\frac{1}{2},\frac{1}{2}\right\rangle_{12} &= \frac{1}{\sqrt{2}}(\uparrow\downarrow - \downarrow\uparrow)\uparrow \\
\left|\frac{1}{2},-\frac{1}{2}\right\rangle_{12} &= \frac{1}{\sqrt{2}}(\uparrow\downarrow - \downarrow\uparrow)\downarrow \\
\left|\frac{1}{2},\frac{1}{2}\right\rangle_{23} &= \frac{\uparrow}{\sqrt{2}}(\uparrow\downarrow - \downarrow\uparrow) \\
\left|\frac{1}{2},-\frac{1}{2}\right\rangle_{23} &= \frac{\downarrow}{\sqrt{2}}(\uparrow\downarrow - \downarrow\uparrow)
\end{aligned}$$

where the subscript ij in ket states denotes the interchange of i-th and j-th quarks[4], and in terms of $SU(2)$ group,

$$2 \otimes 2 \otimes 2 = 4_S \oplus 2_M \oplus 2_M$$

where the subscripts of S and M in right-hand side stand for symmetric and mixed (12 and 23 are asymmetric), respectively. In $SU(3)$ group by including s quark,

$$3 \otimes 3 \otimes 3 = 10_S \oplus 8_M \oplus 8_M \oplus 1_A$$

where the subscript of A in right-hand side stands for asymmetric. Similarly, in $SU(4)$ group by including c quark,

$$4 \otimes 4 \otimes 4 = 20_S \oplus 20_M \oplus 20_M \oplus \overline{4}_A,$$

[3]Since the parities for quarks and anti-quarks are defined as +1 and −1, respectively, anti-particles of baryons have opposite parities.

[4]The interchanges of the first and third quarks are not independent, that is, $|\ \rangle_{13} = |\ \rangle_{12} + |\ \rangle_{23}$.

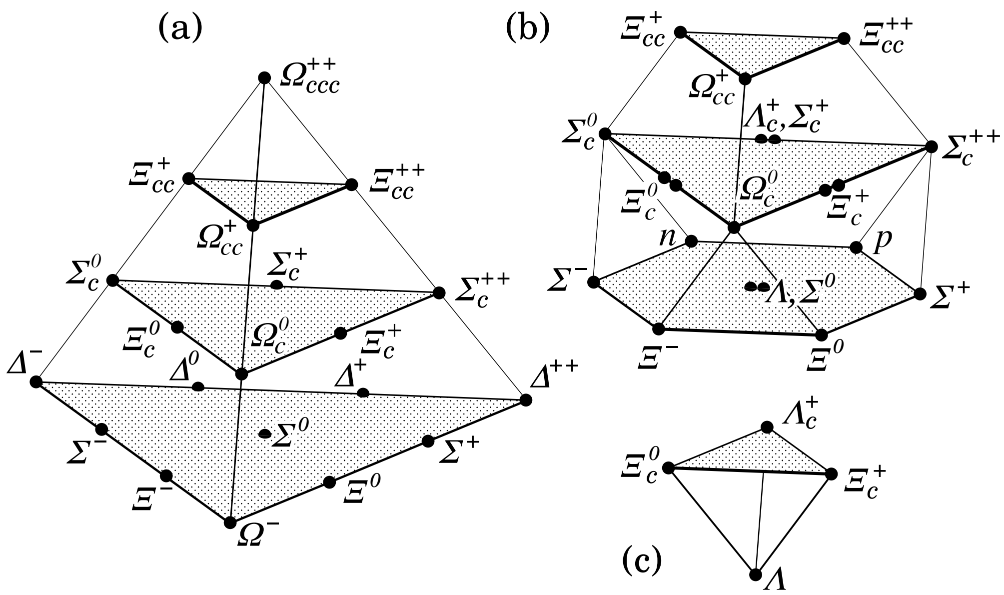

Figure 1.2: $SU(4)$ multiplets of baryons [3]; (a) the multiplet of 20_S with an $SU(3)$ decuplet on the lowest level; (b) the multiplet of 20_M with an $SU(3)$ octet on the lowest level; (c) the $\overline{4}$-plet. Images are taken from Ref. [3].

and the $SU(4)$ multiplets are shown in Fig. 1.2, and known baryons can be viewed in this framework.

1.2 Charmed Baryons

Baryons that consist of qqc where $q = \{u, d, s\}$ are called the charmed baryons. Charmed baryons which does not contain any s quark are classified by their isospin: the Λ_c baryons for isospin 0 and the Σ_c baryons for isospin 1. Charmed baryons which contain an s quark are named the Ξ_c baryons, and charmed baryons with two s quarks are called the Ω_c baryons. By their quark contents, they have different charge states as well as their excited states, therefore, there are 17 known charmed baryons. Tables 1.3 and 1.4 summarize the properties of the charmed baryons.

The charmed baryons have an analogous mass spectrum to the light strange baryons which consist of qqs where $q = \{u, d\}$ as shown in Fig. 1.3. The spectra seem to be similar to each other, especially Λ and Σ to Λ_c and Σ_c because they differ only by the replacement of the s quark with a c quark. In case of the others, however, Ξ and Ω have more than one s quark, the chance for the replacement is larger, therefore, the spectra of Ξ_c and Ω_c are richer than Ξ and Ω spectra.

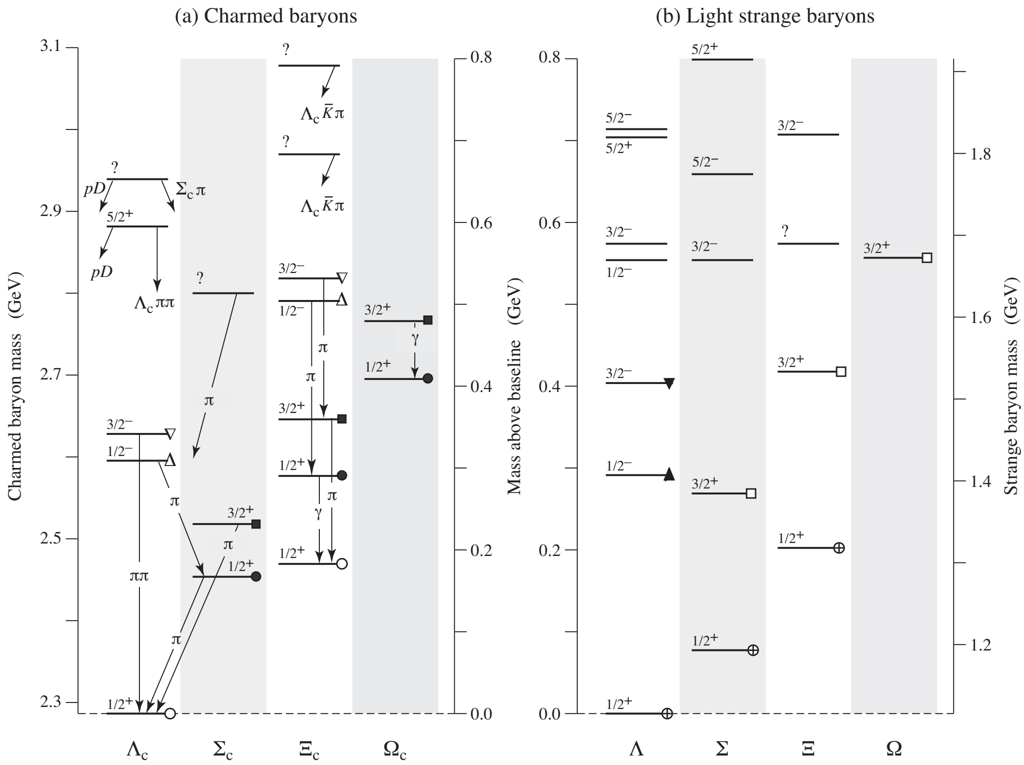

Figure 1.3: Mass spectra of charmed (left) and light strange (right) baryons [3]. The same shapes of marks on the states denote that they belong to the same $SU(4)$ multiplet, and the same colors of marks mean that they belong to the same $SU(3)$ multiplet within the same $SU(4)$ multiplet. Images are taken from Ref. [3].

Charmed baryons	Quark content	I	J^P	Mass (MeV/c^2)	Mean lifetime (fs)	Decay width (MeV/c^2)
Λ_c^+	udc	0	$\frac{1}{2}^+$	2286.46 ± 0.14	200 ± 6	
$\Lambda_c(2595)^+$	udc	0	$\frac{1}{2}^-$	2592.25 ± 0.28		$2.59 \pm 0.30 \pm 0.47$ [28]
$\Lambda_c(2625)^+$	udc	0	$\frac{3}{2}^-$	2628.11 ± 0.19		< 0.97 [28]
$\Lambda_c(2880)^+$	udc	0	$\frac{5}{2}^+$	2881.53 ± 0.35		5.8 ± 1.1
$\Lambda_c(2940)^+$	udc	0	$?^?$	$2939.3^{+1.4}_{-1.5}$		17^{+8}_{-6}
$\Sigma_c(2455)^0$	ddc	1	$\frac{1}{2}^+$	2453.74 ± 0.16		2.16 ± 0.26
$\Sigma_c(2455)^+$	udc	1	$\frac{1}{2}^+$	2453.9 ± 0.4		< 4.6 @ 90% C. L.
$\Sigma_c(2455)^{++}$	uuc	1	$\frac{1}{2}^+$	2453.98 ± 0.16		2.26 ± 0.25
$\Sigma_c(2520)^0$	ddc	1	$\frac{3}{2}^+$	2518.8 ± 0.6		14.5 ± 1.5
$\Sigma_c(2520)^+$	udc	1	$\frac{3}{2}^+$	2517.5 ± 2.3		< 17 @ 90% C. L.
$\Sigma_c(2520)^{++}$	uuc	1	$\frac{3}{2}^+$	2517.9 ± 0.6		14.9 ± 1.5
$\Sigma_c(2800)^0$	ddc	1	$?^?$	2807^{+5}_{-7}		72^{+22}_{-15}
$\Sigma_c(2800)^+$	udc	1	$?^?$	2792^{+14}_{-5}		62^{+37+52}_{-23-38} [29]
$\Sigma_c(2800)^{++}$	uuc	1	$?^?$	2801^{+4}_{-6}		75^{+18+12}_{-13-11} [29]

Table 1.3: Known properties of the Λ_c^+ and Σ_c baryons [3] where I is the magnitude of the isospin, and C. L. is confidence level of the measurements. There are no world averages of some properties marked as "?" because of the insufficient measurements, and the only measurements are included with a citation instead of the average.

Charmed baryons	Quark content	I	J^P	Mass (MeV/c^2)	Mean lifetime (fs)	Decay width (MeV/c^2)
Ξ_c^0	dsc	$\frac{1}{2}$	$\frac{1}{2}^+$	$2470.88^{+0.34}_{-0.80}$	112^{+13}_{-10}	
Ξ_c^+	usc	$\frac{1}{2}$	$\frac{1}{2}^+$	$2467.8^{+0.4}_{-0.6}$	442 ± 26	
$\Xi_c^{\prime 0}$	dsc	$\frac{1}{2}$	$\frac{1}{2}^+$	2577.9 ± 2.9	–	–
$\Xi_c^{\prime +}$	usc	$\frac{1}{2}$	$\frac{1}{2}^+$	2575.6 ± 3.1	–	–
$\Xi_c(2645)^0$	dsc	$\frac{1}{2}$	$\frac{3}{2}^+$	2645.9 ± 0.5		< 5.5 @ 90% C. L. [30]
$\Xi_c(2645)^+$	usc	$\frac{1}{2}$	$\frac{3}{2}^+$	$2645.9^{+0.5}_{-0.6}$		< 3.1 @ 90% C. L. [31]
$\Xi_c(2790)^0$	dsc	$\frac{1}{2}$	$\frac{1}{2}^-$	2791 ± 3.3		< 12 @ 90% C. L. [32]
$\Xi_c(2790)^+$	usc	$\frac{1}{2}$	$\frac{1}{2}^-$	2789 ± 3.2		< 15 @ 90% C. L. [32]
$\Xi_c(2815)^0$	dsc	$\frac{1}{2}$	$\frac{3}{2}^-$	2819.6 ± 1.2		< 6.5 @ 90% C. L. [33]
$\Xi_c(2815)^+$	usc	$\frac{1}{2}$	$\frac{3}{2}^-$	2816.6 ± 0.9		< 3.5 @ 90% C. L. [33]
$\Xi_c(2980)^0$	dsc	$\frac{1}{2}$	$?^?$	2968.0 ± 2.6		20 ± 7
$\Xi_c(2980)^+$	usc	$\frac{1}{2}$	$?^?$	2971.4 ± 3.3		26 ± 7
$\Xi_c(3080)^0$	dsc	$\frac{1}{2}$	$?^?$	3079.9 ± 1.4		5.6 ± 2.2
$\Xi_c(3080)^+$	usc	$\frac{1}{2}$	$?^?$	3077.0 ± 0.4		5.8 ± 1.0
Ω_c^0	ssc	0	$\frac{1}{2}^+$	2695 ± 1.7	69 ± 12	
$\Omega_c(2770)^0$	ssc	0	$\frac{3}{2}^+$	2765.9 ± 2.0	–	–

Table 1.4: Known properties of the Ξ_c and Ω_c baryons [3] where I is the magnitude of the isospin, and C. L. is confidence level of the measurements. There are no world averages of some properties marked as "?" because of the insufficient measurements, and the only measurements are included with a citation instead of the average. The mark "–" denotes that there is no measurement.

1.3 Σ_c Baryons

The charmed baryons which consist of uuc, ddc, or udc with an isospin 1 are called the Σ_c baryons. The Σ_c baryons only decay into $\Lambda_c^+\pi$ [3]. Since the Σ_c baryons have short lifetimes, it is natural to expect that the decay widths appear in their invariant mass distribution from the relation

$$\Gamma = \frac{\hbar}{\tau}$$

where Γ and τ are the decay width and lifetime of a particle, and $\hbar$ is the reduced Planck constant ($= 1.054 \times 10^{-34}$ J·s [3]).

As seen in Table 1.3, their properties are not precisely measured so far, especially for the excite states. For example, the uncertainties for the decay widths of the $\Sigma_c(2520)^{0/++}$ baryons are approximately 10% relative to the central values. The uncertainties are dominated not only statistically but also systematically. Therefore, large data sample and reducing the systematic uncertainties are desirable for the precise measurements of the properties of the Σ_c baryons.

Though the quantum chromodynamics, a theory for the strong interaction, has been successful, the framework of perturbative QCD hardly calculates the masses and decay widths of hadrons. In low-energy regime, the strong coupling constant α_s becomes large, and this makes the calculation practically impossible. To overcome this problem, many theoretical models are introduced, such as the lattice QCD [34, 35, 36], heavy quark effective theory (HQET) [37], quark model [38], QCD sum rule [39], bag model [40], and hyper central model [41, 42], and their predictions are summarized in Table 1.5.

<table>
<tr><th>Theoretical model</th><th>$m(\Sigma_c(2455)^0)$ (MeV/c^2)</th><th>$m(\Sigma_c(2455)^{++})$ (MeV/c^2)</th><th>$m(\Sigma_c(2520)^0)$ (MeV/c^2)</th><th>$m(\Sigma_c(2520)^{++})$ (MeV/c^2)</th></tr>
<tr><td>[34]</td><td colspan="2">$2454 \pm 65^\dagger$</td><td colspan="2">$2527 \pm 73^\dagger$</td></tr>
<tr><td>[35]</td><td colspan="2">$2430 \pm 73^\dagger$</td><td colspan="2">$2510 \pm 80^\dagger$</td></tr>
<tr><td>[36]</td><td colspan="2">2467 ± 40</td><td colspan="2">2538 ± 71</td></tr>
<tr><td>[37]</td><td colspan="2">2455</td><td colspan="2">2519</td></tr>
<tr><td>[38]</td><td colspan="2">2439</td><td colspan="2">2518</td></tr>
<tr><td>[39]</td><td>2400 ± 310</td><td></td><td>2560 ± 240</td><td></td></tr>
<tr><td>[40]</td><td></td><td>2392</td><td></td><td>2489</td></tr>
<tr><td>[41]</td><td>2471</td><td>2451</td><td>2536</td><td>2516</td></tr>
<tr><td>[42]</td><td>2460</td><td>2454</td><td>2533</td><td>2526</td></tr>
</table>

Table 1.5: Theoretical predictions to the masses of the $\Sigma_c(2455)$ and $\Sigma_c(2520)$ baryons. The † mark indicates that the value is average over various parameters.

	$m(\Sigma_c(2455)^{++}) - m(\Sigma_c(2455)^0)$	$m(\Sigma_c(2520)^{++}) - m(\Sigma_c(2520)^0)$
[44]	0.18	
[45]	3.0	
[46]	1.4	
[47]	0.5	
[48]	0.84	
[49]	0.37	0.19

Table 1.6: Theoretical predictions to the mass splittings of $m(\Sigma_c^{++}) - m(\Sigma_c^0)$ in MeV/c^2.

An interesting phenomenon of the Σ_c baryons is the mass hierarchy among them which is referred to as the mass splittings, $m(\Sigma_c^{++}) - m(\Sigma_c^0)$ and $m(\Sigma_c^+) - m(\Sigma_c^0)$. According to the quark model, a d quark is heavier than a u quark, and the quark contents of the Σ_c^0 and Σ_c^{++} baryons are ddc and uud, respectively. Therefore, one may naïvely expect that the Σ_c^0 baryon is heavier than the Σ_c^{++} baryon. However, as seen in Table 1.3, the experimental results seem to contradict the expectation, especially for the masses of $\Sigma_c(2455)^{0/++}$ baryons, although the uncertainties are too large to conclude.

The sources of the mass splitting are known to be: the mass differences of quarks, the Coulomb interaction between charged quarks, and their dipole-dipole (or hyperfine) interaction [43]. Based on the knowledge, theoretical predictions of the mass splitting are performed [43, 44, 45, 46, 47, 48, 49], and they are listed in Table 1.6. Since the contributions of the electromagnetic potential from the Coulomb and hyperfine interaction are large, the mass splittings of $m(\Sigma_c^{++}) - m(\Sigma_c^0)$ are expected to be positive which is contrary to the naïve expectation but consistent with the experimental results. Therefore, the precise measurements of the mass splittings of $m(\Sigma_c^{++}) - m(\Sigma_c^0)$ can verify the theoretical calculation as well.

Many experiments measured the properties of the $\Sigma_c(2455)^{0/++}$ and $\Sigma_c(2520)^{0/++}$ baryons as listed in Tables 1.7 and 1.8. The uncertainties of the results are large, and they are dominated not only statistically but also systematically.

	$\Delta m(\Sigma_c(2455)^0)$	$\Delta m(\Sigma_c(2520)^0)$	$\Gamma(\Sigma_c(2455)^0)$	$\Gamma(\Sigma_c(2520)^0)$
PDG [3]	167.27 ± 0.08	232.3 ± 0.5	2.16 ± 0.26	14.5 ± 1.5
CDF (2011) [28]	$167.28 \pm 0.03 \pm 0.12$	$232.88 \pm 0.43 \pm 0.16$	$1.65 \pm 0.11 \pm 0.49$	$12.51 \pm 1.82 \pm 1.37$
BABAR (2008) [50]	–	–	$2.6 \pm 0.5 \pm 0.3$	–
CLEO (2005) [51]	–	$231.4 \pm 0.5 \pm 0.3$	–	$16.6^{+1.9}_{-1.7} \pm 1.4$
CLEO (2002) [52]	$167.2 \pm 0.1 \pm 0.2$	–	$2.5 \pm 0.2 \pm 0.3$	–
FOCUS (2002) [53]	–	–	$1.55^{+0.41}_{-0.37} \pm 0.38$	–
FOCUS (2000) [54]	$167.38 \pm 0.21 \pm 0.13$	–	–	–
CLEO (1997) [55]	–	$232.6 \pm 1.0 \pm 0.8$	–	$13.0^{+3.7}_{-3.0} \pm 4.0$
E791 (1996) [56]	$167.38 \pm 0.29 \pm 0.15$	–	–	–
EXCHARM (1996) [57]	$167.8 \pm 0.6 \pm 0.2$	–	–	–
E687 (1996) [58]	$166.6 \pm 0.5 \pm 0.6$	–	–	–
CLEO (1993) [59]	$167.1 \pm 0.3 \pm 0.2$	–	–	–
E691 (1989) [60]	$168.4 \pm 1.0 \pm 0.3$	–	–	–

Table 1.7: Comparison to the results in MeV/c^2 from other experiments for the neutral Σ_c baryons. The first uncertainty is statistical and the second is systematic except for the world average shown in the second row as PDG. The uncertainty of the world average is the total uncertainty.

	$\Delta m(\Sigma_c(2455)^{++})$	$\Delta m(\Sigma_c(2520)^{++})$	$\Gamma(\Sigma_c(2455)^{++})$	$\Gamma(\Sigma_c(2520)^{++})$
PDG [3]	167.52 ± 0.08	231.4 ± 0.6	2.26 ± 0.25	14.9 ± 1.5
CDF (2011) [28]	$167.44 \pm 0.04 \pm 0.12$	$230.73 \pm 0.56 \pm 0.16$	$2.34 \pm 0.13 \pm 0.45$	$15.03 \pm 2.12 \pm 1.36$
CLEO (2005) [51]	–	$231.5 \pm 0.4 \pm 0.3$	–	$14.4^{+1.6}_{-1.5} \pm 1.4$
CLEO (2002) [52]	$167.4 \pm 0.1 \pm 0.2$	–	$2.3 \pm 0.2 \pm 0.3$	–
FOCUS (2002) [53]	–	–	$2.05^{+0.41}_{-0.38} \pm 0.38$	–
FOCUS (2000) [54]	$167.35 \pm 0.19 \pm 0.12$	–	–	–
CLEO (1997) [55]	–	$234.5 \pm 1.1 \pm 0.8$	–	$17.9^{+3.8}_{-3.2} \pm 4.0$
E791 (1996) [56]	$167.76 \pm 0.29 \pm 0.15$	–	–	–
E687 (1996) [58]	$167.6 \pm 0.6 \pm 0.6$	–	–	–
CLEO (1993) [59]	$168.2 \pm 0.3 \pm 0.2$	–	–	–
CLEO (1989) [61]	$167.8 \pm 0.4 \pm 0.3$	–	–	–
ARGUS (1988) [62]	$168.2 \pm 0.5 \pm 1.6$	–	–	–
E400 (1987) [63]	$167.4 \pm 0.5 \pm 2.0$	–	–	–

Table 1.8: Comparison to the results in MeV/c^2 from other experiments for the doubly-charged Σ_c baryons. The first uncertainty is statistical and the second is systematic except for the world average shown in the second row as PDG. The uncertainty of the world average is the total uncertainty.

In this dissertation, the measurements of masses, decay widths, and mass splittings of the $\Sigma_c(2455)^{0/++}$ and $\Sigma_c(2520)^{0/++}$ baryons are discussed. In Chapters 2 and 3, the KEKB accelerator and Belle detector that the data used in this study are taken by are introduced. The event reconstruction and selection for this study are discussed in Chapter 4. The studies on backgrounds are covered in Chapters 5 and 6, the fit procedure of this study is described in Chapter 7, and the systematic uncertainties are estimated in Chapter 8. Finally, Chapter 9 is devoted for the results and conclusions of this study.

Chapter 2

The KEKB Accelerator

The KEKB accelerator is a positron-electron (e^+e^-) circular collider with asymmetric energies of a 3.5 GeV positron beam and an 8 GeV electron beam [64, 65]. The KEKB accelerator is located at High Energy Accelerator Research Organization (also known as KEK) in Tsukuba, Japan. It consists of a 3.5 GeV positron storage ring known as low-energy ring (referred to as "LER") and an 8 GeV electron storage ring known as high-energy ring (referred to as "HER"). The rings are approximately 3 km long in circumference each. The asymmetric energies of the electron and positron beams make the produced B mesons boost in the laboratory-frame, therefore, it allows to measure the decay-time differences between the B^0 and $\overline{B}^0$ mesons. This boost makes the produced B mesons have about 200 μm of mean flight length in the laboratory-frame, therefore, it provides a good environment to study time-dependent CP violation of particles.

The electron and positron beams consist of roughly 1,000 bunches with a bunch spacing of 0.59 m and collide with a ± 11 mrad crossing angle near the interaction point (referred to as "IP"). Since the main target of the KEKB accelerator is production of B mesons[1], a nominal center-of-mass energy is tuned to the $\Upsilon(4S)$ resonance at 10.58 GeV although it also produces not only Υ resonances up to $\Upsilon(5S)$ but also quark-antiquark ($q\overline{q}$) fragmentation[2]. Figure 2.1 illustrates the KEKB accelerator and its parameters are shown in Table 2.1.

The target luminosity of the KEKB accelerator at the beginning of its operation was 1×10^{34} cm^{-2}s^{-1}. The peak luminosity was recorded 2.11×10^{34} cm^{-2}s^{-1} in 2009, and it is the world best luminosity ever achieved by any e^+e^- accelerator [66, 67].

[1]Therefore, the KEKB accelerator is a B-factory.

[2]Since the particles studied in this study are made from the quark fragmentation, Υ resonances are not main concern in this dissertation.

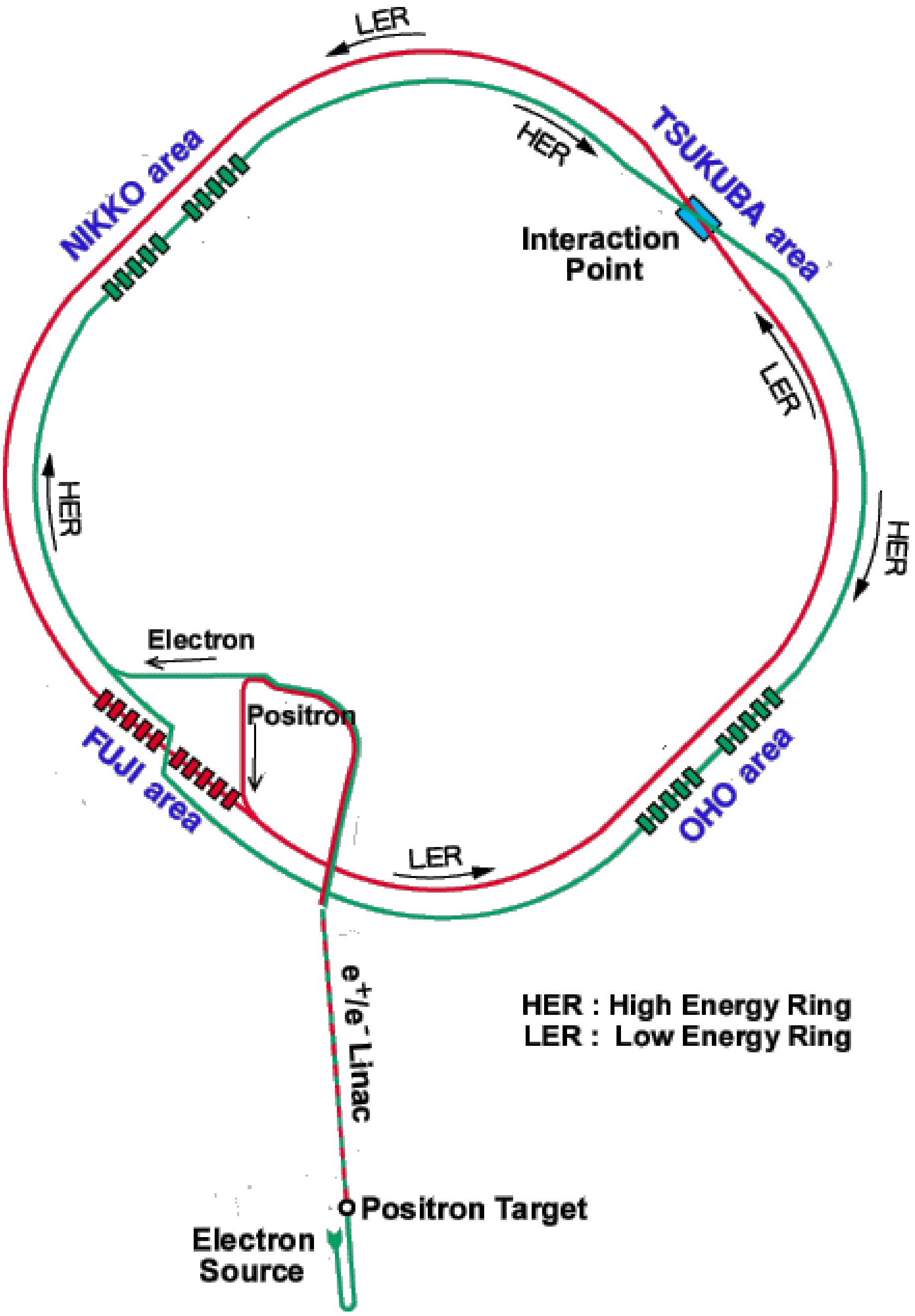

Figure 2.1: The KEKB accelerator. Once the electrons and positrons are produced, they are accelerated in the linear accelerator (Linac) and separately go into the storages. The electron beam (HER) goes clockwise while the positron beam (LER) goes counterclockwise. There are four experimental areas of Fuji, Nikko, Tsukuba, and Oho. The electron and positron beams collide to each other at Tsukuba area where the Belle detector is located. Image is taken from [68].

Parameters	LER	HER
Energy (E)	3.5 GeV	8.0 GeV
Circumference (C)	3016.26 m	
Luminosity ($\mathcal{L}$)	$1 \times 10^{34}\mathrm{cm}^{-2}\mathrm{s}^{-1}$	
Crossing angle (θ_x)	± 11 mrad	
Tune shift (ξ_x/ξ_y)	0.039 / 0.052 m	
Beta function at IP (β_x/β_y)	0.33 / 0.01	
Beam current (I)	2.6 A	1.1 A
Natural bunch length (σ_z)	0.4 cm	
Energy spread (σ_E)	7.1×10^{-4}	6.7×10^{-4}
Bunch spacing (s_B)	0.59 m	
Particles / bunch (N)	3.3×10^{10}	1.4×10^{10}
Emittance (ϵ_x/ϵ_y)	1.8×10^{-8} / 3.6×10^{-10} m	
Synchrotron tune (ν_s)	0.01 - 0.02	
Betatron tune (ν_x/ν_y)	45.52 / 45.08	47.52 / 46.08
Momentum compaction factor (α_p)	$1 \times 10^{-4} - 2 \times 10^{-4}$	
Energy loss / turn (U_0)	0.81 / 1.5 MeV	3.5 MeV
RF voltage (V_c)	5 - 10 MV	10 - 20 MV
RF frequency (f_{RF})	508.887 MHz	
Harmonic number (h)	5120	
Longitudinal damping time (τ_ϵ)	43 / 23 ms	23 ms
Total beam power (P_b)	2.7 / 4.5 MW	4.0 MW
Radiational power (P_{SR})	2.1 / 4.0 MW	3.8 MW
HOM power (P_{HOM})	0.57 MW	0.15 MW
Bending radius (ρ)	16.3 m	104.5 m
Length of bending (l_b)	0.915 m	5.86 m

Table 2.1: Parameter of the KEKB accelerator [68].

Chapter 3

The Belle Detector

3.1 Overview

The Belle detector [69, 70] is a large solid-angle magnetic spectrometer to detect charged and neutral particles. It has a volume of 7.3 m in length and 7.2 m in diameter as illustrated in Fig. 3.1. The Belle detector consists of its sub-detectors to detect various charged and neutral particles. As described in further sections, the sub-detectors of the Belle detector are silicon vertex detector (SVD) [71, 72], central drift chamber (CDC) [73], aerogel Čherenkov counter (ACC) [74], time of flight detector (TOF) [75], electromagnetic calorimeter (ECL) [76], extreme forward calorimeter (EFC) [77], K_L^0 and muon chamber (KLM) [78] with a 1.5 T superconducting solenoid magnet.

In the configuration of the Belle detector, a coordinate is defined as that the z-axis is parallel to the electron beam (HER), and the x- and y-axes are aligned horizontally and vertically corresponding to a right-handed coordinate system, respectively. The origin of the coordinate system is defined as the position of the nominal interaction point. In addition, the polar angle θ is defined as the angle from the positive z-axis, the radial component r is defined as transversal from the z-axis, and the azimuthal angle ϕ is defined as the angle around the z-axis from the positive x-axis which lies in the xy plane.

The sub-detectors cover a full 2π in the azimuthal angle (ϕ) and three ranges in the polar angle (θ); the barrel region which covers from 34° to 127°, the forward endcap region which covers from 17° to 34°, and the backward endcap region which covers from 127° to 150°. Therefore, the maximum coverage of the detector in the polar angle is from 17° to 150° which corresponds to 92% of the solid angle.

The data from each sub-detectors are triggered by the Belle trigger system [79]

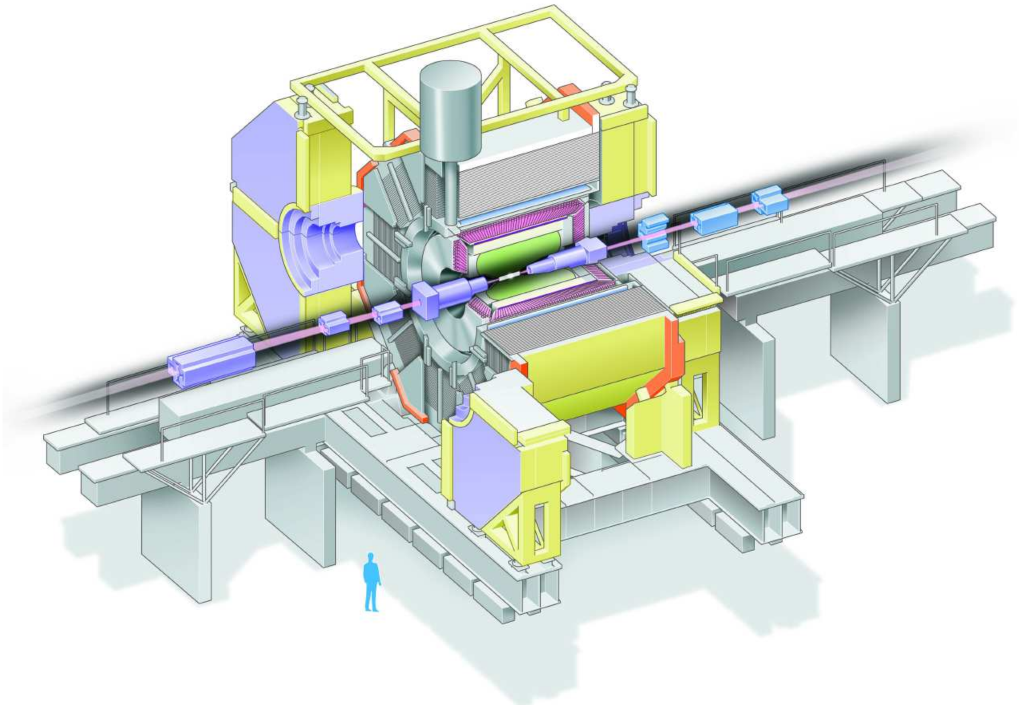

Figure 3.1: The Belle detector. Image is taken from Ref. [81].

and stored through the Belle data acquisition system [80].

3.2 Beam Pipe and Solenoid Magnet

In order to precisely measure the decay vertices of the B mesons, the detector should be placed as close to the interaction point as possible. Also, to minimize the multiple Coulomb scattering in the beam pipe wall, a thin beam pipe [69] is required. The central part of the beam pipe which is defined as -4.6 cm $< z <$ 10.1 cm is a double-wall beryllium cylinder with an inner diameter of 40 mm. The beam pipe is designed to have an 20 and 23 mm of an inner and outer wall radius, and the gap between the inner and outer wall provides a helium gas channel for cooling. With an assumption of a 100 W heat load which is uniformly distributed, the maximum temperatures for the beryllium walls are calculated to be 25°C and 5°C with 2 g/s helium flow velocity at a 1.5 atm pressure and a 0.0007 atm pressure drop, respectively. The outer beryllium wall is coated by a 20 μm thick gold sheet to reduce the low-energy X-ray background from HER.

After the upgrade of the silicon vertex detector in 2003, the beam pipe was replaced of which has the radius of 15 mm, and the thickness of the gold coating of the beryllium wall was changed to be 10 μm [72]. This replacement allows the

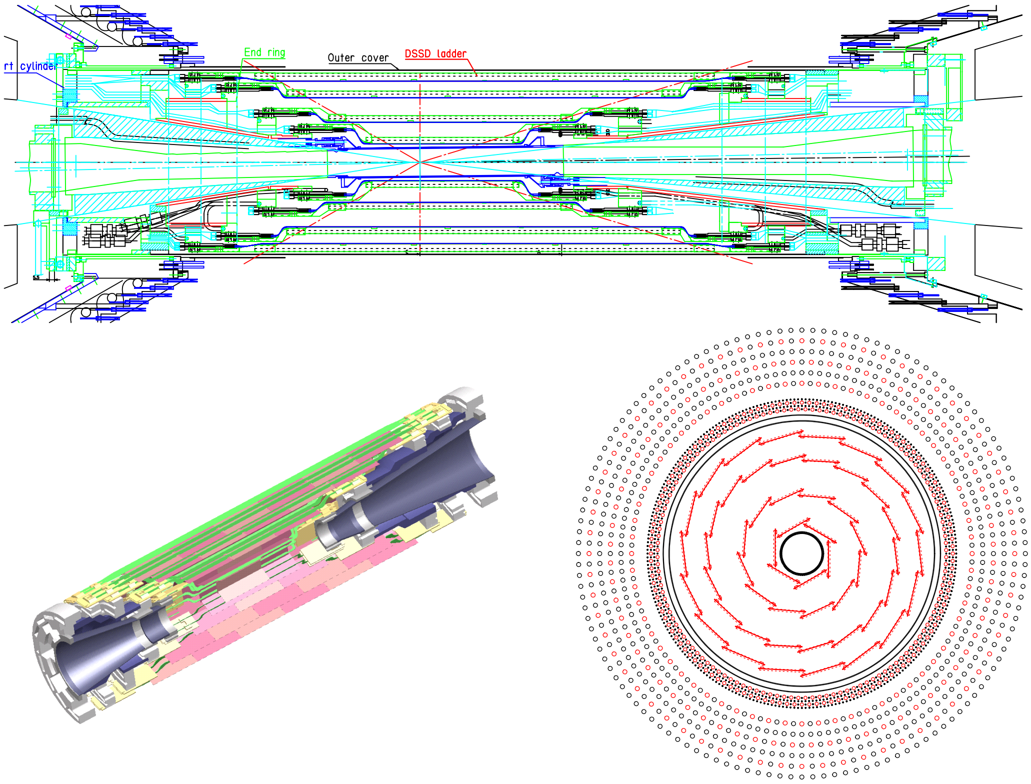

Figure 3.2: The silicon vertex detector of the Belle detector. Side-view (top), quarter-view (left-bottom), and top-view (right-bottom) are illustrated. Images are taken from Ref. [81].

silicon vertex detector to be closer to the interaction point, therefore, it gives better vertex resolution.

To measure the momenta of charged particles, it is necessary to make the trajectory of the particles bend by using a magnetic field. A charged particles traveling in a magnetic field follows a helix path with a radius of curvature given by

$$R = \frac{|\vec{p}_T|}{0.3B}$$

where R is the radius of the curvature in meter, $\vec{p}_T$ is the transversal component of the momentum vector of the charged particle in GeV/c, and B is the magnetic field in Tesla that the charged particle travels in. To give a magnetic field, there is a superconducting solenoid which provides a magnetic field of 1.5 T. The superconducting solenoid has a cylindrical volume of 3.4 m in diameter and 4.4 m in length and consists of a single layer niobium-titanium-copper alloy embedded in a high purity aluminum stabilizer.

3.3 Silicon Vertex Detector (SVD)

The silicon vertex detector (SVD) [71, 72] is the innermost sub-detector and provides an ability to measure the spatial information of the decay vertices of detected particles. The SVD consists of four layers of the double-sided silicon detector (DSSD) which is originally developed for the DELPHI detector [82]. At the beginning of the experiment, the SVD had three layers with 8, 10, and 14 ladders surrounding the z-axis with radii of 30, 45.5, and 60.5 m, and they covered a polar angle of $23° < \theta < 139°$ which corresponds to 86% of the full solid angle (SVD1) [71]. In 2003, the SVD1 was upgraded to cover larger solid angle and to have more layers (SVD2) [72]. The first, second, third, and fourth layers consist of 6, 12, 18, and 18 ladders surrounding the z-axis with radii of 20, 43.5, 70, and 88 mm, respectively, as shown in Fig. 3.2. Each ladders consist of 2, 3, 5, and 6 DSSDs for the first, second, third, and fourth layers. The SVD2 covers the polar angle of $17° < \theta < 150°$ which corresponds to 92% of the full solid angle.

There are two kinds of the DSSD for ladders; 76.4×34.9 mm for the fourth layer and 79.2×28.4 mm for the others. Strips on each side of a DSSD are arranged perpendicular to those on the other side, and this enables to measure not only the z-position but also $r - \phi$ position. The strip pitch of the DSSD for the inner three layers is 75 μm in the z-axis and 50 μm in the ϕ direction while the one for the fourth layer is 73 μm in the z-axis and 65 μm in the ϕ direction. On each sides, 1024 and 512 strips are placed in z-axis and ϕ direction, respectively.

The performance of the SVD1 and SVD2 are measured by the resolution on the point of closest approach to the interaction point, known as the impact parameters. The resolutions in $r - \phi$ plane are given by

$$\sigma_{r-\phi}^{\mathrm{SVD1}} = 19.2 \oplus \frac{54.0}{p\beta \sin^{3/2}\theta}$$

$$\sigma_{r-\phi}^{\mathrm{SVD2}} = 21.9 \oplus \frac{35.5}{p\beta \sin^{3/2}\theta}$$

and along z-axis,

$$\sigma_{z}^{\mathrm{SVD1}} = 42.2 \oplus \frac{44.3}{p\beta \sin^{3/2}\theta}$$

$$\sigma_{z}^{\mathrm{SVD2}} = 27.8 \oplus \frac{31.9}{p\beta \sin^{3/2}\theta}$$

in μm where p is a momentum of a particle, β is a ratio of a particle velocity and the speed of light (v/c), and θ is a polar angle between a momentum vector of a

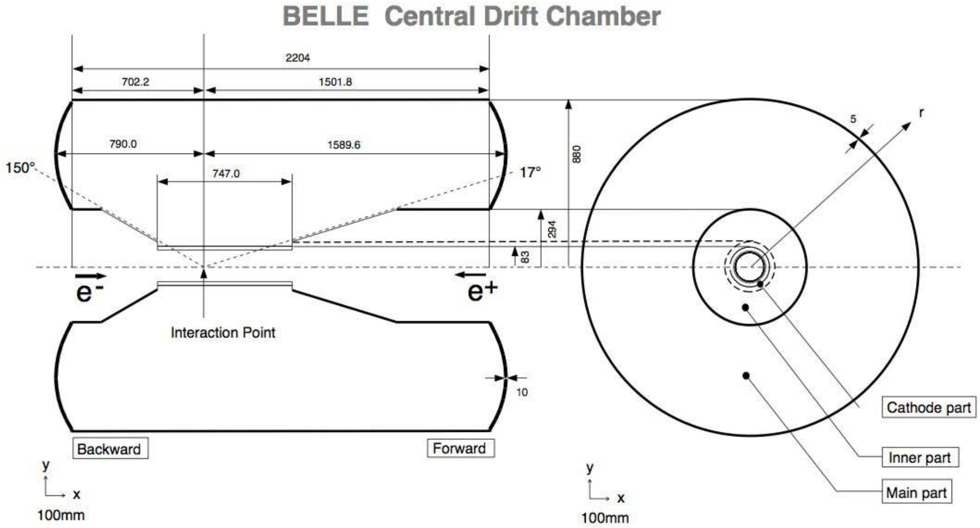

Figure 3.3: The central drift chamber of the Belle detector. Side-view (left) and top-view (right) are illustrated. Lengths are in mm. Image is taken from Ref. [69].

particle and the z-axis.

3.4 Central Drift Chamber (CDC)

The central drift chamber (CDC) [73] is a charged particle tracking system which measures track momentum from a curvature of a charged particle in the magnetic field induced by the solenoid magnet, and is illustrated in Fig. 3.3. The CDC measures the energy deposit per unit length (dE/dx) of a charged track to provide the particle identification information as well. It covers the angular range of $17° < \theta < 150°$ which corresponds to 92% of the full solid angle.

The inner side of the CDC is enclosed with aluminum as well as the outer edges. The outer radius is 880 mm, and the inner radius extends to 80 mm without any walls in order to obtain good tracking efficiency for low momentum tracks with minimal interleaving material. The forward and backward inner regions have conical shapes to clear the accelerator components while maximizing the acceptance.

There are 50 cylindrical layers, each containing between three and six either axial or small-angle stereo layers, and three cathode strip layers. A positively biased sense wire is surrounded by eight negatively biased field wires, and they make a drift cell which is nearly square. The sense wires are gold-plated tungsten wires of 30 μm in diameter to maximize the drift electric field, and the field wires are unplated aluminium of 126 μm in diameter. There are 8,400 drift cells inside the CDC, and each of them has a maximum drift distance between 8 and 10 mm and a radial

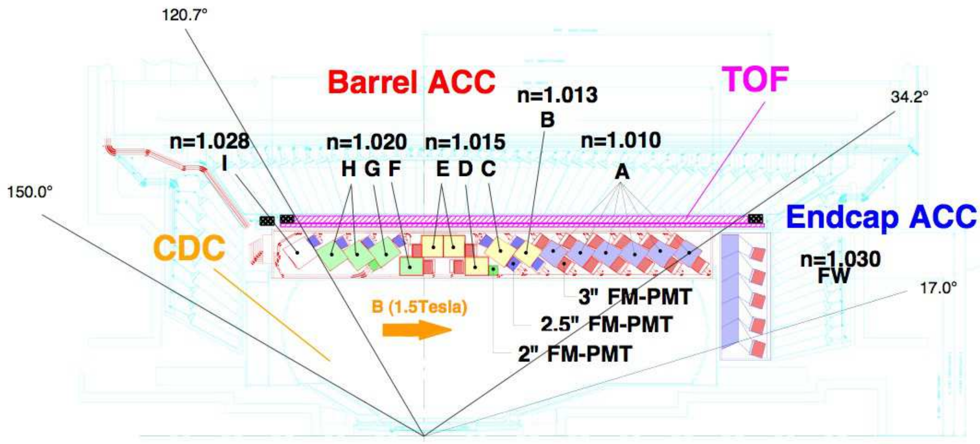

Figure 3.4: The aerogel Čherenkov counter of the Belle detector. Image is taken from Ref. [69].

thickness that ranges from 15.5 and 17 mm except for the inner three layers.

The CDC is filled by a low-Z gas, such as a 50% helium (He) and 50% ethane (C_2H_6) mixture, which is selected to reduce multiple Coulomb scattering for a good momentum resolution, especially for low momentum tracks.

When a charged particle passes through the drift cell, it ionizes electrons which are accelerated by the electric field. The accelerated electrons produce secondary ionizations in the gas, and the resulting avalanche is collected by the sense wires. This process is called gas amplification, and it increases the signal by a factor in excess of 10^6. Before the amplification, the electrons have a specific drift velocity, therefore, the measured pulse height and drift time are related to the energy deposit, dE/dx. Roughly half the wires are in parallel to the z-axis to provide the transverse momentum (p_T) information while the rest of wires are rotated by a small angle of ± 50 mrad to the z-axis to maximize the resolution along the z-axis.

The p_T resolution of the CDC is given by

$$\frac{\sigma_{p_T}}{p_T} = (0.28 p_T) \oplus \left(\frac{0.35}{\beta}\right)$$

with p_T given in GeV/c. If information from the SVD is combined, the resolution improves to

$$\frac{\sigma_{p_T}}{p_T} = (0.19 p_T) \oplus \left(\frac{0.30}{\beta}\right).$$

3.5 Aerogel Čherenkov Counter (ACC)

The aerogel Čherenkov counter (ACC) [74] separates charged kaons and pions which have momenta in the range from approximately 1.2 to 3.5 GeV/c. Charged particles that pass a medium with a velocity larger than the speed of light in the medium c_{medium} emit coherent radiation known as Čherenkov radiation. The speed of light in a medium is related to the refractive index n of the medium by $c_{\text{medium}} = c_{\text{vacuum}}/n$ where c_{vacuum} is the speed of light in vacuum. For a particle with mass m, momentum p, and velocity β, the Čherenkov radiation is emitted if

$$n > \frac{1}{\beta} = \sqrt{1 + \left(\frac{m}{p}\right)^2}.$$

By choosing a suitable refractive index, pions at a given momentum may satisfy the condition above, therefore, they emit Čherenkov radiation while kaons at the same momentum would not. Using this phenomenon, the ACC is able to separate charged kaons and pions.

The ACC consists of 960 counter modules segmented into 60 cells in the azimuthal direction for the barrel part which covers the angle $34^\circ < \theta < 127^\circ$, and 228 modules arranged in 5 concentric layers for the front end-cap part which covers $17^\circ < \theta < 34^\circ$ of the detector as shown in Fig. 3.4. The barrel part consists of five types of silica aerogels with different refractive indices. From the low to high θ angle, 360 modules of aerogels with the refractive index of 1.010, 60 modules with 1.013, 240 modules with 1.015, 240 modules with 1.020, and 60 modules with 1.028 are located in the barrel part of the ACC. Five aerogel tiles are stacked in an aluminum box of approximate dimensions $12 \times 12 \times 12$ cm^3. In order to detect Čherenkov light effectively, one and two fine mesh-type photomultiplier tubes (FM-PMTs) are attached directly to the aerogel on the sides of the box in the end-cap and barrel part, respectively.

3.6 Time-of-Flight Detector (TOF)

The time-of-flight detector (TOF) [75] provides an additional information for the particle identification especially for the K/π separation. The TOF system is designed for the slow particles of momenta $p < 1.2$ GeV/c, which corresponds to 90% of particles produced from $B\overline{B}$ events and is not covered by the momentum range of the ACC detector discussed in Sec. 3.5. The TOF detector has 100 ps time resolution for a 1.2 m flight length.

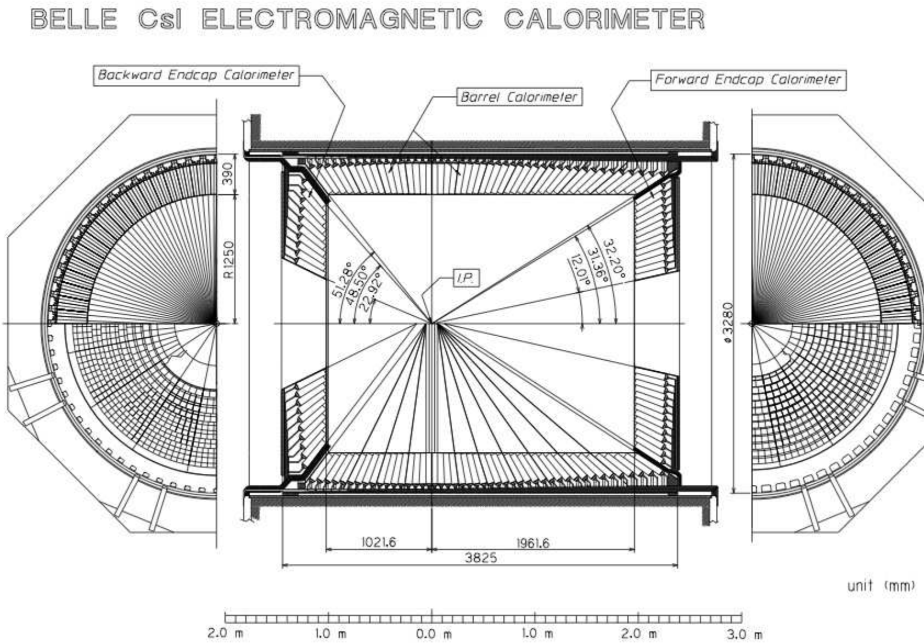

Figure 3.5: The electromagnetic calorimeter of the Belle detector. Image is taken from Ref. [69].

In addition to the particle identification, the TOF provides fast timing signals for the trigger system to generate gate signals for analog-to-digital converters (ADC) and stop signals for time-to-digital converters (TDC). In order to keep the fast trigger rate below 70 kHz, a thin trigger scintillation counters (TSC) is used.

The TOF consists of 128 TOF counters of plastic scintillators and 64 TSCs in a barrel side. Two trapezoidal-shaped TOF counters and a TSC form a TOF module with a 1.5 cm intervening radial gap. The TSC in a module is read out via a single photomultiplier tube (PMT) which is coupled to the TSC via a plastic light guide. In total 64 TOF modules are located at a radius 1.2 m from the interaction point and cover a polar angle range from 34° to 120°.

3.7 Electromagnetic Calorimeter (ECL)

Electrons interacting in a material lose their energy via ionization loss and bremsstrahlung radiation. The bremsstrahlung photons can cause e^+e^- pair production if the energy of the electron is sufficient. The electrons and positrons from the pair production can also make further ionization and bremsstrahlung photons, and the same process can continue, therefore, the electromagnetic shower is produced. The electromagnetic calorimeter (ECL) [76] is designed to measure this electromagnetic shower for the electron and photon identification.

Most of the photons are end products of cascade decays, therefore, they have relatively low-energy of < 500 MeV. Moreover, a few important decays, such as $B \to K^*\gamma$ and $B^0 \to \pi^0\pi^0$ produce photons energies up to 4 GeV, therefore, a high resolution over wide-energy range is required.

The ECL consists of 8,736 cesium iodide crystals, doped with thallium (CsI(Tl)) and consists of three parts: the barrel, forward and backward end-cap parts as shown in Fig. 3.5. The barrel part covers a polar angle $32.2° < \theta < 128.7°$ and consists of 46 and 144 segments in polar and azimuthal angles, therefore, 6,624 crystals in total. The forward end-cap part covers a polar angle $12.4° < \theta < 31.4°$ and consists of 13 segments in polar angle and up to 144 segments in azimuthal angle, therefore, 1152 crystals in total. The backward end-cap part covers $130.7° < \theta < 155.1°$ and consists of 10 segments in polar angle and up to 144 segments in azimuthal angle, therefore, 960 crystals in total. The shape of each crystal varies by position, but a typical crystal has a tower-like shape with a front face of 55 mm $\times$ 55 mm, a rear face of 65 mm $\times$ 65 mm, and a length of 30 cm.

Since the angular coverage of the ECL is the same with the CDC described in Sec. 3.4, photons can be identified by matching charged track from the CDC and a shower profile in the ECL. The position resolution of the ECL is

$$\sigma = 0.27 \oplus \frac{3.4}{\sqrt{E}} \oplus \frac{1.8}{\sqrt[4]{E}}$$

in mm, and the energy resolution is

$$\frac{\sigma_E}{E} = \left(\frac{0.066}{E}\right) \oplus \left(\frac{0.81}{\sqrt[4]{E}}\right) \oplus 1.34$$

with energy E given in GeV.

3.8 Extreme Forward Calorimeter (EFC)

The extreme forward calorimeter (EFC) [77] extends the angular coverage of the ECL to $6.4° < \theta < 11.5°$ by the forward EFC and $163.3° < \theta < 171.2°$ by the backward EFC as shown in Fig. 3.6. It uses radiation-hard crystals of bismuth germanate ($Bi_4Ge_3O_{12}$) and is attached to the front faces of the cryostats of the compensation solenoid magnets of the KEKB accelerator surrounding the beam pipe.

The EFC improves the sensitivity to some physics processes such as $B \to \tau\nu$ and provides ability to function as a beam mask to reduce backgrounds for CDC and

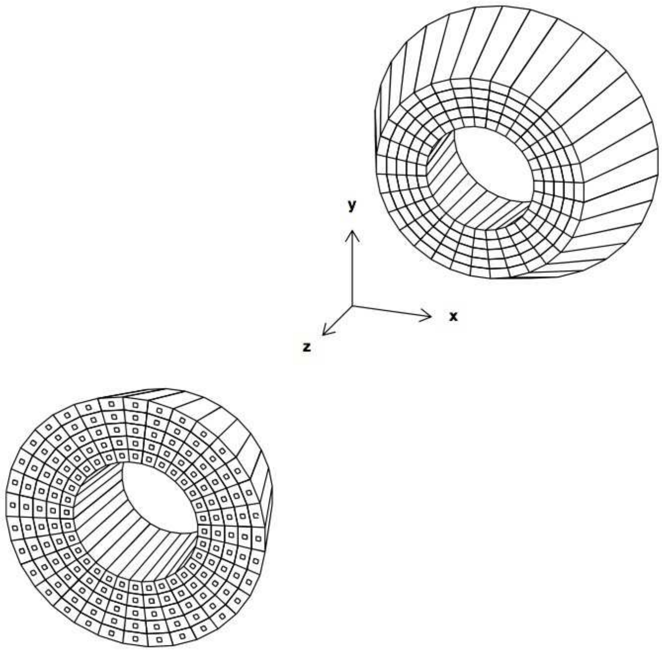

Figure 3.6: The extreme forward calorimeter of the Belle detector. Image is taken from Ref. [69].

information for beam and luminosity monitoring. It can also be used as a tagging device for two-photon physics.

3.9 K_L and Muon Detector (KLM)

Since particles such as K_L and μ are not stopped within the detectors explained so far, the K_L and muon detector (KLM) [78] for detecting K_L and μ is installed at the most outer side of the Belle detector. The KLM consists of a barrel part which covers the polar angle $45^\circ < \theta < 125^\circ$ and end-cap parts which extend the angular coverage to $20^\circ < \theta < 155^\circ$. It consists of alternating 15 detector layers and 14 iron plate layers with a thickness of 4.7 cm. The detector layers detect charged particles by using glass-electrode-resistive plate counters (RPC). The RPC consists of two parallel plates with a gas-filled gap which provides a high resistivity. Figure 3.7 illustrates a superlayer of the KLM.

If a K_L interacts in the iron plates, a shower of ionized particles is created. An ionized particle passing through the gap induces a streamer in the gas and results a local discharge of the plates, and the discharge makes a signal. By matching the track in the CDC, μ can be identified. In contrast, K_L does not make a track in the CDC because they are electrically neutral, therefore, by the lack of a matching track in the

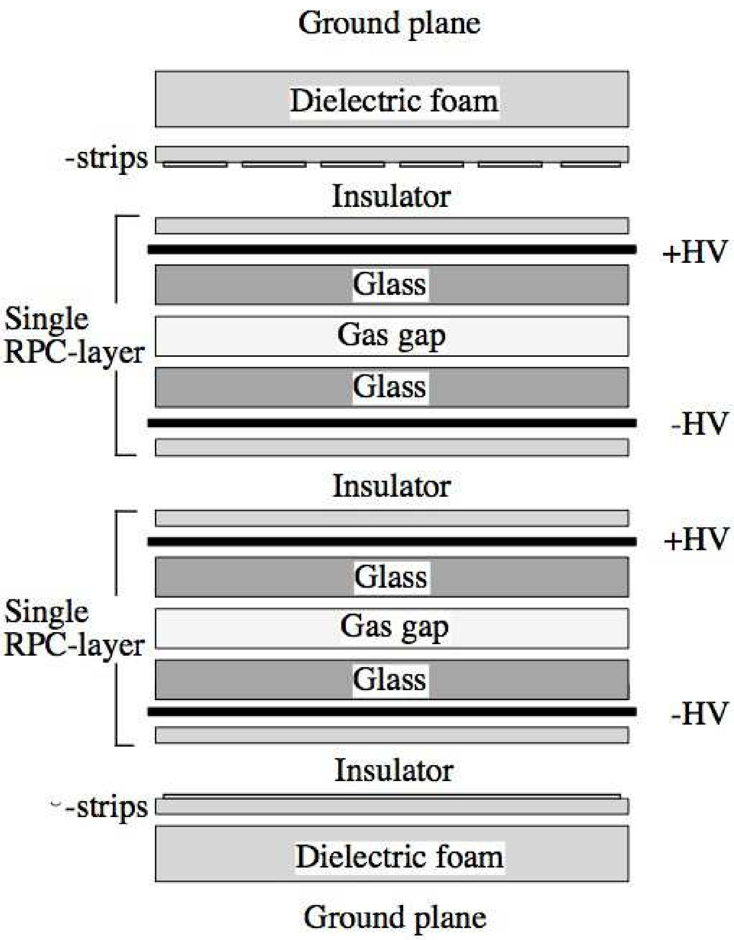

Figure 3.7: Cross-section of a superlayer of KLM of the Belle detector. Image is taken from Ref. [69].

Physics process	Cross-section (nb)	Rate (Hz)
$\Upsilon(4S) \to B\overline{B}$	1.2	12
Hadron production from continuum	2.8	28
$\mu^+\mu^- + \tau^+\tau^-$	1.6	16
Bhabha ($\theta_{\rm lab} \geq 17°$)	44	4.4
$\gamma\gamma$ ($\theta_{\rm lab} \geq 17°$, $p_T \geq 0.1$ GeV/c)	∼15	∼35
Total	∼67	∼96

Table 3.1: Total cross-section and trigger rates with $\mathcal{L} = 10^{34}$ cm^{-2}s^{-1} from various physics processes at $\Upsilon(4S)$ [69].

CDC, K_L can be identified. Furthermore, μ interactions can be distinguishable from hadronic interactions by their increased penetration depth and characteristically narrower clusters.

3.10 Trigger System

The Belle trigger system consists of the Level-1 hardware trigger and the Level-3 software trigger. The Level-1 hardware trigger consists of sub-detector trigger systems and the central trigger system called as the Global Decision Logic (GDL) [79]. The Level-3 software trigger is implemented in an online computing farm as a part of the data acquisition system (DAQ) described in Sec. 3.11.

Table 3.1 summarizes the total cross-section and trigger rates at the designed luminosity of 10^{34} cm^{-2}s^{-1} for various physical processes [69]. Because of the high luminosity and beam current, there are many events which are not manageable by the DAQ system. In order to collect physical interesting events and discard uninteresting events, a powerful trigger system is desired. Based on the simulation studies, approximately 100 Hz beam-related backgrounds are expected, and triggering the backgrounds is necessary. In this section, the Level-1 hardware trigger system is discussed, and its schematic view is shown in Fig. 3.8.

The Belle trigger system extensively utilizes programmable logic chips, such as field programmable gate array (FPGA) and complex programmable logic device (CPLD) chips, which provides the large flexibility of the trigger logic and reduce the number of types of hardware modules.

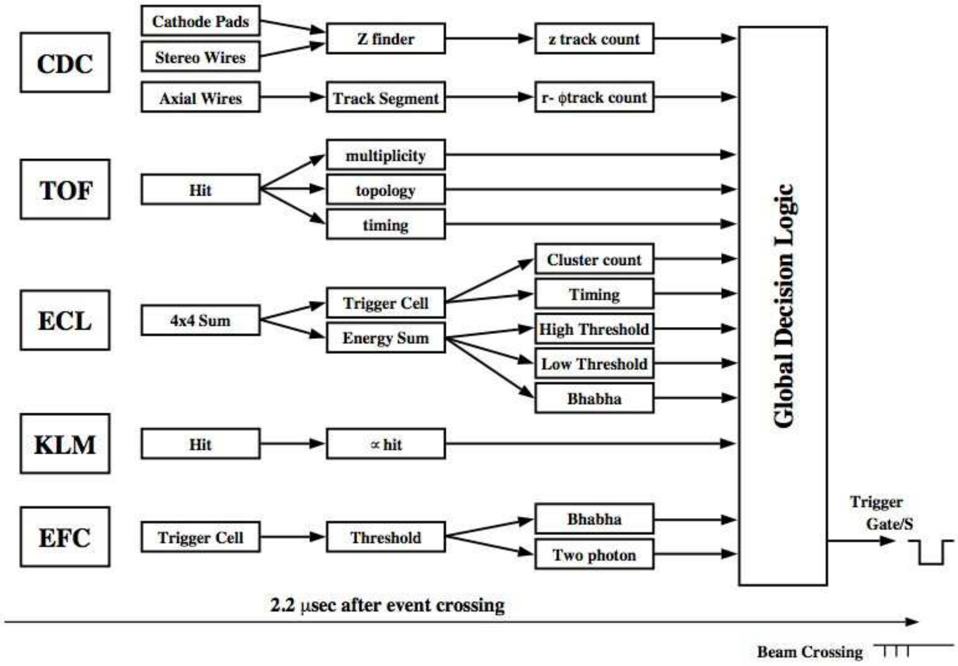

Figure 3.8: The Level-1 trigger system for the Belle detector. Image is taken from Ref. [69].

3.10.1 CDC Trigger System

The CDC trigger system triggers the events detected by the CDC detector. It is required to be fully efficient for tracks originating from the interaction point and relatively insensitive to background tracks from other sources. The CDC trigger provides the capabilities of $r - \phi$ trigger based on signals from axial superlayers.

The $r - \phi$ trigger is the main component of the charged track triggers. It is formed using discriminated axial-wire hit signals. Anode wires in each superlayer are grouped into track segment finder (TSF) cells as shown in Fig. 3.9, and the hit pattern in each cell is examined by a memory lookup (MLU) table to test if a candidate track segment exists. There are 17 and 11 wires in the TSF cells for the innermost and outer superlayers, and 64, 96, 144, 192, 240, and 288 TSF cells are defined as the superlayer radius increases. The TSF cells in the innermost superlayers are important to reject tracks originating away from the interaction point.

The TSF outputs are processed by logical OR operation in a superlayer to form track finder (TF) wedges. There are 64 wedges, and a wedge is shown in Fig. 3.10. The hit patterns of the TF wedge are fed into the next MLU stage, and the second-stage MLU provides several outputs based on different track categories according to short and full track patterns where the short track is in the three innermost trigger

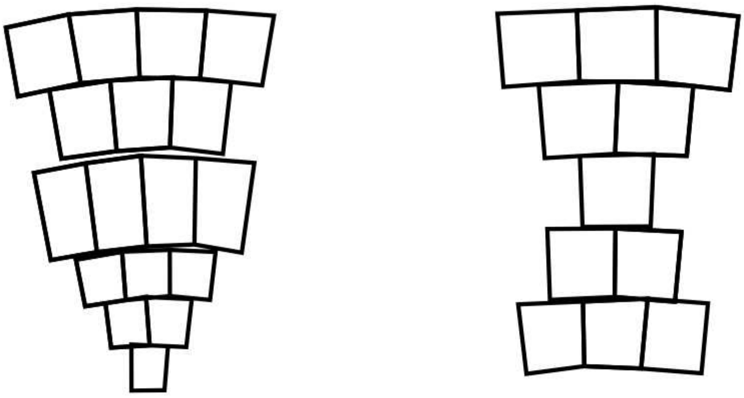

Figure 3.9: CDC track segment finder (TSF) for the innermost (left) and outer (right) superlayers. Image is taken from Ref. [69].

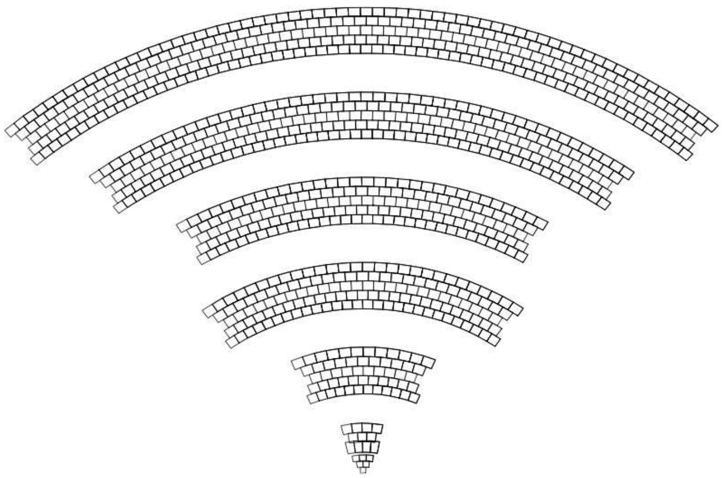

Figure 3.10: CDC track finder (TF) wedge. Image is taken from Ref. [69].

layers with $p_T \geq 200$ MeV/c, and the full track is of which goes through all CDC trigger layers with $p_T \geq 300$ MeV/c. Finally, the output signals from the 64 TF wedges are determined as an event topology by counting the number of short and full tracks, determining the maximum opening angle between tracks, and recognizing the back-to-back topologies. The determined topology signals are sent to the GDL which is discussed later.

3.10.2 TOF Trigger System

The TOF trigger system provides an event timing signal and information on the hit multiplicity and topology to the GDL. The information on the hit multiplicity and topology can be used for the internal event selection and the reduction of the timing signal rate before the delivery to the GDL. The timing signal is referred by the SVD, CDC, and ECL readout electronics, therefore, the TOF trigger system should be able to provide the precise information to them on time. For the CDC and ECL readout electronics, a time jitter is less than 10 ns, and the mean time stays within a small time range from 4.8 to 7.2 ns for the TOF configuration. Since the time jitter is expected to be less than 1 ns at nominal discrimination level, the TOF provides a time jitter about 5 ns. For the SVD readout electronics, the shaping time is required to be faster than 2 μs by GDL to make an event decision. The TOF readout and trigger system provides the information with approximately a 0.85 μs delay which includes about 500 ns to calculate internal event multiplicity and topology.

3.10.3 ECL Trigger System

The ECL is expected to generate fast trigger signals to provide a fully efficient trigger for both neutral and charged particles. The ECL trigger is considered as both a total energy and a cluster counting trigger. The total energy trigger is sensitive to events with high electromagnetic energy deposit while the cluster counting trigger is sensitive to multi-hadronic events that contain low-energy clusters and minimum ionizing particles. Fast shaped signals with a 200 ns shaping time from each counter are generated in Shaper/QT (SHQT) and merged into a trigger cell (TC) composed of adjacent 4×4 crystals that are minimum units for ECL trigger system. Each TC is controlled by a trigger circuit board named sum-trigger module (STM), and a TC signal above a threshold energy from 50 to 100 MeV is recognized as a hit cluster. The noise level of TC units is measured to be about 8 MeV, and the root-mean-square (RMS) timing resolution is less than 20 ns.

Total energy information is one of the most effective triggers to identify hadronic events in high-energy e^+e^- annihilation. The total energy trigger recognizes interesting events by testing the deposit energy in the ECL. Using the total energy deposit composing specific ϕ-rings, which is a logical segment defined along the ϕ direction, a Bhabha event are identified if an event has a larger total energy than the defined threshold energy. Along the θ direction, 12 and 5 ϕ-rings are arranged in the barrel and end-cap regions (3 in the forward and 2 in the backward end-cap regions). The Bhabha events are triggered using back-to-back condition in the center-of-mass frame, and the trigger efficiency is greater than 99%.

3.10.4 KLM Trigger System

The role of the KLM trigger is to save events which include muon tracks as many as possible. Therefore, the high efficient trigger is desired. The KLM subsystem consists of the barrel and end-cap KLM, and both are divided into forward and backward parts. Each of the forward and backward parts of the barrel KLM consists of 8 sectors while each of the end-cap KLM consists of 4 sectors. Each sectors has 15 and 14 superlayers for the barrel and end-cap KLM, and each superlayers consists of two RPC plates. The output of superlayers has 48 (barrel ϕ, z, and end-cap θ readout) or 96 copper strips (end-cap ϕ readout).

Because of the geometric configuration of the KLM, the trigger efficiency drops at $\cos\theta = -0.6$ and $\cos\theta = 0.9$ in polar angle, and $\phi = \pm 1.5$. Except for the geometric effect, the KLM trigger efficiency is estimated to be about 98% in average.

3.10.5 EFC Trigger System

The EFC trigger system provides two types of trigger information according to the energy and location of signals in the $Bi_4Ge_3O_{12}$ crystals: a Bhabha trigger from coplanar forward and backward coincidence of energetic electromagnetic shower, and a two-photon trigger from a single electromagnetic shower together with CDC tracks or ECL clusters.

The EFC trigger consists of defined trigger cells. Two neighboring ϕ segments have three trigger cells according to different θ angles. There are two crystals in the innermost ϕ segment while four crystals in the others. The analog sum of crystal signals from the same trigger cell is fed into a constant fraction discriminator and gives the trigger output. The threshold energy of the trigger cell is approximately

1 GeV. The trigger cells are grouped into four sectors in the azimuthal direction in each of the forward and backward EFC.

For the Bhabha trigger, the trigger output of one sector is used to form a back-to-back logic, and it is also combined with central tracking and calorimeter information for the two-photon trigger.

3.10.6 Global Decision Logic

The Global Decision Logic (GDL) [79] is the central trigger system of the Belle detector, and its schematic design is shown in Fig. 3.11. It receives up to 48 trigger signals from sub-detectors and makes global correlations among them. The GDL is designed to function in a pipelined manner with 32 MHz clock in order to avoid dead-time losses, and it takes 350 ns to generate the final trigger signal. The GDL utilizes the following modules to process the trigger signals:

- Input Trigger Delay (ITD) which adjusts the timing of input trigger signals to satisfy the latency of 1.85 μs,
- Final Trigger Decision (FTD) which performs the global trigger logic, correlating the information from sub-detector trigger systems,
- Prescale and Mask (PSNM) which prescales the high rate input triggers for calibration and monitoring, and disables the unused triggers from FTD,
- Timing Decision (TMD) which generates the final trigger signal at 2.2 μs latency based on the timing trigger from TOF and ECL,

and they utilize the FPGA and CPLD chips for the sufficient flexibility of the Belle trigger system.

The timing decision logic uses a 64 MHz clock to provide 16 ns timing accuracy. The trigger signals from GDL are synchronized to the beam crossing time since clock signals are made from the KEKB RF signal. The trigger signals at each step of GDL are sent to scalers to monitor trigger rates and dead-times.

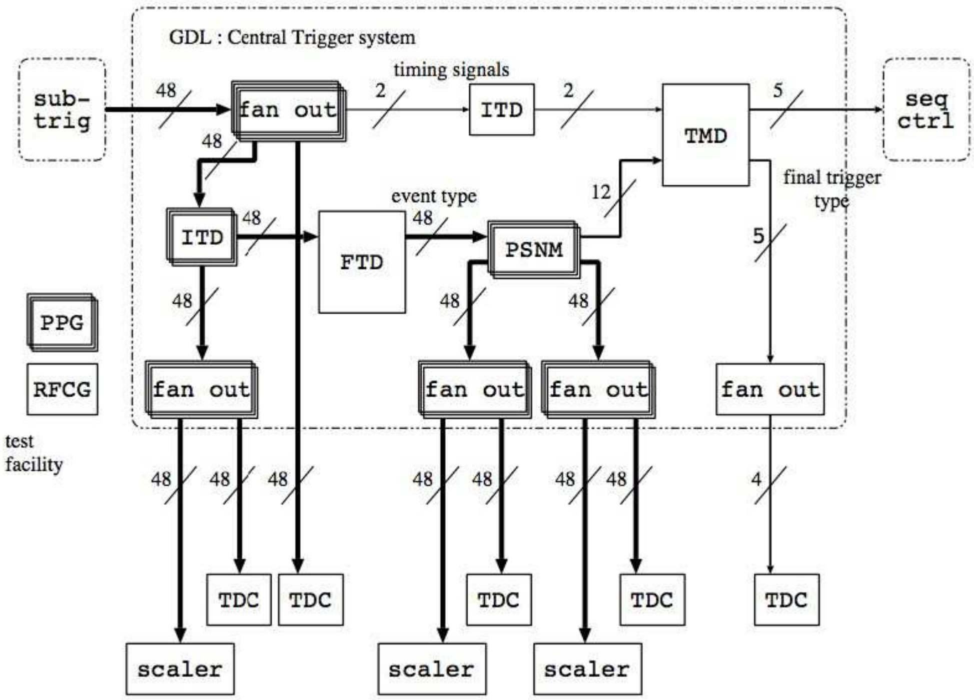

Figure 3.11: Schematic design of the Global Decision Logic. The components are described in the text. Image is taken from Ref. [69].

3.11 Data Acquisition System

In order to satisfy the data acquisition (DAQ) requirements, the DAQ system [80] works at 500 Hz with a dead-time fraction of less than 10% by utilizing the distributed-parallel system. The schematic view of the Belle DAQ system is shown in Fig. 3.12.

The entire system is segmented into seven subsystems in parallel that each handles the data from a sub-detector. Data from the subsystems are merged by an event builder to be handled as an event-by-event data. The event data transferred to an online computing farm, and the farm processes higher level of triggering by doing a fast event reconstruction. The processed data in the online computing farm are sent to a mass storage system via optical fibers.

A typical data size of a hadronic event by $B\overline{B}$ or $q\overline{q}$ production is measured to be approximately 30 kB which corresponds to the maximum data transfer rate of 15 MB/s.

Instead of using analog-to-digital converter to digitize the amplitude of a signal, a charge-to-time (Q-to-T) technique [83] is employed to read out signals from the most of the detectors. By digitizing a time interval between start and stop time of discharge in a capacitor, the timing and amplitude of the input signal is determined. The data from the CDC, ACC, TOF, ECL, and EFC are read out by using the Q-to-T and TDC techniques, and the data from KLM is read out by using the TDC only. However, the data from the SVD are read out by intelligent flash analog-to-digital converter modules with an embedded digital signal processors.

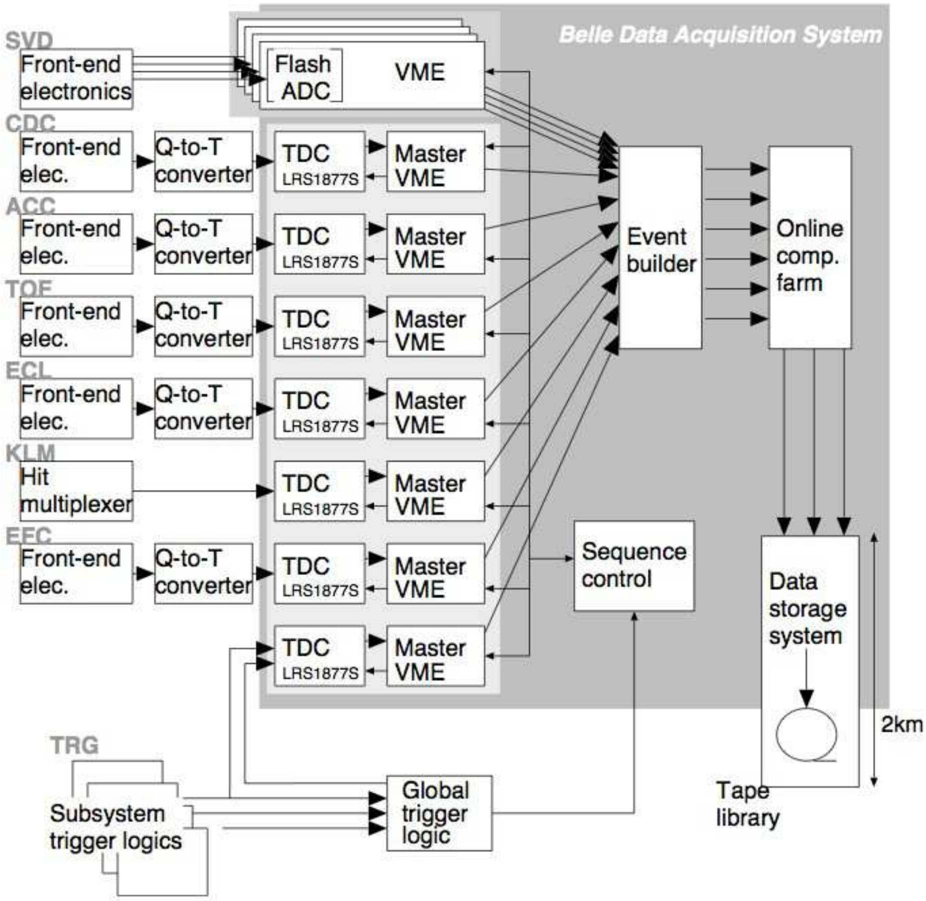

Figure 3.12: Schematic view of the DAQ system. Image is taken from Ref. [69].

3.12 Particle Identification

Using the information collected by the sub-detectors described in this chapter, the particle identification can be done [84]. The particle identification can be divided into three pieces; the kaon, electron, and muon identifications.

3.12.1 Kaon identification

For the kaon identification, the information from the CDC, TOF, and ACC are used. In the CDC, the kaon identification including the separation from proton and pion is done by using the energy-loss (dE/dx) measurement which follows the Bethe-Bloch formula [85],

$$-\frac{dE}{dx} = 2\pi N_a r_e^2 m_e c^2 \rho \frac{Z}{A}\frac{z^2}{\beta^2}\left[\ln\left(\frac{2m_e\gamma^2 v^2 W_{\max}}{I^2}\right) - 2\beta^2\right]$$

where N_a is the Avogadro's number ($= 6.022\times10^{23}$ mol^{-1}), r_e is the classical electron radius ($= 2.817 \times 10^{-13}$ cm), m_e is the electron mass, z is a charge of an incident particle in units of e, β is a v/c of an incident particle, γ is the Lorentz factor ($= 1/\sqrt{1-\beta^2}$,) $W_{\max}$ is a maximum energy transfer in a single collision, and ρ, Z, A are a density, an atomic number, and an atomic weight of an absorbing material. The measured energy-loss in CDC is shown in Fig. 3.13. In the CDC, 47 layers are used to measure dE/dx, and the 80% truncated mean method is employed to get the dE/dx value for a charged track. The particle likelihood in the CDC is defined assuming Gaussian distribution of the energy-loss

$$\mathcal{L}_i^{\mathrm{CDC}} = \frac{e^{-\chi_i^2/2}}{\sqrt{2\pi}\sigma_{dE/dx}}$$

where $\sigma_{dE/dx}$ is resolution of dE/dx, and χ_i^2 is defined as

$$\chi_i^2 = \left(\frac{(dE/dx)_{\mathrm{measured}} - (dE/dx)_i}{\sigma_{dE/dx}}\right)^2$$

where $(dE/dx)_{\mathrm{measured}}$ is the measured energy-loss, and $(dE/dx)_i$ is the expected energy-loss for i-th particle species (e, μ, π, K, or p).

In the TOF, the particle likelihood is defined as

$$\mathcal{L}_i^{\mathrm{TOF}} = \frac{e^{-\chi_i^2/2}}{\prod_{l=1}^{\mathrm{ndf}}\sqrt{2\pi}\sigma_{\mathrm{TOF}}}$$

where σ_{TOF} is TOF resolution, and χ_i^2 is defined as

$$\chi_i^2 = \Delta_i^T E^{-1} \Delta_i$$

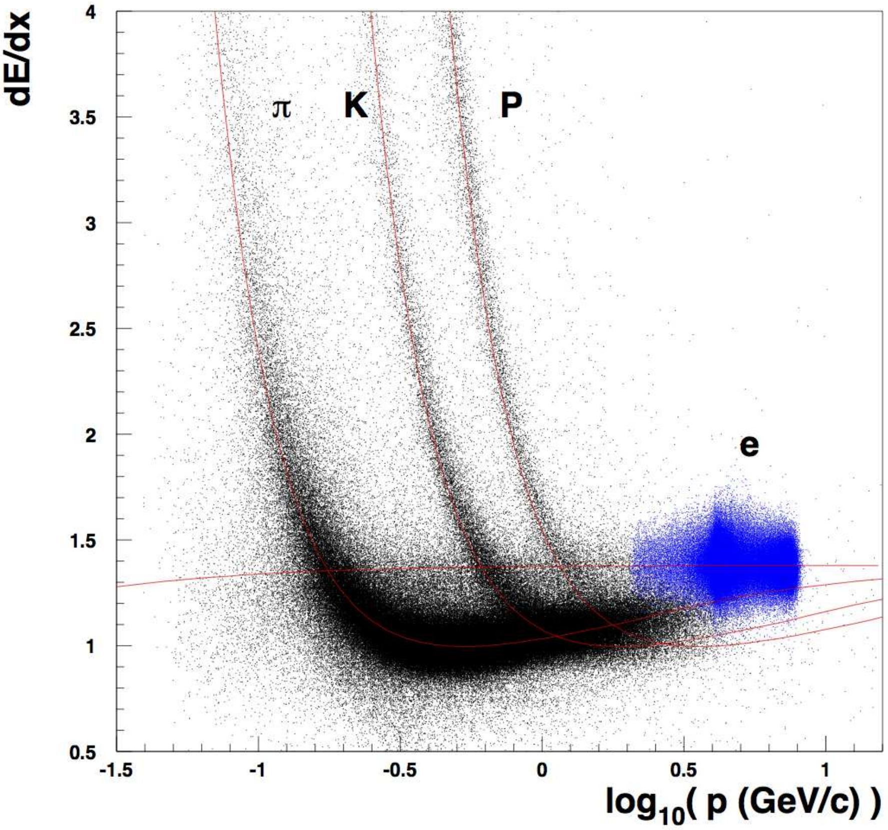

Figure 3.13: Measured energy-loss in CDC as a function of momentum in logarithm for p, K, and π. Image is taken from Ref. [84].

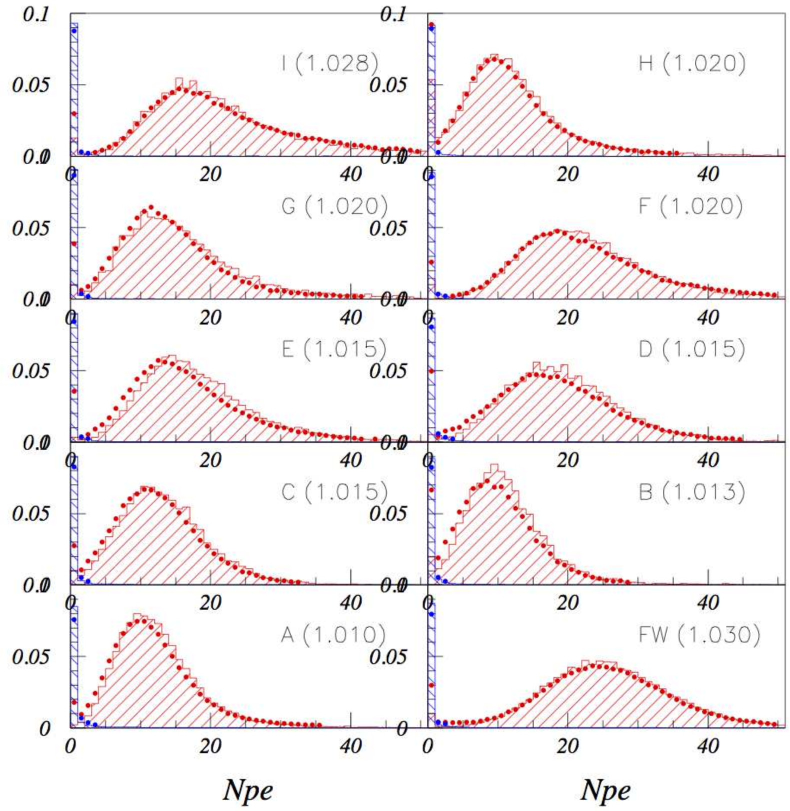

Figure 3.14: Distribution of the number of photoelectrons in ACC for each refractive index. Image is taken from Ref. [84].

where Δ_i is a vector of time difference from the expected time assuming i-th particle, and E is a 2×2 error matrix. The time difference used in the vector Δ_i is defined as $\Delta_i^k = t^k_{\text{measured}} - t^k_i$ where k is 0 or 1 which indicates PMT of two ends of a TOF counter.

In the ACC, the particle likelihood is determined from the number of photoelectron distributions as shown in Fig. 3.14 and probability density function for each particle species expected from Monte Carlo simulation.

Using the particle likelihoods described above, the total likelihood is defined as

$$\mathcal{L}_i \quad = \quad \mathcal{L}_i^{\text{CDC}} \times \mathcal{L}_i^{TOF} \times \mathcal{L}_i^{ACC}$$

for each particle species. Since there is no TOF counter in the end-cap region, and the ACC is installed in the barrel and forward end-cap region, the full kaon identification only works for the barrel region. For the forward end-cap region, the identification is carried out using CDC and ACC. In order to separate particle i from background particle j, the likelihood ratio $P(i:j)$ is defined as

$$P(i:j) \quad = \quad \frac{\mathcal{L}_i}{\mathcal{L}_i + \mathcal{L}_j}.$$

Figure 3.15 shows the momentum versus the likelihood ratio for the K/π separation using the experimental data in the barrel region. The kaon and pion samples are selected from a decay of $D^*(2010)^+ \to D^0(\to D^0\pi^+)\pi_s^+$. By applying a selection of $P(K:\pi) > 0.6$, the momentum dependance of kaon identification efficiency and pion fake rate are shown in Fig. 3.16. The average efficiency and fake rate of momentum range from 0.5 to 4.0 GeV/c in the barrel region are $(87.99 \pm 0.12)\%$ and $(8.53 \pm 0.10)\%$, and $(82.67 \pm 0.43)\%$ and $(7.81 \pm 0.29)\%$ in the forward end-cap region with a momentum range from 0.8 to 4.0 GeV/c.

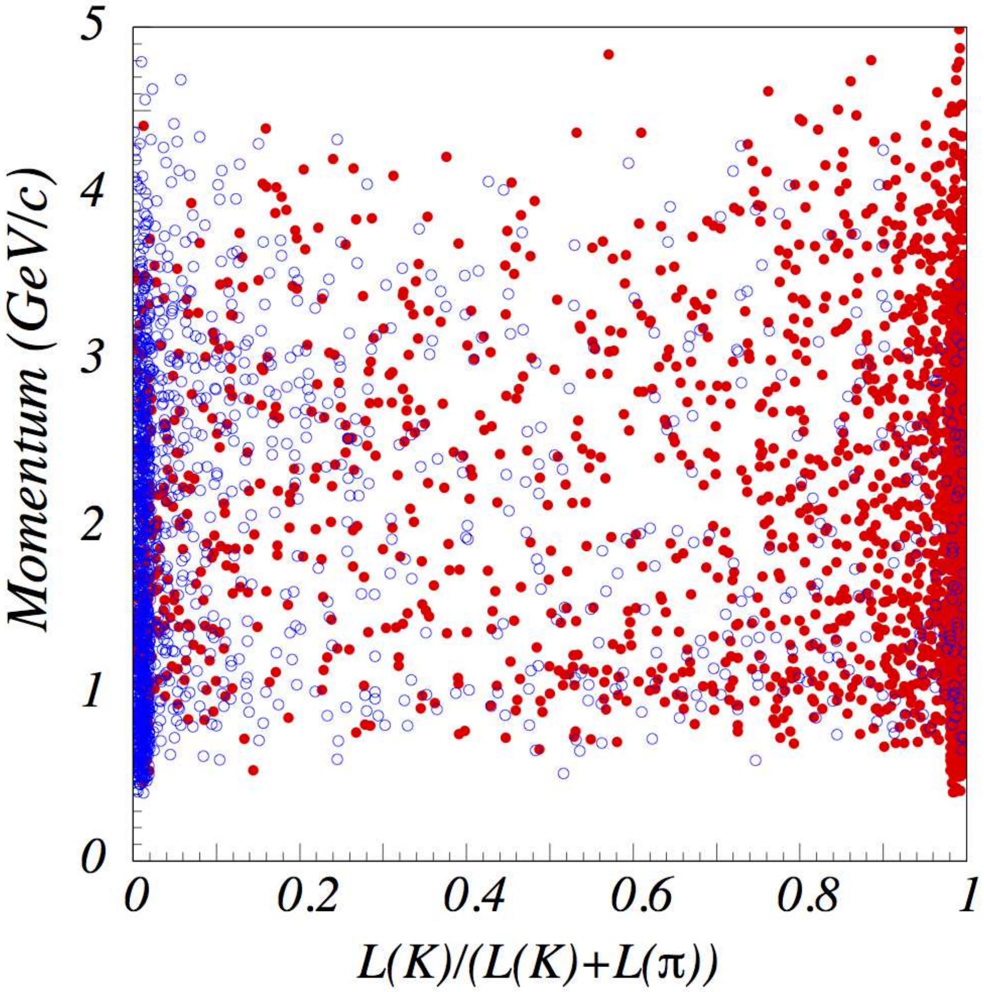

Figure 3.15: Momentum versus the likelihood ratio for the K/π separation in the barrel region. The kaon (red-full circle) and pion (blue-open circle) tracks are clearly separated. Image is taken from Ref. [84].

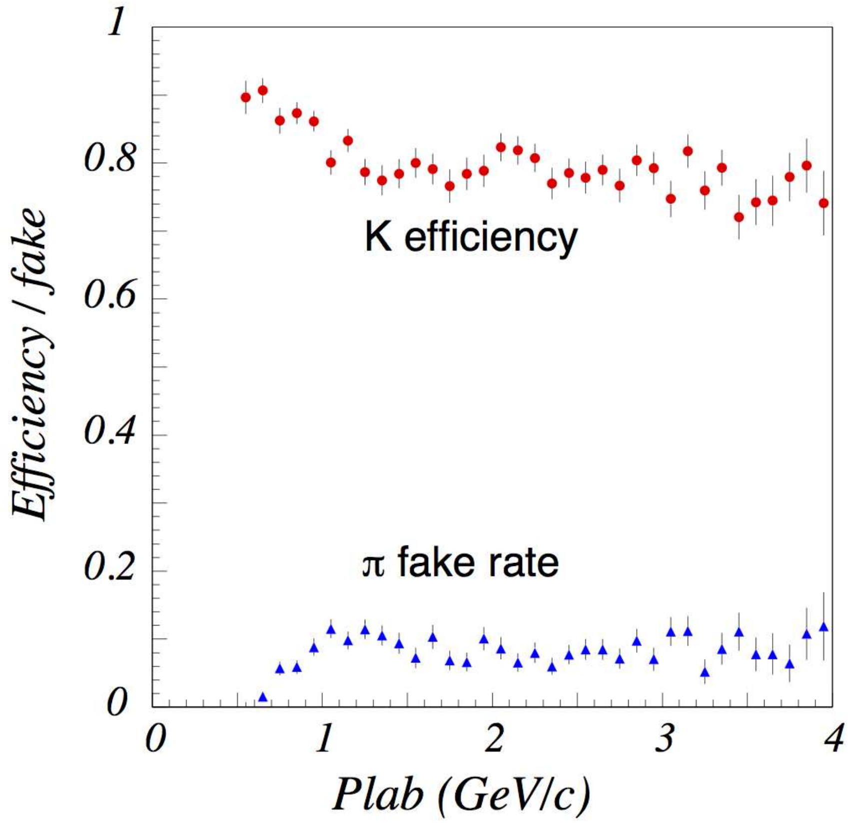

Figure 3.16: Kaon identification efficiency (red circle) and pion fake rate (blue triangle) as a function of the momentum. Image is taken from Ref. [84].

3.12.2 Electron identification

The electron identification is done by five measurements; cluster-track matching χ^2, E/p ratio, shower shape, dE/dx, and the number of photoelectrons.

The cluster-track matching χ^2 is defined between CsI cluster and charged track in which the extrapolated point is nearest to the CsI cluster as

$$\chi^2 = (\Delta\phi/\sigma_{\Delta\phi})^2 + (\Delta\theta/\sigma_{\Delta\theta})^2$$

where $\Delta\phi$ and $\Delta\theta$ are differences between the CsI cluster position and the extrapolated point of charged track at the appropriate depth in CsI, $\sigma_{\Delta\phi}$ and $\sigma_{\Delta\theta}$ are the fitted widths of $\Delta\phi$ and $\Delta\theta$ distribution of the electron sample. Using the cluster-track matching distribution of electrons and pions obtained from $e^+e^- \to e^+e^-e^+e^-$ for electrons and $K_S^0 \to \pi^+\pi^-$ for pions, each probability density function is defined by fitting a function of which is a sum of the exponential and linear functions.

The E/p ratio is defined as a ratio of measured energy in CsI and measured momentum in CDC, and the ratio provides a powerful discrimination in a wide momentum range, for example, if the charged track is required to have E/p greater than 0.8, the electron efficiency and the pion fake rate are 76.1% and 3.4% for the track momentum of greater than 0.8 GeV/c. The probability density functions of electrons and pions are determined by fitting each E/p ratio distribution in each momentum and angle region.

The shower shape is the ratio of energy deposit in 3×3 counters (referred to as $E9$) and 5×5 counters (referred to as $E25$) surrounding a counter which has a peak energy deposit. The electron distribution has a peak $E9/E25 = 0.95$ while the pion distribution has a peak at $E9/E25 = 1.0$. The probability density functions of electrons and pions are determined by fitting each shower distribution.

The energy-loss dE/dx also provides a powerful discrimination, especially in the low momentum region, therefore, it is used as a complementary measurement to the E/p ratio.

Since the Čherenkov threshold of electron is a few MeV/c while that of pion is between 0.5 and 1.0 GeV/c depending on the refractive index, the ACC can be used to separate electron from pion background. The probability density functions for electrons and pions are obtained from a Monte-Carlo simulation of the ACC.

From the measurements, the electron identification likelihood is defined as

$$\mathcal{L}_{\rm eid} = \frac{\prod_{i=1}^{n} \mathcal{L}_e^i}{\prod_{i=1}^{n} \mathcal{L}_e^i + \prod_{i=1}^{n} \mathcal{L}_{\bar{e}}^i}$$

where $\mathcal{L}_e^i$ ($\mathcal{L}_{\bar{e}}^i$) is the likelihood of an i-th measurement assuming electron (not electron). The obtained $\mathcal{L}_{\rm eid}$ is shown in Fig. 3.17.

The electron identification efficiency and the pion fake rate are estimated with a selection of $\mathcal{L}_{\rm eid} > 0.5$ and found to be $(92.4 \pm 0.4)\%$ and $(0.25 \pm 0.02)\%$, respectively, for a momentum range from 1.0 to 3.0 GeV/c, as shown in Fig. 3.18.

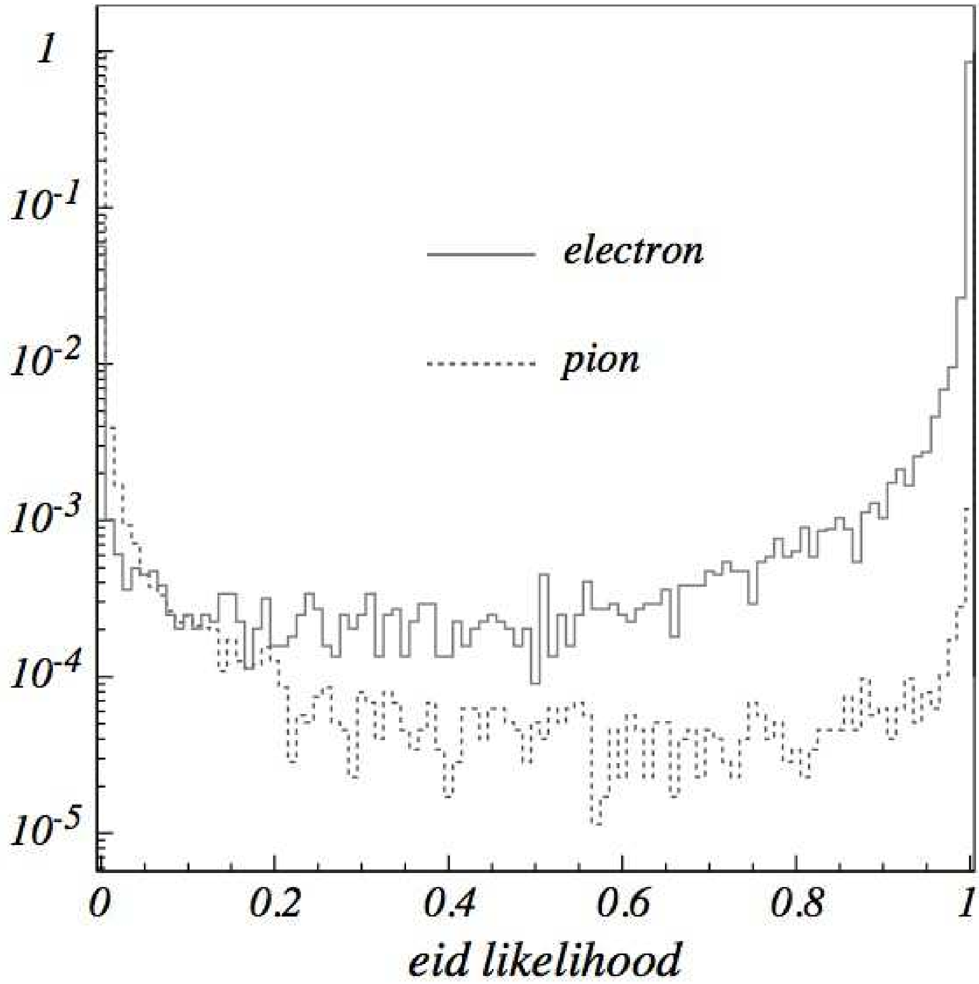

Figure 3.17: $\mathcal{L}_{\text{eid}}$ for electrons (solid) and pions (dashed). Image is taken from Ref. [84].

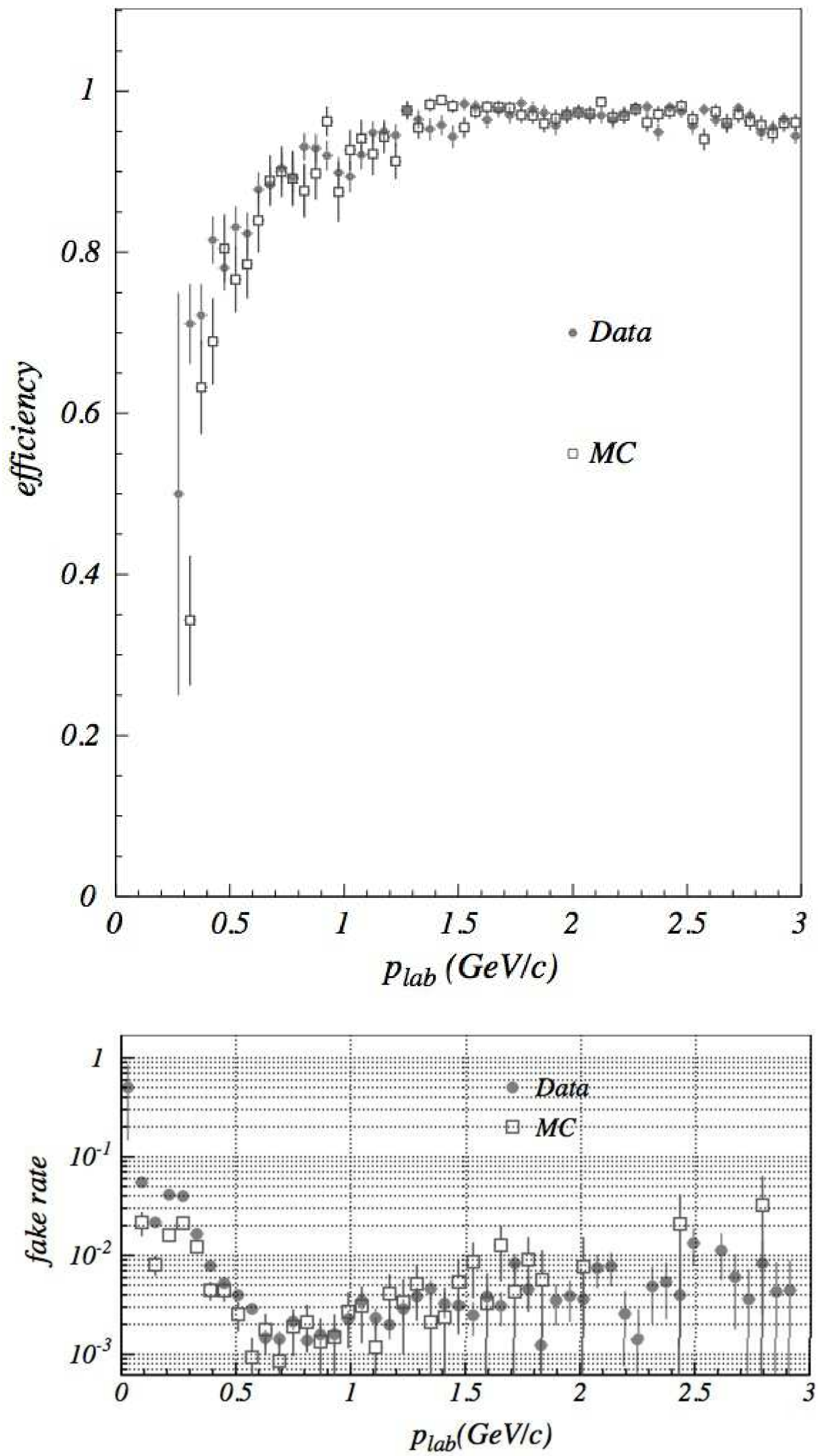

Figure 3.18: Electron identification efficiency (top) and pion fake rate (bottom). The efficiencies and fake rates of experimental (circle) and Monte Carlo simulation (square) are shown. Images are taken from Ref. [84].

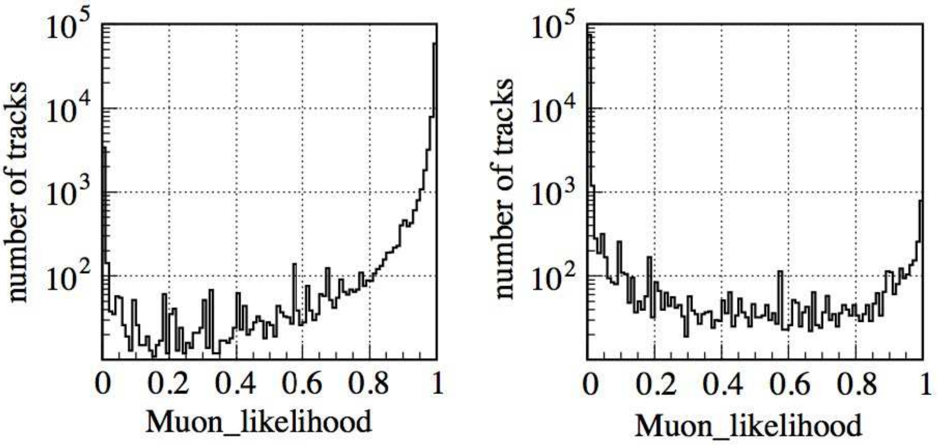

Figure 3.19: Muon likelihoods of muon (left) and pion (right). Images are taken from Ref. [84].

3.12.3 Muon identification

Muon tracks are identified by using the information from KLM. From the KLM hit information, the range difference ΔR between the calculated range using measured momentum and measured range in KLM and hit finding χ_r^2 which is a reduced χ^2 of track fitting within KLM volume are calculated. The probability densities of both ΔR and χ_r^2 are defined by experimentally, and probabilities for muon, pion, and kaon are calculated as

$$P_i = P_{i1}(\Delta R) \times P_{i2}(\chi_r^2)$$

where i indicates muon, pion, and kaon. The muon identification likelihood is constructed with the probabilities as

$$\mathcal{L}_\mu = \frac{P_\mu}{P_\mu + P_\pi + P_K},$$

and it shown Fig. 3.19.

The muon identification efficiency and pion fake rate are estimated using $e^+e^- \to e^+e^-\mu^+\mu^-$ and $K_S^0 \to \pi^+\pi^-$ processes. The efficiencies and pion fake rates with selections of $\mathcal{L}_\mu > 0.9$ (tight cut) and $\mathcal{L}_\mu > 0.1$ (loose cut) are shown in Figs. 3.20 and 3.21. The average of the muon identification efficiency and pion fake rate are (92.5±0.8)% and (2.76±0.09)% for the loose cut, and (88.8±0.9)% and (1.35±0.07)% for the tight cut, respectively.

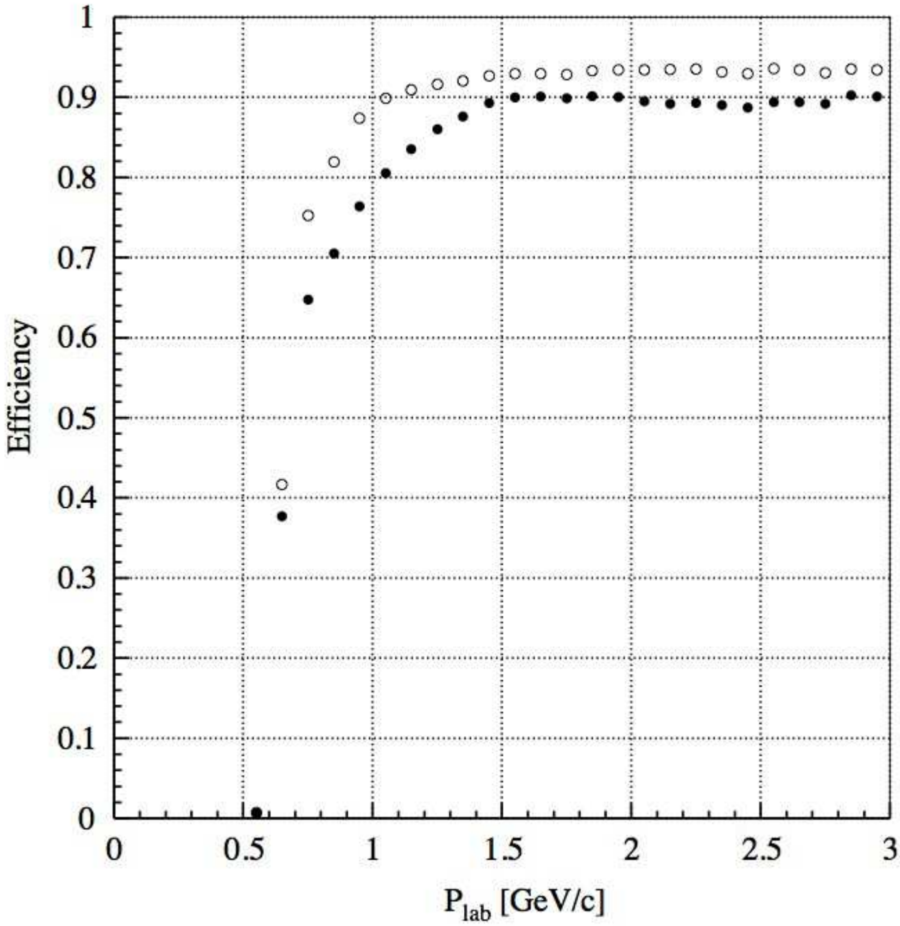

Figure 3.20: Muon identification efficiencies for the loose cut (open circle) and tight cut (full circle) as functions of momentum. Image is taken from Ref. [84].

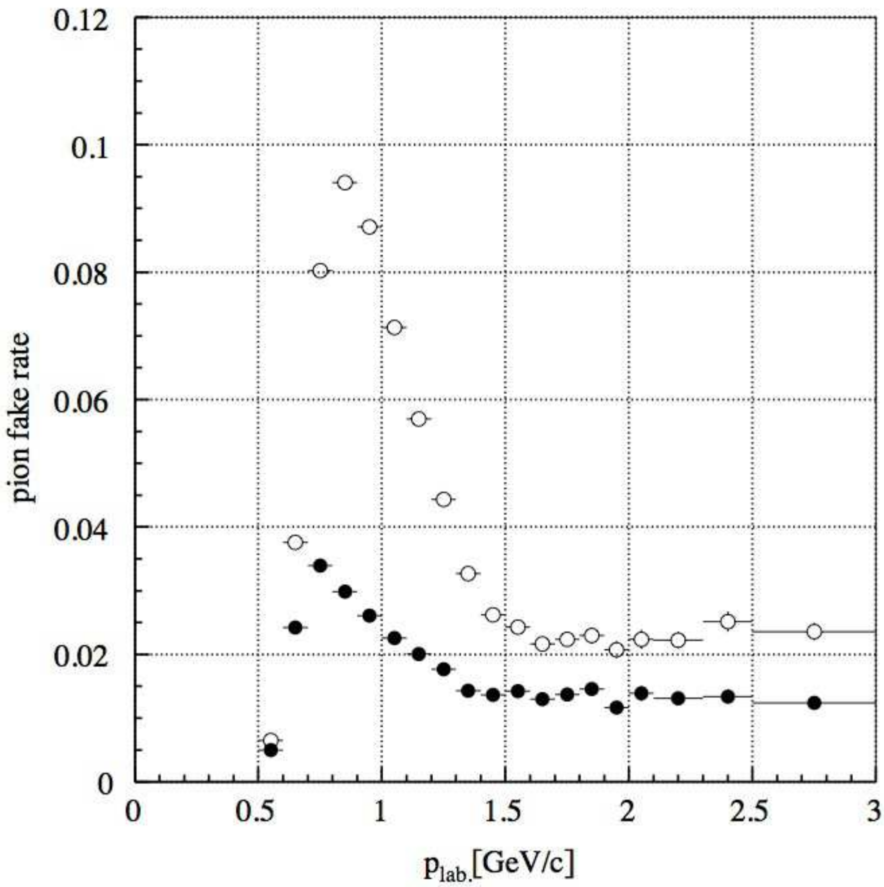

Figure 3.21: Pion fake rate in the muon identification for the loose cut (open circle) and tight cut (full circle) as functions of momentum. Image is taken from Ref. [84].

3.13 Data Statistics

For the operation of the Belle detector for a decade, a huge amount of experimental data were accumulated corresponding to the integrated luminosity of 980 fb^{-1} in total. The experiments were separately performed over the period and named `EXP`n where n is the experiment number of which is conventionally assigned as an odd number from 7 to 73. The integrated luminosities for each experiments are summarized in Table 3.2. Due to the center-of-mass energy of the KEKB accelerator, various Υ resonances can be produced. The corresponding integrated luminosities to the Υ resonances and non-resonances (referred to as "off-resonance") are 5.7, 24.9, 2.9, 702.6, 121.1, and 95 fb^{-1} for $\Upsilon(1S)$, $\Upsilon(2S)$, $\Upsilon(3S)$, $\Upsilon(4S)$, and $\Upsilon(5S)$ resonances, and off-resonance, respectively. From `EXP07` to `EXP65`, $(771.581 \pm 10.566) \times 10^6$ of $B\overline{B}$ pairs were taken. Figure 3.22 shows the integrated luminosity over a decade operation of the Belle detector.

Experiment	$\Upsilon(1S)$	$\Upsilon(2S)$	$\Upsilon(3S)$	$\Upsilon(4S)$	$\Upsilon(5S)$	Off-resonance
7	–	–	–	5.92	–	0.59
9	–	–	–	4.44	–	–
11	–	–	–	8.13	–	1.21
13	–	–	–	10.73	–	1.20
15	–	–	–	12.52	–	1.38
17	–	–	–	11.18	–	0.85
19	–	–	–	24.96	–	3.57
21	–	–	–	4.38	–	–
23	–	–	–	6.27	–	1.42
25	–	–	–	26.95	–	1.67
27	–	–	–	25.43	–	3.75
31	–	–	–	17.73	–	2.38
33	–	–	–	17.51	–	2.70
35	–	–	–	16.69	–	1.94
37	–	–	–	60.91	–	6.05
39	–	–	–	41.16	–	6.17
41	–	–	–	58.75	–	5.54
43	–	–	–	56.21	1.81	6.45
45	–	–	–	12.95	–	2.30
47	–	–	–	37.21	–	3.41
49	–	–	2.92	27.02	–	2.80
51	–	–	–	39.24	–	4.76
53	–	–	–	–	21.37	–
55	–	–	–	72.09	–	7.67
61	–	–	–	34.10	–	4.26
63	–	–	–	32.86	–	4.93
65	5.75	–	–	37.75	–	6.19
67	–	6.57	–	–	27.29	3.21
69	–	–	–	–	47.65	4.83
71	–	18.34	–	–	22.94	2.73
73	–	–	–	–	–	1.03

Table 3.2: Total integrated luminosity over the experiments in fb^{-1}. The integrated luminosity for the energy scan is excluded.

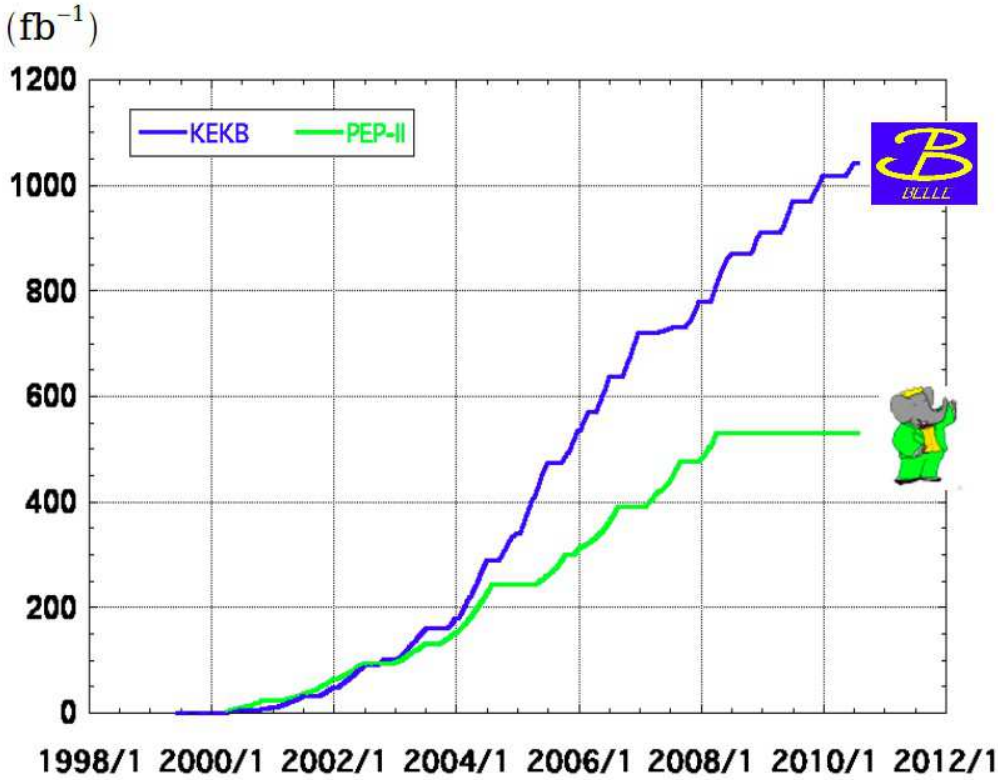

Figure 3.22: Integrated luminosity over a decade operation by the Belle (blue) and its competitor, the BABAR experiment (green) [86]. Image is taken from Ref. [81].

Chapter 4

Event Reconstruction and Selection

As discussed in Sec. 1.3, there is only a known decay of $\Sigma_c(2455/2520)^{0/++} \to \Lambda_c^+\pi_s^{-/+1}$ where π_s is a low-momentum pion (referred to as "the slow pion"). The decay chain of $\Lambda_c^+ \to pK^-\pi^+$ is chosen for the measurements of masses, widths, and mass splittings of $\Sigma_c(2455)^{0/++}$ and $\Sigma_c(2520)^{0/++}$ baryons. In this Chapter, data samples, event reconstruction and selection for the study are discussed. However, not only the data samples of the $\Sigma_c(2455)^{0/++}$ and $\Sigma_c(2520)^{0/++}$ baryons but also other control samples are used for various purposes. Since the track and event selections are different for them, the selection criteria for those samples are described later, accordingly.

4.1 Data Samples

The data used in this study were accumulated during the period from January 2000 to June 2008, and it corresponds to the integrated luminosity of 711 fb^{-1} collected at the $\Upsilon(4S)$ resonance with the Belle detector at the KEKB accelerator described in Chapters 2 and 3.

In addition to the data sample, a Monte Carlo (MC) simulation (referred to as "the generic MC") of which is officially performed by the Belle collaboration and is intended to be the same with the real data obtained from the experiment (referred to as "the data") is utilized in the study for several purposes. MC simulations dedicated to specific decay channels (referred to as "the signal MC") are also used for various purposes. The events in data sets of the MC simulation are generated

[1]Throughout this dissertation, the charge-conjugate decay modes are implied.

with PYTHIA [87], decays of unstable particles are simulated with EVTGEN [88], and detector response is simulated with GEANT3 [89]. Both the data and generic MC are processed with BASF, the Belle analysis framework [90] for the reconstruction of final state particles.

In case of the generic MC, there are a few problems in the sample. First of all, the masses of the Λ_c^+ baryon and its anti-particle, the Λ_c^- baryon, are different because of a wrong input mass of the Λ_c^- baryon in the input table that is used in the generation, therefore, the charge-conjugate decay mode of the generic MC is unusable. Moreover, the input mass of the $\Sigma_c(2455)^{++}$ baryon ($m(\Sigma_c(2455)^{++})_{\mathrm{MC}} = 2440.2$ MeV/c^2) is significantly different from the world average ($m(\Sigma_c(2455)^{++})_{\mathrm{PDG}} = 2453.98 \pm 0.16$ MeV/c^2) [3]. This makes the generic MC sample for the $\Sigma_c(2455)^{++}$ baryon useless.

Another problem is a wrong generation of the $\Sigma_c(2520)^{0/++}$ baryons. The event generation package PYTHIA requires an internal particle codes (known as KC code) to generate a particle, but it turns out that the KC codes for the $\Sigma_c(2520)^{0/++}$ baryons were missed when the generic MC was produced. As a consequence, the $\Sigma_c(2520)^{0/++}$ baryons were not generated properly as shown in Fig. 4.1.

Finally, some of heavier charmed baryons were not generated. For example, the excited Λ_c^+ baryons are necessary to study a background contribution as is to be discussed in Sec. 5.1, however, the excited Λ_c^+ baryons are missed in the generic MC sample as shown in Fig. 4.2. The Ξ_c^0 baryon is also required to study an another background contribution, but it is missed as well.

In conclusion, the generic MC samples for the $\Sigma_c(2455)^{0/++}$ and $\Sigma_c(2520)^{0/++}$ are practically useless for the study of the signal events. However, they are still useful to study the background events, such as random backgrounds, therefore, they are used for the studies of the background events as will be discussed in later sections.

The data samples of both the data and MC need an additional calibration because of the inaccurate momentum scale of the Belle detector. This calibration is discussed in Sec. 8.2 and is applied to all the samples used in this study.

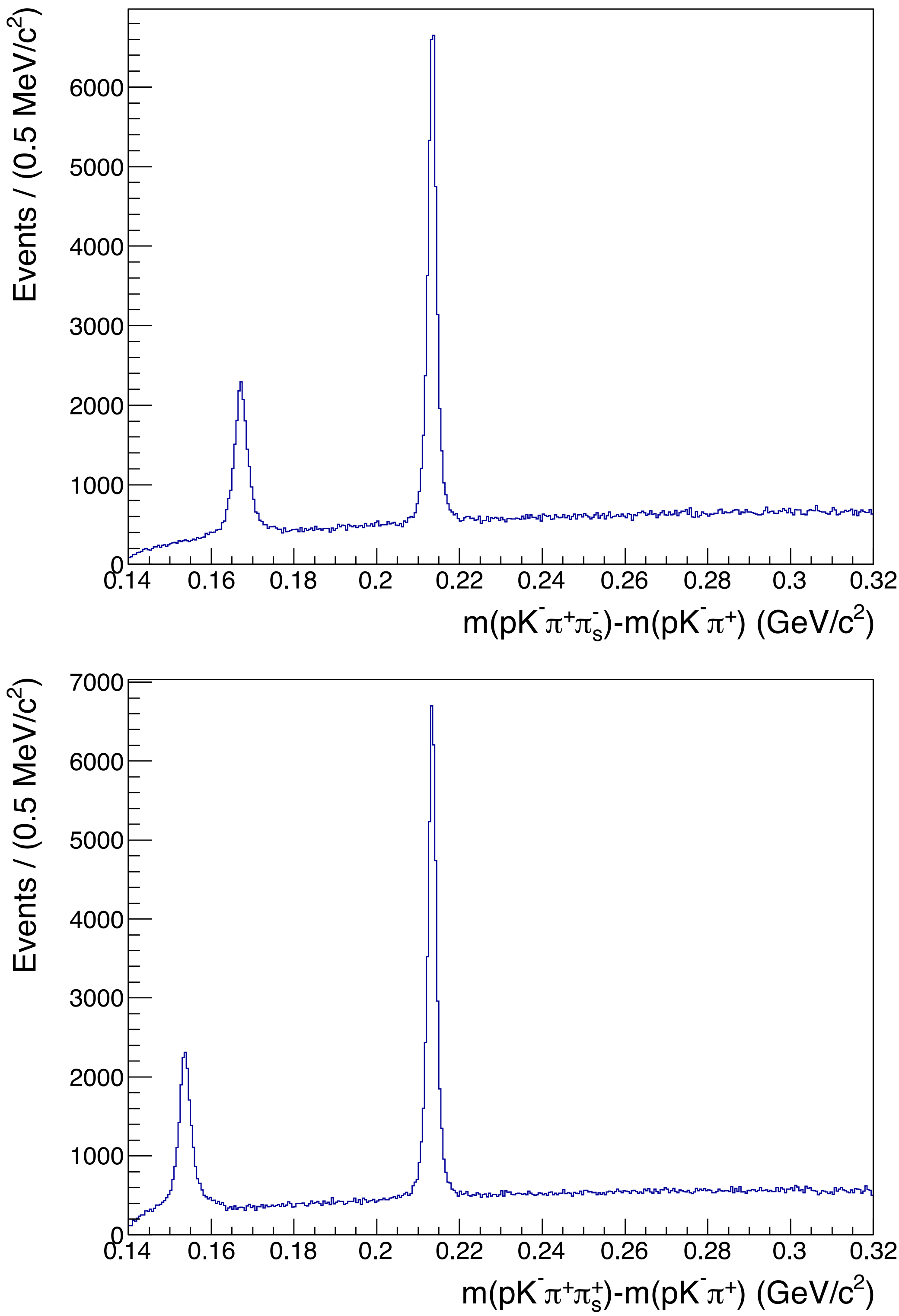

Figure 4.1: Demonstration of incorrect generation of the $\Sigma_c(2455)^{++}$ and $\Sigma_c(2520)^{0/++}$ baryons in the mass differences of $m(pK^-\pi^+\pi_s^-) - m(pK^-\pi^+)$ (top) and $m(pK^-\pi^+\pi_s^+) - m(pK^-\pi^+)$ (bottom) in the generic MC. Because of the wrong input mass of the $\Sigma_c(2455)^{++}$ baryon, the signal events are located at wrong position near 150 MeV/c^2, and the $\Sigma_c(2520)^{0/++}$ baryons are generated with wrong decay widths and the normalization because of the imperfect generation.

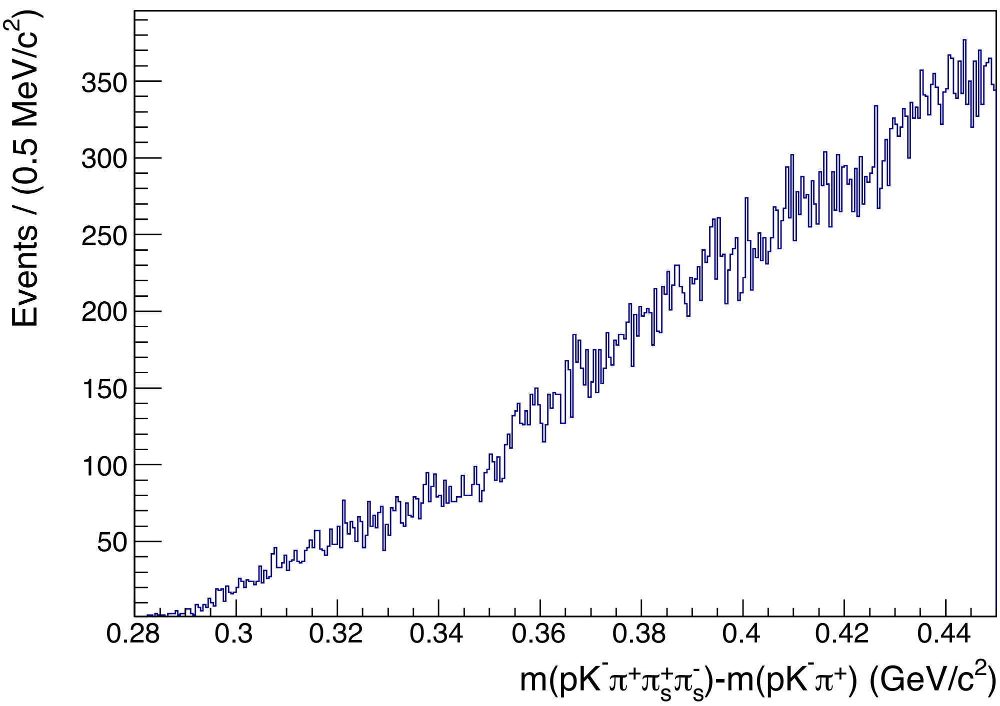

Figure 4.2: Demonstration of missing generation of the excited Λ_c^+ baryons in the generic MC. Charge conjugate mode is excluded because of the wrong input mass of the Λ_c^+ baryon.

4.2 Track Selection

All the charged tracks are required to have an impact parameter with respect to the interaction point of less than 3 cm along the z-axis, and less than 1 cm in the $r-\phi$ plane. These requirements guarantee the charged tracks to be produced near the interaction point. Furthermore, each track is required to make at least two hits on the SVD in each of the two measuring coordinates, the z-axis and $r-\phi$ plane.

The particles are identified by combining the information from the CDC, ACC, and TOF as described in Sec. 3.12. By applying the particle identification likelihood [84] criteria, they are identified as proton, kaon, or pion. The selection criteria for the proton identification are

$$P(p:K) = \frac{\mathcal{L}_p}{\mathcal{L}_p + \mathcal{L}_K} > 0.9$$

$$P(p:\pi) = \frac{\mathcal{L}_p}{\mathcal{L}_p + \mathcal{L}_\pi} > 0.9$$

where $\mathcal{L}(i)$ is the particle identification likelihood for a particle i. For the kaon identification,

$$P(K:p) = \frac{\mathcal{L}_K}{\mathcal{L}_K + \mathcal{L}_p} > 0.9$$

$$P(K:\pi) = \frac{\mathcal{L}_K}{\mathcal{L}_K + \mathcal{L}_\pi} > 0.6,$$

and for the pion identification,

$$P(\pi:p) = \frac{\mathcal{L}_\pi}{\mathcal{L}_\pi + \mathcal{L}_p} > 0.9$$

$$P(\pi:K) = \frac{\mathcal{L}_\pi}{\mathcal{L}_\pi + \mathcal{L}_K} > 0.6.$$

The particle identification efficiencies and the fake rates are estimated for the particle identification selection criteria above. The efficiencies and the fake rates are estimated with signal MC samples. For the proton identification, the criteria $P(p:h) > 0.9$, where h is K or π, have the efficiency of 83.78%. For the kaon identification, the K/π separation efficiency and fake rate are estimated to be $(90.58 \pm 0.53)\%$ and $(9.77 \pm 0.33)\%$, respectively. For the pion identification, one has to treat the pions from Λ_c^+ decay and the slow pions (π_s) from the $\Sigma_c^{0/++}$ decays, differently. The K/π separation efficiency and fake rate for the pions from Λ_c^+ decay are estimated to be $(92.63 \pm 0.69)\%$ and $(7.84 \pm 0.33)\%$, and that for the slow pions from the $\Sigma_c^{0/++}$ decays are $(99.18 \pm 0.89)\%$ and $(5.93 \pm 0.52)\%$, respectively.

4.3 Λ_c^+ and $\Sigma_c^{0/++}$ Reconstruction

With selected charged particles, a Λ_c^+ candidate is reconstructed by combining p, K^-, and π^+. Daughter tracks of the Λ_c^+ candidate are refit to a common vertex, and those candidates with fit failure are discarded.

After the reconstruction of the Λ_c^+ candidates, they are combined with the slow pion tracks to form the $\Sigma_c^{0/++}$ candidates. With the assumption of that the lifetime of the $\Sigma_c^{0/++}$ baryons are short, the Λ_c^+ production vertex is found by fitting the trajectory of the Λ_c^+ candidate to the e^+e^- interaction point. If the fit fails, the event is discarded. Finally, a slow pion track is refit to the Λ_c^+ production vertex, and the fit results such as the confidence level of the fit are taken as additional information for further event selection. If the slow pion vertex fit fails, the event is discarded as well.

4.4 Event Selection

To improve the signal-to-background ratio, further event selection is performed. Only the events that the Λ_c^+ candidates have invariant masses within a Λ_c^+ mass signal region are selected. The Λ_c^+ mass signal region is defined as from 2278.07 to 2295.79 MeV/c^2 which corresponds to $\pm 2.1\sigma$ around the nominal Λ_c^+ mass where σ represents the Λ_c^+ invariant mass resolution, and the sideband region is defined as from 2259.16 to 2267.76 MeV/c^2 or from 2305.58 to 2314.18 MeV/c^2 to have the same area with that of the defined signal region. as shown in Fig. 4.3. Furthermore, candidates with confidence level of the slow pion vertex fit constrained to the Λ_c^+ production vertex greater than 0.1% are kept to improve the momentum resolution of the slow pion. Finally, the $\Sigma_c^{0/++}$ candidates are required to have their momentum in the center-of-mass frame (p^*) greater than 2.0 GeV/c to suppress combinatorial backgrounds.

Figure 4.4 shows the mass difference distribution of $m(pK^-\pi^+\pi_s^-) - m(pK^-\pi^+)$ and $m(pK^-\pi^+\pi_s^+) - m(pK^-\pi^+)$ after the reconstruction with the selection described so far.

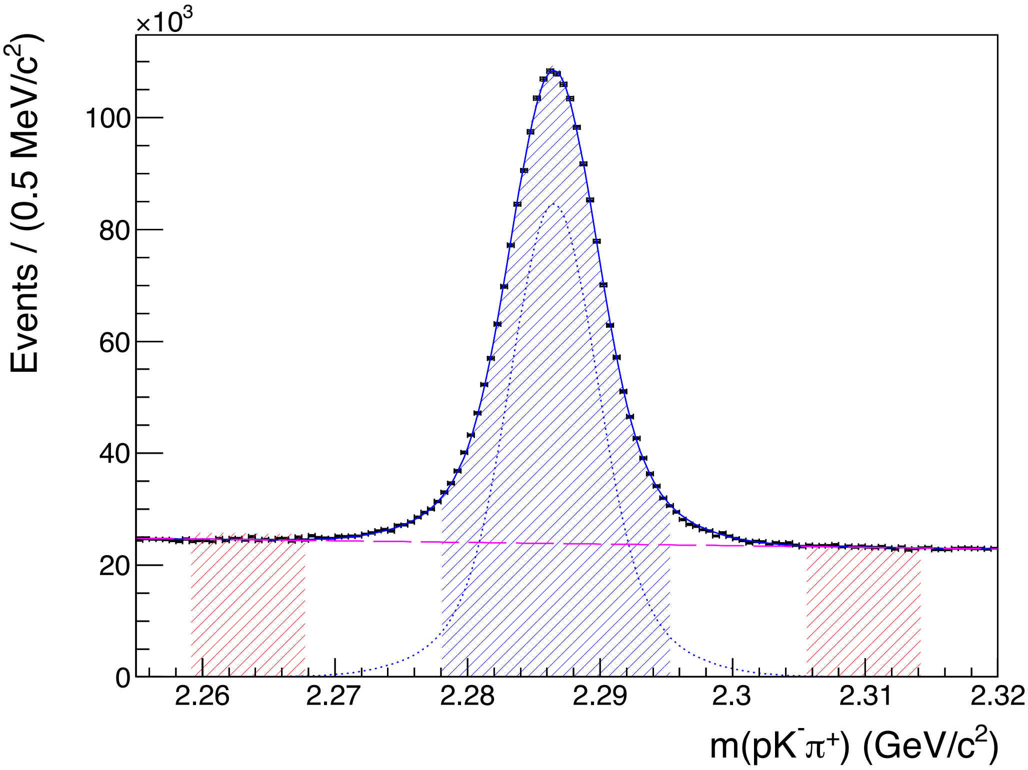

Figure 4.3: Signal (red-hatched) and sideband (blue-hatched) region of the Λ_c^+ baryon mass. The signal regions are corresponding to $\pm 2.1\sigma$ around the nominal Λ_c^+ mass where σ represents the Λ_c^+ invariant mass resolution and are intended to have the same area with the sideband regions defined. Sum of two Gaussian distributions and a linear function are used in the fit as signal and background probability density function, respectively.

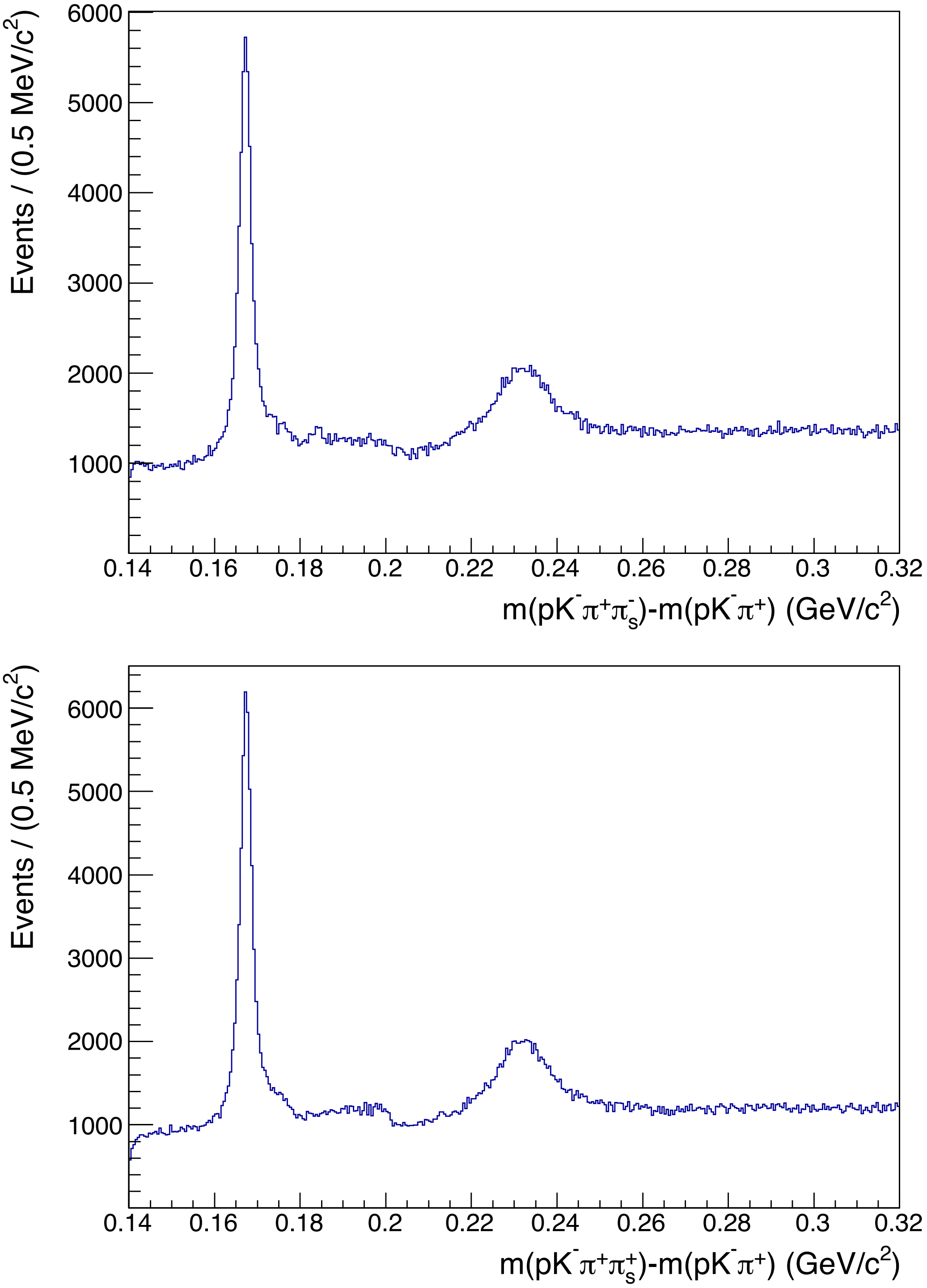

Figure 4.4: The mass differences of $m(pK^-\pi^+\pi_s^-) - m(pK^-\pi^+)$ (top) and $m(pK^-\pi^+\pi_s^+) - m(pK^-\pi^+)$ (bottom) after the selections described in the text.

Chapter 5

Backgrounds

In the mass difference distribution of $m(pK^-\pi^+\pi_s^\pm) - m(pK^-\pi^+)$, uninterested events usually called as backgrounds exist. It is necessary to extract these backgrounds correctly for the unbiased description of the signal events. From the study on these backgrounds, the background components are categorized as:

- Background from the excited Λ_c^+ decays
- Backgrounds from the $D^*(2010)^+$ and $\Xi_c^0 \to \Lambda_c^+\pi^-$ decays
- Background due to the wrong combinations (referred to as the "random background").

5.1 Backgrounds from Excited Λ_c^+ Decays

5.1.1 Excited Λ_c^+ Decays

There are four known excited states of Λ_c^+ baryons (referred to as Λ_c^{*+}); $\Lambda_c(2595)^+$, $\Lambda_c(2625)^+$, $\Lambda_c(2880)^+$, and $\Lambda_c(2940)^+$. There is also an excited state of $\Lambda_c(2765)^+$ which is not well observed to date. The properties of these excited Λ_c^+ baryons are summarized in Table 5.1.

The final states of these excited Λ_c^+ baryons are very similar to those of $\Sigma_c^{0/++}$ baryons except for an additional pion. For example, the $\Lambda_c(2595)^+$, $\Lambda_c(2625)^+$, $\Lambda_c(2765)^+$, and $\Lambda_c(2880)^+$ baryons decay to $\Lambda_c^+\pi_s^+\pi_s^-$ (referred to as "non-resonant decay"). If a pion is missed in these decays, the final states are identical to the decay of the $\Sigma_c^{0/++}$ baryons. Furthermore, the excited Λ_c^+ also has resonant decays that include $\Sigma_c^{0/++}$ baryons, for example, the $\Lambda_c(2625)^+ \to \Sigma_c^{0/++}\pi_s^{+/-}$. Therefore, the reconstruction of the $\Sigma_c^{0/++}$ candidates is a partial reconstruction for these excited

	Mass (MeV/c^2)	Decay modes	Fraction (Γ_i/Γ)
$\Lambda_c(2595)^+$	2592.25 ± 0.28	$\Lambda_c^+\pi_s^+\pi_s^-$	$\simeq 67$ %
		$\Sigma_c(2455)^{++}\pi_s^-$	(24 ± 7) %
		$\Sigma_c(2455)^0\pi_s^+$	(24 ± 7) %
		$\Lambda_c^+\pi_s^+\pi_s^-$ 3-body	(18 ± 10) %
$\Lambda_c(2625)^+$	2628.11 ± 0.19	$\Lambda_c^+\pi_s^+\pi_s^-$	$\simeq 67$ %
		$\Sigma_c(2455)^{++}\pi_s^-$	< 5 @ 90% C. L.
		$\Sigma_c(2455)^0\pi_s^+$	< 5 @ 90% C. L.
		$\Lambda_c^+\pi_s^+\pi_s^-$ 3-body	large
$\Lambda_c(2765)^+$	2766.6 ± 2.4	$\Lambda_c^+\pi_s^+\pi_s^-$ 3-body	*seen*
$\Lambda_c(2880)^+$	2881.53 ± 0.35	$\Lambda_c^+\pi_s^+\pi_s^-$	*seen*
		$\Sigma_c(2455)^{0/++}\pi_s^{+/-}$	*seen*
		$\Sigma_c(2520)^{0/++}\pi_s^{+/-}$	*seen*
$\Lambda_c(2940)^+$	$2939.3^{+1.4}_{-1.5}$	$\Sigma_c(2455)^{0/++}\pi_s^{+/-}$	*seen*

Table 5.1: Properties of the excited Λ_c^+ baryons [3]. Only channels that have the final state of the $\Lambda_c^+\pi_s^+\pi_s^-$ are listed. The $\Lambda_c(2765)^+$ baryon is not promoted yet.

Λ_c^+ baryons, and there are three cases of the partial reconstruction as described below.

- Signal resonant decay: Although the reconstruction is a partial reconstruction of the Λ_c^{*+} baryon that a pion is not included, the reconstructed candidate is a signal event of the $\Sigma_c^{0/++}$ baryons. For example, although a positively charged pion (π_s^+) is missed in the reconstruction of the decay of $\Lambda_c(2625)^+ \to \Sigma_c^0\pi_s^+$, the candidate is the signal event of the Σ_c^0 decay.

- Background resonant decay: If a pion is missed in the reconstruction, and the decay of the Λ_c^{*+} baryon does not contain the signal particle but other particle, the reconstructed candidate is a background event. For example if a positively charged pion (π_s^+) is missed in the reconstruction of the decay of $\Lambda_c(2625)^+ \to \Sigma_c^{++}(\to \Lambda_c^+\pi_s^+)\pi_s^-$, the candidate has a wrong combination, therefore, it comes as a background event.

- Non-resonant decay: The partial reconstruction of the $\Lambda_c^+\pi_s^+\pi_s^-$ that a pion is missed is always a background event.

The backgrounds from these excited Λ_c^+ decays are referred to as "feed-down" backgrounds throughout this study.

The existence of the feed-down backgrounds are confirmed from the MC simulation dedicated to the decays of the Λ_c^{*+} baryons. In the simulation, 1,000,000 events are generated with PYTHIA [87], decayed with EVTGEN [88], and simulated the detector response with GEANT3 [89] for each decay channel. The simulated events are reconstructed with the same method described in Chapter 4.

In the decays of the $\Lambda_c(2595)^+$ baryon, all events are shown in the mass difference region up to 175 MeV/c^2 as described in Fig. 5.1. Correctly reconstructed $\Sigma_c^{0/++}$ events are located at the same position with the input mass of the simulation, and incorrectly reconstructed events from the resonant decay, for instance, the combination of the $\Lambda_c^+\pi_s^-$ from the $\Lambda_c(2595)^+ \to \Sigma_c^{++}\pi_s^-$ decay in the $m(pK^-\pi^+\pi_s^-) - m(pK^-\pi^+)$ space, is located near 140 MeV/c^2. The events from the non-resonant decay of $\Lambda_c(2595)^+ \to \Lambda_c^+\pi_s^+\pi_s^-$ are widely distributed over the space.

In the decays of the $\Lambda_c(2625)^+$ baryon, the events are distributed from 140 to 210 MeV/c^2 as shown in Fig. 5.2. The events from the resonant decay that includes the signal events are located at the expected position, and wrongly reconstructed events from the resonant decay are shown next to the signal events near 175 MeV/c^2 while the events from the non-resonant decay are distributed widely over the space.

In case of the decay of the $\Lambda_c(2765)^+$ baryon, the only known decay channel is the non-resonant decay, $\Lambda_c(2765)^+ \to \Lambda_c^+\pi_s^+\pi_s^-$. The distribution is broad over the space. Together with it, the ones from the $\Lambda_c(2595)^+$ and $\Lambda_c(2625)^+$ baryons are shown in Fig. 5.3, and the numbers of the events shown in the interest region (140 to 320 MeV/c^2) are small, therefore, it is concluded that the contribution from $\Lambda_c(2765)^+$ decay is negligible.

In the decays of the $\Lambda_c(2880)^+$ baryon, there are five known decay channels of $\Lambda_c(2880) \to \Sigma_c(2455)^0\pi_s^+$, $\Lambda_c(2880) \to \Sigma_c(2455)^{++}\pi_s^-$, $\Lambda_c(2880) \to \Sigma_c(2520)^0\pi_s^+$, $\Lambda_c(2880) \to \Sigma_c(2520)^{++}\pi_s^-$, and $\Lambda_c(2880) \to \Lambda_c^+\pi_s^+\pi_s^-$, and all decay channels are simulated accordingly. As shown in Fig. 5.4, the distribution is dominated by the signal events, and the feed-down backgrounds are negligible because the wrong combinations from the resonant decays are kinematically distributed in higher mass region.

The feed-down backgrounds from the $\Lambda_c(2595)^+$ and $\Lambda_c(2625)^+$ decays are also found in 2-dimensional scatter plot of the mass differences $m(pK^-\pi^+\pi_s^-) - m(pK^-\pi^+)$ and $m(pK^-\pi^+\pi_s^+) - m(pK^-\pi^+)$ taken from the data sample of the $pK^-\pi^+\pi_s^+\pi_s^-$ combinations as shown in Fig. 5.5.

Therefore, the feed-down backgrounds can be dominated only by the decays of the $\Lambda_c(2595)^+$ and $\Lambda_c(2625)^+$ baryons.

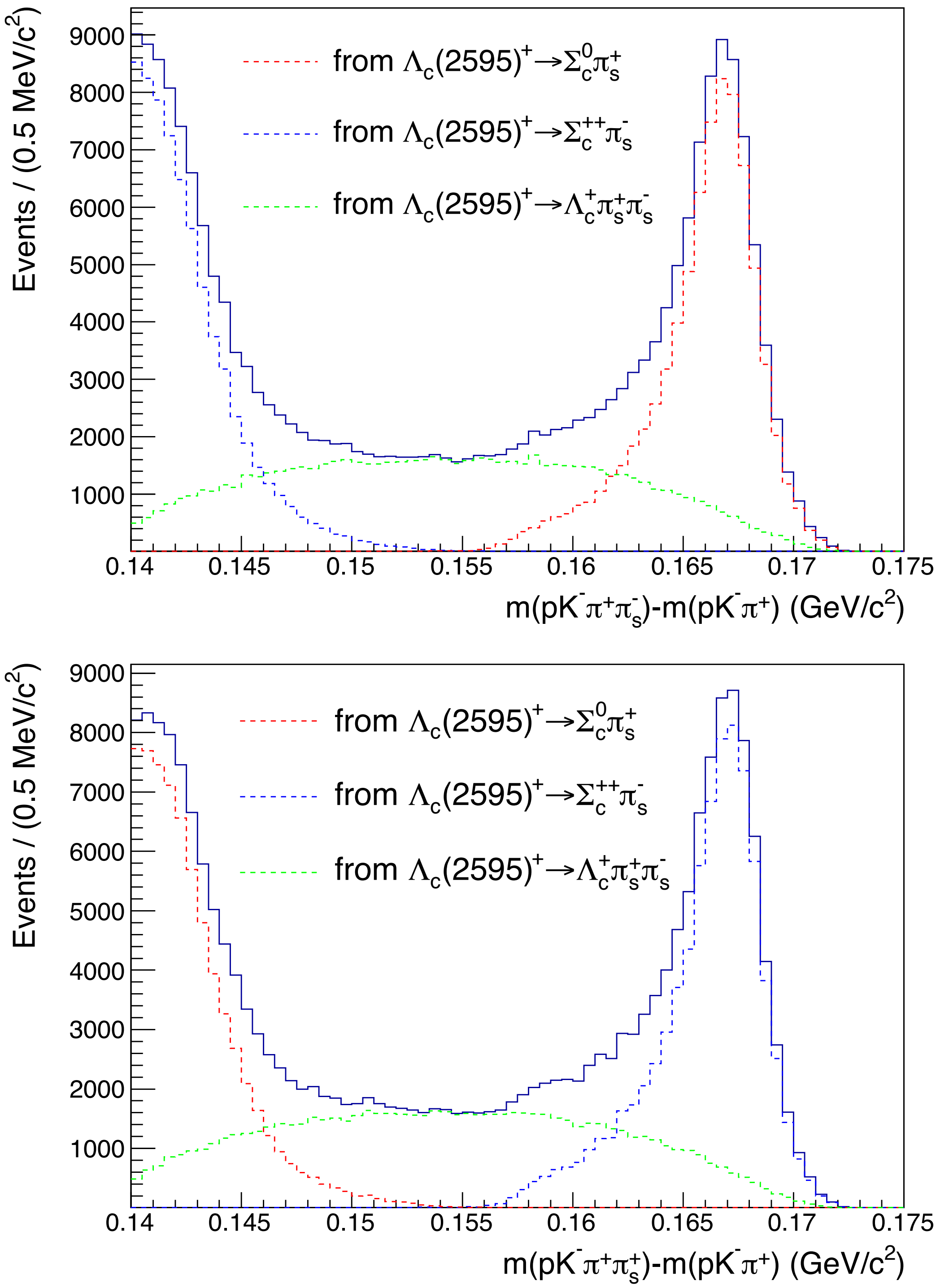

Figure 5.1: The feed-down backgrounds (blue-solid line) in the decays of the $\Lambda_c(2595)^+$ baryons in $m(pK^-\pi^+\pi_s^-) - m(pK^-\pi^+)$ (top) and $m(pK^-\pi^+\pi_s^+) - m(pK^-\pi^+)$ (bottom) spaces obtained from the signal MC. The decay contributions of the $\Lambda_c(2595)^+ \to \Sigma_c(2455)^0\pi_s^+$ (red-dashed line), $\Lambda_c(2595)^+ \to \Sigma_c(2455)^{++}\pi_s^-$ (blue-dashed line), and $\Lambda_c(2595)^+ \to \Lambda_c^+\pi_s^+\pi_s^-$ (green-dashed line) are also shown. They do not reflect the real branching fractions because the production rates are unknown.

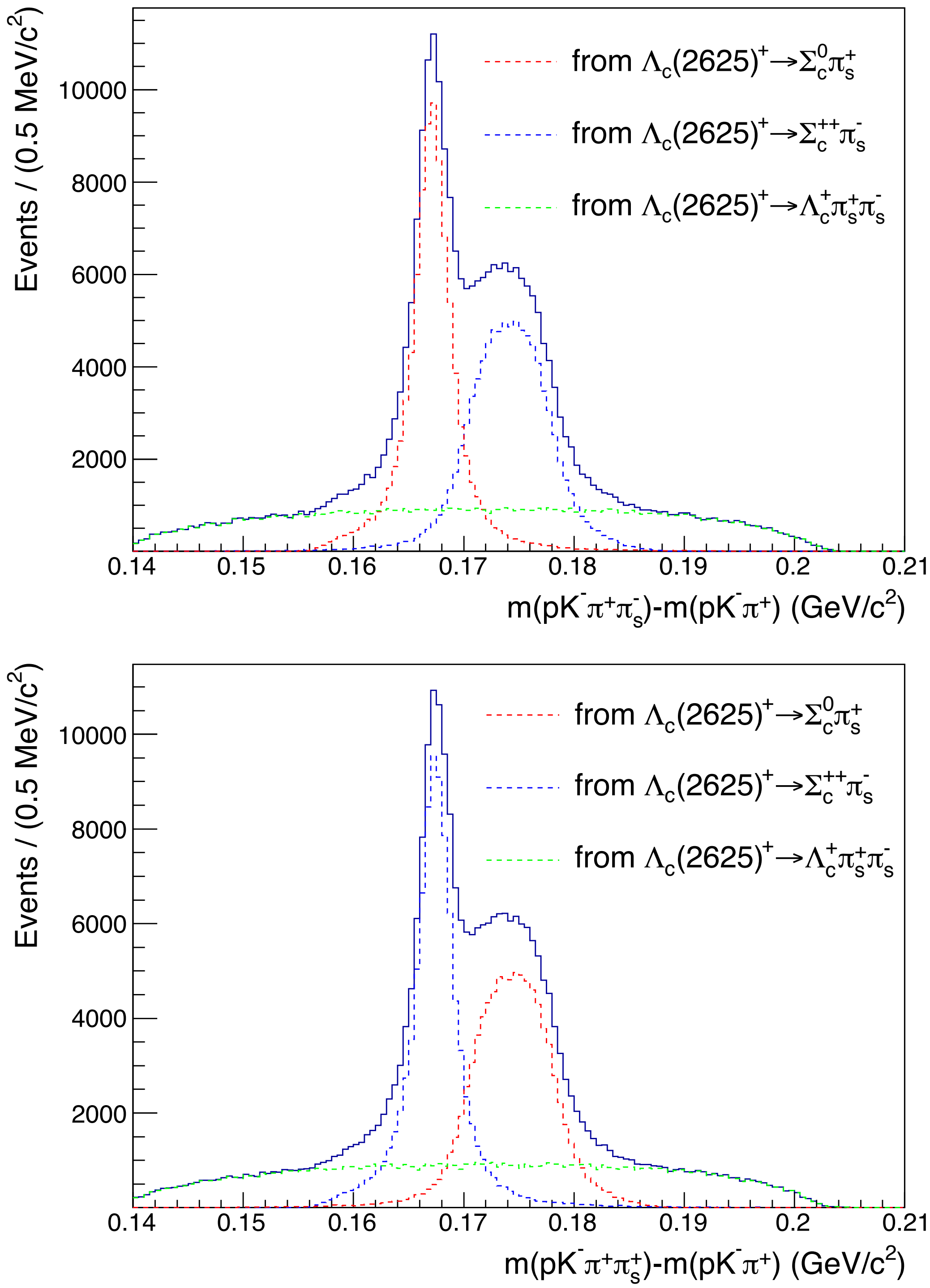

Figure 5.2: The feed-down backgrounds (blue-solid line) in the decays of the $\Lambda_c(2625)^+$ baryon in $m(pK^-\pi^+\pi_s^-) - m(pK^-\pi^+)$ (top) and $m(pK^-\pi^+\pi_s^+) - m(pK^-\pi^+)$ (bottom) spaces obtained from the signal MC. The decay contributions of $\Lambda_c(2625)^+ \to \Sigma_c(2455)^0\pi_s^+$ (red-dashed line), $\Lambda_c(2595)^+ \to \Sigma_c(2455)^{++}\pi_s^-$ (blue-dashed line), and $\Lambda_c(2625)^+ \to \Lambda_c^+\pi_s^+\pi_s^-$ (green-dashed line) are also shown. They do not reflect the real branching fractions because the production rates are unknown.

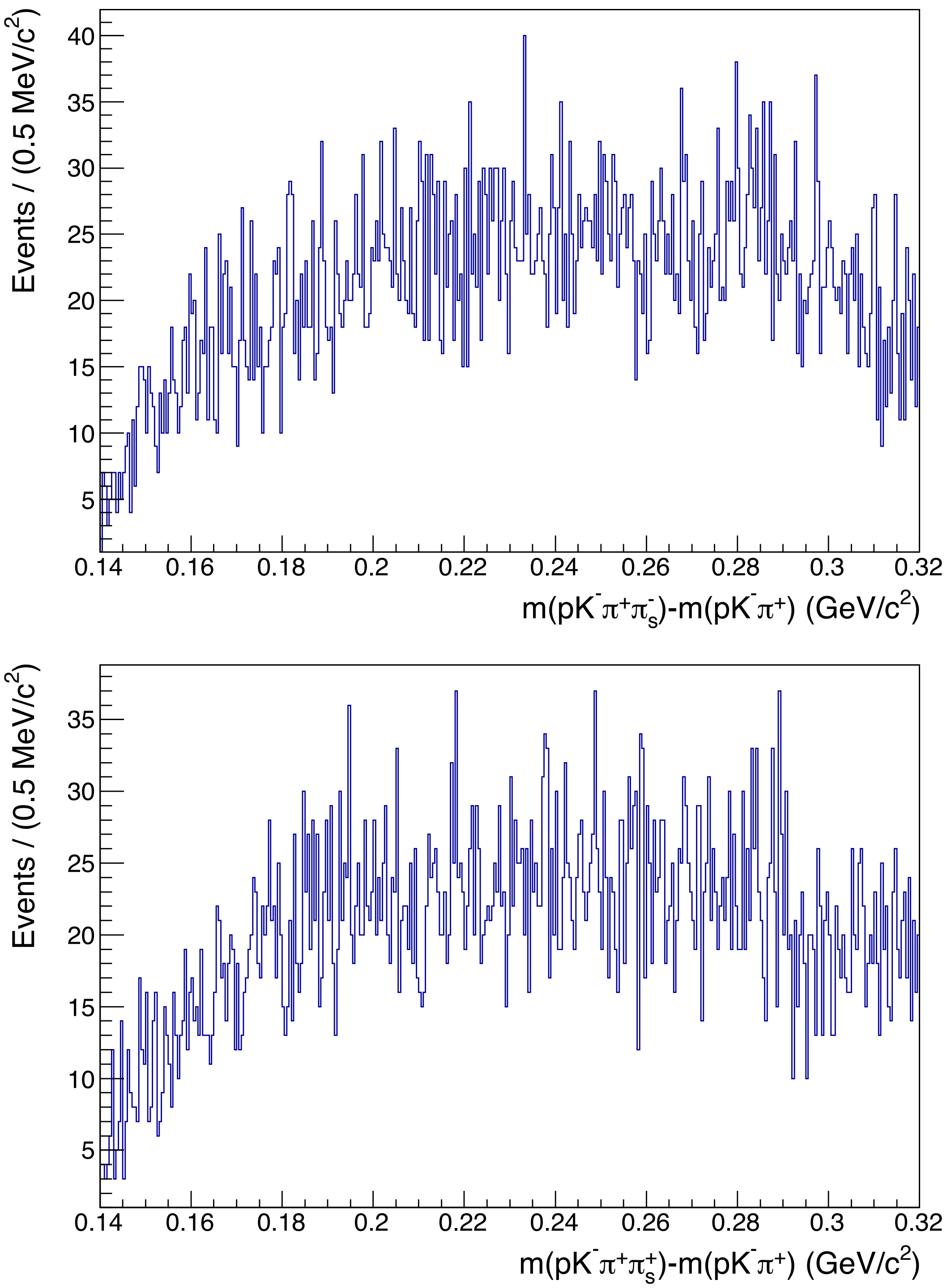

Figure 5.3: The feed-down backgrounds (blue-solid line) in the decays of the $\Lambda_c(2765)^+$ baryon in $m(pK^-\pi^+\pi_s^-) - m(pK^-\pi^+)$ (top) and $m(pK^-\pi^+\pi_s^+) - m(pK^-\pi^+)$ (bottom) spaces obtained from the signal MC. There are only a known decay of $\Lambda_c(2765) \to \Lambda_c^+\pi_s^+\pi_s^-$, and the normalization is not accounted.

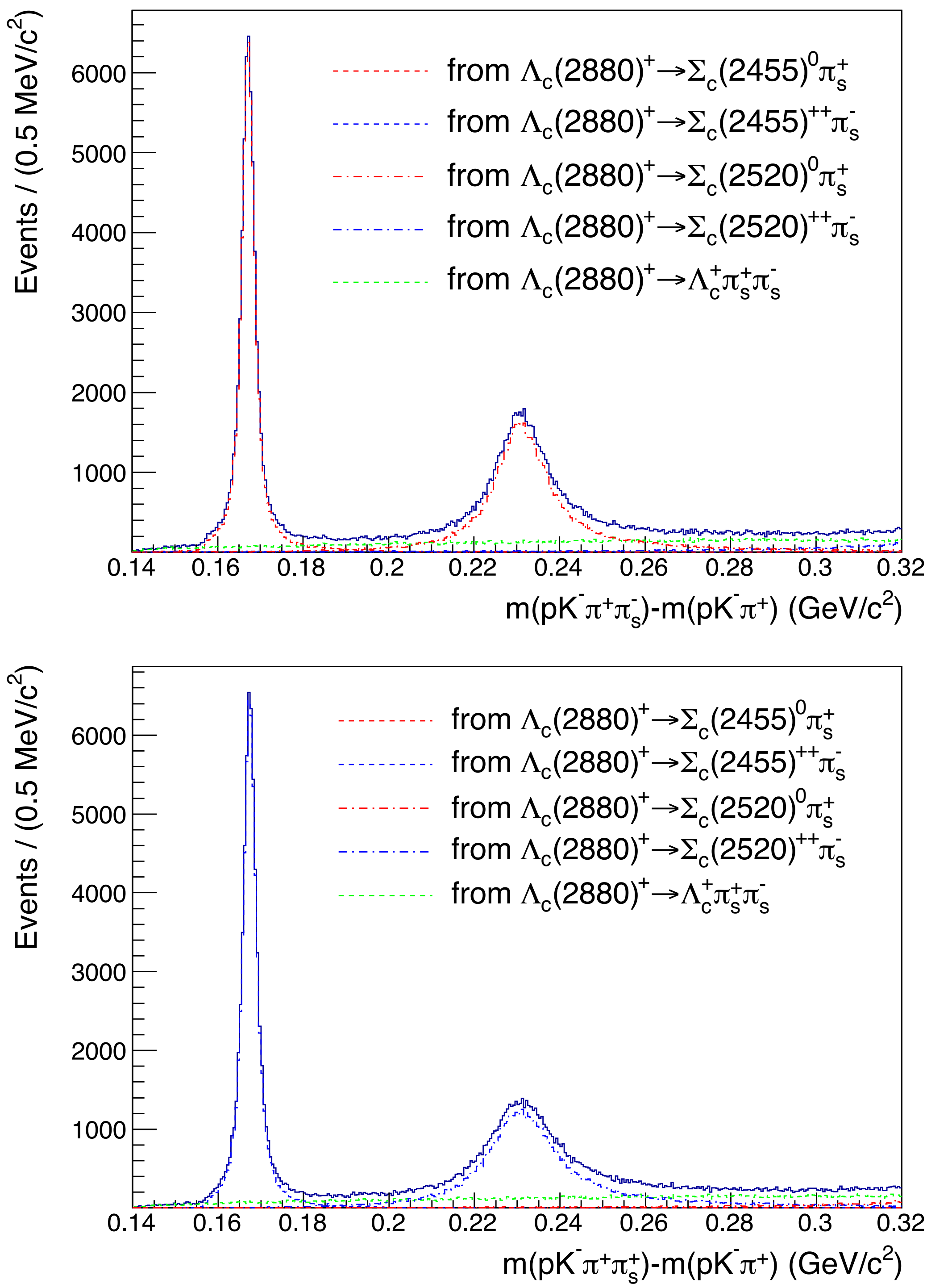

Figure 5.4: The feed-down backgrounds (blue-solid line) in the decays of the $\Lambda_c(2880)^+$ baryon in $m(pK^-\pi^+\pi_s^-) - m(pK^-\pi^+)$ (top) and $m(pK^-\pi^+\pi_s^+) - m(pK^-\pi^+)$ (bottom) spaces obtained from the signal MC. The decay contributions of $\Lambda_c(2880)^+ \to \Sigma_c(2455)^0\pi_s^+$ (red-dashed line), $\Lambda_c(2595)^+ \to \Sigma_c(2455)^{++}\pi_s^-$ (blue-dashed line), $\Lambda_c(2880)^+ \to \Sigma_c(2520)^0\pi_s^+$ (red-dotted-dashed line), $\Lambda_c(2595)^+ \to \Sigma_c(2520)^{++}\pi_s^-$ (blue-dotted-dashed line), and $\Lambda_c(2880)^+ \to \Lambda_c^+\pi_s^+\pi_s^-$ (green-dashed line) are also shown. They do not reflect the real branching fractions because the production rates are unknown.

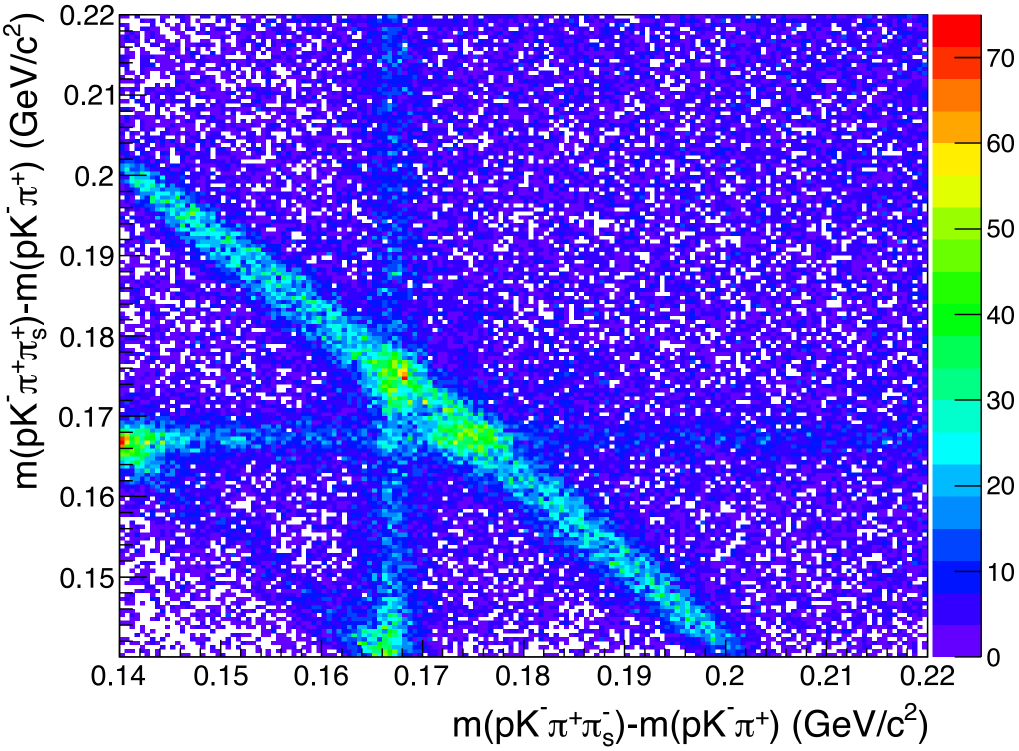

Figure 5.5: 2-dimensional scatter plot of $m(pK^-\pi^+\pi_s^-) - m(pK^-\pi^+)$ and $m(pK^-\pi^+\pi_s^+) - m(pK^-\pi^+)$ in the $pK^-\pi^+\pi_s^+\pi_s^-$ combinations. The feed-down backgrounds appear in those mass differences because of interferences between $\Sigma_c(2455)^{0/++}$ and Λ_c^{*+} signal events.

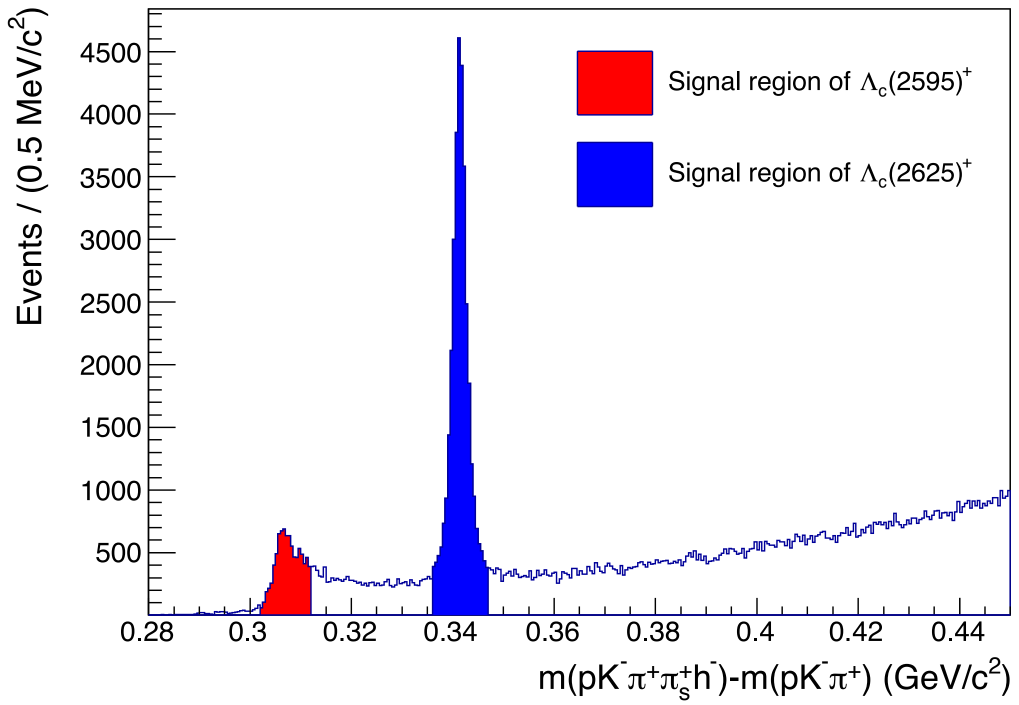

Figure 5.6: $m(pK^-\pi^+\pi_s^+h^-) - m(pK^-\pi^+)$ distribution with the defined signal regions of the $\Lambda_c(2595)^+$ (red) and $\Lambda_c(2625)^+$ (blue) baryons in the data.

5.1.2 Feed-down Background Tagging

The shape of the feed-down backgrounds can be obtained from the simulation, and it can be used as a non-parametric probability density function (PDF) in the fit. Unfortunately, the generic MC does not contain the excited Λ_c^+ baryons, and therefore, there should be other options to extract the feed-down backgrounds. One option is to use the signal MC, but the normalization of the feed-down events is practically impossible to estimate because the cross sections and branching fractions of the excited Λ_c^+ decays are not well established. As a consequence, the feed-down extraction has to rely on the data.

In order to extract the feed-down backgrounds, a tagging method is applied. During the reconstruction of $pK^-\pi^+\pi_s^\pm$ events, an additional charged track is attached to the candidate event, and the combination is tested if it is suitable in forming the excited Λ_c^+ baryons. In other words, if a $pK^-\pi^+\pi_s^{+/-}$ event and an additional charged hadron ($h^{-/+}$) has a mass within a defined mass window of the excited Λ_c^+ baryon, the event is tagged as a feed-down background event. For this purpose, the

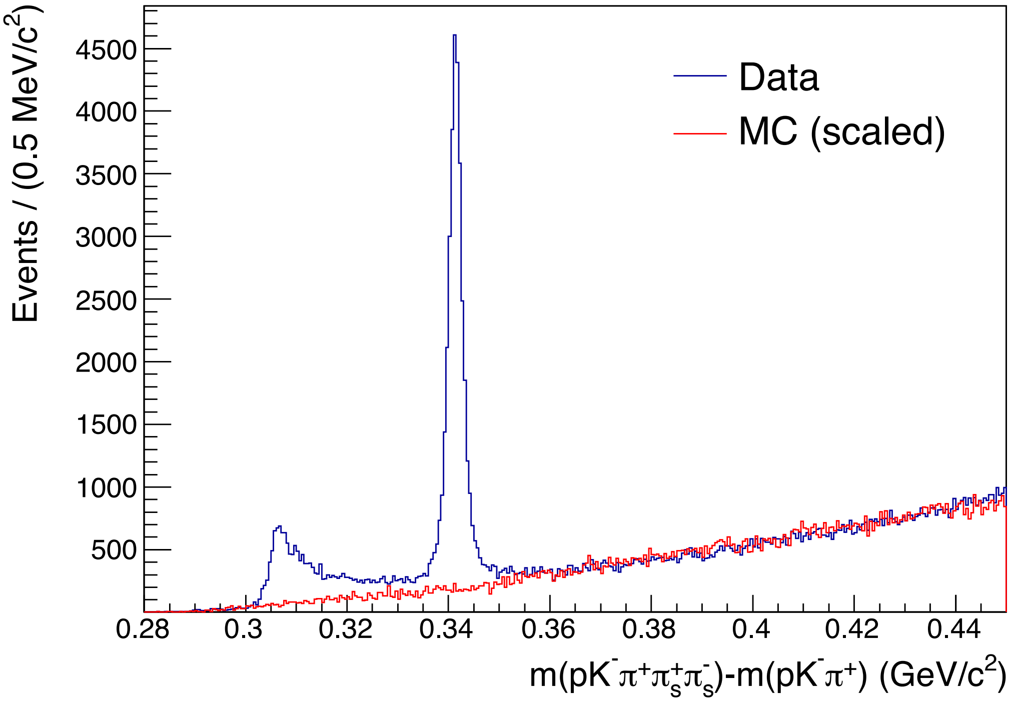

Figure 5.7: Comparison between the data (blue) and scaled generic MC (red). The generic MC sample is scaled to fit to the data.

signal regions of the excited Λ_c^+ baryons are defined as:

$$
\begin{aligned}
m(\Lambda_c(2595)^+) - m(\Lambda_c^+) &\in [302, 312]\ \mathrm{MeV}/c^2 \\
m(\Lambda_c(2625)^+) - m(\Lambda_c^+) &\in [336, 347]\ \mathrm{MeV}/c^2
\end{aligned}
$$

and are illustrated in Fig. 5.6. As shown in Fig. 5.6, wrong combination events also exist below the excited Λ_c^+ signal events, and they have to be removed from the feed-down backgrounds for the unbiased estimation of the fit. Since the generic MC does not contain any signal events of the excited Λ_c^+ baryons, it is a good sample to describe the wrong combination events of the excited Λ_c^+ baryons. The normalizations of the wrong combination events are determined by scaling the MC sample to fit the data in the mass difference of $m(pK^-\pi^+\pi_s^+\pi_s^-) - m(pK^-\pi^+)$ as shown in Fig. 5.7. In order to confirm how the scaled MC sample fits to the the data, it is compared with the data in the sideband region of the mass difference, $m(pK^-\pi^+\pi_s^+\pi_s^-) - m(pK^-\pi^+)$, as shown in Fig. 5.8.

To obtain the unbiased feed-down shape, the shape of the wrong combination events of the excited Λ_c^+ signal events obtained from the scaled generic MC are subtracted from the shape of the tagged events as feed-down obtained from the data. Finally, the obtained feed-down backgrounds are subtracted from the mass

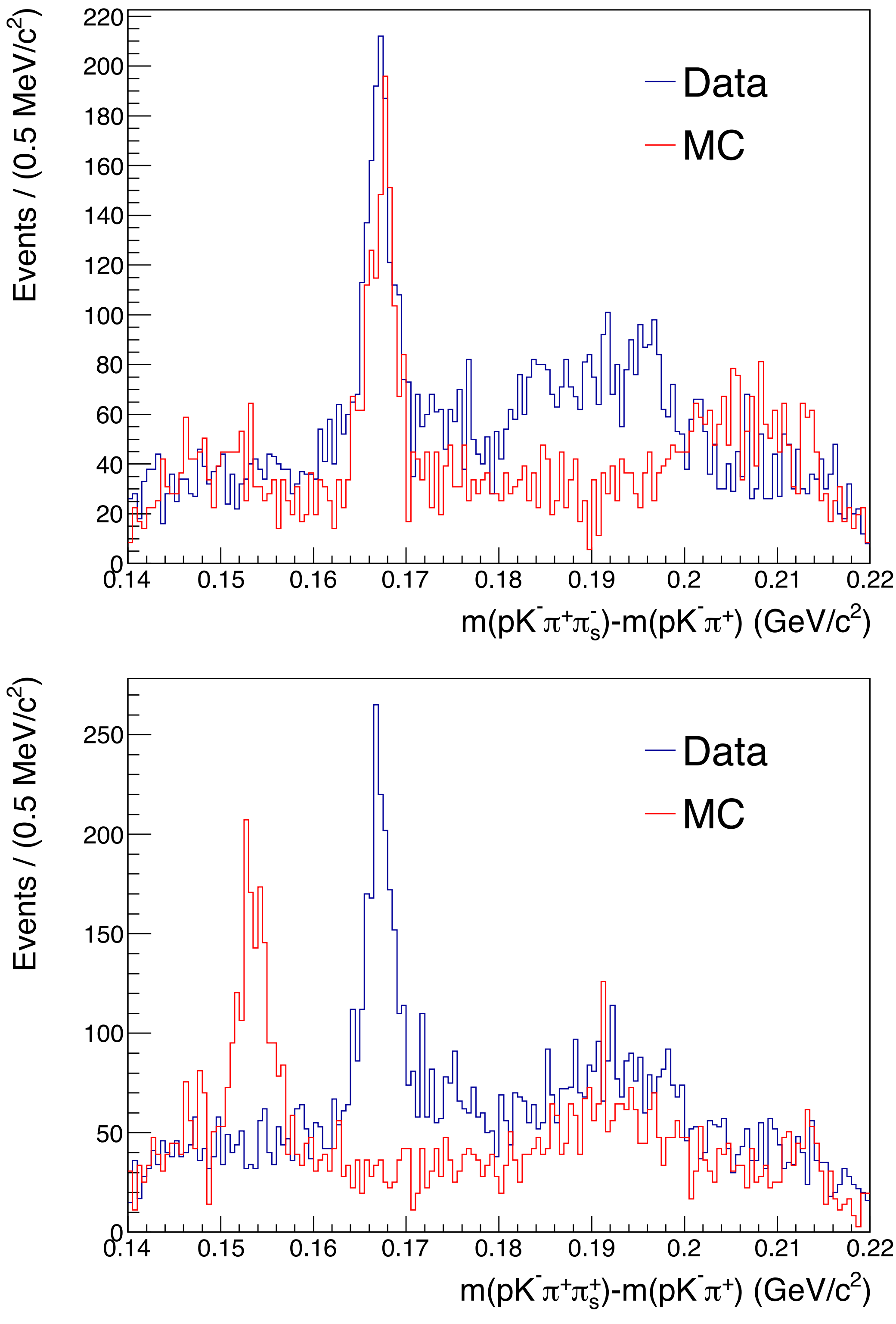

Figure 5.8: Comparison between data (blue) and scaled generic MC (red) in the defined sideband regions of the $\Lambda_c(2625)^+$ mass. The sideband regions of the $\Lambda_c(2625)^+$ mass are defined as from 322.5 to 328.0 MeV/c^2 (top) and from 355.0 to 360.5 MeV/c^2 (bottom). The generic MC sample is scaled to fit to the data. Because of the wrong input mass of the $\Sigma_c(2455)^{++}$ baryon in generic MC, the peaks originated to $\Sigma_c(2455)^{++}$ are at wrong positions ($\sim$ 210 MeV/c^2 instead of $\sim$ 190 MeV/c^2 (top) and $\sim$ 155 MeV/c^2 instead of $\sim$ 167 MeV/c^2 (bottom)).

difference distribution of $m(pK^-\pi^+\pi_s^\pm) - m(pK^-\pi^+)$. The feed-down backgrounds after the subtraction are shown in Fig. 5.9, and the mass difference distribution of $m(pK^-\pi^+\pi_s^\pm) - m(pK^-\pi^+)$ before and after the feed-down background subtraction are shown in Fig. 5.10.

5.1.3 Feed-down Background Correction

To tag the feed-down background events, full reconstruction of the $\Lambda_c^+\pi_s^+\pi_s^-$ is performed, and therefore, the tagged events imply the track finding efficiency and acceptance due to the detector geometry for an additional charged hadron while the feed-down backgrounds appear in the mass difference of $m(pK^-\pi^+\pi_s^\pm) - m(pK^-\pi^+)$ do not. Therefore, the obtained feed-down backgrounds are underestimated and have to be corrected by taking into account of the efficiency and acceptance for the additional charged hadron. In addition, the feed-down backgrounds have different behavior as a function of the momentum of the additional charged hadron as shown in Figs. 5.11 and 5.12. To correct for the feed-down backgrounds, the efficiency and acceptance are obtained as a function of the momentum of the additional charged track.

From the signal MC of the excited Λ_c^+ baryons, the momenta of charged pions are almost in the momentum region up to 600 MeV/c as shown in Fig. 5.13. Since only negligible events exceed momentum of 600 MeV/c, and the charged tracks are required to have momentum greater than 100 MeV/c in the reconstruction, we set the momentum bins to be 100 to 150, 150 to 200, 200 to 325, and 325 to 600 MeV/c to apply the efficiency and acceptance as a function of the charged track momentum. From the signal MC, we found that the charged pions directly from the $\Lambda_c(2595)^+$ baryon are softer than the ones from the $\Sigma_c^{0/++}$ baryons. In the decays of the $\Lambda_c(2625)^+$ baryon, however, the momentum of charged pions directly from the excited $\Lambda_c(2625)^+$ baryon are slightly harder than the ones from the $\Sigma_c^{0/++}$ baryons although their momentum distributions are almost the same.

The track finding efficiency is imported from the former study of the Belle experiment (Ref. [91] for $p(h^\pm) < 0.2$ GeV/c and Ref. [92] for $p(h^\pm) > 0.2$ GeV/c) and summarized in Table 5.5. Since the momentum bins of the charged track in the former study are different from the defined bins in this study, the efficiencies are calculated again by taking weighted average with the numbers of charged hadrons obtained from the signal MC accordingly.

In addition to the track finding efficiency, the acceptance due to the detector geometry also has to be considered. The acceptance is obtained from the signal

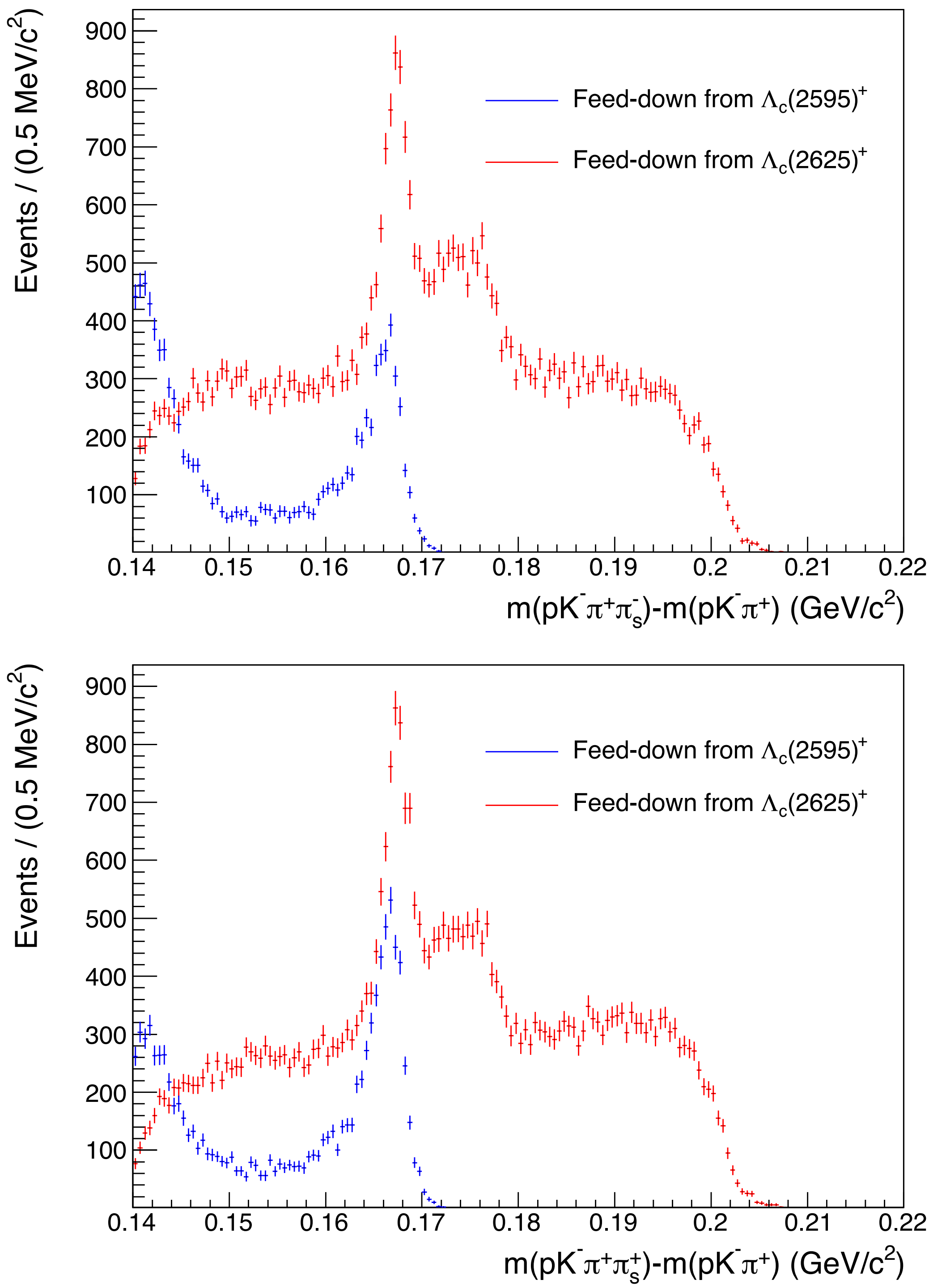

Figure 5.9: Feed-down background from the $\Lambda_c(2595)^+$ (blue) and $\Lambda_c(2625)^+$ (red) decays in the mass difference of $m(pK^-\pi^+\pi_s^-) - m(pK^-\pi^+)$ (top) and $m(pK^-\pi^+\pi_s^+) - m(pK^-\pi^+)$ (bottom) after the subtraction of the wrong combination events of the excited Λ_c^+ baryons.

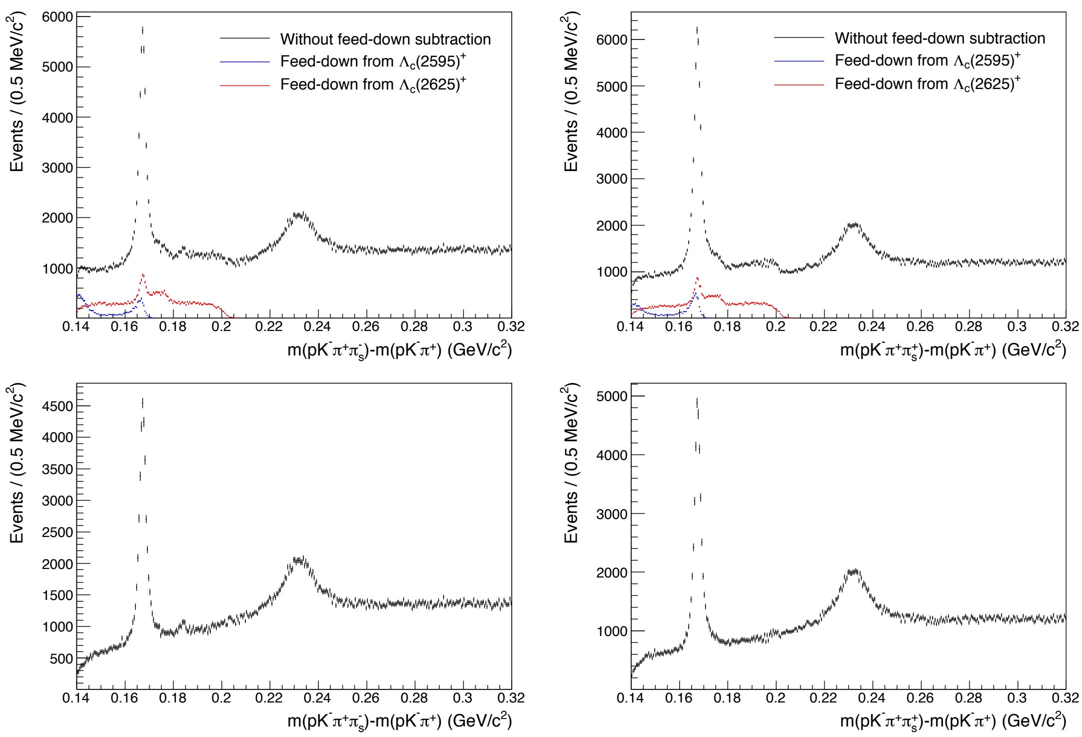

Figure 5.10: $m(pK^-\pi^+\pi_s^-) - m(pK^-\pi^+)$ (left) and $m(pK^-\pi^+\pi_s^+) - m(pK^-\pi^+)$ (left) distributions before (top) and after (bottom) the feed-down subtraction. The feed-down backgrounds from the $\Lambda_c(2595)^+$ (blue) and $\Lambda_c(2625)^+$ (red) decays are also shown.

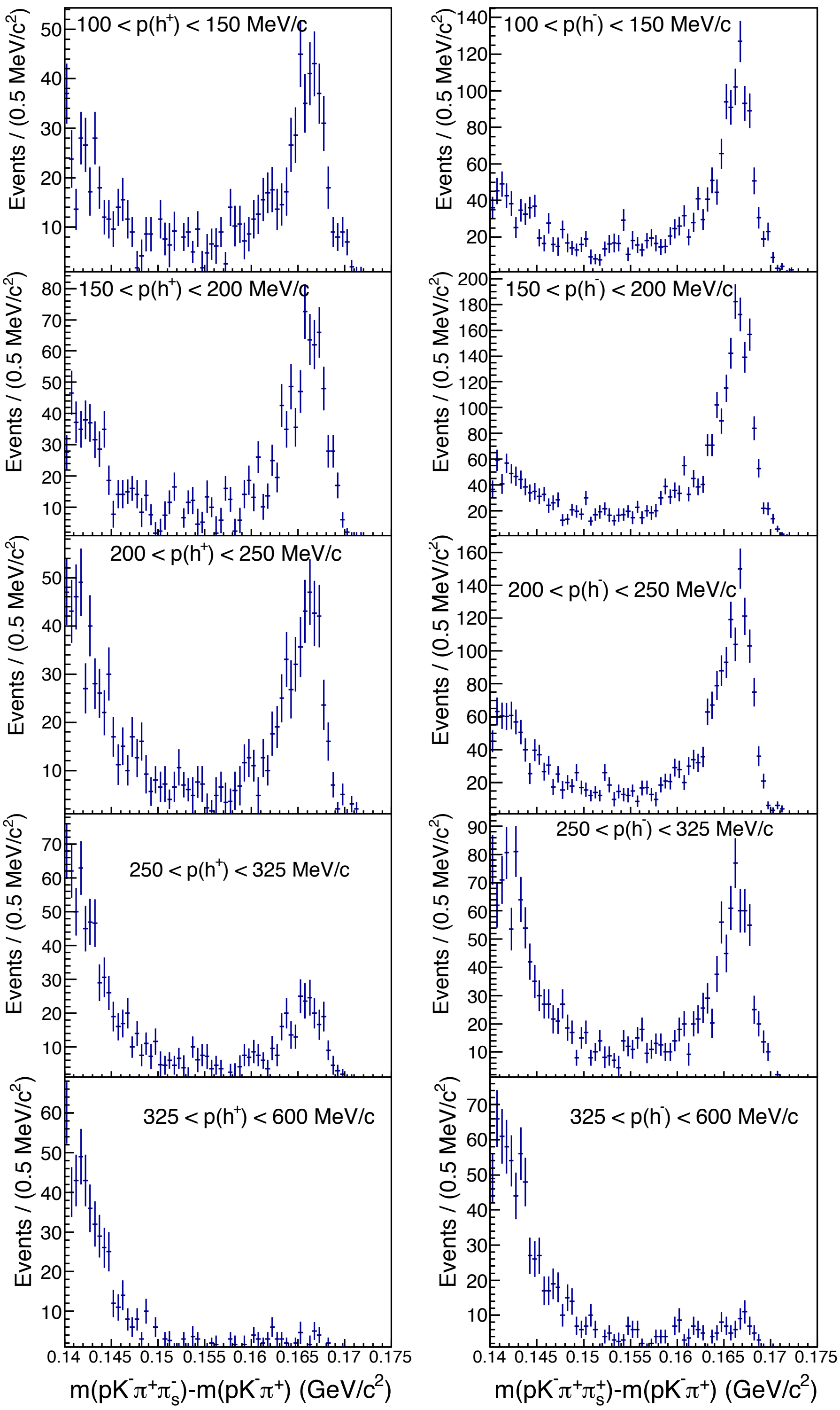

Figure 5.11: Feed-down background from the $\Lambda_c(2595)^+$ decay in different momentum bins of the additional charged hadron ($h^{\pm}$) in the $m(pK^-\pi^+\pi_s^-) - m(pK^-\pi^+)$ (left) and $m(pK^-\pi^+\pi_s^+) - m(pK^-\pi^+)$ (right).

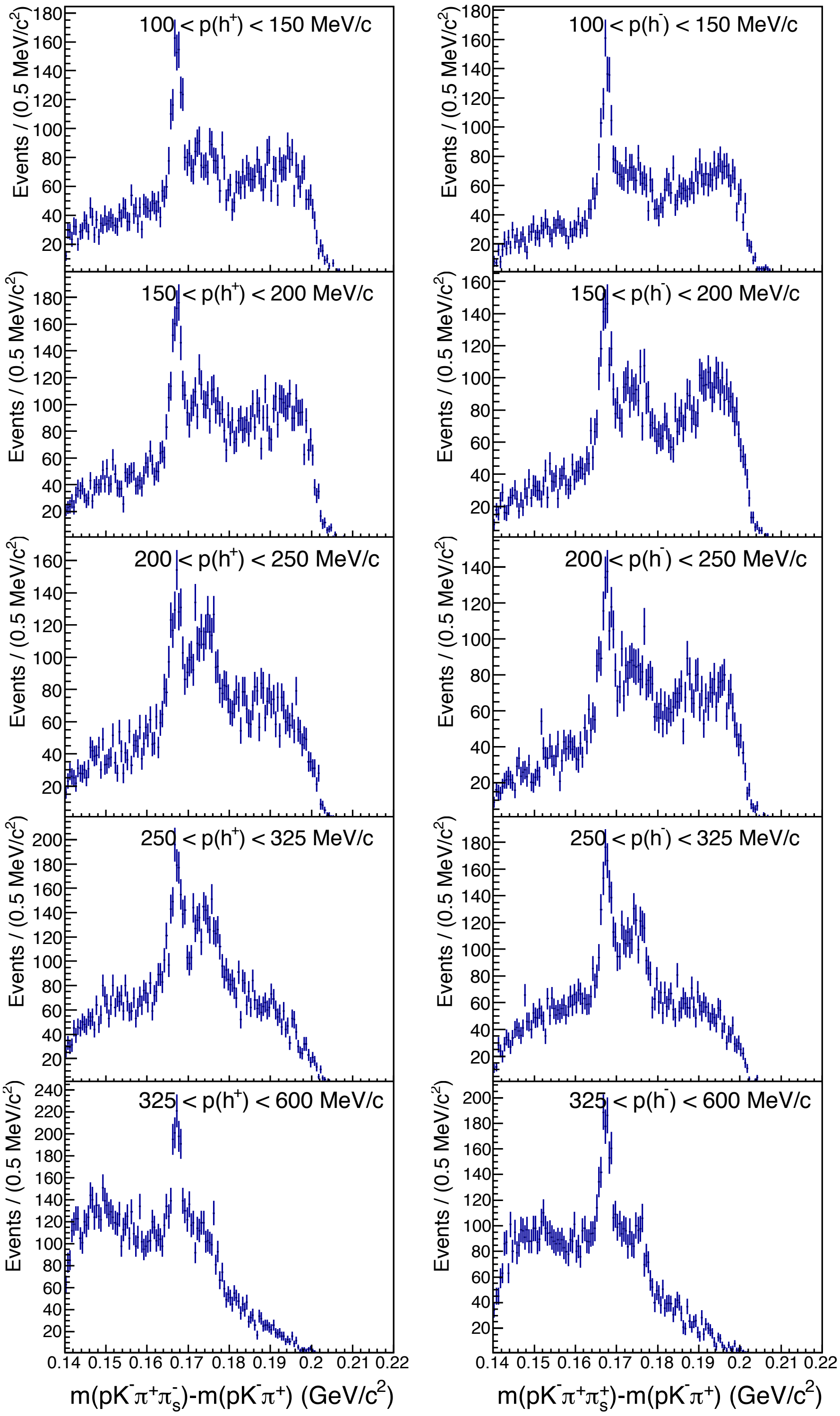

Figure 5.12: Feed-down background from the $\Lambda_c(2625)^+$ decay in different momentum bins of the additional charged hadron ($h^{\pm}$) in the $m(pK^-\pi^+\pi_s^-) - m(pK^-\pi^+)$ (left) and $m(pK^-\pi^+\pi_s^+) - m(pK^-\pi^+)$ (right).

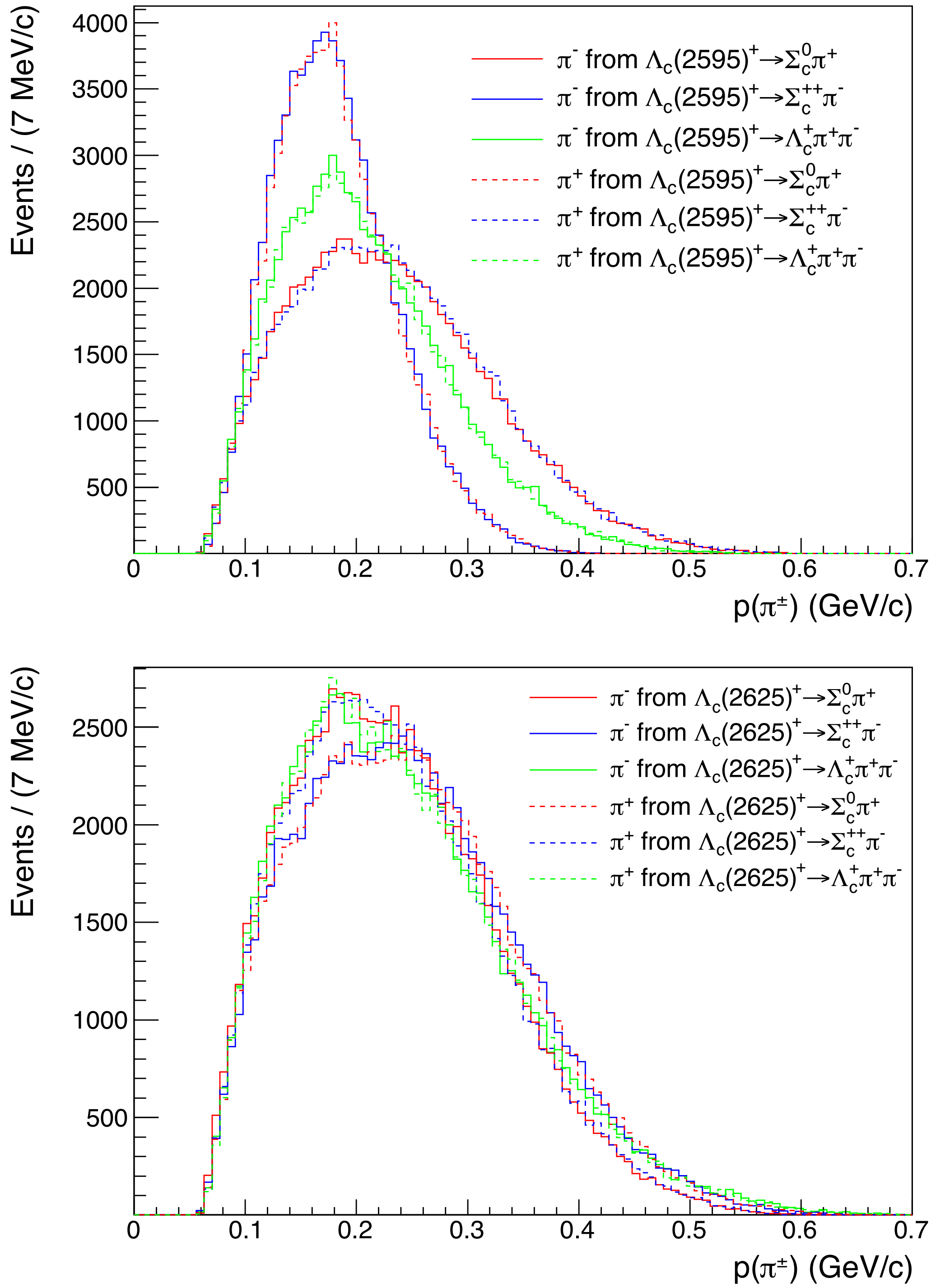

Figure 5.13: Momentum distributions of π_s^- (solid line) and π_s^+ (dashed line) from the decay of $\Lambda_c^{*+} \to \Sigma_c^0 \pi_s^+$ (red), $\Lambda_c^{*+} \to \Sigma_c^{++} \pi_s^-$ (blue), and $\Lambda_c^{*+} \to \Lambda_c^+ \pi_s^+ \pi_s^-$ (green) are shown for the $\Lambda_c(2595)^+$ (top) and $\Lambda_c(2625)^+$ (bottom) decays.

$p(h^{\pm})$ (MeV/c)	$\mathcal{N}_{\text{generated}}(h^{\pm})$	$\mathcal{N}_{\text{accepted}}(h^{\pm})$	$\epsilon_{\text{acceptance}}(h^{\pm})$
100 - 150	155,709	141,601	90.94 %
150 - 200	173,964	158,118	90.89 %
200 - 250	158,707	145,574	91.73 %
250 - 325	179,307	164,574	91.78 %
325 - 600	211,793	178,717	84.38 %
Total	879,480	788,584	89.66 %

Table 5.2: The acceptance for the positively charged hadrons from the decay of $\Lambda_c(2625)^+ \to \Sigma_c^0 \pi_s^+$.

MC of the excited Λ_c^+ decays. Since the acceptance for a charged track can be assumed to be similar between the $\Lambda_c(2595)^+$ and $\Lambda_c(2625)^+$ baryons, the acceptances are studied from the decays of $\Lambda_c(2625)^+ \to \Sigma_c^0 \pi_s^+$, $\Lambda_c(2625)^+ \to \Sigma_c^{++} \pi_s^-$, and $\Lambda_c(2625)^+ \to \Lambda_c^+ \pi_s^+ \pi_s^-$. One million events are generated and simulated for each, and the acceptance is estimated by

$$\epsilon_{\text{acceptance}}(h^{\pm}) \quad = \quad \frac{\mathcal{N}_{\text{accepted}}(h^{\pm})}{\mathcal{N}_{\text{generated}}(h^{\pm})} \tag{5.1}$$

where $\epsilon_{\text{acceptance}}(h^{\pm})$ is the acceptance for a charged hadron, $\mathcal{N}_{\text{generated}}(h^{\pm})$ and $\mathcal{N}_{\text{accepted}}(h^{\pm})$ are the numbers of the charged hadrons from the excited Λ_c^+ decays generated and accepted by the geometry, respectively. The numbers of the accepted charged hadrons are counted by checking if the hadron is within the detector geometry ($17° < \theta < 150°$ where θ is the polar angle from the beam axis). In other words, if the cosine value of the angle ($\cos\theta$) between a charged hadron momentum vector and the beam axis satisfies

$$-0.8660 < \cos\theta < 0.9563,$$

the charged hadron is counted as an accepted one. The numbers of generated and accepted charged hadrons, and acceptances as a function of the charged hadron momentum are summarized in Tables 5.2, 5.3, 5.4 and 5.5.

$p(h^-)$ (MeV/c)	$\mathcal{N}_{\text{generated}}(h^\mp)$	$\mathcal{N}_{\text{accepted}}(h^\mp)$	$\epsilon_{\text{acceptance}}(h^\mp)$
100 - 150	156,494	142,244	90.89 %
150 - 200	175,532	159,496	90.86 %
200 - 250	160,235	146,941	91.70 %
250 - 325	179,266	164,390	91.70 %
325 - 600	211,342	178,412	84.42 %
Total	882,869	791,483	89.65 %

Table 5.3: The acceptance for the negatively charged hadrons from the decay of $\Lambda_c(2625)^+ \to \Sigma_c^{++}\pi_s^-$.

$p(h^{\pm})$ (MeV/c)	$\mathcal{N}_{\text{generated}}(h^{\pm})$	$\mathcal{N}_{\text{accepted}}(h^{\pm})$	$\epsilon_{\text{acceptance}}(h^{\pm})$	$\mathcal{N}_{\text{accepted}}(h^{\mp})$	$\epsilon_{\text{acceptance}}(h^{\mp})$
100 - 150	166,071	151,954	91.50 %	151,922	91.48 %
150 - 200	183,425	167,528	91.33 %	176,790	91.40 %
200 - 250	160,966	146,728	91.15 %	146,849	91.23 %
250 - 325	173,409	156,332	90.15 %	156,224	90.09 %
325 - 600	185,959	156,958	84.40 %	156,670	84.25 %
Total	869,830	779,500	89.62 %	788,455	90.64 %

Table 5.4: The acceptance for the charged hadrons from the decay of $\Lambda_c(2625)^+ \to \Lambda_c^+\pi_s^+\pi_s^-$.

$p(h^{\pm})$ (GeV/c)	0.1 - 0.15	0.15 - 0.2	0.2 - 0.25	0.25 - 0.325	0.325 - 0.6
$\epsilon_{\text{tracking}}(h^{\pm})$	75.00 %	75.00 %	83.50 %	84.80 %	90.40 %
$\epsilon_{\text{acceptance}}(h^{\pm})$	91.20 %	91.12 %	91.45 %	90.93 %	84.36 %

Table 5.5: The track finding efficiency and the acceptance of a charged hadron obtained from the former study of the Belle experiment (Ref. [91] for $p(h^{\pm}) < 0.2$ GeV/c and Ref. [92] for $p(h^{\pm}) > 0.2$ GeV/c) and the signal MC, respectively. The efficiencies are calculated for the defined momentum regions by taking weighted average with the numbers of charged hadrons accordingly.

The obtained efficiency and the acceptance are applied to the feed-down backgrounds as a function of the momentum of the additional charged hadron by

$$\mathcal{N}_{\text{corrected}}(\text{Feed-down}) = \frac{\mathcal{N}_{\text{uncorrected}}(\text{Feed-down})}{\epsilon_{\text{tracking}}(h^{\pm}) \cdot \epsilon_{\text{acceptance}}(h^{\pm})} \tag{5.2}$$

where $\mathcal{N}_{\text{corrected}}(\text{Feed-down})$ and $\mathcal{N}_{\text{uncorrected}}(\text{Feed-down})$ are the yields of corrected and uncorrected feed-down backgrounds, $\epsilon_{\text{tracking}}(h^{\pm})$ is the track finding efficiency, and $\epsilon_{\text{acceptance}}(h^{\pm})$ is the acceptance. Figure 5.14 illustrates the corrected and uncorrected feed-down backgrounds.

Finally, the wrong combination events of the excited Λ_c^+ baryons subtracted and corrected feed-down backgrounds are removed from the mass difference distribution, $m(pK^-\pi^+\pi_s^{\pm}) - m(pK^-\pi^+)$, as shown in Fig. 5.15.

5.2 Reflection Backgrounds from $D^*(2010)^+$ Decays

Another possible contribution to backgrounds is a wrong combination of a proton and a $D^*(2010)^+$ in the decay of $D^*(2010)^+ \to D^0\pi_s^+$. Since the pion in the decay of $D^*(2010)^+ \to D^0\pi_s^+$ has low momentum, there is a probability of which the wrong combination can be identified of a background source. Furthermore, the decay chains of $D^0 \to K^-\pi^+X$ where X is additional massive hadron(s) increase the probability to form a background event. Table 5.6 summarizes possible decays of D^0 to contribute this background.

If the decays of $D^*(2010)^+ \to D^0\pi_s^+$ with $D^0 \to K^-\pi^+X$ are partially involved in the wrong combination, they make a reflection background event. For example, if a negatively charged kaon (K^-) and a positively charged pion (π^+) of a decay of the $D^*(2010)^+$ meson with $D^0 \to K^-\pi^+\pi^+\pi^-$, and the soft pion from the $D^*(2010)^+$ meson are combined with a random proton, then it becomes the same final state particles of $pK^-\pi^+\pi_s^+$ with the decays of the $\Sigma_c(2455)^{++}$ and $\Sigma_c(2520)^{++}$ baryons.

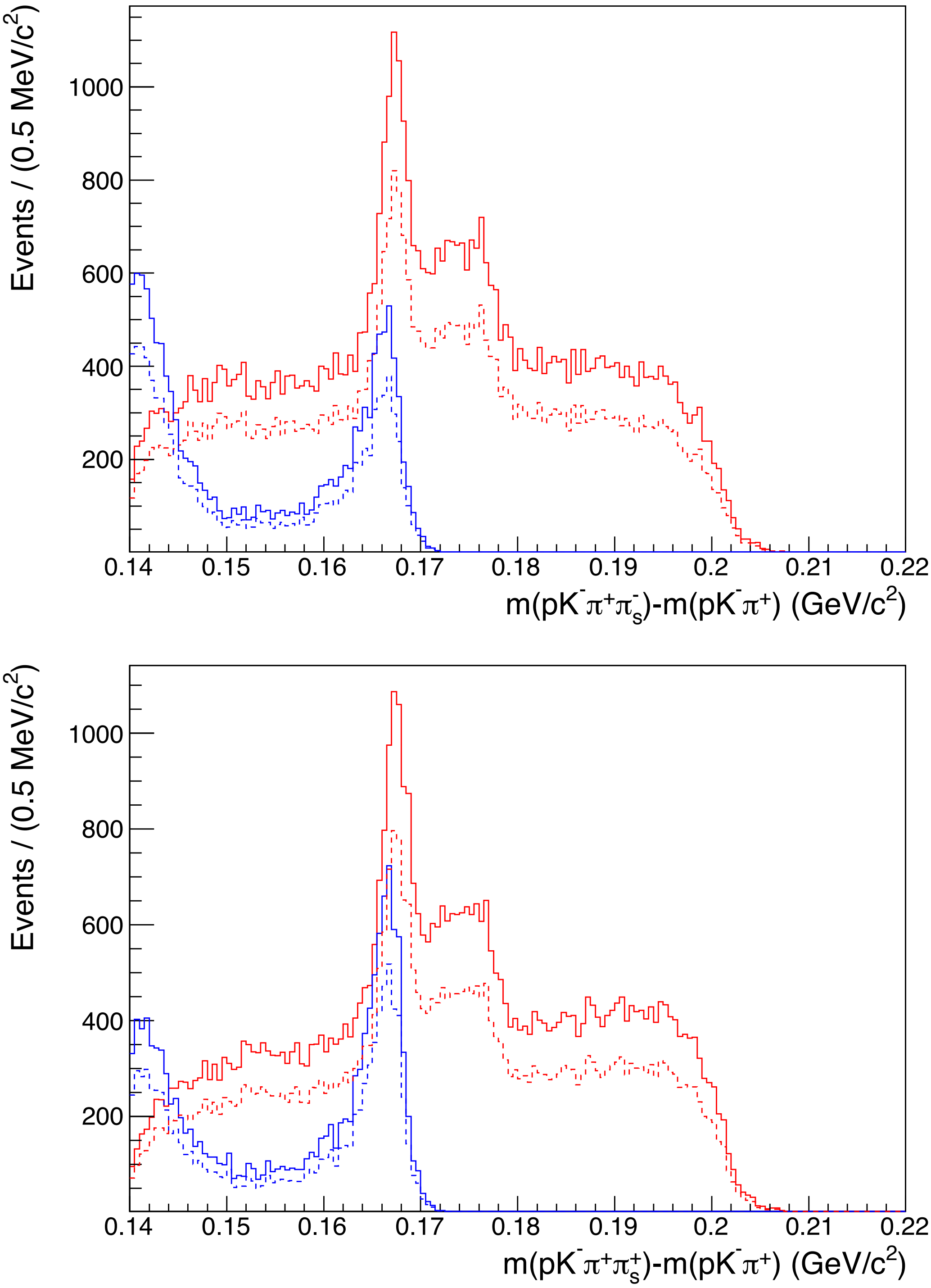

Figure 5.14: Corrected (solid-line) and uncorrected (dashed-line) feed-down backgrounds from the $\Lambda_c(2595)^+$ (blue) and $\Lambda_c(2625)^+$ (red) decays in the mass differences of $m(pK^-\pi^+\pi_s^-)-m(pK^-\pi^+)$ (top) and $m(pK^-\pi^+\pi_s^+)-m(pK^-\pi^+)$ (bottom).

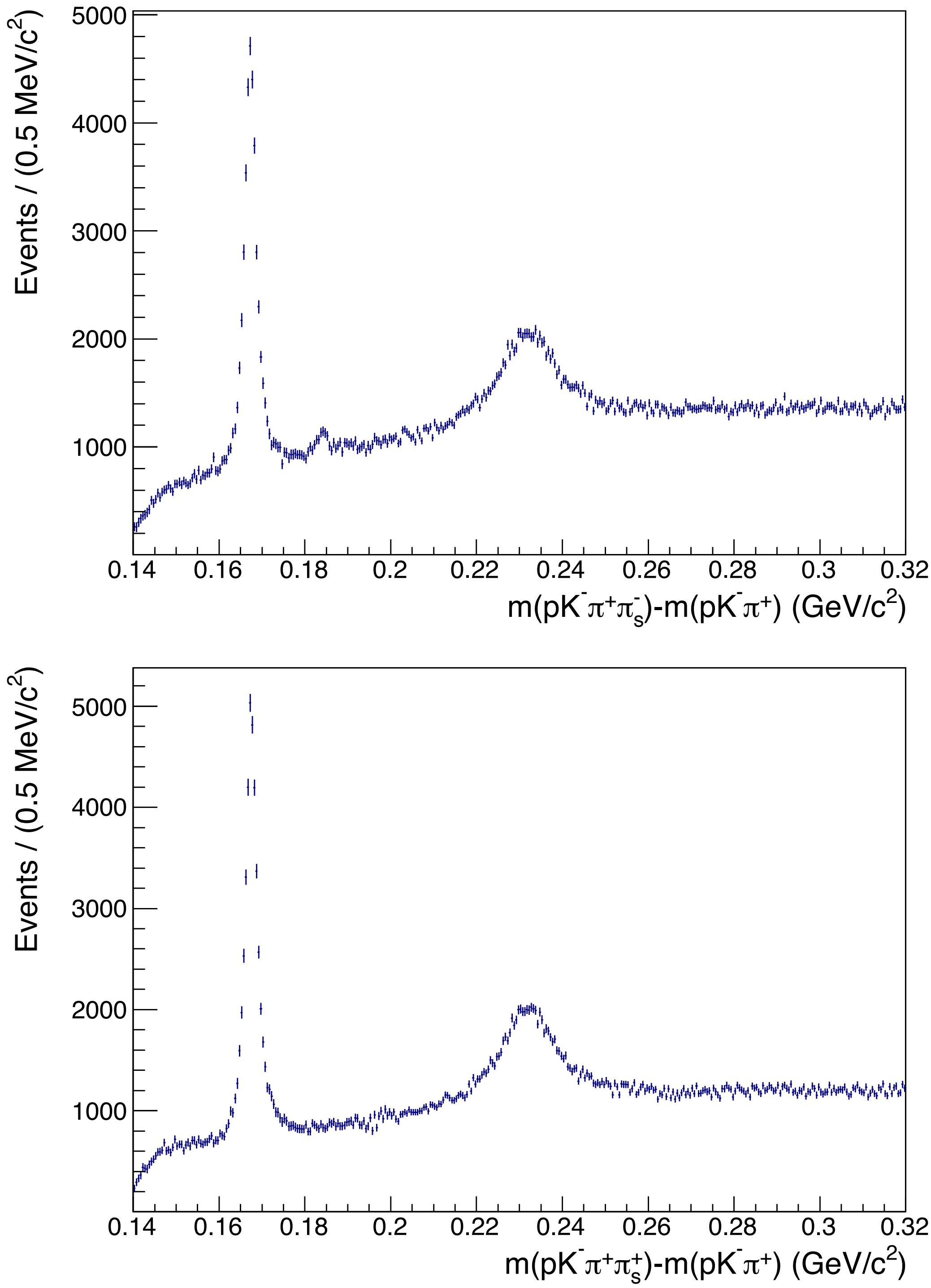

Figure 5.15: $m(pK^-\pi^+\pi_s^-)-m(pK^-\pi^+)$ (top) and $m(pK^-\pi^+\pi_s^+)-m(pK^-\pi^+)$ (bottom) distributions after the final feed-down subtraction.

Decay mode	Branching fraction
K^-X	(54.7 ± 2.8) %
$K^-\pi^+$	(3.88 ± 0.05) %
$K^-\pi^+\pi^0$	(13.9 ± 0.5) %
$K^-\pi^+\pi^+\pi^-$	$(8.07^{+0.21}_{-0.19})$ %
$K^-\pi^+\pi^+\pi^-\pi^0$	(4.2 ± 0.4) %

Table 5.6: D^0 decays of which is possible to be a background [3]. X is additional massive hadrons. Only significant decays are summarized in this table.

However, in the case of the $\Sigma_c(2455)^0$ and $\Sigma_c(2520)^0$ baryons, the reflection background can only exist if the $D^*(2010)^-$ meson is involved because a negatively charged soft pion is necessary to form the combination of the same final state particles. Since the decay of the $D^*(2010)^-$ meson includes $\overline{D^0}$, the charge conjugations of the decays summarized in Table 5.6 cannot form the same final state. Only possibility is that the decay of D^0 includes $K^+\pi^-$, but the branching fraction of $D^0 \to K^+X$ is small ($=(3.4 \pm 0.4)$ %) comparing with the decays of $D^0 \to K^-X$ ((54.7 ± 2.8) %) [3], therefore, the reflection backgrounds from the $D^*(2010)^+$ meson are dominant and only appear in the decay of the $\Sigma_c(2455)^{++}$ and $\Sigma_c(2520)^{++}$ baryons.

The reflection backgrounds are investigated by using generic MC as shown in Fig. 5.16. As expected, the reflection backgrounds are only significantly found in the mass difference of $m(pK^-\pi^+\pi_s^+) - m(pK^-\pi^+)$. These backgrounds can be treated as random backgrounds due to wrong combinations. As discussed in Sec. 5.3.1, the reflection backgrounds from the $D^*(2010)^+$ decays are described as a part of the random backgrounds.

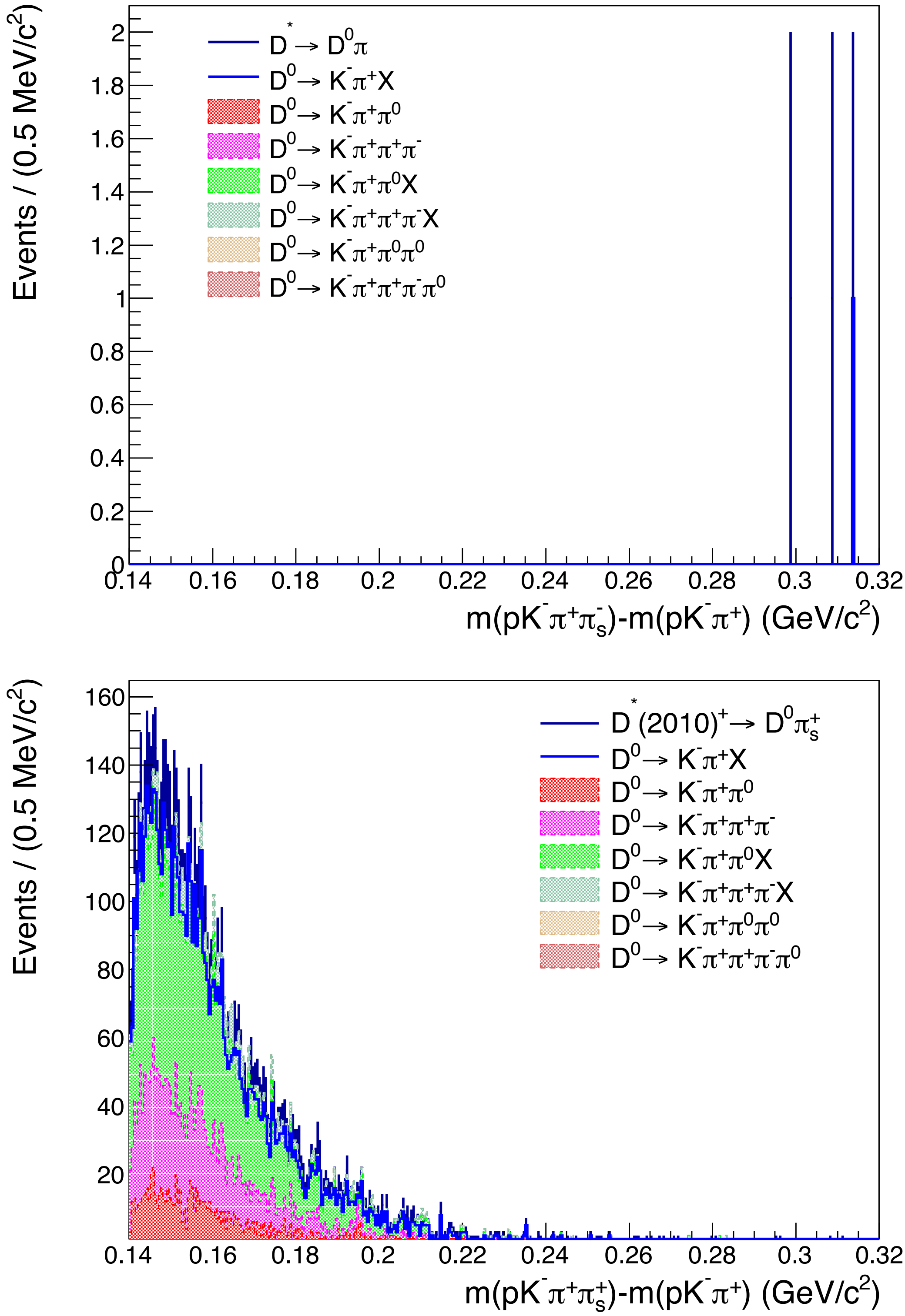

Figure 5.16: Reflection background from the $D^*(2010)^+$ decays in $m(pK^-\pi^+\pi_s^-) - m(pK^-\pi^+)$ (top) and $m(pK^-\pi^+\pi_s^+) - m(pK^-\pi^+)$ (bottom) from the generic MC. Dominant sources of the reflection backgrounds appear only in $m(pK^-\pi^+\pi_s^+) - m(pK^-\pi^+)$, and they are the $D^*(2010)^+ \to D^0\pi_s^+$ decays with $D^0 \to K^-\pi^+\pi^0$, $D^0 \to K^-\pi^+\pi^+\pi^-$, and $D^0 \to K^-\pi^+\pi^0X$ where X is additional massive hadron(s).

5.3 Random Backgrounds

Since the events are combinations of four charged tracks, there are naturally contributions from background events due to wrong combinations of tracks. The random background is classified into a random background associated with true and fake Λ_c^+ because a Λ_c^+ candidate also can be a wrong combination of three charged tracks.

5.3.1 Random Background associated with Fake Λ_c^+

Although the selection criteria include the reconstructed Λ_c^+ mass to be within 2278.07 to 2295.27 MeV/c^2, it does not guarantee that the selection includes the true Λ_c^+ baryons only because of the potential wrong combination of p, K^-, and π^+ tracks. The random background associated with the fake Λ_c^+ candidates can be extracted from the Λ_c^+ mass sidebands. For this purpose, the sideband regions of the Λ_c^+ mass are defined as

$$\begin{aligned} m(\Lambda_c^+ \text{ left-sideband}) &\in [2259.16, 2267.76] \text{ MeV}/c^2 \\ m(\Lambda_c^+ \text{ right-sideband}) &\in [2305.58, 2314.18] \text{ MeV}/c^2, \end{aligned}$$

and the sum of two sideband area is intended to be the same with the area below the signal in the signal region ($m(\Lambda_c^+) \in$[2278.07, 2295.27] MeV/c^2 which corresponds to $\pm 2.1\sigma$ from the nominal Λ_c^+ mass where σ represents the Λ_c^+ invariant mass resolution). The signal and sideband regions of the Λ_c^+ mass are already shown in Fig. 4.3.

The obtained shapes of the random background associated with the fake Λ_c^+ are shown in Figs. 5.17 (from the generic MC) and 5.18 (from data). As discussed in Sec. 5.2, the contribution of reflection backgrounds from the $D^*(2010)^+$ decays is only significant in the mass difference of $m(pK^-\pi^+\pi_s^+) - m(pK^-\pi^+)$. Since the reflection backgrounds from the $D^*(2010)^+$ decays are already included in the random background associated with the fake Λ_c^+ candidates, the obtained shapes of the random background associated with the fake Λ_c^+ candidates are used to describe both backgrounds. For the further test of the consistency of the sideband, the behaviors of the random backgrounds associated with the fake Λ_c^+ are compared between the signal and sideband regions as shown in Fig. 5.19, and it is confirmed that the random background associated with the fake Λ_c^+ candidates from the Λ_c^+ mass sideband well describes the behavior of the actual random background associated with the fake Λ_c^+ candidates.

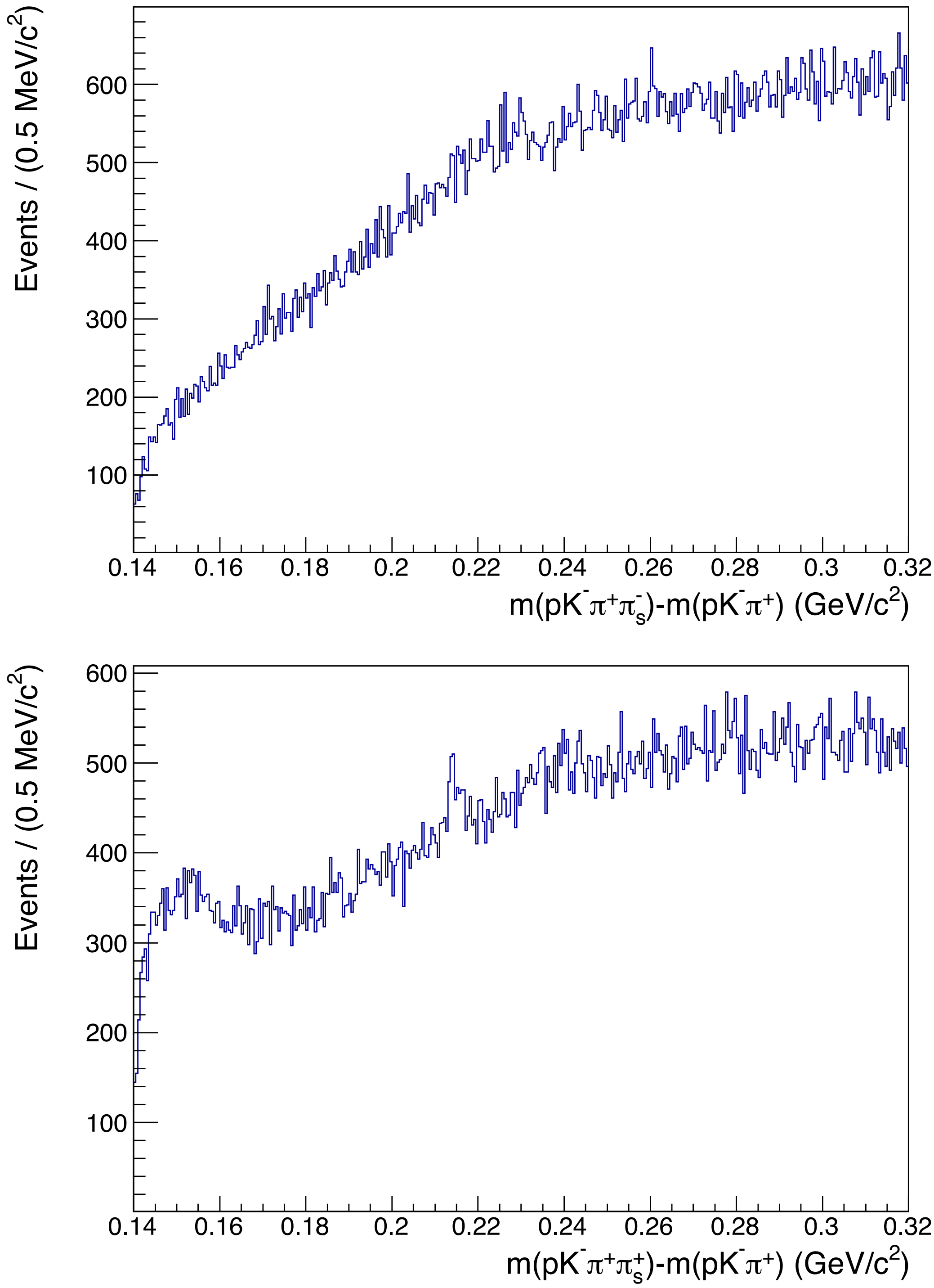

Figure 5.17: Random background associated with the fake Λ_c^+ in $m(pK^-\pi^+\pi_s^-) - m(pK^-\pi^+)$ (top) and $m(pK^-\pi^+\pi_s^+) - m(pK^-\pi^+)$ (bottom) obtained from the generic MC.

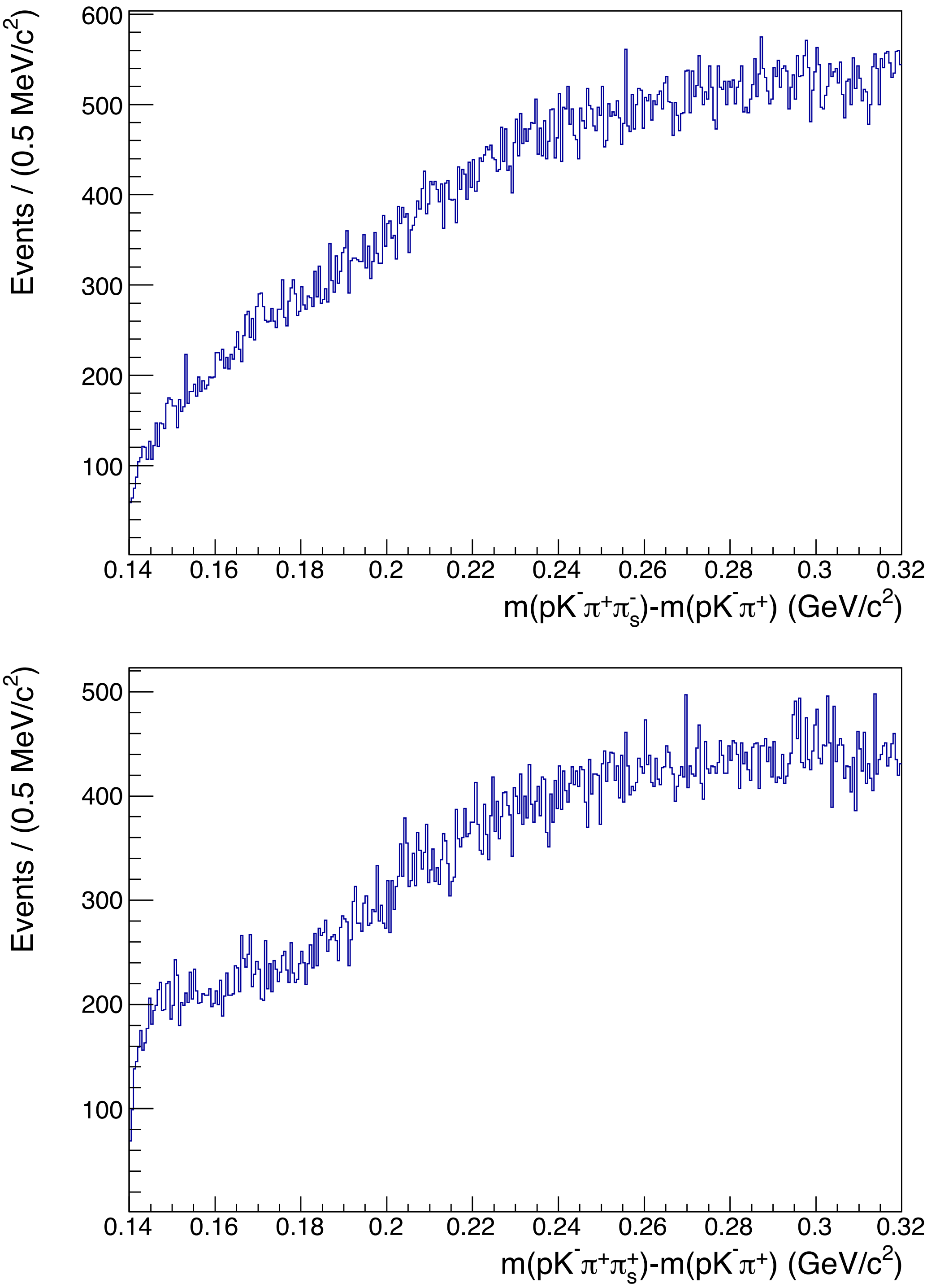

Figure 5.18: Random background associated with the fake Λ_c^+ in $m(pK^-\pi^+\pi_s^-) - m(pK^-\pi^+)$ (top) and $m(pK^-\pi^+\pi_s^+) - m(pK^-\pi^+)$ (bottom) obtained from the data.

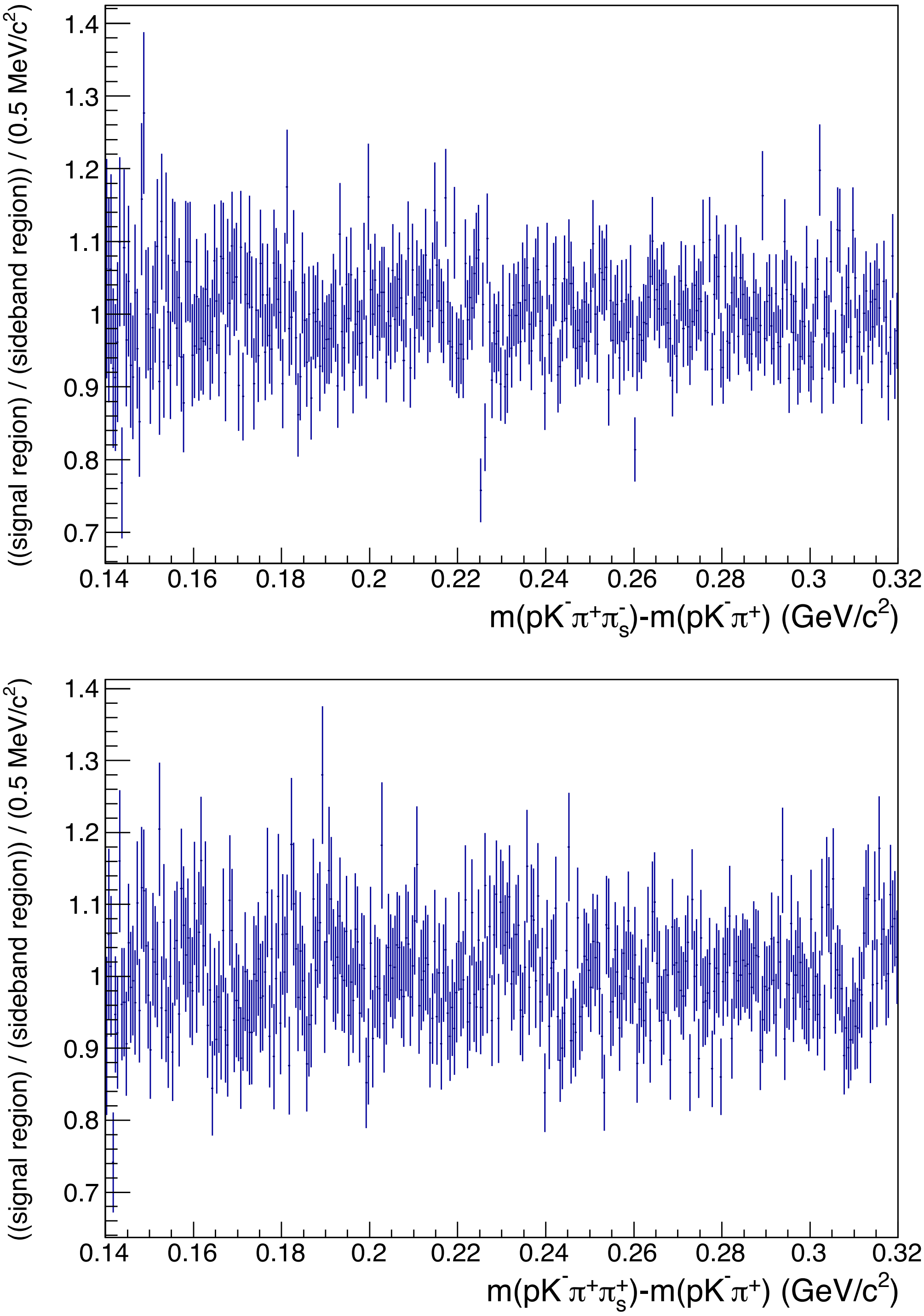

Figure 5.19: Comparison of random backgrounds associated with fake Λ_c^+ between the signal and sideband of the Λ_c^+ mass in $m(pK^-\pi^+\pi_s^-) - m(pK^-\pi^+)$ (top) and $m(pK^-\pi^+\pi_s^+) - m(pK^-\pi^+)$ (bottom) obtained from the generic MC. The vertical axis is the numbers of backgrounds in the signal region divided by the one in the sideband region.

In the fits to the mass differences of $m(pK^-\pi^+\pi_s^\pm) - m(pK^-\pi^+)$, the obtained shapes of random backgrounds associated with fake Λ_c^+ candidates are used as histogram PDFs with fixed normalizations. For the normalizations, the numbers of events in the random backgrounds associated with the fake Λ_c^+ candidates are found from the Λ_c^+ mass sidebands in the data to be 187441 ± 433 and 125734 ± 355 in the mass difference space $m(pK^-\pi^+\pi_s^\mp) - m(pK^-\pi^+)$, respectively. The uncertainties of the normalizations are accounted as sources of systematic uncertainties as discussed in Sec. 8.4.3.

5.3.2 Random Background associated with True Λ_c^+

The random background associated with the true Λ_c^+ is parameterized by a threshold function,

$$B(\Delta m; c_0, c_1) = (\Delta m - m_\pi)^{c_0} e^{-c_1(\Delta m - m_\pi)}, \tag{5.3}$$

where Δm is the mass difference of $m(pK^-\pi^+\pi_s^\pm) - m(\Lambda_c^+)$ as a random variable, m_π is a nominal mass of the pion ($m_\pi = 139.57$ MeV/c^2 [3]), c_0 and c_1 are fit parameters. The PDF is confirmed by using the generic MC which only includes random background associated with the true Λ_c^+ baryons as shown in Fig. 5.20. The variations of the PDF for the background are a possible source of systematic uncertainties, and it is discussed in Sec. 8.4.4.

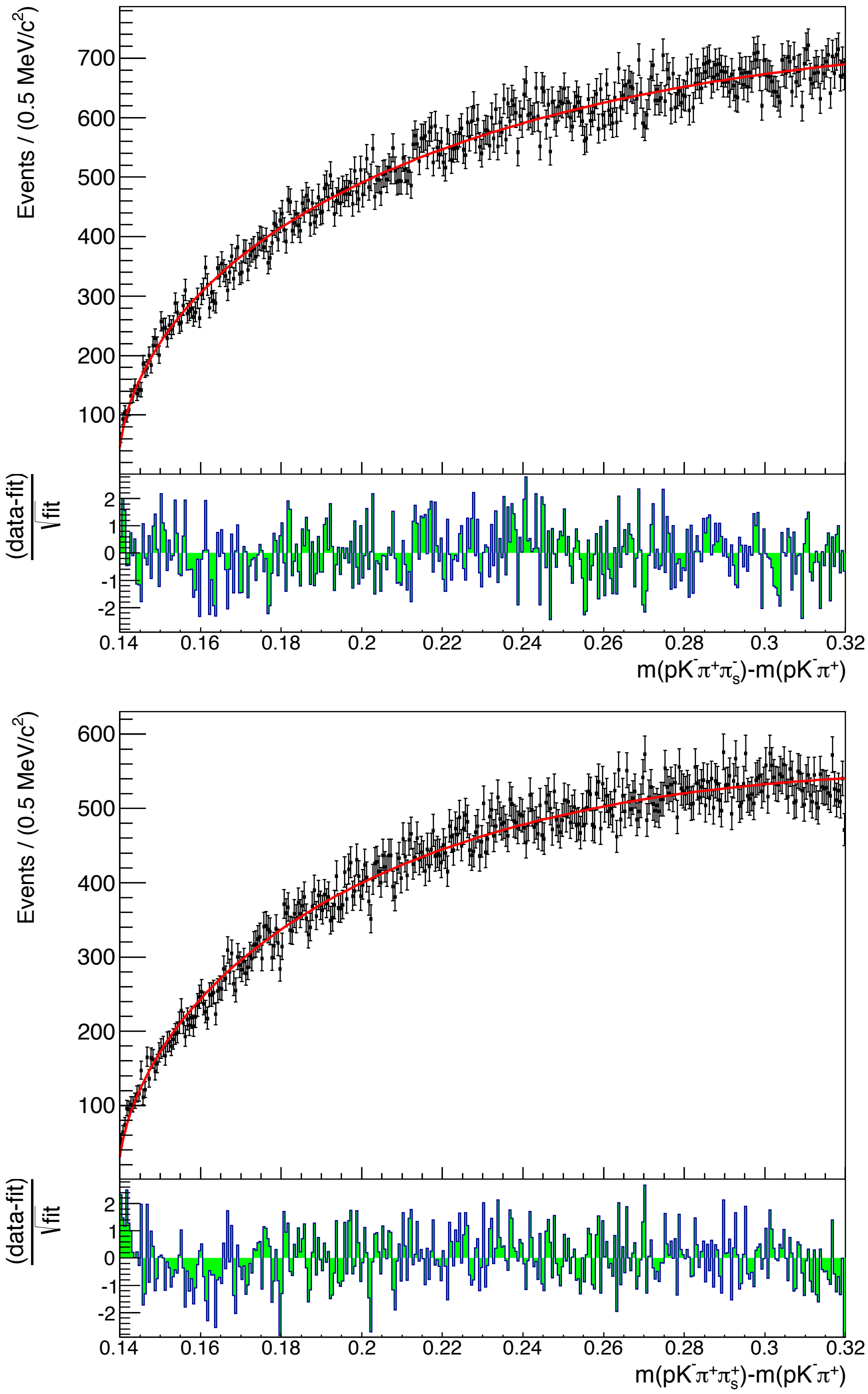

Figure 5.20: Random background associated with the true Λ_c^+ candidates in $m(pK^-\pi^+\pi_s^-) - m(pK^-\pi^+)$ (top) and $m(pK^-\pi^+\pi_s^+) - m(pK^-\pi^+)$ (bottom) obtained from the generic MC. The background events (point with error bar) are described by Eq. (5.3) (red line) as discussed in the text. The bottom plots are the differences between the data and fit results divided by fit errors, and they represent the fit quality.

Chapter 6

$\Xi_c^0 \to \Lambda_c^+ \pi^-$ Decay

In the mass difference of $m(pK^-\pi^+\pi_s^-) - m(pK^-\pi^+)$, a small peak near 185 MeV/c^2 is found as shown in Fig. 5.15. This peak is quite significant to be considered as a statistical fluctuation, and no such a fluctuation is found in the mass difference of $m(pK^-\pi^+\pi_s^+) - m(pK^-\pi^+)$. If a nominal mass of the Λ_c^+ baryons is added to the peak position, that is, $185 + 2286.46 = 2471.46$ MeV/c^2, it is very likely to originate from the Ξ_c^0 baryon ($m(\Xi_c^0) = 2470.88^{+0.34}_{-0.80}$ MeV/c^2 [3]). Therefore, this peak is thought to be from a decay of the Ξ_c^0 baryon, but there are no known decay of $\Xi_c^0 \to pK^-\pi^+\pi^-$ to date. One may expect that the peak is a reflection background of the Ξ_c^0 decays, and Table 6.1 summarizes the candidates of the Ξ_c^0 decays.

To check the contributions from the known Ξ_c^0 decays, signal MC data sets are generated and simulated. Most probable decays, such as the $\Xi_c^0 \to pK^-K^-\pi^+$ (100,000 events generated), $\Xi_c^0 \to \Lambda K_S^0$ (100,000 events generated), $\Xi_c^0 \to \Lambda K^-\pi^+$ (1,000,000 events generated), and $\Xi_c^0 \to \Lambda K^-\pi^+\pi^+\pi^-$ (1,000,000 events generated) are tested as shown in Fig. 6.1, but only small contributions are found from the decays of $\Xi_c^0 \to \Lambda K^-\pi^+$ while others are negligible. Furthermore, the contribution from the decays of $\Xi_c^0 \to \Lambda K^-\pi^+$ have broad width comparing with the small peak found in data. To validate some decay modes which include the Λ baryon, the existence of and contribution from the Λ baryon in data are checked. From the $m(p\pi^-)$ distribution, a small portion of the Λ baryon is found. To check the contribution from the Λ baryon without the random background of $p\pi^-$, a signal region of the Λ baryon is define as $m(\Lambda) \in [1112, 1120]$ MeV/c^2, and the sideband regions are defined as $m(\Lambda) \in [1100, 1104]$ MeV/c^2 or $m(\Lambda) \in [1130, 1134]$ MeV/c^2 as shown in Fig. 6.2 (left). It turns out that there is no contribution from the Λ baryon to the peak as shown in Fig. 6.2 (right).

Decay mode	Fraction (Γ_i/Γ)
$pK^-K^-\pi^+$	*seen*
$\quad pK^-\overline{K}^*(892)^0$	*seen*
$\quad pK^-K^-\pi^+$ no $\overline{K}^*(892)^0$	*seen*
ΛK_S^0	*seen*
$\Lambda\overline{K}^0\pi^+\pi^-$	*seen*
$\Lambda K^-\pi^+\pi^+\pi^-$	*seen*
$\Xi^-\pi^+$	*seen*
$\Xi^-\pi^+\pi^+\pi^-$	*seen*
ΩK^+	*seen*

Table 6.1: Decays of the Ξ_c^0 baryon [3]. Only probable candidates are summarized. The branching ratios of the listed decays are not well measured to date.

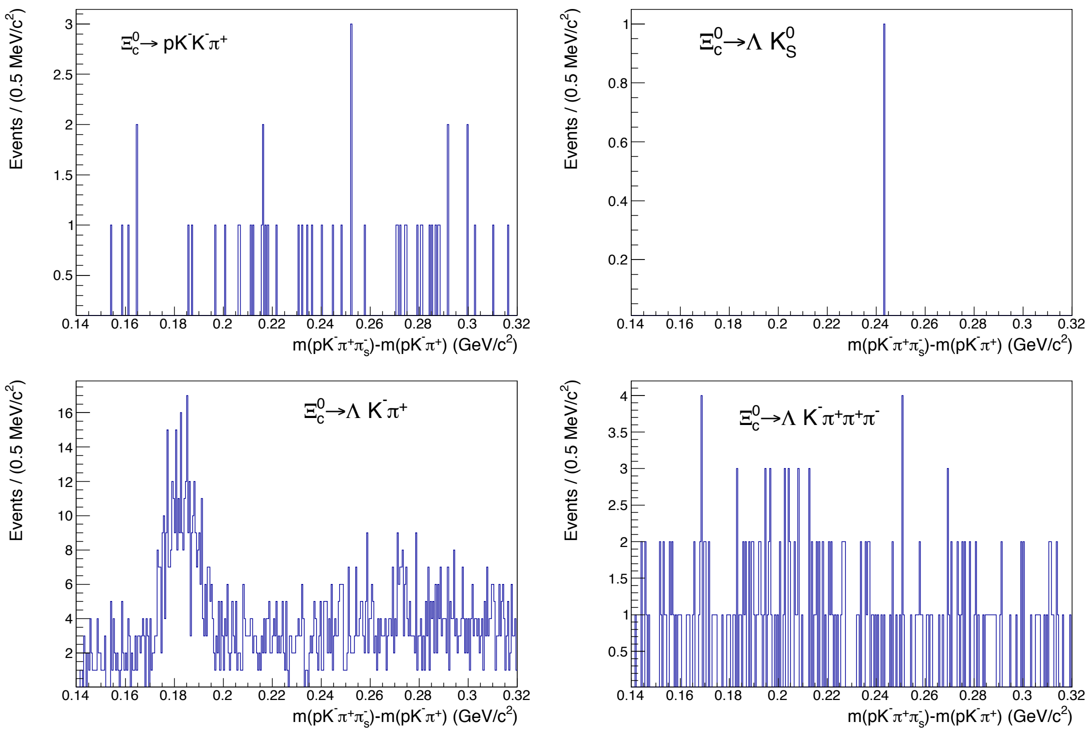

Figure 6.1: $m(pK^-\pi^+\pi_s^-) - m(pK^-\pi^+)$ distributions of the $\Xi_c^0 \to pK^-K^-\pi^+$ (top-left), $\Xi_c^0 \to \Lambda K_S^0$ (top-right), $\Xi_c^0 \to \Lambda K^-\pi^+$ (bottom-left), and $\Xi_c^0 \to \Lambda K^-\pi^+\pi^+\pi^-$ (bottom-right) decays.

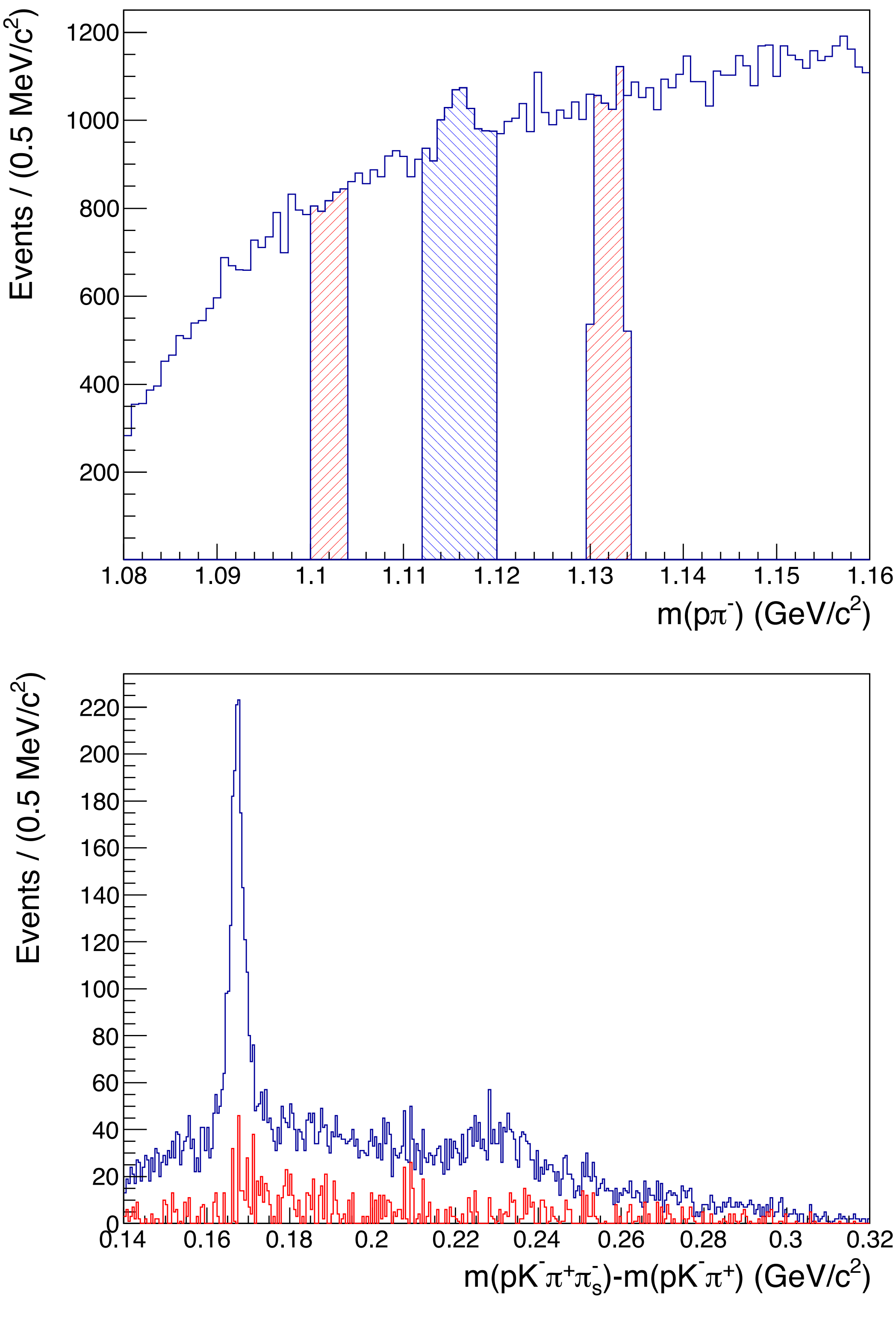

Figure 6.2: $m(pK^-)$ distribution in the reconstructed data of $pK^-\pi^+\pi_s^-$ (top) and the contribution to the peak from the Λ candidates (bottom). Defined signal (blue-hatched in top) and sideband (red-hatched in top) regions, and the contributions from the Λ signal without (blue in bottom) and with (red in bottom) the Λ sideband subtraction are shown.

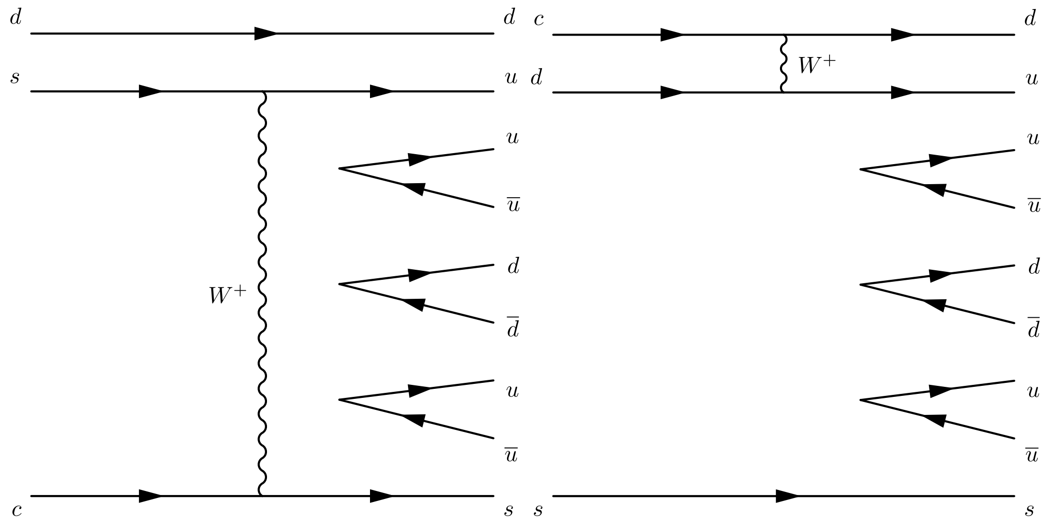

Figure 6.3: Feynman diagrams for the decay of $\Xi_c^0 \to pK^-\pi^+\pi^-$. Cabibbo factor $|V_{us}|$ is involved in the $s \to u$ (left) quark transition and $|V_{cd}|$ is involved in the $c \to d$ (right) quark transitions via W boson exchange.

Another possibility is a decay of $\Xi_c^0 \to pK^-\pi^+\pi^-$ that is not observed yet. This decay implies a weak decay with $s \to u$ or $c \to d$ quark transition as shown in Fig. 6.3. From the MC simulation, the width is found to be much broader than the peak found in the data.

From the 2-dimensional plot of the $m(pK^-\pi^+\pi_s^-) - m(pK^-\pi^+)$ and $m(pK^-\pi^+)$, the peak seems to be correlated with the Λ_c^+ baryon as shown in Figs. 6.4 and 6.5. In addition, if the decay includes the Λ_c^+ baryon, the width of $m(pK^-\pi^+\pi_s^-) - m(pK^-\pi^+)$ is expected to be comparable with the peak. In this context, an another possibility of $\Xi_c^0 \to \Lambda_c^+\pi^-$ decay is considered. The decay also implies a weak decay with $s \to u$ quark transition, therefore, a Cabibbo-suppressed decay as shown in Fig. 6.6. From a simulated data sample of $\Xi_c^0 \to \Lambda_c^+\pi^-$ decay, the decay mode is fit to the properties of the peak found in data better than the phase-space decay of $\Xi_c^0 \to pK^-\pi^+\pi^-$ as shown in Fig. 6.7. To confirm the decay channel, the mass distribution of $m(pK^-\pi^+\pi^-)$ is studied with a data sample that is not constrained to have the Λ_c^+ baryon in the data as shown in Fig. 6.8.

To reconstruct the Ξ_c^0 candidates without the constraint to the Λ_c^+ baryon, all charged tracks of p, K^-, and $\pi^\pm$ are required to have an impact parameter with respect to the interaction point of less than 1 cm along the electron beam direction and less than 0.1 cm in the plane transverse to the electron beam direction. Moreover, each track is required to have at least two associated vertex detector hits in each of the two measuring coordinates of the $r-\phi$ plane and z-axis. The charged particles are identified by applying the particle identification likelihood criteria of

$$P(p:K) = \frac{\mathcal{L}(p)}{\mathcal{L}(p)+\mathcal{L}(K)} > 0.9$$

$$P(p:\pi) = \frac{\mathcal{L}(p)}{\mathcal{L}(p)+\mathcal{L}(\pi)} > 0.9$$

for the proton identification,

$$P(K:p) = \frac{\mathcal{L}(K)}{\mathcal{L}(K)+\mathcal{L}(p)} > 0.9$$

$$P(K:\pi) = \frac{\mathcal{L}(K)}{\mathcal{L}(K)+\mathcal{L}(\pi)} > 0.6$$

for the kaon identification, and

$$P(\pi:p) = \frac{\mathcal{L}(\pi)}{\mathcal{L}(\pi)+\mathcal{L}(p)} > 0.9$$

$$P(\pi:K) = \frac{\mathcal{L}(\pi)}{\mathcal{L}(\pi)+\mathcal{L}(K)} > 0.6.$$

for the pion identification. The Ξ_c^0 candidates are reconstructed from four charged particles of p, K^-, and $\pi^\pm$, and the daughter tracks are refit to a common vertex. If the vertex fit fails, the event is discarded, and only the events that the χ^2 value of the vertex fit less than 20 are selected. To improve the signal-to-background ratio, the Ξ_c^0 candidates are required to have a center-of-mass frame momentum greater than 2.5 GeV/c.

From the sample, the existence of the peak is tested with accepting or rejecting the Λ_c^+ and Ξ_c^0 candidates as shown in Fig. 6.9. To accept the Λ_c^+ and Ξ_c^0 candidates, they are required to be $m(\Lambda_c^+) \in [2278.07, 2295.27]$ MeV/c^2 as defined in previous section, and $m(\Xi_c^0) \in [2470.08, 2471.68]$ MeV/c^2 according to the world average of Ξ_c^0 mass [3]. To reject them, $m(\Lambda_c^+) \notin [2278.07, 2295.27]$ MeV/c^2 and $m(\Xi_c^0) \notin [2470.08, 2471.68]$ MeV/c^2 are required. As shown in Fig. 6.9, the dominant portion of the peak is found with accepting the Λ_c^+ and Ξ_c^0 baryons both. In our conclusion, the peak is from the decay of $\Xi_c^0 \to \Lambda_c^+\pi^-$ that is not observed from any other experiments as of today.

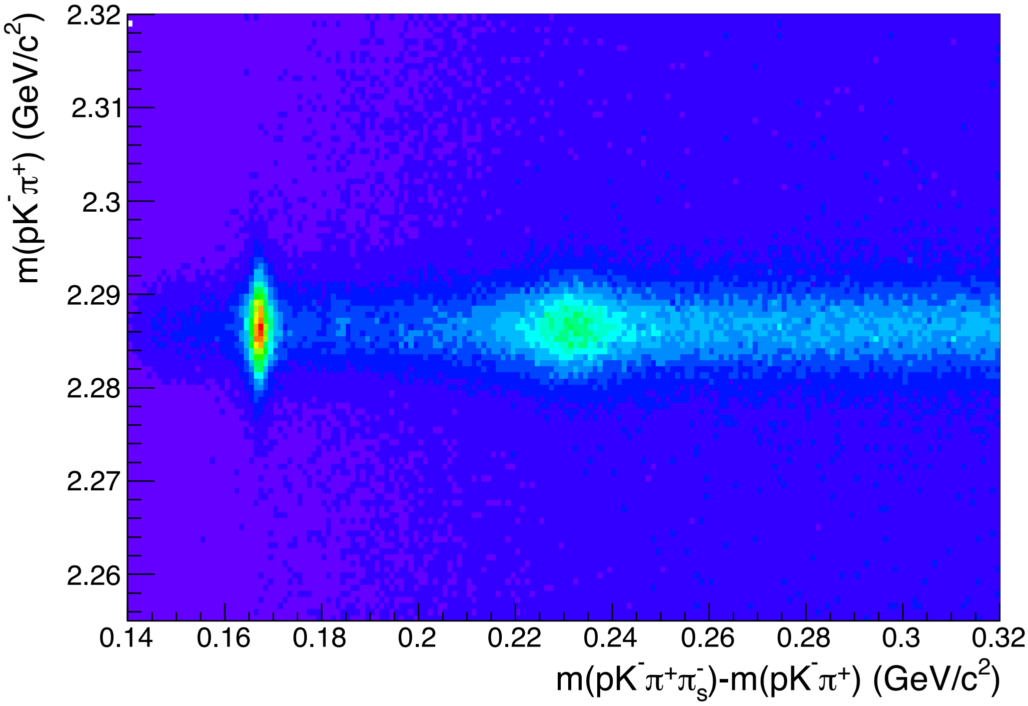

Figure 6.4: 2-dimensional plot of $m(pK^-\pi^+\pi_s^-) - m(pK^-\pi^+)$ versus $m(pK^-\pi^+)$. The peak near 185 MeV$/c^2$ in $m(pK^-\pi^+\pi_s^-) - m(pK^-\pi^+)$ seems to associate with the Λ_c^+ candidates.

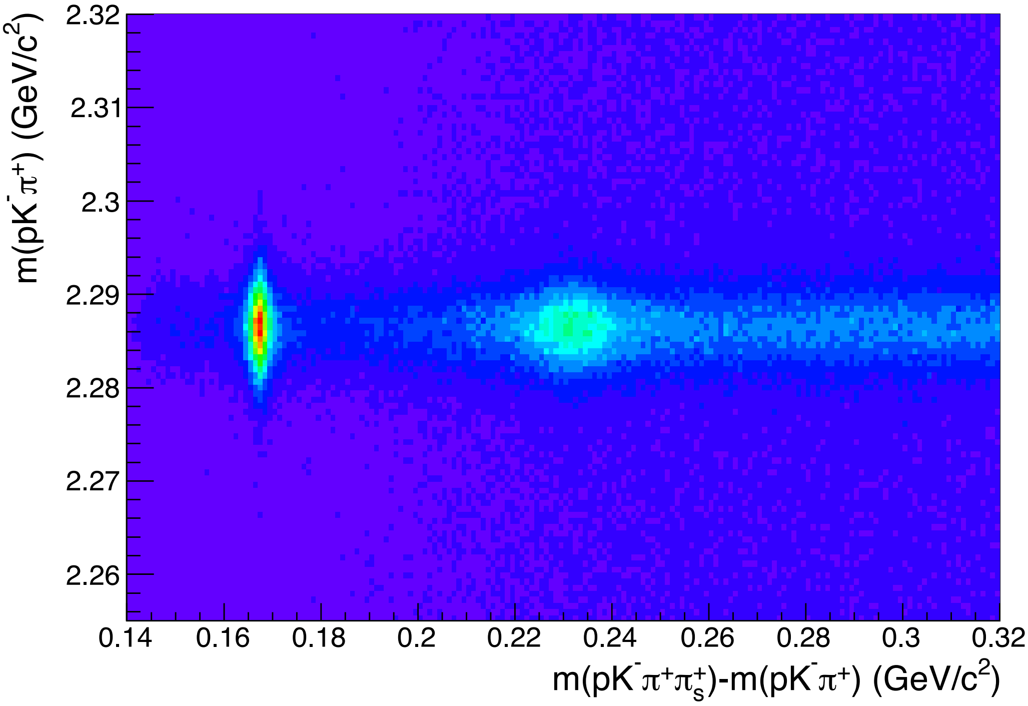

Figure 6.5: 2-dimensional plot of $m(pK^-\pi^+\pi^+_s) - m(pK^-\pi^+)$ versus $m(pK^-\pi^+)$. No peak found around 185 MeV/c^2 in $m(pK^-\pi^+\pi^+_s) - m(pK^-\pi^+)$.

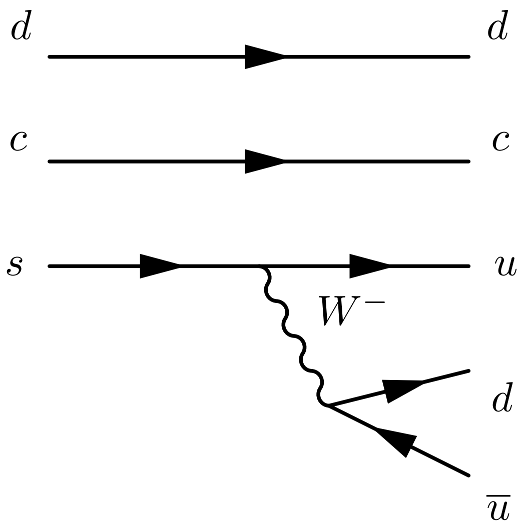

Figure 6.6: Feynman diagram for the decay of $\Xi_c^0 \to \Lambda_c^+ \pi^-$. Cabibbo factor $|V_{us}|$ is involved in the $s \to u$ quark transition via W^- boson decay.

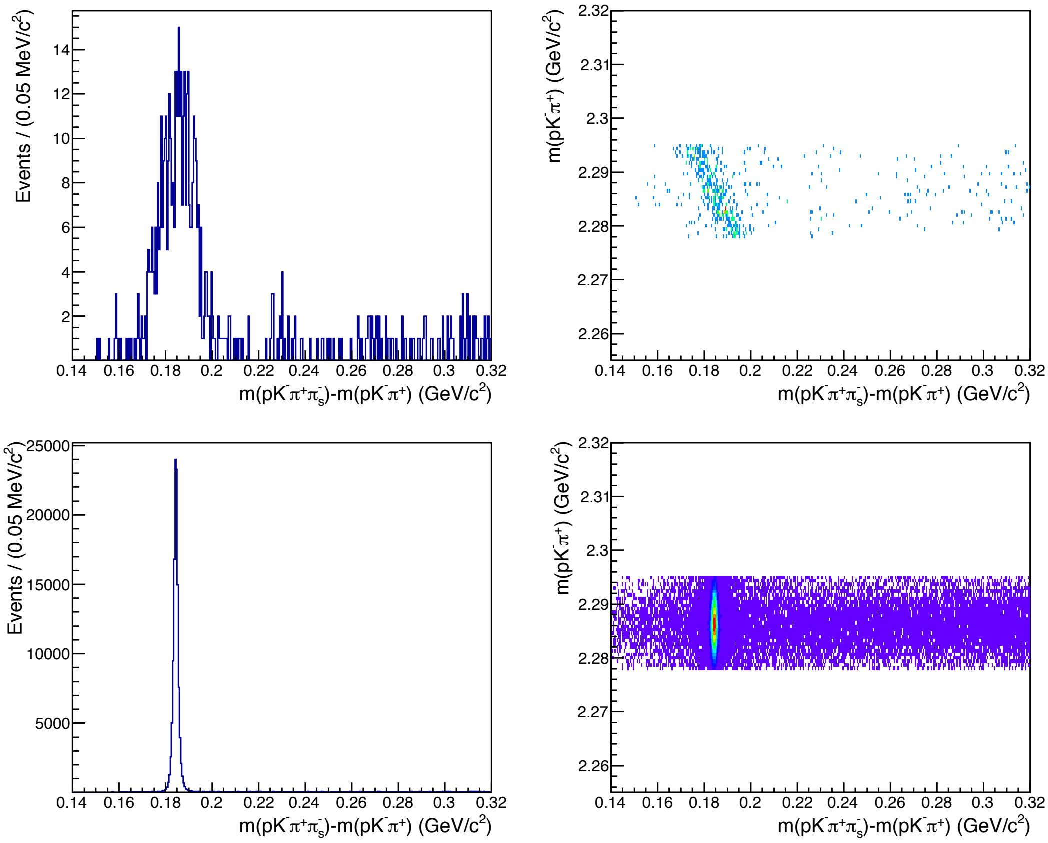

Figure 6.7: The mass difference distributions of $m(pK^-\pi^+\pi_s^-) - m(pK^-\pi^+)$ (left), and the 2-dimensional scatter plot of $m(pK^-\pi^+)$ and $m(pK^-\pi^+\pi_s^-) - m(pK^-\pi^+)$ (right) of the $\Xi_c^0 \to pK^-\pi^+\pi^-$ (top) and $\Xi_c^0 \to \Lambda_c^+\pi_s^-$ (bottom) decays. Since the combination of $pK^-\pi^+$ in the phase-space decay of $\Xi_c^0 \to pK^-\pi^+\pi^-$ is not suitable for the Λ_c^+ mass, the mass difference distribution of $m(pK^-\pi^+\pi_s^-) - m(pK^-\pi^+)$ is naturally broader than the one of $\Xi_c^0 \to \Lambda_c^+\pi_s^-$ decay which is consistent with the peak found in data. In the 2-dimensional scatter plot, only events within the Λ_c^+ signal region are taken.

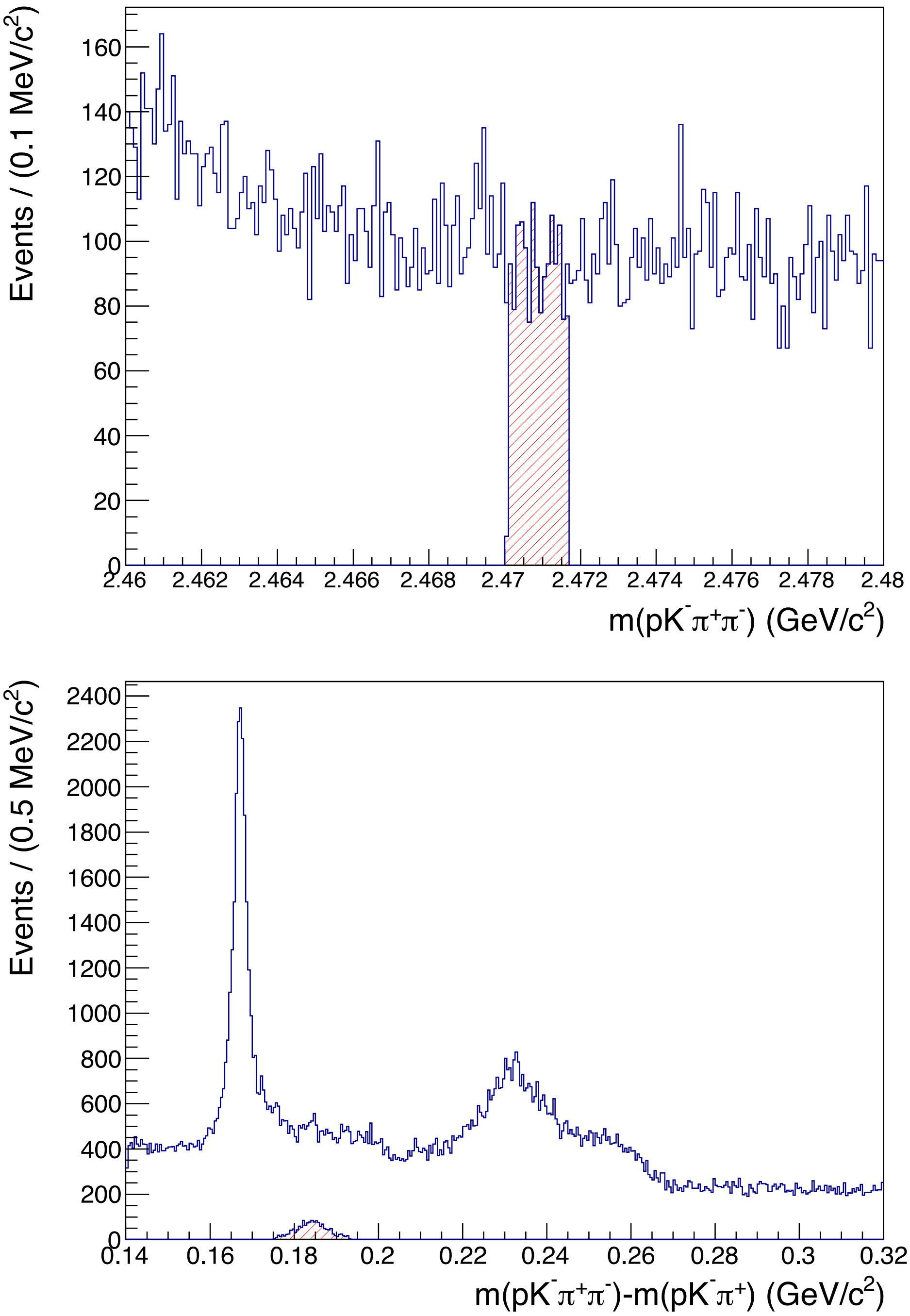

Figure 6.8: $m(pK^-\pi^+\pi^-)$ (top) and $m(pK^-\pi^+\pi^-) - m(pK^-\pi^+)$ (bottom) from the data that is not constrained to have Λ_c^+ candidates with requiring $m(pK^-\pi^+) \in [2278.07, 2295.27]$ MeV$/c^2$. The hatched region (top) is the defined signal region of the Ξ_c^0 mass according to the world average [3] and the hatched region (bottom) is the mass difference of $m(pK^-\pi^+\pi^-) - m(pK^-\pi^+)$ corresponding to the defined signal region. Because of many background events, the Ξ_c^0 events cannot be distinguishable in the mass distribution of $m(pK^-\pi^+\pi^-)$. In addition, since there is random background events below the signal events of Ξ_c^0, the mass difference of $m(pK^-\pi^+\pi^-) - m(pK^-\pi^+)$ corresponding to the defined signal region appears broader than the peak.

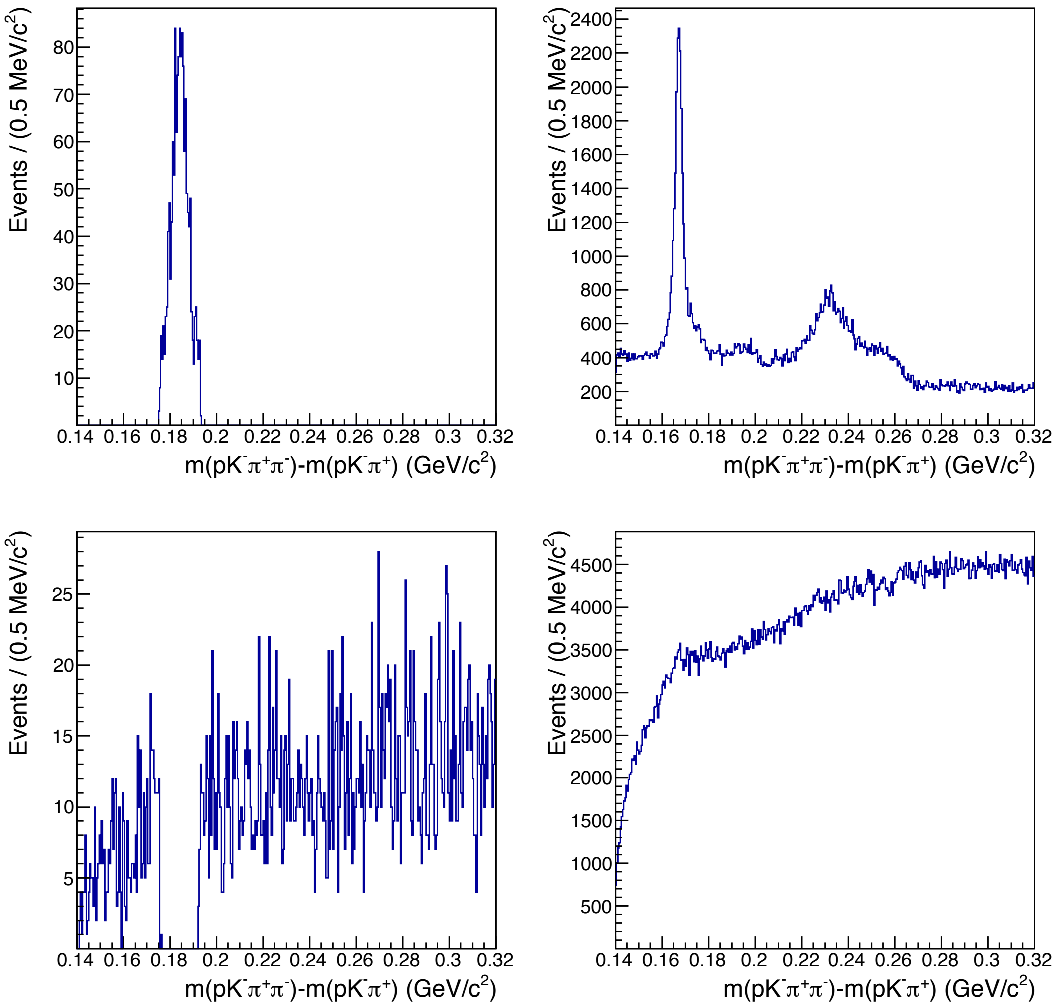

Figure 6.9: $m(pK^-\pi^+\pi^-) - m(pK^-\pi^+)$ from data that is not constrained to have the Λ_c^+ baryons with accepting the Λ_c^+ and Ξ_c^0 (top-left), accepting the Λ_c^+ and rejecting the Ξ_c^0 (top-right), rejecting the Λ_c^+ and accepting the Ξ_c^0 (bottom-left), and rejecting the Λ_c^+ and Ξ_c^0 (bottom-right).

Chapter 7

Fit Procedure

7.1 Fit Model

Since the $\Sigma_c(2455)^{0/++}$ and $\Sigma_c(2520)^{0/++}$ baryons have relatively short lifetime, one should consider both the detector resolution and decay widths at the same time. Therefore, the convolution of the two effects is used to describe the mass spectra of the $\Sigma_c(2455)^{0/++}$ and $\Sigma_c(2520)^{0/++}$ baryons. The convolution method used in this study is described in Appendix A. Using the convolution method, our model to describe the data becomes

$$\begin{aligned} M(\Delta m; \Delta m_0, \Gamma) &= T(\Delta m; \Delta m_0, \Gamma) \otimes R(\Delta m) \\ &= \int_{-\infty}^{+\infty} T(\Delta m; \Delta m_0, \Gamma) R(\Delta m - \Delta m') d(\Delta m') \end{aligned} \tag{7.1}$$

where $M(\Delta m; \Delta m_0, \Gamma)$ is the fit model, $T(\Delta m; \Delta m_0, \Gamma)$ is the theoretical model, $R(\Delta m)$ is the detector response function with the mass difference Δm as a random variable, Δm_0 and Γ are the mass difference and the decay width as fit parameters.

7.1.1 Theoretical Model

A relativistic Breit-Wigner line shape is employed for the theoretical model $T(\Delta m; \Delta m_0, \Gamma)$ in Eq. (7.1). It is the simplest form of all Breit-Wigner line shape which takes into account the threshold behavior that the transition amplitude has to vanish at threshold. Therefore, the relativistic Breit-Wigner line shape is believed to describe the $\Sigma_c(2455)^{0/++}$ and $\Sigma_c(2520)^{0/++}$ baryons better than non-relativistic Breit-Wigner that does not take into account the threshold behavior and is only a first approximation [93]. The Breit-Wigner line shape is discussed in Appendix B.

The relativistic Breit-Wigner function is defined as [94]

$$\frac{dN}{dm} \propto \frac{m_0 m\Gamma(m)}{(m_0^2 - m^2)^2 + m_0^2\Gamma^2(m)} \tag{7.2}$$

where m is the mass defined as $m \equiv \Delta m + m_{\Lambda_c^+}$ with a nominal mass of the Λ_c^+ baryon ($m_{\Lambda_c^+} = 2286.46$ MeV/c^2 [3]) as a random variable, m_0 is a nominal mass of the $\Sigma_c^{0/++}$ baryon, respectively, and $\Gamma(m)$ is

$$\Gamma(m) = \Gamma_0 \frac{m_0}{m}\left(\frac{q}{q_0}\right)^{2L+1}\frac{F(Rq)}{F(Rq_0)} \tag{7.3}$$

where

$$\begin{aligned} q &= \frac{\sqrt{(m^2 - (m_{\Lambda_c^+} + m_\pi)^2)\cdot(m^2 - (m_{\Lambda_c^+} - m_\pi)^2)}}{2m} \\ q_0 &= \frac{\sqrt{(m_0^2 - (m_{\Lambda_c^+} + m_\pi)^2)\cdot(m_0^2 - (m_{\Lambda_c^+} - m_\pi)^2)}}{2m_0}, \end{aligned}$$

L is an orbital angular momentum quantum number, R is the Blatt-Weisskopf damping radius, Γ_0 is a nominal decay width of the $\Sigma_c^{0/++}$ baryon, and $F(x)$ is the Blatt-Weisskopf form factor [95] defined as

$$\begin{aligned} F^{L=0}(x) &= 1 \\ F^{L=1}(x) &= \frac{1}{1+x^2} \\ F^{L=2}(x) &= \frac{1}{9+3x^2+x^4}. \end{aligned}$$

Since the $\Sigma_c(2455)^{0/++}$ and $\Sigma_c(2520)^{0/++}$ baryons are known to be ground states with spin $\frac{1}{2}$ and $\frac{3}{2}$, respectively, they have no orbital excitations (L=0). Furthermore, the relation between parity (P) and the angular momentum quantum number for baryons is known as

$$P = (-1)^L,$$

and the total angular momenta and parities J^P of the $\Sigma_c(2455)^{0/++}$ and $\Sigma_c(2520)^{0/++}$ baryons are $\frac{1}{2}^+$ and $\frac{3}{2}^+$, respectively, according to the quark model prediction [3]. This makes the Blatt-Weisskopf form factor vanish in Eq. (7.3). Therefore, the decay width term for the $\Sigma_c(2455)^{0/++}$ and $\Sigma_c(2520)^{0/++}$ baryons becomes

$$\Gamma(m) = \Gamma_0 \frac{m_0}{m}\frac{q}{q_0}. \tag{7.4}$$

Therefore, the theoretical model to describe the $\Sigma_c(2455)^{0/++}$ and $\Sigma_c(2520)^{0/++}$ baryons are

$$\frac{dN}{dm} \propto \frac{m_0 m^2\left(\Gamma_0\frac{m_0}{m}\frac{q}{q_0}\right)}{(m_0^2 - m^2)^2 + m_0^2\left(\Gamma_0\frac{m_0}{m}\frac{q}{q_0}\right)^2}. \tag{7.5}$$

7.1.2 Detector Resolution

In case of the particles that have relatively long lifetime, one can assume that the mass distribution of such particles only reflects the detector resolution because of their negligible decay widths and a finite resolution of the detector. In case of the $\Sigma_c(2455)^{0/++}$ and $\Sigma_c(2520)^{0/++}$ baryons, however, the mass distributions cannot be described with the resolution only because of their large decay widths. Therefore, the models for the $\Sigma_c(2455)^{0/++}$ and $\Sigma_c(2520)^{0/++}$ baryons should take into account the decay widths and the detector resolution simultaneously.

One may expect that the Λ_c^+ momentum resolution in the mass difference of $m(\Lambda_c^+\pi_s^\pm) - m(\Lambda_c^+)$ significantly cancels. If Δm is only dominated by the soft pion momentum resolution, it is possible to extract the detector response function $R(\Delta m)$ in Eq. (7.1) from a control sample. However, it turns out that a small contribution from the Λ_c^+ momentum resolution still exists. From the energy-momentum relation,

$$\begin{aligned}\Delta m &= m(\Lambda_c^+\pi_s^\pm) - m(\Lambda_c^+) \\ &= \sqrt{(E_{\Lambda_c^+} + E_{\pi_s^\pm})^2 - |\vec{p}_{\Lambda_c^+} + \vec{p}_{\pi_s^\pm}|^2} - m(\Lambda_c^+) \\ &= \sqrt{m^2(\Lambda_c^+) + m^2(\pi_s^\pm) + 2(E_{\Lambda_c^+}E_{\pi_s^\pm} - |\vec{p}_{\Lambda_c^+}||\vec{p}_{\pi_s^\pm}|\cos\theta)} - m(\Lambda_c^+) \quad (7.6)\end{aligned}$$

where E is an energy of a particle, $\vec{p}$ is a momentum vector of a particle. The resolution of Δm in Eq. (7.6) can be written as a function of momenta of the Λ_c^+ and the soft pion, that is,

$$\delta(\Delta m)^2 = \left(\frac{\partial(\Delta m)}{\partial p_{\Lambda_c^+}}\right)^2 (\delta p_{\Lambda_c^+})^2 + \left(\frac{\partial(\Delta m)}{\partial p_{\pi_s^\pm}}\right)^2 (\delta p_{\pi_s^\pm})^2, \quad (7.7)$$

and the factors of $\left(\frac{\partial(\Delta m)}{\partial p_{\Lambda_c^+}}\right)^2$ and $\left(\frac{\partial(\Delta m)}{\partial p_{\pi_s^\pm}}\right)^2$ in Eq. (7.7) represent contributions from the momentum resolutions of the Λ_c^+ and the soft pion. The ratio between those factors are given as

$$\frac{\left(\frac{\partial(\Delta m)}{\partial p_{\Lambda_c^+}}\right)^2}{\left(\frac{\partial(\Delta m)}{\partial p_{\pi_s^\pm}}\right)^2} = \frac{\left(|\vec{p}_{\Lambda_c^+}|\sqrt{\frac{m^2(\pi_s^\pm)+|\vec{p}_{\pi_s^\pm}|^2}{m^2(\Lambda_c^+)+|\vec{p}_{\Lambda_c^+}|^2}} - |\vec{p}_{\pi_s^\pm}|\cos\theta\right)^2}{\left(|\vec{p}_{\pi_s^\pm}|\sqrt{\frac{m^2(\Lambda_c^+)+|\vec{p}_{\Lambda_c^+}|^2}{m^2(\pi_s^\pm)+|\vec{p}_{\pi_s^\pm}|^2}} - |\vec{p}_{\Lambda_c^+}|\cos\theta\right)^2}, \quad (7.8)$$

and using a rough estimation of each quantity in Eq. (7.8) obtained from the signal MC samples, the contribution from the Λ_c^+ momentum resolution is found to be about 10%. Therefore, the resolution of Δm is dominated by the soft pion momentum resolution, but there is a contribution from the Λ_c^+ momentum resolution. As a consequence, the detector response functions for the $\Sigma_c(2455)^{0/++}$ and $\Sigma_c(2520)^{0/++}$

baryons cannot be obtained from samples of similar processes, for example, a well known decay of $D^*(2010)^+ \rightarrow D^0\pi_s^+$. Therefore, the detector response function $R(\Delta m)$ in Eq. (7.1) is obtained from signal MC samples for the $\Sigma_c(2455)^{0/++}$ and $\Sigma_c(2520)^{0/++}$ baryons.

Since the decay widths should be decoupled from the mass distribution, the generated $\Sigma_c(2455)^{0/++}$ and $\Sigma_c(2520)^{0/++}$ baryons are set not to have the widths by modifying the property table of particles in `PYTHIA` [87]. The events are generated with `PYTHIA`, decays of unstable particles are simulated with `EVTGEN` [88], and the detector response is simulated with `GEANT3` [89] for the $\Sigma_c(2455)^{0/++}$ and $\Sigma_c(2520)^{0/++}$ baryons separately. For the unbiased description to the detector response, a sum of three Gaussian functions is used, that is,

$$\begin{aligned} R(\Delta m; \mu, \sigma_c, \sigma_m, \sigma_t, f_1, f_2) &= f_1 G(\Delta m; \mu, \sigma_c) + f_2 G(\Delta m; \mu, \sigma_m) \\ &\quad + (1 - f_1 - f_2) \cdot G(\Delta m; \mu, \sigma_t) \end{aligned}$$

where f_1 and f_2 are fractions of the Gaussians, μ is the central value which is shared by all Gaussians, and σ_i (i={core (c), middle (m), and tail (t)}) is the resolution of each Gaussians as fit parameters. The resolutions of each Gaussians are constrained to be $\sigma_c \leq \sigma_m \leq \sigma_t$ in order to describe the core, middle, and tail parts of the detector response properly. Although the sample to obtain the detector response is a signal MC, a small contribution of wrong combination, in other words, random background is found. In order to prevent any bias from the random background, a threshold function Eq. (5.3) is used. Figures 7.1 and 7.2 show the simulated detector responses, and the obtained parameters of the detector response functions are summarized in Table. 7.1.

The obtained resolutions are assumed that the simulation is consistent with the data. In fact, however, there is a discrepancy between the data and MC, therefore, the discrepancy is accounted as a source of systematic uncertainty as discussed in Sec. 8.1.

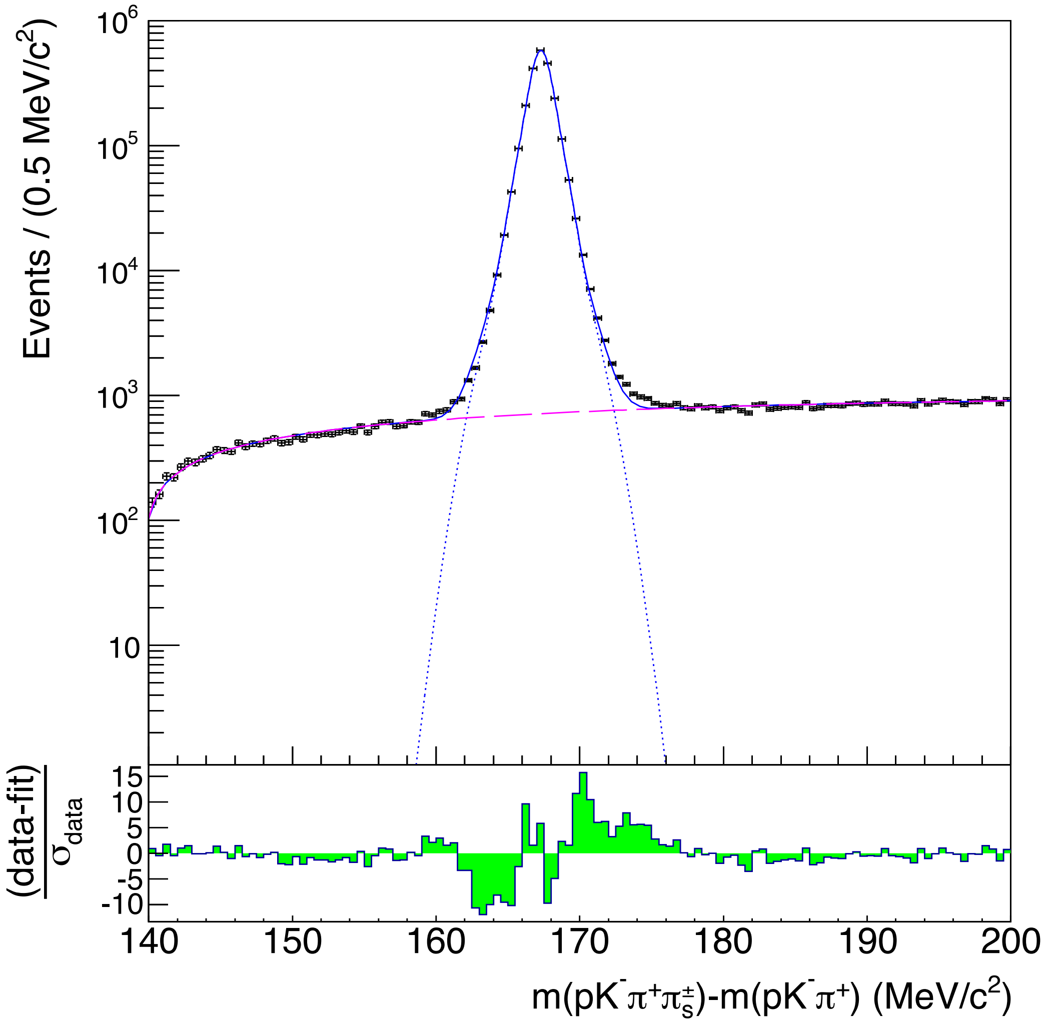

Figure 7.1: Simulated detector response for the $\Sigma_c(2455)$ baryon. The vertical axis in top plot is in logarithmic scale. The bottom plots are the differences between the data and fit results divided by the statistical uncertainty of the data, and they represent the fit quality.

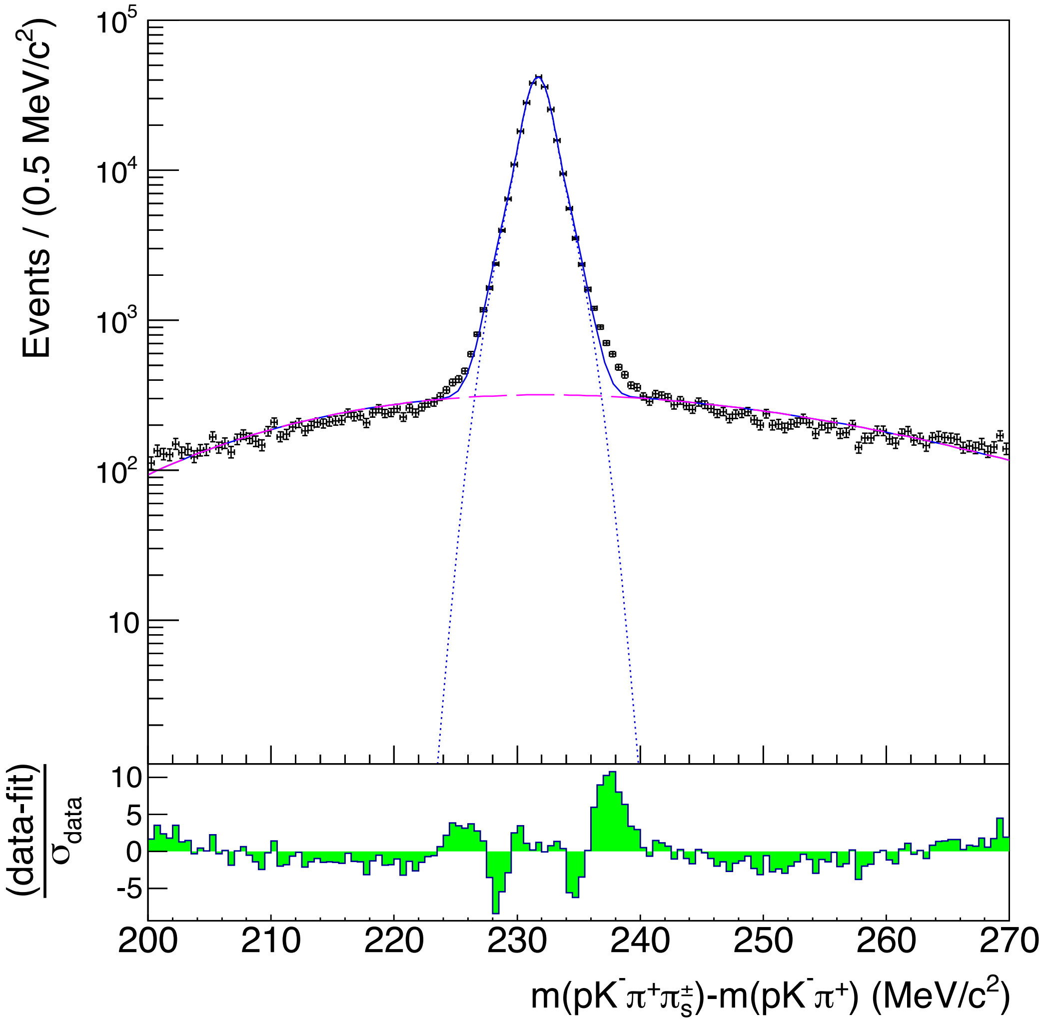

Figure 7.2: Simulated detector response for the $\Sigma_c(2520)$ baryon. The vertical axis in top plot is in logarithmic scale. The bottom plots are the differences between the data and fit results divided by the statistical uncertainty of the data, and they represent the fit quality.

	Estimated parameters for $\Sigma_c(2455)^{0/++}$	Estimated parameters for $\Sigma_c(2520)^{0/++}$
σ_c	0.541 ± 0.004 MeV/c^2	0.883 ± 0.038 MeV/c^2
σ_m	1.022 ± 0.008 MeV/c^2	1.544 ± 0.113 MeV/c^2
σ_t	1.947 ± 0.024 MeV/c^2	3.035 ± 0.298 MeV/c^2
f_1	0.383 ± 0.008	0.436 ± 0.069
f_2	0.520 ± 0.005	0.446 ± 0.044
$\overline{\sigma}$	1.012 ± 0.001 MeV/c^2	1.578 ± 0.013 MeV/c^2

Table 7.1: Estimated parameters of the detector response functions for the $\Sigma_c(2455)^{0/++}$ and $\Sigma_c(2520)^{0/++}$ baryons. The weighted averages of the detector resolutions $\overline{\sigma}$ which is defined as $\overline{\sigma} = \sqrt{f_1\sigma_c^2 + f_2\sigma_m^2 + (1 - f_1 - f_2)\sigma_t^2}$ are shown together.

7.2 Background Model

As discussed in Chapter 5, various sources of backgrounds are studied. Since the feed-down backgrounds are subtracted, and the reflection backgrounds from the $D^*(2010)^+$ decays belong to in the random background associated with fake Λ_c^+ candidates, there are only two contributions of the random backgrounds associated with the true and fake Λ_c^+.

The random background associated with the fake Λ_c^+ are obtained from the sidebands of Λ_c^+ mass in the data as discussed in Sec. 5.3.1. The obtained shape of the random background associated with the fake Λ_c^+ is used as a histogram PDF with a fixed normalization. The normalizations are also obtained from the sidebands of the Λ_c^+ mass in the data, and they are 187441 ± 433 and 125734 ± 355 for the mass differences of $m(pK^-\pi^+\pi_s^-) - m(pK^-\pi^+)$ and $m(pK^-\pi^+\pi_s^+) - m(pK^-\pi^+)$, respectively. The statistical uncertainties of the fixed normalizations are accounted as a source of systematic uncertainty as discussed in Sec. 8.4.3.

The random background associated with the true Λ_c^+ candidates is parameterized with a threshold function (5.3).

The contribution from the $\Xi_c^0 \to \Lambda_c^+\pi^-$ decay described in Chapter 6 is also included as a source of the backgrounds. Since the Ξ_c^0 baryon is known to have a short decay widths, a Gaussian function is added to describe the peak in the data for the unbiased estimation of the fit parameters.

7.3 Fit Results

By combining the signal and background PDFs discussed so far, the mass difference distributions of $m(pK^-\pi^+\pi_s^-) - m(pK^-\pi^+)$ and $m(pK^-\pi^+\pi_s^+) - m(pK^-\pi^+)$ are parameterized with the binned maximum likelihood method. The fit results are shown in Figs. 7.3 and 7.4, and summarized in Table 7.2. The fits are performed from 150 to 320 MeV/c^2, and the threshold region up to 150 MeV/c^2 is excluded from the fit in order to avoid the complication of backgrounds.

The fits are done with a popular analysis framework, `ROOT` [96], especially utilizing `RooFit` [97], a data modeling package, and `PyROOT` [98], a `Python` [99] interface to `ROOT`. For the minimization, `MINUIT` [100] with `MIGRAD`, `HESSE`, and `MINOS` is used as a package in `ROOT`.

Since the subtraction of the feed-down background implies a correction accounting the track finding efficiency and detector acceptance, a few bins in the data sam-

	Δm (MeV/c^2)	Γ (MeV/c^2)	$\mathcal{N}_{\text{signal}}$	Reduced χ^2 (ndf)
$\Sigma_c(2455)^0$	167.29 ± 0.01	1.76 ± 0.04	32484 ± 291	1.01 (347)
$\Sigma_c(2455)^{++}$	167.51 ± 0.01	1.84 ± 0.04	35984 ± 311	0.98 (350)
$\Sigma_c(2520)^0$	231.98 ± 0.11	15.41 ± 0.41	40796 ± 851	1.01 (347)
$\Sigma_c(2520)^{++}$	231.99 ± 0.10	14.77 ± 0.25	43728 ± 511	0.98 (350)

Table 7.2: Fit results of the $\Sigma_c(2455)^{0/++}$ and $\Sigma_c(2520)^{0/++}$ baryons. Δm is the mass differences of $m(\Sigma_c(2455)^{0/++}) - m(\Lambda_c^+)$ and $m(\Sigma_c(2520)^{0/++}) - m(\Lambda_c^+)$, Γ is the decay widths of the $\Sigma_c(2455)^{0/++}$ and $\Sigma_c(2520)^{0/++}$ baryons, $\mathcal{N}_{\text{signal}}$ is the signal yields of the $\Sigma_c(2455)^{0/++}$ and $\Sigma_c(2520)^{0/++}$ baryons, and reduced χ^2 is the χ^2 divided by the numbers of degrees of freedom (ndf).

ples may have weighted errors that is not compatible with the maximum likelihood method. The weights appear in covariance matrix elements without any correction

$$H_{\mu\nu} = \sum_{i=1}^{N} w_i \frac{df(x_i)}{d\theta_\mu} \frac{df(x_i)}{d\theta_\nu} \tag{7.9}$$

where N is the total number of measurements, w_i and $f(x_i)$ are the weight and the probability of the i-th measurement, respectively, and θ is a fit parameter. In this case, the covariance matrix of $\vec{\theta}$ is $\text{cov}(\vec{\theta}) = H^{-1}$, and the errors scale depends on $1/\sum_{i=1}^{N} w_i$ which is incorrect. To get the correct errors with weighted events, the errors scale should depend on $\sum_{i=1}^{N} w_i^2 / \sum_{i=1}^{N} w_i$, therefore, the covariance matrix should be [101]

$$\text{cov}(\vec{\theta}) = H^{-1} H' H^{-1} \tag{7.10}$$

where

$$H'_{\mu\nu} = \sum_{i=1}^{N} w_i^2 \frac{df(x_i)}{d\theta_\mu} \frac{df(x_i)}{d\theta_\nu}.$$

Since `HESSE` gives wrong errors based on Eq. (7.9), the correction to the weighted errors is applied by using `RooFit` which recalculates the errors according to Eq. (7.10).

As discussed in Sec. 7.2, an additional Gaussian function is added to describe the contribution from the $\Xi_c^0 \to \Lambda_c^+ \pi^-$ decay in the mass difference of $m(pK^-\pi^+\pi_s^-) - m(pK^-\pi^+)$ only. The mean and width of the Gaussian from the fit are found to be 184.08 ± 0.15 and 1.21 ± 0.18 MeV/c^2, respectively, and 710 ± 105 signal events are found. The estimated properties are consistent with the ones obtained from the signal MC and world average [3].

The signal significance of the $\Xi_c^0 \to \Lambda_c^+ \pi^-$ decay from the fit is roughly estimated. From the fits with and without the Gaussian for the $\Xi_c^0 \to \Lambda_c^+ \pi^-$ signal, logarithms of likelihood values are

$$\begin{aligned} \ln \mathcal{L}_{\text{test}} &= 6369761.86232 \\ \ln \mathcal{L}_{\text{null}} &= 6369701.08839 \end{aligned}$$

where $\mathcal{L}_{\text{test}}$ and $\mathcal{L}_{\text{null}}$ are the likelihood values obtained from the fit with and without the Gaussian, respectively. By taking the ratio of two likelihood, that is,

$$\begin{aligned} -2 \ln \lambda &\equiv -2 \ln \frac{\mathcal{L}_{\text{null}}}{\mathcal{L}_{\text{test}}} \\ &= -2 \ln \mathcal{L}_{\text{null}} + 2 \ln \mathcal{L}_{\text{test}} \\ &= 121.54786, \end{aligned}$$

and the numbers of degrees of freedom of λ is 3, therefore, the p-value can be approximately estimated from the χ^2 distribution to be 3.58×10^{-26}. This significance corresponds to 10.58σ where σ is a standard deviation of a normal distribution.

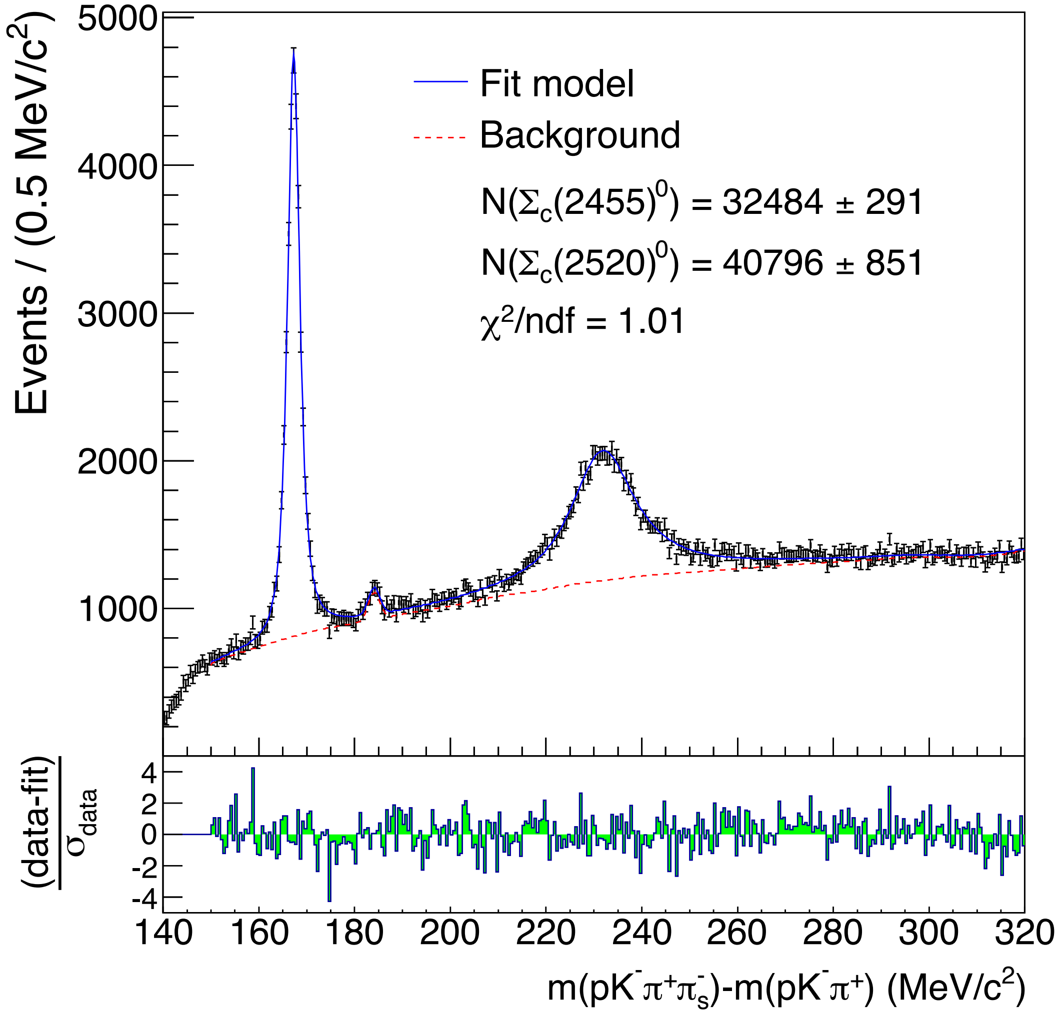

Figure 7.3: Fit to the mass difference of $m(pK^-\pi^+\pi_s^-) - m(pK^-\pi^+)$ obtained from the data (points with error bar) with the model (solid lines). The backgrounds (dashed lines) are shown as well. The bottom histogram is the difference between the values of the data and fit divided by the statistical uncertainty of the data to illustrate the fit quality.

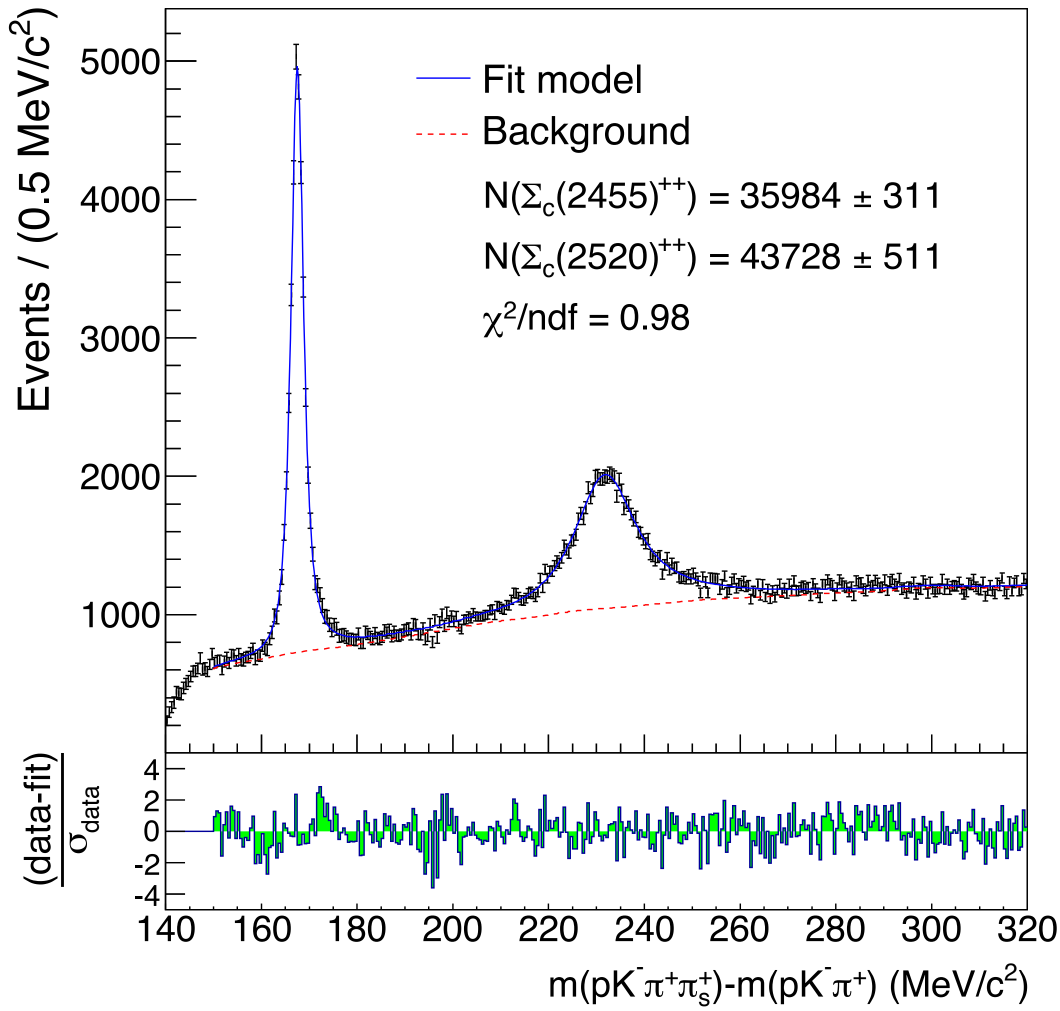

Figure 7.4: Fit to the mass difference of $m(pK^-\pi^+\pi_s^+) - m(pK^-\pi^+)$ obtained from the data (points with error bar) with the model (solid lines). The backgrounds (dashed lines) are shown as well. The bottom histogram is the difference between the values of the data and fit divided by the statistical uncertainty of the data to illustrate the fit quality.

Chapter 8

Systematic Uncertainties

Because of many reasons, for example, an imperfection of the detector performance, there are naturally systematic uncertainties. Various sources of the systematic uncertainties that affect to the results of this study have been studied. Some sources affect to the $m(\Sigma_c(2455)^{0/++}) - m(\Lambda_c^+)$ and $m(\Sigma_c(2520)^{0/++}) - m(\Lambda_c^+)$, some affect to the decay widths of the $\Sigma_c(2455)^{0/++}$ and $\Sigma_c(2520)^{0/++}$ baryons while some affect to both. In this chapter, various sources of the systematic uncertainties are discussed, and the systematic uncertainties are estimated.

8.1 Resolution Model

Since the detector response functions are obtained from the MC simulation as discussed in Sec. 7.1.2, and there is no guarantee of which the data and MC are consistent, one has to account the discrepancy between the data and MC as a source of a systematic uncertainty. Since the detector responses affect to the measurements of the decay widths of the $\Sigma_c(2455)^{0/++}$ and $\Sigma_c(2520)^{0/++}$ baryons, the systematic uncertainty from the discrepancy between the data and MC is expected to be a dominant source for the systematic uncertainties of the decay widths.

To estimate the discrepancy between the data and MC, a decay of $D^*(2010)^+ \to D^0(\to K^-\pi^+)\pi_s^+$ is chosen as a control sample. Since the decay width of $D^*(2010)^+$ meson is small, and the decay is well known, it would be a good sample to study the discrepancy.

For the estimation, the full dataset of the data and generic MC corresponding to the integrated luminosity of 710 fb^{-1} are used. In the reconstruction of the events, all charged tracks of K^-, π^+, and π_s^+ are required to have an impact parameter with respect to the interaction point of less than 3 cm along the z-axis and less than 1 cm in the $r - \phi$ plane. Furthermore, the tracks are required to have at least two associated vertex detector hits in each of the two measuring coordinates of the z-axis and $r - \phi$ plane. For the particle identification, the particle identification likelihood criteria

$$P(K:\pi) = \frac{\mathcal{L}(K)}{\mathcal{L}(K) + \mathcal{L}(\pi)} > 0.6$$

for the kaon identification, and

$$P(\pi:K) = \frac{\mathcal{L}(\pi)}{\mathcal{L}(\pi) + \mathcal{L}(K)} > 0.6$$

for the pion identification are applied. The D^0 candidate is reconstructed by combining K^- and π^+ tracks, and they are refit to have a common vertex. During the vertex fit, the events of which the vertex fit fails are discarded. The $D^*(2010)^+$ candidates are reconstructed by appending a positively charged pion[1]. The trajectory of the D^0 candidates are fit to the interaction point to find the production vertex of the D^0 candidate, and the soft pion is refit to the production vertex of the D^0 candidate. The events of which the vertex fit fails are discarded as well. To improve the soft pion momentum resolution, only the events of which the confidence level of the π_s^+ vertex fit greater than 0.1% are kept. To improve the signal-to-background ratio, the D^0 candidates are required to have an invariant mass in the range from 1810 to 1910 MeV/c^2, and the $D^*(2010)^+$ candidates are required to have a center-of-mass momentum greater than 2.5 GeV/c.

After the reconstruction of the events, a binned maximum likelihood fit is performed in the mass difference of $m(K^-\pi^+\pi_s^+) - m(K^-\pi^+)$. To parameterize the signal events, a sum of a Gaussian and a bifurcated Gaussian distribution function is used as a PDF, which is,

$$fG(\Delta m; \mu, \sigma_c) + (1-f) \cdot BG(\Delta m; \mu, \sigma_L, \sigma_R)$$

where G is a Gaussian function, BG is a bifurcated Gaussian function, Δm is the mass difference of $m(K^-\pi^+\pi_s^+) - m(K^-\pi^+)$ as a random variable, and μ, σ_c, σ_L, σ_R, and f are the mass difference of $m(D^*(2010)^+) - m(D^0)$, a width of a Gaussian, left and right widths of a bifurcated Gaussian, and a fraction of the Gaussian, respectively, as fit parameters. For the background parameterization, a threshold function in Eq. (5.3) is employed.

[1] The pions from the $D^*(2010)^+ \to D^0\pi_s^+$ decay have a low momentum, therefore, they are the soft pions.

$p(\pi_s^+)$ (MeV/c)	$\overline{\sigma}_{\mathrm{data}}$ (MeV/c^2)	$\overline{\sigma}_{\mathrm{MC}}$ (MeV/c^2)	$\overline{\sigma}_{\mathrm{data}}/\overline{\sigma}_{\mathrm{MC}}$
100 – 170	0.603 ± 0.007	0.551 ± 0.004	1.094 ± 0.014
170 – 215	0.546 ± 0.005	0.497 ± 0.004	1.099 ± 0.014
215 – 240	0.528 ± 0.006	0.483 ± 0.004	1.093 ± 0.015
240 – 270	0.525 ± 0.002	0.476 ± 0.004	1.103 ± 0.015
270 – 300	0.522 ± 0.006	0.478 ± 0.004	1.092 ± 0.015
300 – 340	0.527 ± 0.004	0.478 ± 0.004	1.103 ± 0.012
340 – 400	0.525 ± 0.005	0.485 ± 0.004	1.083 ± 0.013
400 – 700	0.502 ± 0.005	0.487 ± 0.004	1.031 ± 0.014

Table 8.1: Estimated detector resolutions of the data and MC from the $D^*(2010)^+$ decay. $\overline{\sigma}_{\mathrm{data}}$ and $\overline{\sigma}_{\mathrm{MC}}$ are the weighted averages of the resolution defined as $\overline{\sigma} \equiv \sqrt{f\sigma_c^2 + (1-f)\sigma_R^2}$ $(\sigma_R > \sigma_L)$.

Since the detector response varies by the soft pion momentum, the fits are done in various momentum bins of the soft pion. The momentum bins of the soft pion are defined as 100 to 175, 175 to 215, 215 to 240, 240 to 270, 270 to 300, 300 to 340, 340 to 400, and 400 to 700 MeV/c. The fit results are summarized in Table 8.1, and the discrepancy is shown in Fig. 8.1.

The systematic uncertainties from this discrepancy are estimated by varying the widths of the detector response function from +1.7% to +11.8%. The range of the variance of the width is chosen by taking the minimum discrepancy in the momentum bin of $400 < p(\pi_s^+) < 700$ MeV/c and the maximum discrepancy in the momentum bin of $240 < p(\pi_s^+) < 270$ MeV/c with considering their statistical errors. The scale factors are shared by all Gaussians in the detector response function (7.9).

From the fit to the mass differences of $m(pK^-\pi^+\pi_s^\pm) - m(pK^-\pi^+)$ with varying the detector resolution, the systematic uncertainties are estimated as single-sided values of 0.19, 0.25, and 0.24 MeV/c^2 for the decay widths of the $\Sigma_c(2455)^{0/++}$, $\Sigma_c(2520)^0$, and $\Sigma_c(2520)^{++}$ baryons, respectively, and they are summarized in Table 8.2.

Since the obtained detector response functions have statistical errors as shown in Table 7.1, the statistical fluctuation of the detector resolution can be a source of the systematic uncertainty. The widths in the detector response functions are fluctuated by $\pm 1\sigma$ deviation to estimate the statistical effect, and the systematic uncertainties are found to be 0.01 and 0.04 MeV/c^2 for the $\Sigma_c(2455)^{0/++}$ and $\Sigma_c(2520)^{0/++}$ baryons, respectively, and summarized in Table 8.3. The uncertainties due to the

	Δm (MeV/c^2)	Γ (MeV/c^2)
$\Sigma_c(2455)^0$	–	-0.19
$\Sigma_c(2455)^{++}$	–	-0.19
$\Sigma_c(2520)^0$	–	-0.25
$\Sigma_c(2520)^{++}$	–	-0.24

Table 8.2: Systematic uncertainties due to the discrepancy between the data and MC. Δm is the mass difference of $m(\Sigma_c) - m(\Lambda_c^+)$, and Γ is the decay width. No uncertainty is found for the mass differences.

	Δm (MeV/c^2)	Γ (MeV/c^2)
$\Sigma_c(2455)^0$	–	± 0.01
$\Sigma_c(2455)^{++}$	–	± 0.01
$\Sigma_c(2520)^0$	–	± 0.04
$\Sigma_c(2520)^{++}$	–	± 0.04

Table 8.3: Systematic uncertainties due to the statistical effect of the detector responses. Δm is the mass difference of $m(\Sigma_c) - m(\Lambda_c^+)$, and Γ is the decay width. No uncertainty is found for the mass differences.

statistical effect are small comparing with the uncertainty from the discrepancy between the data and MC.

8.2 Momentum Scale

There is a possible bias in the measurement of charged track momenta because of the wrong momentum scale of the Belle detector, for example, the energy loss of a charged particle in materials. This bias may affect to the measurements of mass of a particle significantly, therefore, it should be accounted as a source of a systematic uncertainty. To study this effect, the control sample of a mesonic decay of $D^*(2010)^+ \to D^0(\to K^-\pi^+)\pi_s^+$ defined in Sec. 8.1 is used. As shown in Fig. 8.2, the measured mass difference of $m(D^*(2010)^+) - m(D^0)$ depends on the soft pion momentum. In order to minimize the systematic uncertainty from this effect, a momentum scale calibration is performed.

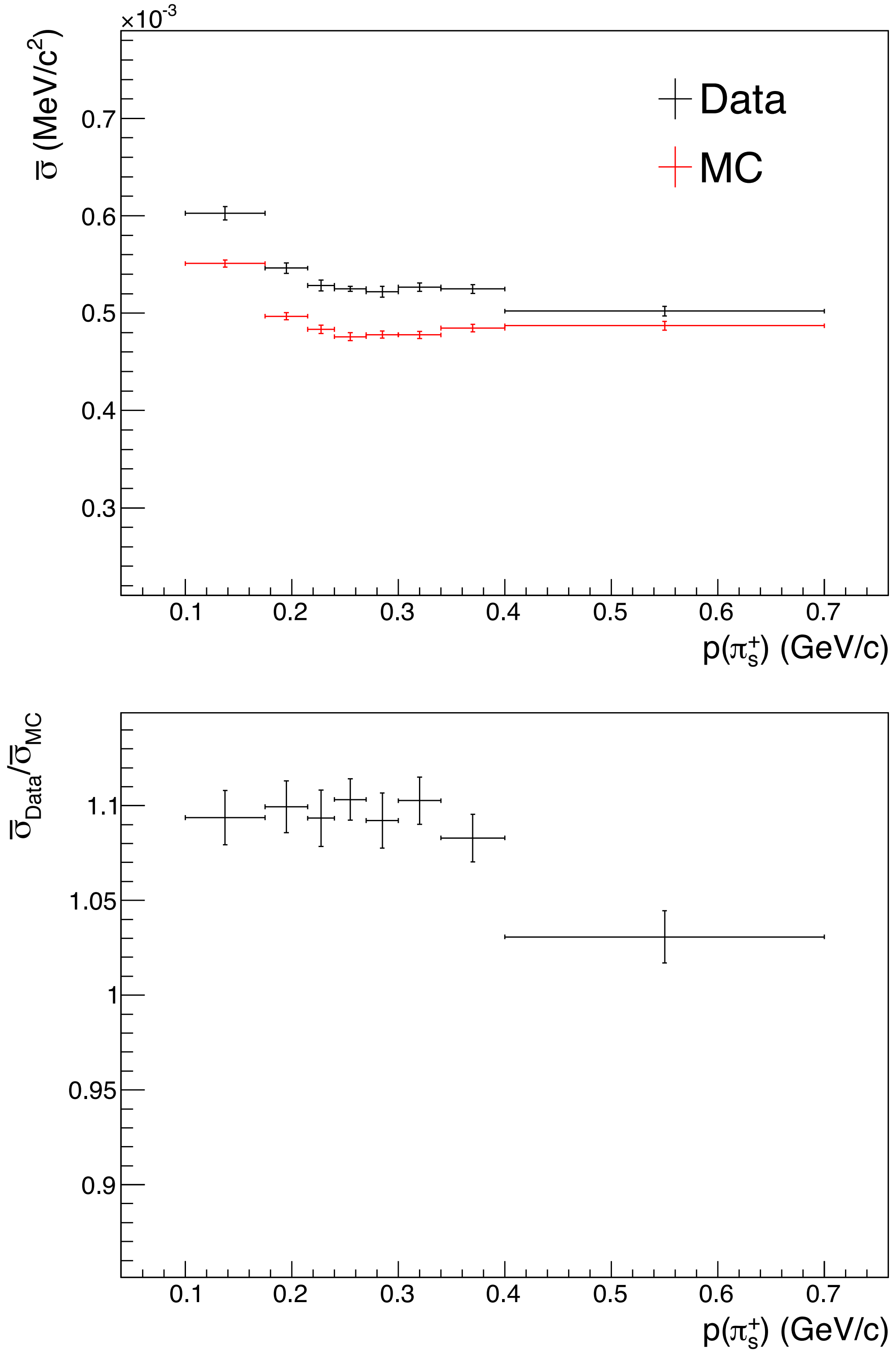

Figure 8.1: Weighted averages of the detector resolution ($\overline{\sigma}$) obtained from the data (black point with error bar) and MC (red point with error bar) using the decay of $D^{*}(2010)^{+} \to D^{0}(\to K^{-}\pi^{+})\pi_{s}^{+}$ as a function of π_{s}^{+} momentum (top). The ratio of the resolutions between the data and MC ($\overline{\sigma}_{\mathrm{data}}/\overline{\sigma}_{\mathrm{MC}}$) is also shown (bottom) as a function of π_{s}^{+} momentum.

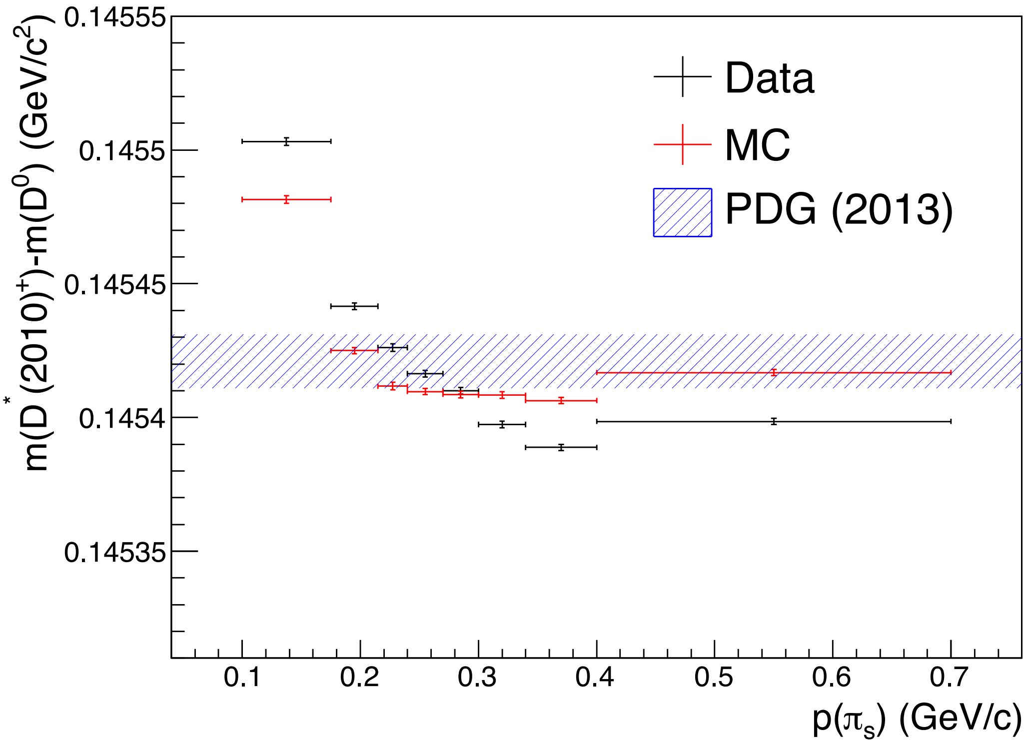

Figure 8.2: The mass difference of $m(D^*(2010)^+) - m(D^0)$ as a function of π_s^+ momentum obtained from the data (black points) and MC (red points). The world average of the mass difference $m(D^*(2010)^+) - m(D^0) = 145.421 \pm 0.010$ MeV$/c^2$ [3] is also shown (hatched). The same model in Sec. 8.1 is used in the fit.

8.2.1 Momentum Scale Calibration with K_S^0 Sample

For the study of the momentum scale calibration, a mesonic decay of $K_S^0 \to \pi^+\pi^-$ is chosen as a control sample. Since the pions from the K_S^0 decay cover wide range of momentum, and there are a lot of the K_S^0 mesons in the data samples, the decay of K_S^0 meson is a good sample to calibrate the momentum scale.

Partial sample of the full data set corresponding to the integrated luminosity of 72 fb^{-1} is used for the calibration. For the event selection, `goodKs()` [102] which is the Belle standard method to select a good K_S^0 candidate is applied. In addition, the daughter tracks of the K_S^0 candidate are required to have at least two associated vertex detector hits in each of the two measuring coordinates of the z-axis and $r-\phi$ plane. Since the low momentum pions are desirable, the pion tracks are also required to have a transverse momentum in the range from 100 MeV/c to 800 MeV/c.

The calibration is performed in two steps. First, the charged pions of which have higher momentum than 200 MeV/c are calibrated. In this step, two charged pions are required to have similar momenta to simplify the formula ($|p(\pi^+) - p(\pi^-)| <2$ MeV/c). After the calibration for the higher momentum pions, the charged pions which have the momentum less than 200 MeV/c are calibrated. To simplify the formula, only one pion is required to have the momentum less than 200 MeV/c, and the other is required to have the momentum greater than 200 MeV/c which is supposed to be calibrated in the first step.

The reconstructed mass of the K_S^0 meson can be written as

$$M^2 = 4m_\pi^2 + 2p^2(1-\cos\Theta) \tag{8.1}$$

where M is a reconstructed mass of a K_S^0 meson, m_π is a nominal mass of a pion, p is a momentum of a pion ($\because\ p(\pi^+) \simeq p(\pi^-)$), and Θ is an angle between two charged pion momentum vectors assumed to have negligible error. With a definition of $\tilde{M}^2 \equiv M^2 - 4m_\pi^2$, Eq. (8.1) can be written as

$$\begin{aligned} \tilde{M}^2 &= 2p^2(1-\cos\Theta) \\ \tilde{M}d\tilde{M} &= 2pdp(1-\cos\Theta) \end{aligned}$$

$$\therefore \frac{d\tilde{M}}{\tilde{M}} = \frac{dp}{p}. \tag{8.2}$$

The ratio in Eq. (8.2) can be obtained as functions of the momentum (p), inverse of the transverse momentum ($1/p_T$) of a pion, and the cosine value of the angle between a pion momentum vector and the beam axis ($\cos\theta$). By using the functions, the momenta of charged pions are calibrated iteratively as the first step of the momentum scale calibration.

In the second step of the calibration, the mass of the K_S^0 meson can be written as

$$M^2 = 2m_\pi^2 + 2(E_h E_l - p_h p_l \cos\Theta) \tag{8.3}$$

where E_h and p_h are the energy and momentum of the pions of which have the momentum greater than 200 MeV/c, and E_l and p_l are energy and momentum of the pions of which have the momentum less than 200 MeV/c. Since the pions of which have the momentum greater than 200 MeV/c are calibrated in the first step, there should not be any difference of the momentum, that is, $dp_h = 0$. By requiring $|\cos\Theta| < 0.01$ to neglect the cosine term in Eq. (8.3),

$$M^2 \simeq 2m_\pi^2 + 2E_h E_l.$$

By defining $\tilde{M}^2 \equiv M^2 - 2m_\pi^2$,

$$\begin{aligned} \tilde{M}^2 &= 2E_h E_l \\ &= 2E_h\sqrt{m_\pi^2 + p_l^2}, \end{aligned}$$

therefore,

$$\begin{aligned} \tilde{M}d\tilde{M} &= E_h \cdot \frac{p_l dp_l}{\sqrt{m_\pi^2 + p_l^2}} \qquad (\because dp_h = 0) \\ &= \frac{E_h p_l dp_l}{E_l}. \end{aligned}$$

Thus, the ratio can be written,

$$\begin{aligned} \frac{d\tilde{M}}{\tilde{M}} &= \frac{p_l dp_l}{2E_l^2} \\ &= \frac{dp_l}{2p_l(1 + \frac{m_\pi^2}{p_l^2})}. \end{aligned} \tag{8.4}$$

From the approximation of $m_\pi^2/p_l^2 \approx m_\pi^2/ < p_l^2 > \equiv \alpha$ where $< p_l^2 >$ is an average value of p_l^2, Eq. (8.4) becomes

$$\frac{d\tilde{M}}{\tilde{M}} \simeq \frac{dp_l}{2\alpha p_l}, \tag{8.5}$$

and the factor α is found to be 3.48 and 3.72 in the data and MC, respectively.

The ratio in Eq. (8.5) is obtained as functions of p_l, $1/p_{lT}$, and $\cos\theta$ as done in the first step, and the pions of which have the momentum less than 200 MeV/c are calibrated accordingly. Figures 8.3, 8.4, and 8.5 compare $d\tilde{M}/\tilde{M}$ for each steps of the calibration as functions of p and $1/p_T$ of K_S^0, and $\cos\theta$ where θ is an polar angle of K_S^0 momentum vector from the beam axis, respectively.

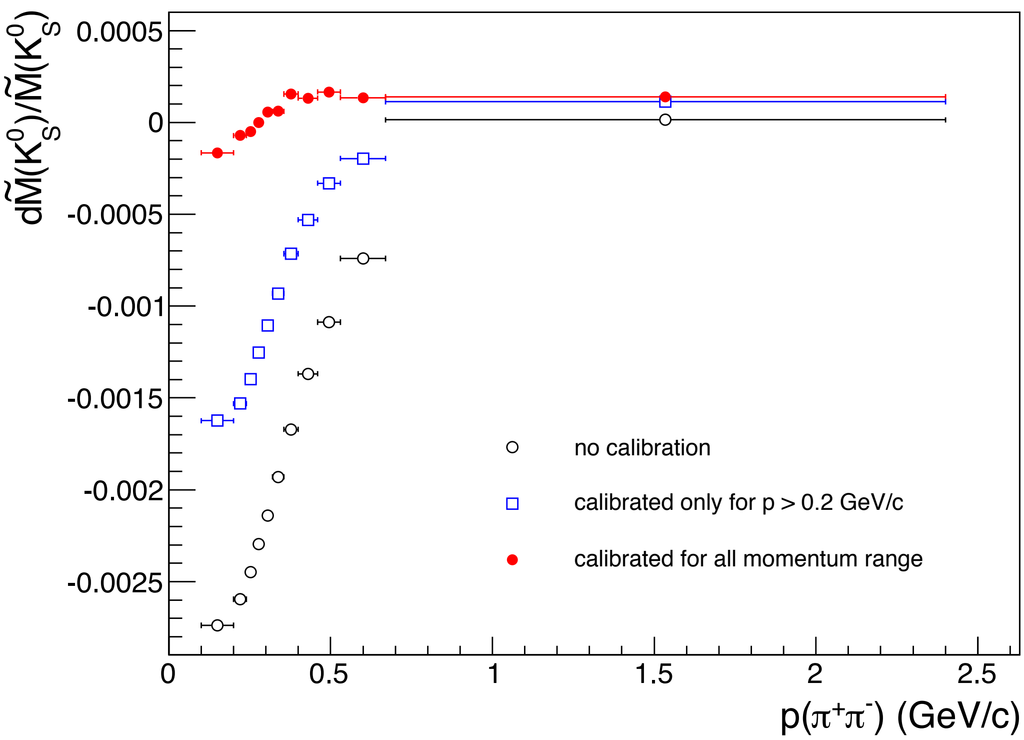

Figure 8.3: Calibrated K_S^0 mass as a function of $p(\pi^+\pi^-)$ before the calibration (open black circle), after the calibration only for $p(\pi^+\pi^-) > 200$ MeV/c events (open blue square), and after the calibration for all momentum range (open red circle) using the generic MC sample.

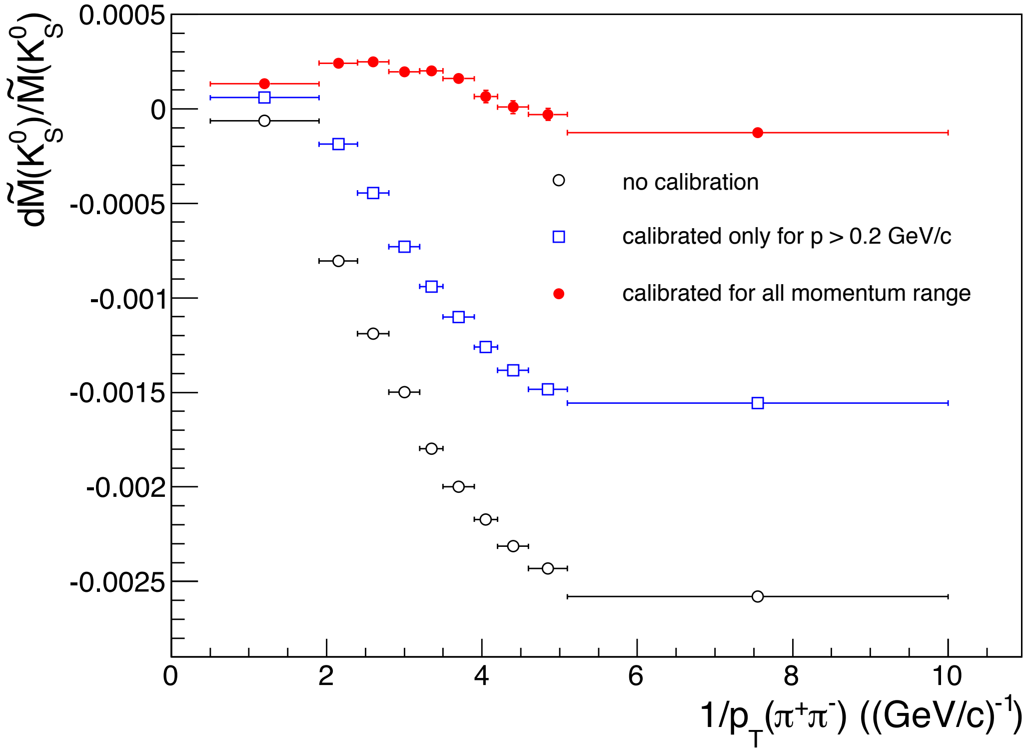

Figure 8.4: Calibrated K_S^0 mass as a function of $1/p_T(\pi^+\pi^-)$ before the calibration (open black circle), after the calibration only for $p(\pi^+\pi^-) > 200$ MeV/c events (open blue square), and after the calibration for all momentum range (open red circle) using the generic MC sample.

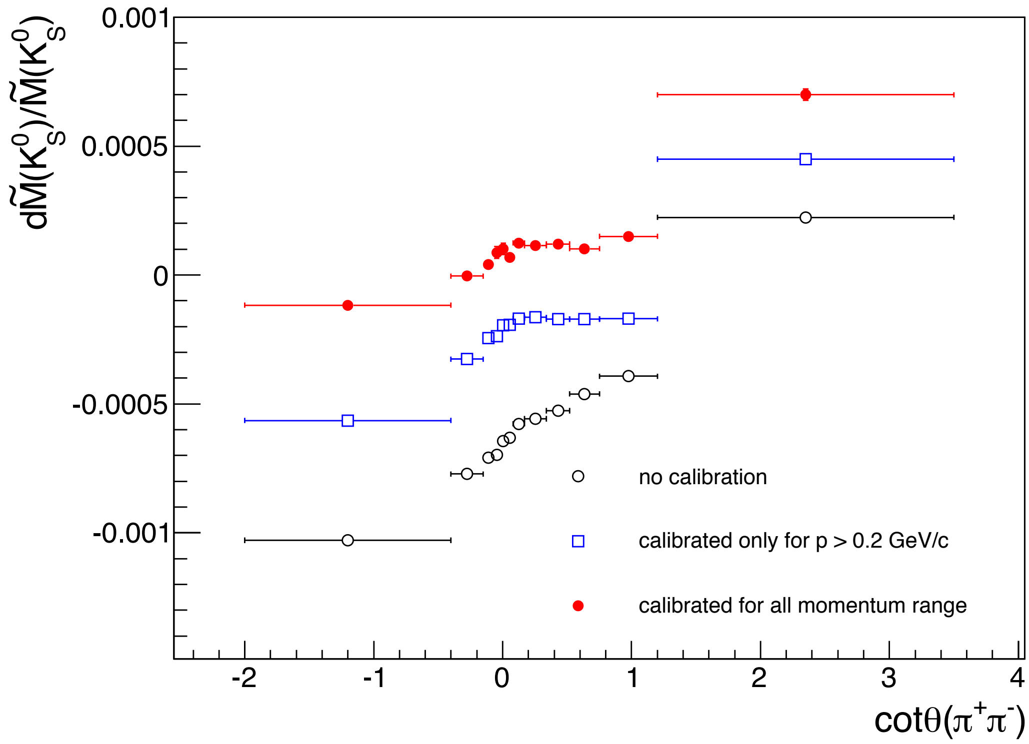

Figure 8.5: Calibrated K_S^0 mass as a function of $\cot\theta$ before the calibration (open black circle), after the calibration only for $p(\pi^+\pi^-) > 200$ MeV/c events (open blue square), and after the calibration for all momentum range (open red circle) using the generic MC sample.

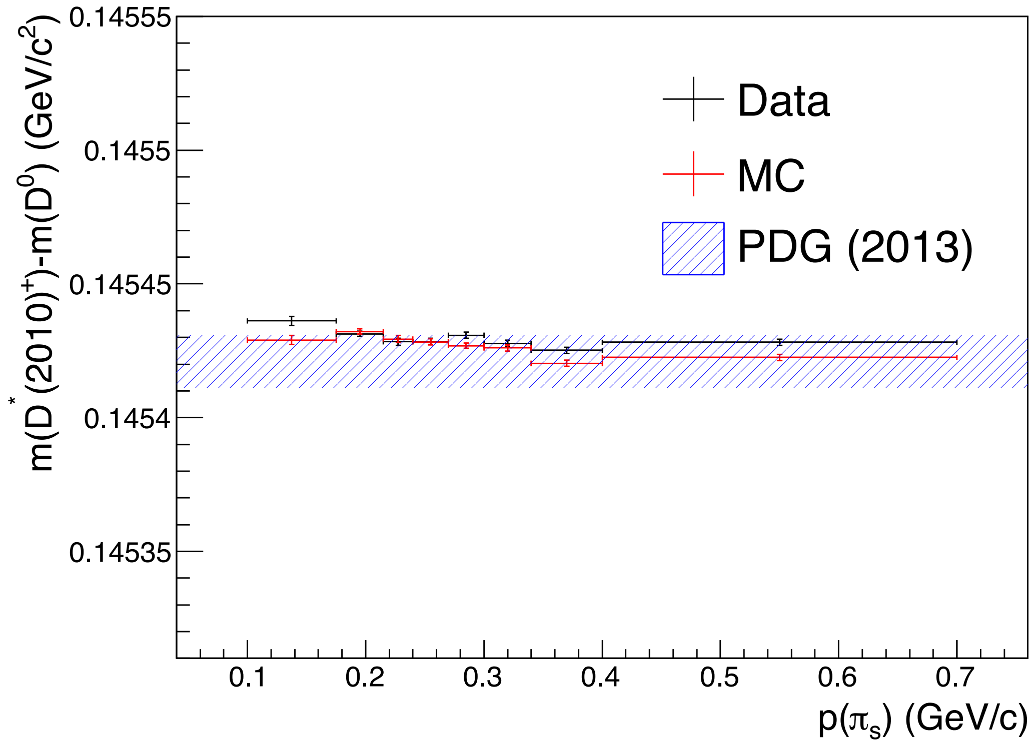

Figure 8.6: The mass difference of $m(D^*(2010)^+) - m(D^0)$ as a function of the π_s^+ momentum after the calibration obtained from the data (black points) and MC (red points). The world average of the mass difference $m(D^*(2010)^+) - m(D^0) = 145.421 \pm 0.010$ MeV$/c^2$ [3] is also shown (hatched). The same model in Sec. 8.1 is employed in the fit.

8.2.2 Systematic Uncertainties

The obtained calibration function from the K_S^0 decay is applied to the decay of $D^*(2010)^+ \to D^0(\to K^-\pi^+)\pi_s^+$ decay to confirm the calibration. As shown in Fig. 8.6, the result of the calibration seems to be fine. The calibration function is applied to the data and MC for this study as well.

To estimate the systematic uncertainty due to the momentum scale, the calibrated sample of the $D^*(2010)^+$ decay is compared to the world average value, $m(D^*(2010)^+) - m(D^0) = 145.421 \pm 0.010$ MeV$/c^2$ [3]. By taking the maximum difference between the measured and the world average of the mass difference, the systematic uncertainty is conservatively assigned with 0.02 MeV$/c^2$.

8.3 Fit Model

The systematic uncertainties due to the fit model are also studied. Possible sources are fit bias, effects from various bin sizes of the sample and from the fit ranges.

8.3.1 Fit Bias

Fit bias can be a source of the systematic uncertainty. The uncertainty is tested by utilizing pseudo-experiments. During the production of 10,000 pseudo-experiments, they are intended to be kept in data-driven way, in other words, the detector resolutions and the normalizations of the signal and background events are the same with the values obtained from the fit in Chapter 7. After the production of the pseudo-experiments, all data sets are fit with the same probability density functions used in Chapter 7. By comparing the input and fit values, the systematic uncertainties are estimated. The fit results of the pseudo-experiments are shown in Fig. 8.7 and summarized in Table 8.4. No uncertainty is found for the mass differences of $m(\Sigma_c(2455)^{0/++}) - m(\Lambda_c^+)$ and $m(\Sigma_c(2520)^{0/++}) - m(\Lambda_c^+)$, and only minor uncertainties are found for the widths of the $\Sigma_c(2455)^{0/++}$ and $\Sigma_c(2520)^{0/++}$ baryons. The systematic uncertainties for the widths of the $\Sigma_c(2455)^{0/++}$ and $\Sigma_c(2520)^{0/++}$ baryons are assigned to be 0.02 and 0.04 MeV/c^2, respectively.

The pull distributions of the pseudo-experiments are also shown in Fig. 8.8. The pull is defined as

$$\frac{x - \mu}{\sigma}$$

where x is estimated fit parameters for a pseudo-experiment, μ is true value, and σ is fit error of the parameter. From fits to the pull distributions with a Gaussian function, it is confirmed that the pull distributions are close to a normal distribution which has a Gaussian with a mean of 0 and a width of 1.

8.3.2 Binning Effect

Since maximum likelihood fits are done to the binned data sets, the parameter estimation in the fit can be affected by the size of the bins. The size of the bin used in the fit is 0.5 MeV/c^2. To estimate the effect of the size of the bin, the bin size is varied from 0.1 MeV/c^2 to 1.0 MeV/c^2, and the estimated parameters are summarized in Tables 8.5 and 8.6. The uncertainties for the mass differences of

	Input (MeV/c^2)	Fit (MeV/c^2)	|Input - Fit| (MeV/c^2)
$\Delta m(\Sigma_c(2455)^{0/++})$	167.30	167.30	–
$\Delta m(\Sigma_c(2520)^{0/++})$	231.90	231.90	–
$\Gamma(\Sigma_c(2455)^{0/++})$	2.20	2.22	0.02
$\Gamma(\Sigma_c(2520)^{0/++})$	14.90	14.94	0.04

Table 8.4: Input and fit values of the pseudo-experiments for the test of fitter. By comparing the input and fit values, the differences |Input - Fit| are assigned as the systematic uncertainties due to the biased estimation of the fitter.

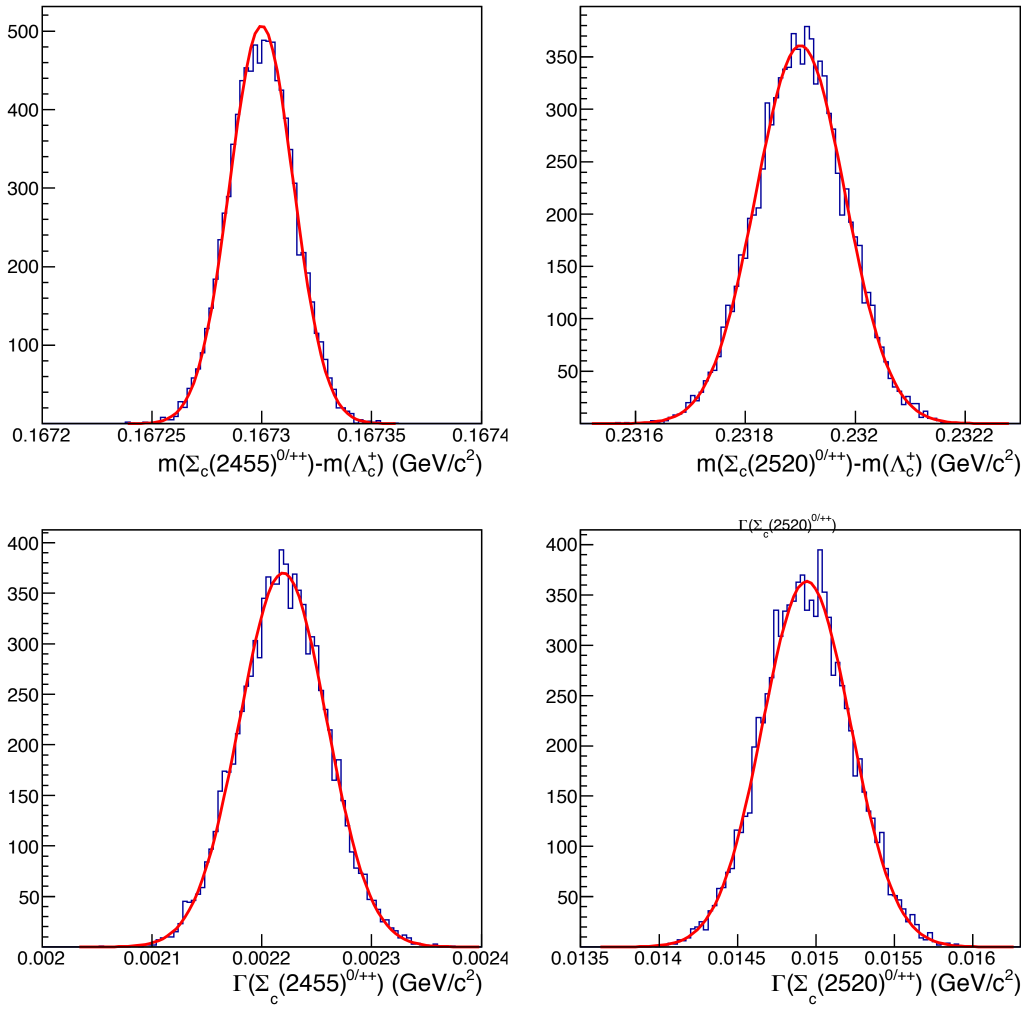

Figure 8.7: Bias check from the fitter using 10,000 pseudo-experiments (histogram) for the mass difference of the $\Sigma_c(2455)^{0/++}$ (top-left) and $\Sigma_c(2520)^{0/++}$ baryons (top-right), and the widths of the $\Sigma_c(2455)^{0/++}$ (bottom-left) and $\Sigma_c(2520)^{0/++}$ baryons (bottom-right). Fits with a Gaussian function (red line) are also shown.

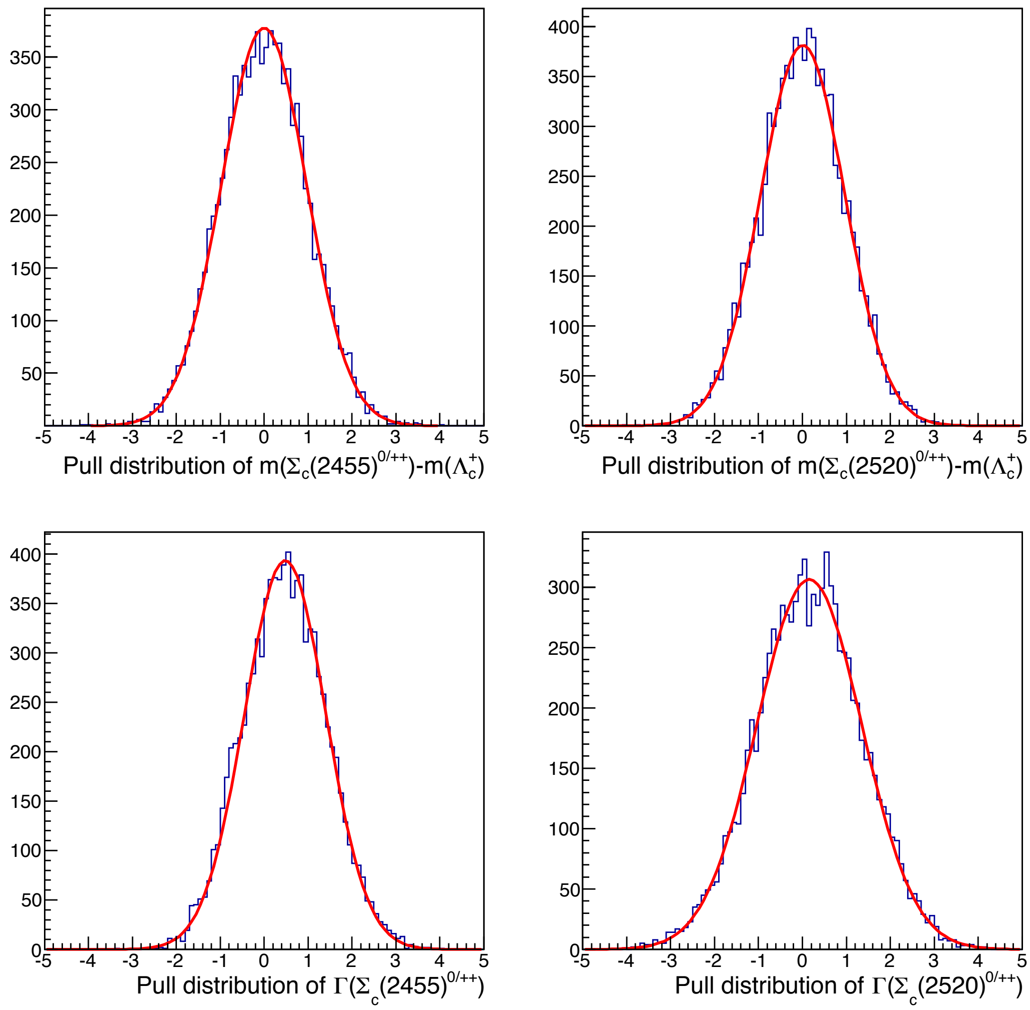

Figure 8.8: Pull distributions of 10,000 pseudo-experiments (histogram) for the mass difference of the $\Sigma_c(2455)^{0/++}$ (top-left) and $\Sigma_c(2520)^{0/++}$ baryons (top-right), and the widths of the $\Sigma_c(2455)^{0/++}$ (bottom-left) and $\Sigma_c(2520)^{0/++}$ baryons (bottom-right). Fits with a Gaussian function (red line) are also shown.

$m(\Sigma_c(2455)^{0/++}) - m(\Lambda_c^+)$ and $m(\Sigma_c(2520)^{0/++}) - m(\Lambda_c^+)$ are found to be negligible. The uncertainties for the decay widths are found to be 0.09, 0.06, 0.04, and 0.05 MeV/c^2 for the $\Sigma_c(2455)^0$, $\Sigma_c(2455)^{++}$, $\Sigma_c(2520)^0$, and $\Sigma_c(2455)^{++}$, respectively.

8.3.3 Effect of the Fit Range

The effect due to the various fit ranges is also studied. To estimate the uncertainty, 12 different fit ranges are defined to include the $\Sigma_c(2455)^{0/++}$ and $\Sigma_c(2520)^{0/++}$ both, and separately; 140 to 320, 150 to 320, 190 to 280, 190 to 290, 190 to 300, 190 to 310, 190 to 320, 200 to 280, 200 to 290, 200 to 300, 200 to 310, and 200 to 320 MeV/c^2. The uncertainties for the $\Sigma_c(2455)^{0/++}$ baryons are found to be negligible. In case of the $\Sigma_c(2520)^{0/++}$ baryons, non-negligible uncertainties are found, especially for the decay widths. The estimated parameters in the various fit ranges are summarized in Tables 8.7 and 8.8. The root-mean-square (RMS) values of the estimated parameters in the various fit ranges are assigned as the systematic uncertainties due to the fit range. The uncertainties are found to be 0.03 and 0.01 MeV/c^2 for the mass differences of $m(\Sigma_c(2520)^0) - m(\Lambda_c^+)$ and $m(\Sigma_c(2520)^{++}) - m(\Lambda_c^+)$, and 0.19 and 0.17 MeV/$c^2$ for the decay widths of the $\Sigma_c(2520)^0$ and $\Sigma_c(2520)^{++}$ baryons, respectively.

Since the fit qualities are fine, and the uncertainties due to the fit range are consistent within the statistical uncertainties, one might be redundant to account them as a systematic uncertainty, but they are assigned as a systematic uncertainty in a conservative manner.

Bin size	$\Delta m(\Sigma_c(2455)^0)$	$\Delta m(\Sigma_c(2520)^0)$	$\Gamma(\Sigma_c(2455)^0)$	$\Gamma(\Sigma_c(2520)^0)$	$\mathcal{N}(\Sigma_c(2455)^0)$	$\mathcal{N}(\Sigma_c(2520)^0)$	χ^2/ndf
0.1	167.29 ± 0.01	231.98 ± 0.11	1.75 ± 0.04	15.37 ± 0.40	32497 ± 291	40698 ± 852	0.86
0.5	167.29 ± 0.01	231.98 ± 0.11	1.76 ± 0.04	15.41 ± 0.41	32484 ± 291	40796 ± 851	1.01
1.0	167.29 ± 0.01	231.98 ± 0.11	1.85 ± 0.04	15.44 ± 0.41	32732 ± 294	40917 ± 857	1.03
Δ	–	–	± 0.09	± 0.04	± 248	± 98	–

Table 8.5: Estimated parameters for the neutral Σ_c baryons in various bin sizes. Δm, Γ, $\mathcal{N}$, and χ^2/ndf are the mass difference of $m(\Sigma_c) - m(\Lambda_c^+)$, decay width, number of signal events, and χ^2 divided by the numbers of degrees of freedom, respectively. Δ in the last row is the difference of the value from the central value estimated with the bin size of 0.5 MeV/c^2. The values are in MeV/c^2 for the bin size, Δm, and Γ.

Bin size	$\Delta m(\Sigma_c(2455)^{++})$	$\Delta m(\Sigma_c(2520)^{++})$	$\Gamma(\Sigma_c(2455)^{++})$	$\Gamma(\Sigma_c(2520)^{++})$	$\mathcal{N}(\Sigma_c(2455)^{++})$	$\mathcal{N}(\Sigma_c(2520)^{++})$	χ^2/ndf
0.1	167.52 ± 0.01	231.99 ± 0.10	1.82 ± 0.04	14.74 ± 0.26	35915 ± 312	43652 ± 542	0.89
0.5	167.51 ± 0.01	231.99 ± 0.10	1.84 ± 0.04	14.77 ± 0.25	35984 ± 311	43728 ± 511	0.98
1.0	167.52 ± 0.01	231.98 ± 0.10	1.91 ± 0.04	14.82 ± 0.26	36164 ± 310	43839 ± 544	1.07
Δ	± 0.01	± 0.01	± 0.06	± 0.05	± 180	± 111	–

Table 8.6: Estimated parameters for the doubly-charged Σ_c baryons in various bin sizes. Δm, Γ, $\mathcal{N}$, and χ^2/ndf are the mass difference of $m(\Sigma_c) - m(\Lambda_c^+)$, decay width, number of signal events, and χ^2 divided by the numbers of degrees of freedom, respectively. Δ in the last row is the difference of the value from the central value estimated with the bin size of 0.5 MeV/c^2. The values are in MeV/c^2 for the bin size, Δm, and Γ.

Fit ranges	$\Delta m(\Sigma_c(2520)^0)$	$\Gamma(\Sigma_c(2520)^0)$	χ^2/ndf
140 – 320	231.99 ± 0.11	14.74 ± 0.37	1.01
150 – 320	231.99 ± 0.11	15.41 ± 0.41	1.01
190 – 280	231.93 ± 0.12	15.20 ± 0.38	1.10
190 – 290	231.93 ± 0.11	15.11 ± 0.32	1.07
190 – 300	231.93 ± 0.11	15.02 ± 0.33	1.07
190 – 310	231.93 ± 0.11	14.79 ± 0.32	1.04
190 – 320	231.92 ± 0.11	14.60 ± 0.31	1.06
200 – 280	231.91 ± 0.12	15.21 ± 0.44	1.17
200 – 290	231.91 ± 0.12	15.12 ± 0.46	1.13
200 – 300	231.91 ± 0.12	15.07 ± 0.42	1.11
200 – 310	231.90 ± 0.12	14.87 ± 0.37	1.08
200 – 320	231.88 ± 0.12	14.77 ± 0.36	1.10

Table 8.7: Estimated parameters for the $\Sigma_c(2520)^0$ baryon in various fit ranges. Δm, Γ, and χ^2/ndf are the mass difference of $m(\Sigma_c)-m(\Lambda_c^+)$, decay width, and χ^2 divided by the numbers of degrees of freedom, respectively. The values are in MeV/c^2 for the fit range, Δm, and Γ.

Fit ranges	$\Delta m(\Sigma_c(2520)^{++})$	$\Gamma(\Sigma_c(2520)^{++})$	χ^2/ndf
140 – 320	232.00 ± 0.09	14.47 ± 0.31	1.02
150 – 320	231.99 ± 0.10	14.77 ± 0.25	0.98
190 – 280	231.97 ± 0.10	14.76 ± 0.34	1.12
190 – 290	231.96 ± 0.10	14.93 ± 0.31	1.09
190 – 300	231.96 ± 0.10	14.73 ± 0.29	1.09
190 – 310	231.96 ± 0.10	14.53 ± 0.29	1.09
190 – 320	231.96 ± 0.10	14.43 ± 0.28	1.09
200 – 280	231.97 ± 0.10	14.67 ± 0.40	1.04
200 – 290	231.97 ± 0.10	14.92 ± 0.41	1.01
200 – 300	231.96 ± 0.10	14.70 ± 0.35	1.03
200 – 310	231.95 ± 0.10	14.53 ± 0.33	1.02
200 – 320	231.95 ± 0.10	14.44 ± 0.31	1.03

Table 8.8: Estimated parameters for the $\Sigma_c(2520)^{++}$ baryon in various fit ranges. Δm, Γ, and χ^2/ndf are the mass difference of $m(\Sigma_c) - m(\Lambda_c^+)$, decay width, and χ^2 divided by the numbers of degrees of freedom, respectively. The values are in MeV/c^2 for the fit range, Δm, and Γ.

8.4 Background Model

There are possible sources of the systematic uncertainties due to the background modeling; uncertainty from the feed-down correction, statistical effect of the random background associated with the fake Λ_c^+ candidates, and various modeling of the random background associated with the true Λ_c^+ candidates.

8.4.1 Feed-down Correction

As discussed in Sec. 5.1.3, the feed-down backgrounds from the excited Λ_c^+ decays are corrected by taking into account the tracking efficiency and the acceptance of the Belle detector. Since there are uncertainties of the tracking efficiency and the acceptance, one has to account the uncertainties as a systematic uncertainties.

The feed-down backgrounds are corrected by using Eq. (5.2). From the error propagation of Eq. (5.2), the uncertainty due to the feed-down correction can be described as

$$\begin{aligned}\frac{\delta\mathcal{N}_{\text{corrected}}(\text{Feed-down})}{\mathcal{N}_{\text{corrected}}(\text{Feed-down})} &= \left[\left(\frac{\delta\mathcal{N}_{\text{uncorrected}}(\text{Feed-down})}{\mathcal{N}_{\text{uncorrected}}(\text{Feed-down})}\right)^2\right. \\ &\quad \left. + \left(\frac{\delta\epsilon_{\text{tracking}}(h^\pm)}{\epsilon_{\text{tracking}}(h^\pm)}\right)^2 + \left(\frac{\delta\epsilon_{\text{acceptance}}(h^\pm)}{\epsilon_{\text{acceptance}}(h^\pm)}\right)^2\right]^{1/2} \qquad (8.6)\end{aligned}$$

and the quantities of each terms are found to be

$$\begin{aligned}\frac{\delta\mathcal{N}_{\text{uncorrected}}(\text{Feed-down})}{\mathcal{N}_{\text{uncorrected}}(\text{Feed-down})} &= 0.46\% \\ \frac{\delta\epsilon_{\text{tracking}}(h^\pm)}{\epsilon_{\text{tracking}}(h^\pm)} &= 1.80\% \\ \frac{\delta\epsilon_{\text{acceptance}}(h^\pm)}{\epsilon_{\text{acceptance}}(h^\pm)} &= 0.17\%,\end{aligned}$$

therefore, the total uncertainty is found to be 1.87%. The systematic uncertainties are found by varying the normalization of the feed-down backgrounds $\pm 1.87\%$ and the estimated parameters are summarized in Tables 8.9 and 8.10. Only small uncertainties are found for the decay widths of $\Sigma_c(2520)^{0/++}$ baryons, but they are consistent within the statistical uncertainties.

	$\Delta m(\Sigma_c(2455)^0)$	$\Delta m(\Sigma_c(2520)^0)$	$\Gamma(\Sigma_c(2455)^0)$	$\Gamma(\Sigma_c(2520)^0)$	$\mathcal{N}(\Sigma_c(2455)^0)$	$\mathcal{N}(\Sigma_c(2520)^0)$	χ^2/ndf
-1.87%	167.29 ± 0.01	231.99 ± 0.11	1.77 ± 0.04	15.30 ± 0.40	32593 ± 292	40492 ± 844	1.01
±0%	167.29 ± 0.01	231.98 ± 0.11	1.76 ± 0.04	15.41 ± 0.41	32484 ± 291	40796 ± 851	1.01
+1.87%	167.29 ± 0.01	231.98 ± 0.11	1.75 ± 0.04	15.52 ± 0.40	32380 ± 289	41115 ± 863	1.01
Δ	–	±0.01	±0.01	±0.11	±109	±319	–

Table 8.9: Estimated parameters for the neutral Σ_c baryons with fluctuated normalizations of the feed-down background. Δm, Γ, $\mathcal{N}$, and χ^2/ndf are the mass difference $m(\Sigma_c) - m(\Lambda_c^+)$, the decay width, the number of signal events, and the χ^2 divided by the numbers of degrees of freedom, respectively. The first column indicates the fluctuation of the normalizations of the feed-down background, and Δ in the last row is the difference of the value from the central value estimated without the fluctuation of the feed-down background. The values are in MeV/c^2 for Δm and Γ.

	$\Delta m(\Sigma_c(2455)^{++})$	$\Delta m(\Sigma_c(2520)^{++})$	$\Gamma(\Sigma_c(2455)^{++})$	$\Gamma(\Sigma_c(2520)^{++})$	$\mathcal{N}(\Sigma_c(2455)^{++})$	$\mathcal{N}(\Sigma_c(2520)^{++})$	χ^2/ndf
-1.87%	167.52 ± 0.01	231.99 ± 0.10	1.85 ± 0.04	14.66 ± 0.27	36085 ± 313	43355 ± 540	0.98
±0%	167.51 ± 0.01	231.99 ± 0.10	1.84 ± 0.04	14.77 ± 0.25	35984 ± 311	43728 ± 511	0.98
+1.87%	167.51 ± 0.01	231.98 ± 0.10	1.84 ± 0.04	14.90 ± 0.26	35885 ± 306	44115 ± 545	0.98
Δ	±0.01	±0.01	±0.01	±0.13	±101	±387	–

Table 8.10: Estimated parameters for the doubly-charged Σ_c baryons with fluctuated normalizations of the feed-down background. Δm, Γ, $\mathcal{N}$, and χ^2/ndf are the mass difference $m(\Sigma_c) - m(\Lambda_c^+)$, the decay width, the number of signal events, and the χ^2 divided by the numbers of degrees of freedom, respectively. The first column indicates the fluctuation of the normalization of the feed-down background, and Δ in the last row is the difference of the value from the central value estimated without the fluctuation of the feed-down background. The values are in MeV/c^2 for Δm and Γ.

8.4.2 Wrong Combination Events Subtraction in the Feed-down Background

As discussed in Sec. 5.1.2, the wrong combination events of the excited Λ_c^+ candidates are subtracted by using the generic MC. Since the wrong combination events obtained from the generic MC might be underestimated or overestimated, therefore, this can be a source of a systematic uncertainty. To estimate the uncertainty, the normalization of the wrong combination events of the excited Λ_c^+ candidates is varied by $\pm 1\sigma$ where σ is the statistical uncertainty of the random background. Only small systematic uncertainties are found for the decay widths of $\Sigma_c(2520)^{0/++}$ baryons, and they are consistent within the statistical uncertainties.

8.4.3 Statistical Effect of the Random Background associated with fake Λ_c^+

In the fit, the random backgrounds associated with the fake Λ_c^+ candidates are obtained from the sideband of the Λ_c^+ mass as discussed in Sec. 5.3.1. The normalizations of the random background associated with the fake Λ_c^+ candidates are fixed in the fit as obtained from the sideband of the Λ_c^+ mass in the data, and the statistical effect of the normalization can be a source of a systematic uncertainty. To estimate this effect, the normalization of the random background associated with the fake Λ_c^+ candidates are varied by $\pm 1\sigma$ where σ is the statistical uncertainty of the random background associated with the fake Λ_c^+ candidates obtained from the data. Since the statistical uncertainties of the random backgrounds are small (433 for $m(pK^-\pi^+\pi^-) - m(pK^-\pi^+)$ and 355 for $m(pK^-\pi^+\pi^+) - m(pK^-\pi^+)$), only negligible systematic uncertainties are found.

8.4.4 Background Model of the Random Background associated with true Λ_c^+

To describe the random background associated with the true Λ_c^+ candidates, Eq. (5.3) is used. To estimate the possibility of other PDFs for the background, the following functions are tested:

$$
\begin{aligned}
B_1(\Delta m; c_0, c_1) &= c_0(\Delta m - m_\pi)^{1/2} + c_1(\Delta m - m_\pi)^{3/2} \\
B_2(\Delta m; c_0, c_1, c_2) &= c_0(\Delta m - m_\pi)^{1/2} + c_1(\Delta m - m_\pi)^{3/2} + c_2(\Delta m - m_\pi)^{5/2}
\end{aligned}
$$

where Δm is the mass difference $m(pK^-\pi^+\pi_s^\pm) - m(pK^-\pi^+)$ as a random variable, m_π is a nominal mass of a pion [3], c_0, c_1, and c_2 are the fit parameters. No systematic uncertainties are found from the various background PDFs.

8.5 Total Systematic Uncertainties

The systematic uncertainties discussed so far are summarized in Tables 8.11 and 8.12.

The systematic uncertainties for the mass difference of $m(\Sigma_c(2455)^0) - m(\Lambda_c^+)$ and $m(\Sigma_c(2455)^{++}) - m(\Lambda_c^+)$ are found to be ± 0.02 MeV/c^2 and they are comparable with the statistical uncertainties. In case of the mass difference $m(\Sigma_c(2520)^0) - m(\Lambda_c^+)$ and $m(\Sigma_c(2455)^{++}) - m(\Lambda_c^+)$, the systematic uncertainties are found to be ± 0.04 and ± 0.02 MeV/c^2, and they are small comparing with the statistical uncertainties.

The systematic uncertainties for the decay widths of the $\Sigma_c(2455)^0$ and $\Sigma_c(2455)^{++}$ baryons are found to be $^{+0.09}_{-0.21}$ and $^{+0.07}_{-0.20}$ MeV/c^2, and they are large compared with the statistical uncertainties by factor 5 in maximum. They are dominated by the resolution model as expected. Small contributions from the fit model are found. In case of the decay widths of the $\Sigma_c(2520)^0$ and $\Sigma_c(2520)^{++}$ baryons, the systematic uncertainties are found to be $^{+0.20}_{-0.32}$ and $^{+0.18}_{0.30}$ MeV/c^2, and they are comparable with the statistical uncertainties. Both resolution model and the fit model contribute to the uncertainties.

	$\Delta m(\Sigma_c(2455)^0)$	$\Delta m(\Sigma_c(2520)^0)$	$\Gamma(\Sigma_c(2455)^0)$	$\Gamma(\Sigma_c(2520)^0)$
Resolution Model	–	–	$^{+0.01}_{-0.19}$	$^{+0.04}_{-0.25}$
Momentum Scale	±0.02	±0.02	–	–
Fit Model	±0.01	±0.03	±0.09	±0.20
Total	±0.02	±0.04	$^{+0.09}_{-0.21}$	$^{+0.20}_{-0.32}$

Table 8.11: Total systematic uncertainties for the neutral Σ_c baryons. Δm and Γ are the mass difference of $m(\Sigma_c) - m(\Lambda_c^+)$ and the decay width, respectively. The values are in MeV/c^2.

	$\Delta m(\Sigma_c(2455)^{++})$	$\Delta m(\Sigma_c(2520)^{++})$	$\Gamma(\Sigma_c(2455)^{++})$	$\Gamma(\Sigma_c(2520)^{++})$
Resolution Model	–	–	${}^{+0.01}_{-0.19}$	${}^{+0.04}_{-0.24}$
Momentum Scale	± 0.02	± 0.02	–	–
Fit Model	± 0.01	± 0.01	± 0.07	± 0.18
Total	± 0.02	± 0.02	${}^{+0.07}_{-0.20}$	${}^{+0.18}_{-0.30}$

Table 8.12: Total systematic uncertainties for the doubly-charged Σ_c baryons. Δm and Γ are the mass difference of $m(\Sigma_c) - m(\Lambda_c^+)$ and the decay width, respectively. The values are in MeV/c^2.

Chapter 9

Results and Discussions

As discussed throughout this dissertation, the mass differences of $m(\Sigma_c(2455)^{0/++}) - m(\Lambda_c^+)$ and $m(\Sigma_c(2520)^{0/++}) - m(\Lambda_c^+)$, and the decay widths of the $\Sigma_c(2455)^{0/++}$ and $\Sigma_c(2520)^{0/++}$ baryons are measured. From the mass differences, the invariant masses of the $\Sigma_c(2455)^{0/++}$ and $\Sigma_c(2520)^{0/++}$ baryons are also calculated by adding the world average mass of the Λ_c^+ baryon [3]. The mass, mass difference, and decay width values are summarized in Table 9.1.

The mass splittings of $m(\Sigma_c(2455)^{++}) - m(\Sigma_c(2455)^0)$ and $m(\Sigma_c(2520)^{++}) - m(\Sigma_c(2520)^0)$ are also calculated from the mass differences of $m(\Sigma_c(2455)^{0/++}) - m(\Lambda_c^+)$ and $m(\Sigma_c(2520)^{0/++}) - m(\Lambda_c^+)$. They are calculated to be $m(\Sigma_c(2455)^{++}) - m(\Sigma_c(2455)^0) = 0.22 \pm 0.01 \pm 0.01$ MeV/c^2 and $m(\Sigma_c(2520)^{++}) - m(\Sigma_c(2520)^0) = 0.01 \pm 0.15 \pm 0.03$ MeV/c^2 where the first error is statistical and the second is systematic. In the calculation of the mass splittings, the most of the systematic uncertainties are canceled, for example, the systematic uncertainty due to the momentum scale.

These measurements are far more accurate compared with the results from other experiments. The comparison with others are summarized in Tables 9.2 and 9.3, and visualized in Figs. 9.1 and 9.2. The measurements in this dissertation significantly reduce the total uncertainties of the measurements. Comparing with the world averages [3], the total uncertainties of the mass differences of $m(\Sigma_c(2455)^{0/++}) - m(\Lambda_c^+)$ and $m(\Sigma_c(2520)^{0/++}) - m(\Lambda_c^+)$ are roughly reduced by a factor four, the decay widths of the $\Sigma_c(2455)^{0/++}$ baryons approximately by a factor two with taking average of the asymmetric uncertainties, and the decay widths of the $\Sigma_c(2520)^{0/++}$ baryons roughly by factors of three and five, respectively. These improvements are achieved not only in statistical but also in systematic.

For the mass splittings of $m(\Sigma_c(2455)^{++}) - m(\Sigma_c(2455)^0)$ and $m(\Sigma_c(2520)^{++}) - m(\Sigma_c(2520)^0)$, the total uncertainties are roughly reduced by factors of nine and six, respectively. As many theoretical calculations indicate, the $\Sigma_c(2455)^{++}$ baryon is heavier than the $\Sigma_c(2455)^0$ baryon because the electromagnetic coupling is more dominant than the mass difference between u and d quarks. But in case of the mass splitting of the $\Sigma_c(2520)^{0/++}$ baryons, the statistical and systematic uncertainties are still large to determine which is heavier. By comparing the theoretical expectations, Ref. [44] gives a close prediction for the mass splitting of $m(\Sigma_c(2455)^{++}) - m(\Sigma_c(2455)^0)$. For the mass splitting of $m(\Sigma_c(2520)^{++}) - m(\Sigma_c(2520)^0)$, it is hard to conclude due to the large statistical uncertainty. To improve the measurement of the mass splittings of $m(\Sigma_c(2520)^{++}) - m(\Sigma_c(2520)^0)$, larger data sample is desired.

	Δm (MeV/c^2)	m (MeV/c^2)	Γ (MeV/c^2)
$\Sigma_c(2455)^0$	$167.29 \pm 0.01 \pm 0.02$	$2453.75 \pm 0.01 \pm 0.02 \pm 0.14$	$1.76 \pm 0.04^{+0.09}_{-0.21}$
$\Sigma_c(2455)^{++}$	$167.51 \pm 0.01 \pm 0.02$	$2453.97 \pm 0.01 \pm 0.02 \pm 0.14$	$1.84 \pm 0.04^{+0.07}_{-0.20}$
$\Sigma_c(2520)^0$	$231.98 \pm 0.11 \pm 0.04$	$2518.44 \pm 0.11 \pm 0.04 \pm 0.14$	$15.41 \pm 0.41^{+0.20}_{-0.32}$
$\Sigma_c(2520)^{++}$	$231.99 \pm 0.10 \pm 0.02$	$2518.45 \pm 0.10 \pm 0.02 \pm 0.14$	$14.77 \pm 0.25^{+0.18}_{-0.30}$

Table 9.1: Measurements of the masses and widths of the $\Sigma_c(2455)^{0/++}$ and $\Sigma_c(2520)^{0/++}$ baryons. Δm is the mass difference of $m(\Sigma_c(2455)^{0/++}) - m(\Lambda_c^+)$ and $m(\Sigma_c(2520)^{0/++}) - m(\Lambda_c^+)$, m and Γ are the invariant mass and decay width of the $\Sigma_c(2455)^{0/++}$ and $\Sigma_c(2520)^{0/++}$ baryons. The first uncertainty is statistical, the second is systematic, and the third is the total uncertainty of the world average of the Λ_c^+ mass [3].

	$\Delta m(\Sigma_c(2455)^0)$	$\Delta m(\Sigma_c(2520)^0)$	$\Gamma(\Sigma_c(2455)^0)$	$\Gamma(\Sigma_c(2520)^0)$
This work	$167.29 \pm 0.01 \pm 0.02$	$231.98 \pm 0.11 \pm 0.04$	$1.76 \pm 0.04^{+0.09}_{-0.21}$	$15.41 \pm 0.41^{+0.20}_{-0.32}$
PDG [3]	167.27 ± 0.08	232.3 ± 0.5	2.16 ± 0.26	14.5 ± 1.5
CDF (2011) [28]	$167.28 \pm 0.03 \pm 0.12$	$232.88 \pm 0.43 \pm 0.16$	$1.65 \pm 0.11 \pm 0.49$	$12.51 \pm 1.82 \pm 1.37$
BABAR (2008) [50]	–	–	$2.6 \pm 0.5 \pm 0.3$	–
CLEO (2005) [51]	–	$231.4 \pm 0.5 \pm 0.3$	–	$16.6^{+1.9}_{-1.7} \pm 1.4$
CLEO (2002) [52]	$167.2 \pm 0.1 \pm 0.2$	–	$2.5 \pm 0.2 \pm 0.3$	–
FOCUS (2002) [53]	–	–	$1.55^{+0.41}_{-0.37} \pm 0.38$	–
FOCUS (2000) [54]	$167.38 \pm 0.21 \pm 0.13$	–	–	–
CLEO (1997) [55]	–	$232.6 \pm 1.0 \pm 0.8$	–	$13.0^{+3.7}_{-3.0} \pm 4.0$
E791 (1996) [56]	$167.38 \pm 0.29 \pm 0.15$	–	–	–
EXCHARM (1996) [57]	$167.8 \pm 0.6 \pm 0.2$	–	–	–
E687 (1996) [58]	$166.6 \pm 0.5 \pm 0.6$	–	–	–
CLEO (1993) [59]	$167.1 \pm 0.3 \pm 0.2$	–	–	–
E691 (1989) [60]	$168.4 \pm 1.0 \pm 0.3$	–	–	–

Table 9.2: Comparison with the results in MeV/c^2 from other experiments for the neutral Σ_c baryons. The first uncertainty is statistical and the second is systematic except for the world average shown in the third row as PDG. The uncertainty of the world average is the total uncertainty.

	$\Delta m(\Sigma_c(2455)^{++})$	$\Delta m(\Sigma_c(2520)^{++})$	$\Gamma(\Sigma_c(2455)^{++})$	$\Gamma(\Sigma_c(2520)^{++})$
This work	$167.51 \pm 0.01 \pm 0.02$	$231.99 \pm 0.10 \pm 0.02$	$1.84 \pm 0.04^{+0.07}_{-0.20}$	$14.77 \pm 0.25^{+0.18}_{-0.30}$
PDG [3]	167.52 ± 0.08	231.4 ± 0.6	2.26 ± 0.25	14.9 ± 1.5
CDF (2011) [28]	$167.44 \pm 0.04 \pm 0.12$	$230.73 \pm 0.56 \pm 0.16$	$2.34 \pm 0.13 \pm 0.45$	$15.03 \pm 2.12 \pm 1.36$
CLEO (2005) [51]	–	$231.5 \pm 0.4 \pm 0.3$	–	$14.4^{+1.6}_{-1.5} \pm 1.4$
CLEO (2002) [52]	$167.4 \pm 0.1 \pm 0.2$	–	$2.3 \pm 0.2 \pm 0.3$	–
FOCUS (2002) [53]	–	–	$2.05^{+0.41}_{-0.38} \pm 0.38$	–
FOCUS (2000) [54]	$167.35 \pm 0.19 \pm 0.12$	–	–	–
E791 (1996) [56]	$167.76 \pm 0.29 \pm 0.15$	–	–	–
E687 (1996) [58]	$167.6 \pm 0.6 \pm 0.6$	–	–	–
CLEO (1993) [59]	$168.2 \pm 0.3 \pm 0.2$	–	–	–
CLEO (1989) [61]	$167.8 \pm 0.4 \pm 0.3$	–	–	–
ARGUS (1988) [62]	$168.2 \pm 0.5 \pm 1.6$	–	–	–
E400 (1987) [63]	$167.4 \pm 0.5 \pm 2.0$	–	–	–

Table 9.3: Comparison with the results in MeV/c^2 from other experiments for the doubly-charged Σ_c baryons. The first uncertainty is statistical and the second is systematic except for the world average shown in the third row as PDG. The uncertainty of the world average is the total uncertainty.

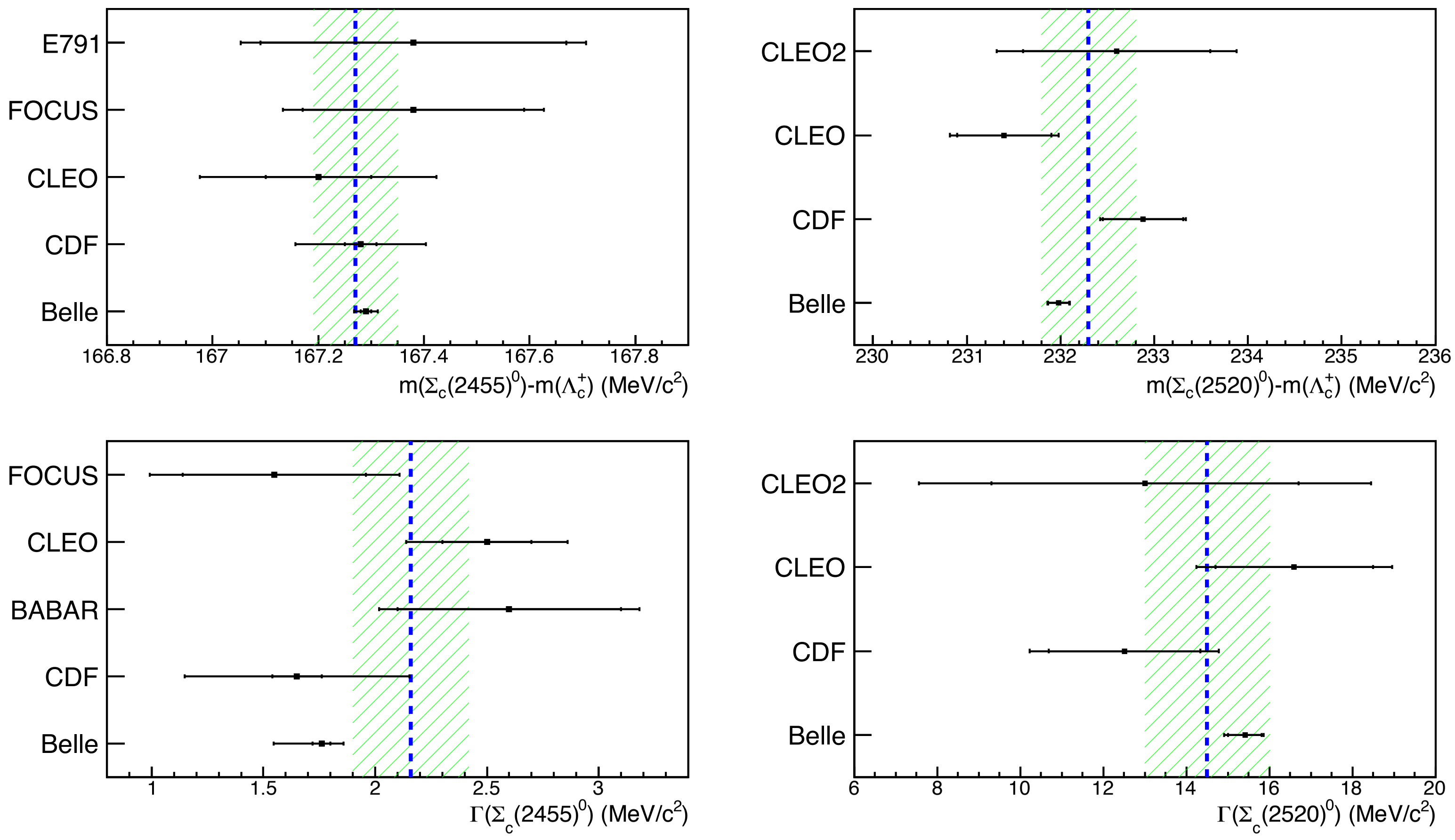

Figure 9.1: Comparison of the mass differences and widths of the $\Sigma_c(2455)^0$ and $\Sigma_c(2520)^0$ baryons with the results from other experiments. Only recent measurements from CDF [28], BABAR [50], CLEO [51, 52], FOCUS [53, 54], CLEO2 [55], and E791 [56], and the result from this study (Belle) are shown.

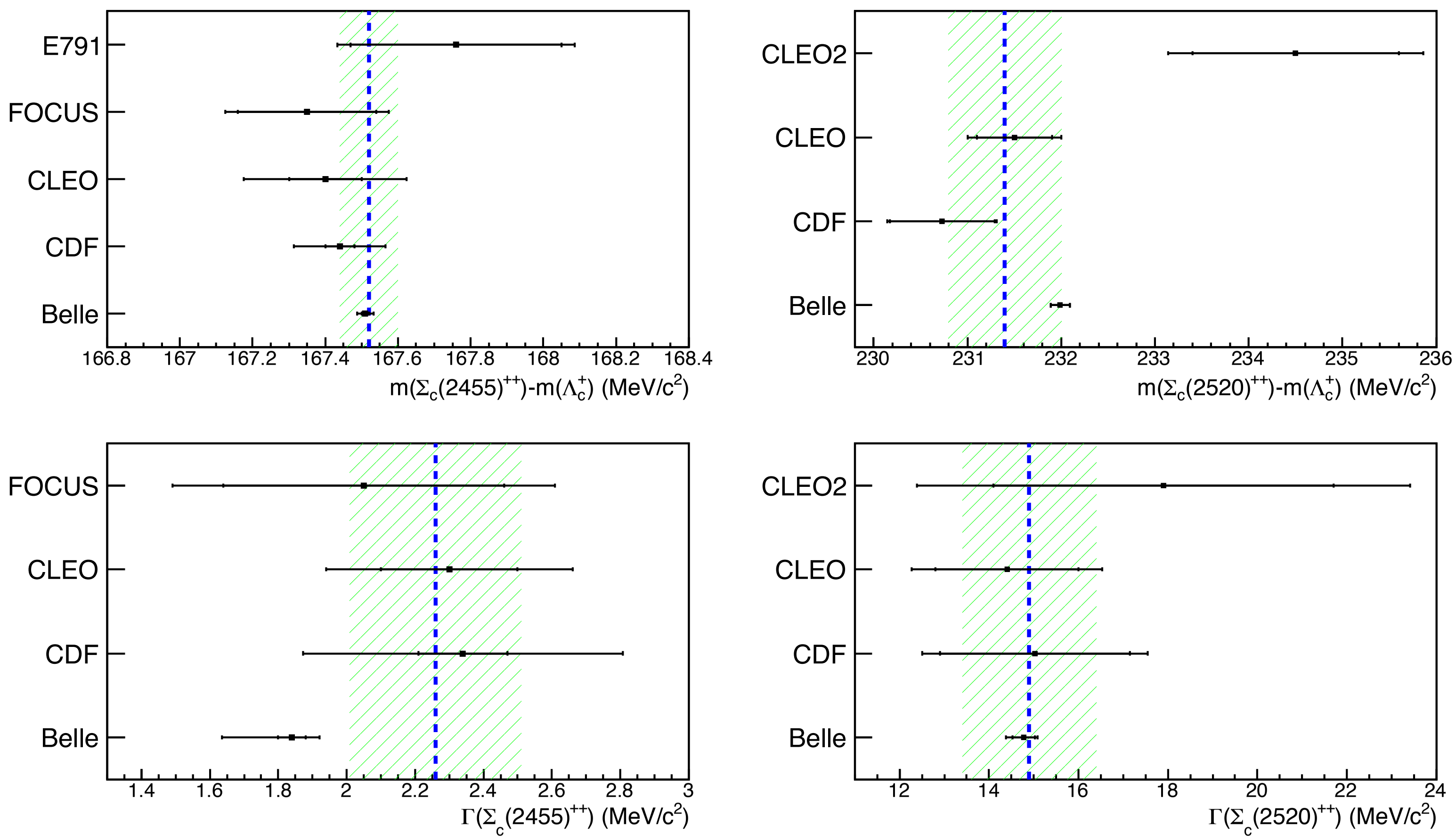

Figure 9.2: Comparison of the mass differences and widths of the $\Sigma_c(2455)^{++}$ and $\Sigma_c(2520)^{++}$ baryons with the results from other experiments. Only recent measurements from CDF [28], CLEO [51, 52], FOCUS [53, 54], CLEO2 [55], and E791 [56], and the result from this study (Belle) are shown.

Appendix A

Technical Details of Convolution Method

Convolution theorem is defined as

$$f \otimes g \equiv \frac{1}{\sqrt{2\pi}} \int_{-\infty}^{\infty} g(y) f(x-y) dy \tag{A.1}$$

with a consideration of two functions $f(x)$ and $g(x)$ with Fourier transforms of $F(t)$ and $G(t)$ [103]. Equation (A.1) can be transformed by introducing the Fourier transforms as

$$\begin{aligned} \int_{-\infty}^{\infty} g(y) f(x-y) dy &= \frac{1}{\sqrt{2\pi}} \int_{-\infty}^{\infty} g(y) \int_{-\infty}^{\infty} F(t) e^{-it(x-y)} dt dy \\ &= \frac{1}{\sqrt{2\pi}} \int_{-\infty}^{\infty} \left[\int_{-\infty}^{\infty} g(y) e^{ity} dy \right] e^{-itx} dt \\ &= \int_{-\infty}^{\infty} F(t) G(t) e^{-itx} dt, \end{aligned} \tag{A.2}$$

and this reads that the Fourier inverse transform of a product of Fourier transforms is the convolution of the original functions $f \otimes g$.

The convolution theorem is often used to describe an experimental data of which a theoretical distribution is modified by a detector response function. In that case, a theoretical model and a detector response function can be the original functions of $f(x)$ and $g(x)$ with a random variable x. The relation, Eq. (A.2), is useful to calculated the convolved distribution function, especially the analytical form of the functions are not given.

In addition, an explicit way for normalization is required for PDFs, however, a convolution of two normalized PDFs on a finite domain is not generally normalized [97]. Therefore, the convolved probability density function should include its normalization term as

$$f(x) \otimes g(x) = \frac{\int_{-\infty}^{\infty} f(x)g(x-y)dy}{\int_{x_{\min}}^{x_{\max}} \int_{-\infty}^{\infty} f(x)g(x-y)dydx}.$$

In this study, the convolution is calculated by using `RooFit` [97], a data modeling package included in `ROOT` [96]. In `RooFit`, a class named `RooFFTConvPdf` enables the calculation by using Eq. (A.2). It samples $f(x)$ and $g(x)$ for discrete Fourier transforms and calculate the convolution $F(t)G(t)$ in the frequency domain. Then, it performs inverse Fourier transform to the convolved function. Finally, it represents the discrete result as a continuous function through the interpolation.

`RooFit` also provides other ways to calculate the convolution such as a numerical calculation of the integral using `RooNumConvPdf` class, however, it is not practically useful because of a huge processing time.

Appendix B

Breit-Wigner Line Shape

The Breit-Wigner line shape was introduced by Breit and Wigner in 1936 [104] and is the most commonly used parameterization of dynamics of scattering [93]. In this chapter, various form of the Breit-Wigner line shapes are discussed.

B.1 Non-relativistic Breit-Wigner Line Shape

The non-relativistic Breit-Wigner line shape is the simplest one. It is symmetric and does not take into account any threshold behaviors of transition amplitude, therefore, it is only a first approximation [93]. The non-relativistic Breit-Wigner is given as a function of mass (m),

$$\frac{m_0 \Gamma_0}{m_0^2 - m^2 - i m_0 \Gamma_0}$$

where m_0 and Γ_0 are a nominal mass and width of a particle.

B.2 Relativistic Breit-Wigner Line Shape

In dynamics of partial amplitudes, K-matrix formalism [105, 106] and F-vector approach [107] are often used. In these formalism, the Breit-Wigner line shape is derived as the parameterization of the dynamics, and the Blatt-Weisskopf form factor [95] is employed in the form of the Breit-Wigner line shape. The non-relativistic Breit-Wigner line shape treat the Blatt-Weisskopf factor as a constant for a simple approximation, but this may be invalid if the distribution is near a kinematic threshold. The transition amplitude at the threshold should vanish because the breakup momentum is zero at the threshold. This is referred to as a threshold behavior, and the Blatt-Weisskopf factor is employed to vanish the transition amplitude at the threshold.

From the F-vector approach [107], the relativistic Breit-Wigner line shape is derived. The relativistic Breit-Wigner line shape is given by

$$\frac{m_0\Gamma_0 B_L\left(\frac{p^2}{p_R^2}, \frac{p_0^2}{p_R^2}\right)}{m_0^2 - m^2 - i m_0 \Gamma(m)}$$

where p, p_0, and p_R are a momentum, a nominal momentum, and the Fermi momentum [108] of a particle, B_L is the Blatt-Weisskopf form factor, and

$$\Gamma(m) \quad = \quad \Gamma_0 B_L^2\left(\frac{p^2}{p_R^2}, \frac{p_0^2}{p_R^2}\right) \cdot \frac{2p_R}{m}.$$

The relativistic Breit-Wigner line shape is asymmetric, and the width in the denominator depends on the mass, therefore, the line shape is referred to as "relativistic" which in terms of relativity is not quite correct [93].

Appendix C

Development of the High Level Trigger System for the Belle II Experiment

During the Ph. D. course, a development of the high level trigger (HLT) system for the Belle II experiment, an upgrade of the Belle experiment, is performed as a service to the collaboration [111, 112, 113, 114].

The Belle II experiment [115] is planned to start its operation in 2016, and the research and development are being performed for the upgrade. Since the target luminosity of the Belle II experiment is 8×10^{35} $\mathrm{cm}^{-2}\mathrm{s}^{-1}$ which is a factor 10 higher than that of the Belle experiment, the requirement for the online processing is crucial. The event rate and data transfer rate to be processed by HLT is expected to be approximately 30 kHz and 2 GB/s, therefore, it is a challenge in the aspect of computing. Furthermore, the analysis software for the Belle II experiment is being developed from the scratch, and it is required that the online software is compatible with the offline software. Since the former software [90] was developed in an old-fashioned way and is not capable to handle `ROOT` files which are the most popular format for handling data in high energy physics. To satisfy the requirements, a new high level trigger software is being developed.

To satisfy the requirement of the software consistency between online and offline, the Belle II analysis software, `basf2` [116], is used in the essential part of the high level trigger software. The `basf2` has modular structure on a software pipeline architecture, therefore, it is flexible and versatile in the data processing. To extend the software to meet the requirements for the high level trigger system, a super-framework which wraps the `basf2` is considered. For the similar naming policy, the

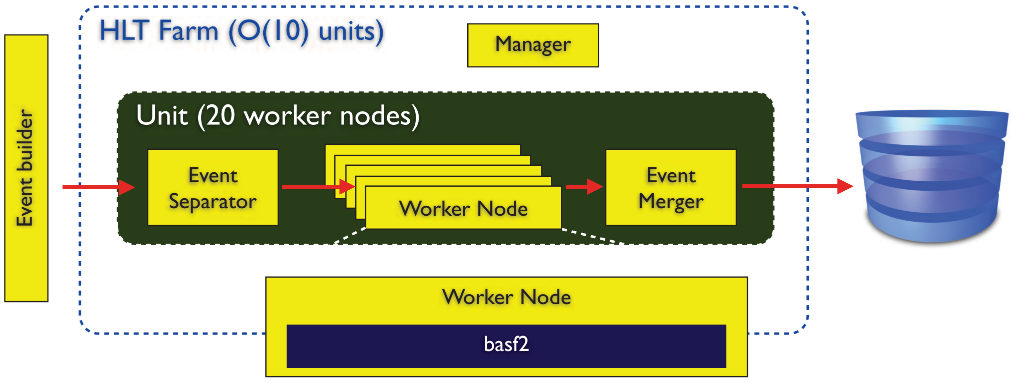

Figure C.1: Illustration of the Belle II HLT system. The system consists of $\mathcal{O}(10)$ units, and a unit contains 20 worker nodes that process the event data. The data taken from the detector is reduced by sub-detector triggers first, and an event builder collects them and builds event data. The event data are passed to the HLT system and are distributed over worker nodes by an event separator. After the event processing, the event data are collected by an event merger and are sent to an online storage.

high level trigger software is named as `hbasf2` [114], where `h` stands for the high level trigger. By making a super-framework, the online and offline software are essentially the same, and the modules to process event data are kept exactly the same.

Since the amount of data to be processed in HLT is huge, massive parallel processing utilizing many CPU cores is necessary. The Belle II high level trigger system is designed to consist of many units where a unit consists of $\mathcal{O}(10)$ computers with many CPU cores as illustrated in Fig. C.1. The computers are connected via 10Gb ethernet connection for the data transfer and 1Gb ethernet connection for the node control. Though the essential part of the processing is done by `basf2`, it does not provide further key functions; networking, node management and monitoring. Therefore, the `hbasf2` should provide functions to transfer data over network, to manage and to monitor the nodes.

For the global management of nodes, there is a special node called manager node which is in charge of node initialization and management. Once an input file that contains the information of the HLT farm formatted as `XML` [117] is provided from outside of the system, the manager node parses it and distributes an individual node information to a proper node according to the input file. The node accepts particular node information and initializes itself accordingly. The node behaviors are predefined in `Python` scripts as same as a typical execution of `basf2`. The node management system is illustrated in Fig. C.2.

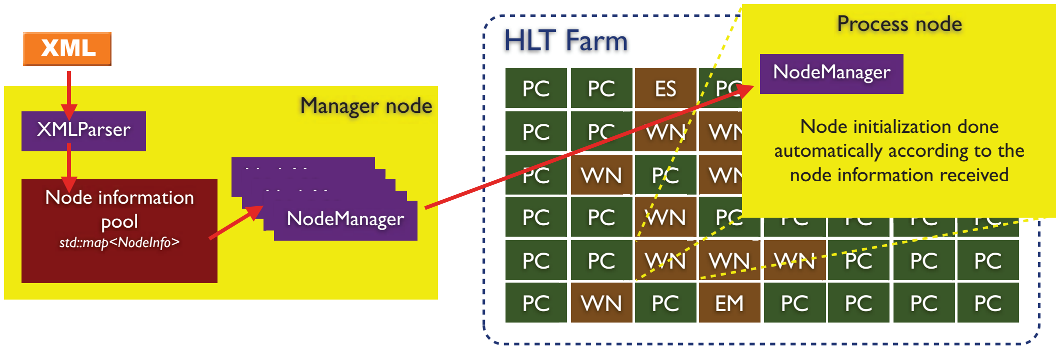

Figure C.2: Node management of the Belle II HLT system. An input XML file contains all the information of HLT farm. Once a XMLParser parses the XML file, node information are stored into an internal node information pool formatted as a map container of standard template library (STL) [118]. The information are sent to particular nodes by a NodeManager, and the nodes in the HLT farm initialize themselves according to the received information.

Between two nodes, the hbasf2 uses a standard transmission control protocol (TCP) [119] socket based on the IPv4 specification [120, 121, 122] for the data communication. The C++ style implementation has been developed, namely, B2Socket as a base class. Inherited classes from the B2Socket, a HLTSender and HLTReceiver, provide interfaces for the data transfer. Since they are separated processes from the framework, there are shared memories based on FIFO (First-In-First-Out) for the interprocess communication.

The B2Socket is used not only for the node information distribution but also for the actual event data distribution. Since the B2Socket utilizes the standard TCP socket, the data should be serialized for the communication. The event data are serialized by using TMessage [123] of ROOT for the communication while the node information are serialized as plain text by boost package [124].

The interface between a HLTSender/HLTReceiver and the basf2 framework is provided by modules, the HLTInput and HLTOutput. These modules access FIFOs for the data communication. The data flow between nodes in the HLT system is summarized in Fig. C.3.

In 2012, the working version of the hbasf2 was tested with three sets of the HLT test bench installed at Tsukuba experimental hall in KEK. The specification of the test bench is summarized in Table C.1.

Before the performance test of the framework, the components of the framework have been tested as unit tests; a data transfer rate test of the B2Socket, a perfor-

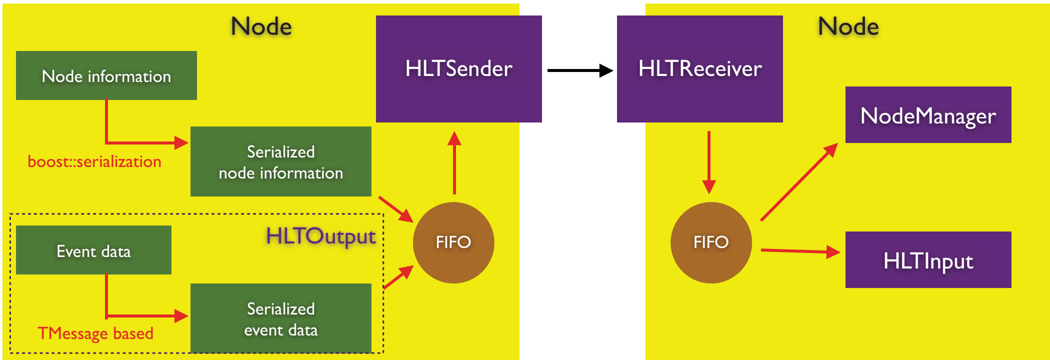

Figure C.3: Data flow in the HLT system. Since there is only one FIFO drawn in the left node, it seems that two separated flows of node information and event data share one FIFO, but they use different FIFOs in the actual implementation.

	CPU	Memory	Total CPU cores
Test set 1	Intel Xeon 3.2 GHz (12-core) * 10	48 GB	120 cores
Test set 2	Intel Xeon 2.7 GHz (12-core) * 4	24 GB	48 cores
Test set 3	Intel Xeon 2.5 GHz (8-core) * 2	12 GB	16 cores

Table C.1: Test bench for the Belle II high level trigger system. 172 cores are available in total.

mance test of FIFOs in various situations, and `HLTInput`/`HLTOutput` performance test.

From the `B2Socket` unit test, the transfer rate is evaluated as 392.4 MB/s for 1.4 GB data transfer. The performance is expected to be even better by a TCP tuning of the test bench in future.

For the FIFO unit test, three different situations are considered; worker node (one-to-one), event separator (one-to-many), and event merger (many-to-one). In a worker node, a FIFO is shared by only one `HLTSender`/`HLTReceiver` and only one `HLTOutput`/`HLTInput`, respectively. In an event separator, a FIFO is shared by one `HLTOutput` and many `HLTSenders`. On the other hand, a FIFO is shared by many `HLTReceivers` and a `HLTInput` in an event merger. From the unit test of the FIFO in different situations, the performance of FIFO is evaluated as summarized in Table C.2. The performance is high enough as expected.

In the reality of the HLT operation, all data are given by an event builder and passed to an online storage over the network. But for the HLT system test, the input and output (I/O) of data rely on a local hard disk because there are no event

Table C.2: FIFO performance. The cases listed are; one-to-one is that a process writes, and another process reads; one-to-many is that a process writes, and 4 processes read; many-to-one is that 4 processes write, and a process reads, simultaneously.

	Transfer rate (GB/s)
one-to-one	2.34
one-to-many	2.21
many-to-one	1.60

builder and online storage available at the moment. For this purpose, specialized I/O modules that read and write serialized data are developed. The I/O modules, `SeqRootInput` and `SeqRootOutput`, certainly make overheads during the test so that the overheads should be analyzed as well. From the test, the I/O rate of the module is measured 110.1 MB/s for 416 MB data.

After confirming the performance of each components, the maximum performance of the framework is carried out utilizing up to 172 CPU cores as shown in Fig. C.4. The expectations are estimated by extending a result of single CPU processing, and it is confirmed that the linearity of the performance is kept as the number of CPU cores increases.

The test results conclude that the developed HLT software satisfies the requirement of high performance with $\sim \mathcal{O}(10)$ CPUs. The performance is expected to be improved with more tunings of software and network in future.

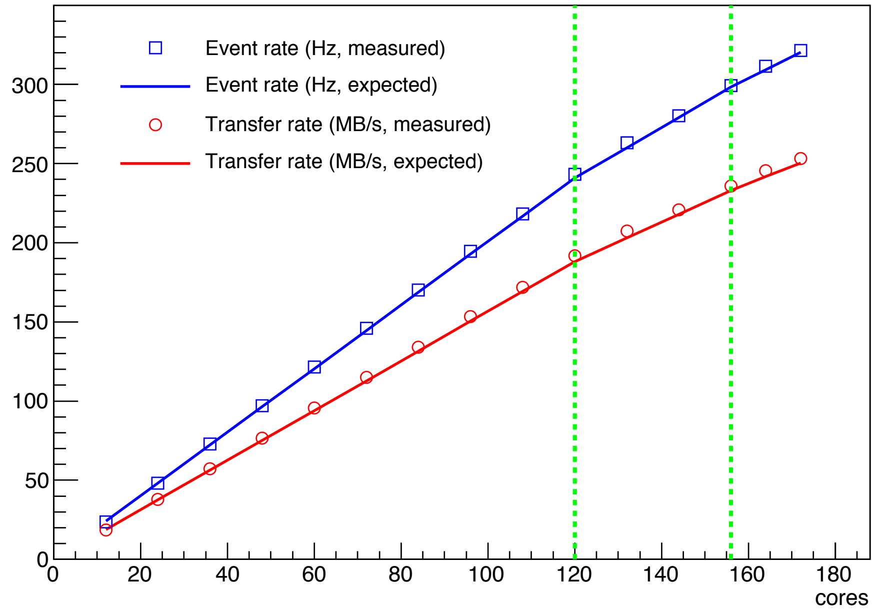

Figure C.4: Performance test of the Belle II high level trigger software. The measured (data points) and the expected (line) performance are shown. The event rate (blue open-square) and the transfer rate (red open-circle) exceed 300 Hz and 250 MB/s with utilizing up to 172 CPU cores. The vertical dashed-lines at 120 and 156 CPU cores indicate different test sets defined in Table C.1. Test set 1 is used before the first vertical dashed-line (up to 120 cores), test set 2 is used between the first and second vertical dashed-lines (from 120 to 156 cores), and test set 3 is used after the second vertical dashed-line (from 156 to 172 cores).

Bibliography

[1] D. Griffiths, "Introduction to Elementary Particles", WILEY-VCH (2004).

[2] `http://www.wikipedia.org`.

[3] J. Beringer *et al.* (Particle Data Group), "Review of Particle Physics", Phys. Rev. D **86**, 010001 (2012).

[4] A. Das and T. Ferbel, "Introduction to Nuclear and Particle Physics", World Scientific (2003).

[5] S. Tomonaga, "On a Relativistically Invariant Formulation of the Quantum Theory of Wave Fields", Prog. Theor. Phys. **1**, 27 (1946).

[6] J. Schwinger, "On Quantum-Electrodynamics and the Magnetic Moment of the Electron", Phys. Rev. **73**, 416 (1948).

[7] J. Schwinger, "Quantum Electrodynamics. I. A. Covariant Formulation", Phys. Rev. **74**, 1439 (1948).

[8] R. P. Feynman, "The Theory of Positrons", Phys. Rev. **76**, 749 (1949).

[9] R. P. Feynman, "Space-Time Approach to Quantum Electrodynamics", Phys. Rev. **76**, 769 (1949).

[10] R. P. Feynman, "Mathematical Formulation of the Quantum Theory of Electromagnetic Interaction", Phys. Rev. **80**, 440 (1950).

[11] M. Gell-Mann, "A schematic model of baryons and mesons", Phys. Lett. **8**, 214 (1964).

[12] H. Fritzsch, M. Gell-Mann, and H. Leutwyler, "Advantages of the color octet gluon picture", Phys. Lett. B**47**, 365 (1973).

[13] D. J. Gross and F. Wilczek, "Ultraviolet Behavior of Non-Abelian Gauge Theories", Phys. Rev. Lett. **30**, 1343 (1973).

[14] H. D. Politzer, "Reliable Perturbative Results for Strong Interactions?", Phys. Rev. Lett. **30**, 1346 (1973).

[15] R. P. Feynman and M. Gell-Mann, "Theory of the Fermi Interaction", Phys. Rev. **109**, 193 (1958).

[16] S. L. Glashow, "Partial-Symmetries of Weak Interactions", Nucl. Phys. **22**, 579 (1961).

[17] S. Weinberg, "A Model of Leptons", Phys. Rev. Lett. **19**, 1264 (1967).

[18] T. D. Lee and C. N. Yang, "Question of Parity Conservation in Weak Interactions", Phys. Rev. **104**, 254 (1956).

[19] C. S. Wu *et al.*, "Experimental Test of Parity Conservation in Beta Decay", Phys. Rev. **105**, 1413 (1957).

[20] J. H. Christenson *et al.*, "Evidence for the 2π Decay of the K_2^0 Meson", Phys. Rev. Lett. **13**, 138 (1964).

[21] D. Fourier, "NA31 Results on CP Violation in K Decays, and a Test of CPT", 14th International Symposium on Lepton and Photon Interactions, Stanford, CA, USA (1989).

[22] A. Alavi-Harati *et al.*, "Observation of Direct CP Violation in $K_{S,L} \to \pi\pi$ Decays", Phys. Rev. Lett. **83**, 22 (1999).

[23] V Fanti *et al.* (NA48 Collaboration), "A new measurement of direct CP violation in two pion decays of the neutral kaon", Phys. Lett. B **465**, 335 (1999).

[24] B. Aubert *et al.* (BaBar Collaboration), "Observation of CP Violation in the B^0 Meson System", Phys. Rev. Lett. **87**, 091801 (2001).

[25] K. Abe *et al.* (Belle Collaboration), "Observation of Large CP Violation in the Neutral B Meson System", Phys. Rev. Lett. **87**, 091802 (2001).

[26] F. Halzen and A. D. Martin, "Quarks and Leptons: An Introductory Course in Modern Particle Physics", John Wiley & Sons (1994).

[27] S. S. M. Wong, "Introductory Nuclear Physics", John Wiley & Sons (1998).

[28] T. Alltonen *et al.* (CDF Collaboration), "Measurements of the properties of $\Lambda_c(2595)$, $\Lambda_c(2625)$, $\Sigma_c(2455)$, and $\Sigma_c(2520)$ baryons", Phys. Rev. D **84**, 012003 (2011).

[29] R. Mizuk *et al.* (Belle Collaboration), "Observation of a Isotriplet of Excited Charmed Baryons Decaying to $\Lambda_c^+\pi$", Phys. Rev. Lett. **94**, 122002 (2005).

[30] P. Avery *et al.* (CLEO Collaboration), "Observation of a Narrow State Decaying into $\Xi_c^+\pi^-$", Phys. Rev. Lett. **75**, 4364 (1995).

[31] L. Gibbons *et al.* (CLEO Collaboration), "Observation of an Excited Charmed Baryon Decaying into $\Xi_c^0\pi^+$", Phys. Rev. Lett. **77**, 810 (1996).

[32] S. E. Csoma *et al.* (CLEO Collaboration), "Evidence of New States Decaying into $\Xi_c^*\pi$", Phys. Rev. Lett. **86**, 4243 (2001).

[33] J. P. Alexander *et al.* (CLEO Collaboration), "Evidence of New States Decaying into $\Xi_c^*\pi$", Phys. Rev. Lett. **83**, 3390 (1999).

[34] R. Lewis, N. Mathur, and R. M. Woloshyn, "Charmed baryons in lattice QCD", Phys. Rev. D **64**, 094509 (2001).

[35] N. Mathur, R. Lewis, and R. M. Woloshyn, "Charmed and bottom baryons from lattice nonrelativistic QCD", Phys. Rev. D **66**, 014502 (2002).

[36] Y. Namekawa *et al.*, "Charmed baryons at the physical point in 2+1 flavor lattice QCD", Phys. Rev. D **87**, 094512 (2013).

[37] W. Roberts and M. Pervin, "Heavy Baryons in a Quark Model", Int. J. Mod. Phys. A **23**, 2817 (2008).

[38] D. Ebert, R. N. Faustov, and V. O. Galkin, "Masses of excited heavy baryons in the relativistic quark-diquark picture", Phys. Lett. B **659**, 612 (2008).

[39] J. -R. Zhang and M. -Q. Huang, "Heavy baryon spectroscopy in QCD", Phys. Rev. D **78**, 094015 (2008).

[40] A. Bernotas and V.Šimonis, "Heavy Hadron Spectroscopy and the Bag Model", Lith. J. Phys. **49**, 19 (2009).

[41] B. Patel, A. K. Rai, and P. C. Vinodkumar, "Masses and magnetic moments of heavy flavour baryons in the hyper central model", J. Phys. G: Nucl. Part. Phys. **35**, 065001 (2008).

[42] Z. Ghalenovi and A. A. Rajabi, "Single charm and beauty baryon masses in the hypercentral approach", Eur. Phys. J. Plus **127**, 141 (2012).

[43] M. Genovese *et al.*, "Isospin mass splittings of baryons in potential models", Phys. Rev. D **59**, 014012 (1998).

[44] L. -H. Chan, "Isospin mass splittings of hadrons with heavy quarks", Phys. Rev. D **31**, 204 (1985).

[45] W-Y. P. Hwang and D. B. Lichtenberg, "Mass splitting of heavy baryon isospin multiplets", Phys. Rev. D **35**, 3526 (1987).

[46] S. Capstick, "Isospin violations in baryons and the $\Sigma_c^0 - \Sigma_c^{++}$ mass difference", Phys. Rev. D **36**, 2800 (1987).

[47] R. C. Verma and S. Srivastava, "Photon-cloud effects on isomultiplet mass differences of charmed and uncharmed baryons", Phys. Rev. D **38**, 1623 (1988).

[48] R. E. Cutkosky and P. Geiger, "Isospin splitting in heavy baryons and mesons", Phys. Rev. D **48**, 1315 (1993).

[49] B. Silvestre-Brac, F. Brau, and C. Semay, "Electromagnetic splitting for mesons and baryons using dressed constituent quarks", J. Phys. G: Nucl. Part. Phys. **29**, 2685 (2003).

[50] B. Aubert *et al.* (BABAR Collaboration), "Measurements of $\mathcal{B}(\overline{B}^0 \to \Lambda_c^+\overline{p})$ and $\mathcal{B}(B^- \to \Lambda_c^+\overline{p}\pi^-)$ and studies of $\Lambda_c^+\pi^-$ resonances", Phys. Rev. D **78**, 112003 (2008).

[51] S. B. Athar *et al.* (CLEO Collaboration), "New measurement of the masses and widths of the Σ_c^{*++} and Σ_c^{*0} charmed baryons", Phys. Rev. D **71**, 051101(R) (2005).

[52] M. Artuso *et al.* (CLEO Collaboration), "Measurement of the masses and widths of the Σ_c^{++} and Σ_c^0 charmed baryons", Phys. Rev. D **65**, 071101(R) (2002).

[53] J. M. Link *et al.* (FOCUS Collaboration), "Measurement of natural widths of Σ_c^0 and Σ_c^{++} baryons", Phys. Lett. B **525**, 205 (2002).

[54] J. M. Link *et al.* (FOCUS Collaboration), "Measurement of the Σ_c^0 and Σ_c^{++} mass splittings", Phys. Lett. B **488**, 218 (2000).

[55] G. Brandenburg *et al.* (CLEO Collaboration), "Observation of Two Excited Charmed Baryons Decaying into $\Lambda_c^+\pi^\pm$", Phys. Rev. Lett. **78**, 2304 (1997).

[56] E. M. Aitala *et al.* (Fermilab E791 Collaboration), "Mass splitting and production of Σ_c^0 and Σ_c^{++} measured in 500 GeV $\pi^- - N$ interaction", Phys. Lett. B **379**, 292 (1996).

[57] A. N. Aleev *et al.* (EXCHARM Collaboration), "Observation of Σ_c^0 Charmed Baryon in the Experiment EXCHARM", Joint Inst. for Nucl. Res. **3-77**, 31 (1996).

[58] P. L. Frabetti *et al.* (Fermilab E687 Collaboration), "Study of higher mass charm baryons decaying to Λ_c^+", Phys. Lett. B **365**, 461 (1996).

[59] G. Crawford *et al.* (CLEO Collaboration), "Observation of the charmed baryons Σ_c^+ and measurement of the isospin mass splittings of the Σ_c", Phys. Rev. Lett. **71**, 3259 (1993).

[60] J. C. Anjos *et al.* (Fermilab E691Collaboration), "Observation of $\Sigma_c^0 \to \Lambda_c^+\pi^-$ decays", Phys. Rev. Lett. **62**, 1721 (1989).

[61] T. J. V. Bowcock *et al.* (CLEO Collaboration), "Σ_c^{++} and Σ_c^0 production from e^+e^- annihilation in the Υ energy region", Phys. Rev. Lett. **62**, 1240 (1989).

[62] H. Albrecht *et al.* (ARGUS Collaboration), "Observation of the charmed Baryon Σ_c in e^+e^- annihilations", Phys. Lett. B **211**, 489 (1988).

[63] M. Diesburg *et al.* (Fermilab E400 Collaboration), "Measurements of the $\Sigma_c^0 - \Lambda_c^+$ and $\Sigma_c^{++} - \Lambda_c^+$ Mass Differences", Phys. Rev. Lett. **59**, 2711 (1987).

[64] S. Kurokawa and E. Kikutani, "Overview of the KEKB accelerators", Nucl. Instrum. Methods Phys. Res. Sect. A **499**, 1 (2003), and other papers included in this Volume.

[65] T. Abe *et al.*, "Achievements of KEKB", Prog. Theor. Exp. Phys. **2013**, 03A001 (2013), and following articles up to 03A011.

[66] High Energy Accelerator Research Organization (KEK), "Using Crab Cavities, KEKB Breaks Luminosity World Record", KEK Press Release, `http://legacy.kek.jp/intra-e/press/2009/KEKBluminosity2.html` (2009).

[67] CERN Courier, "KEKB breaks luminosity record", CERN Courier, `http://cerncourier.com/cws/article/cern/39147` (2009).

[68] `http://belle.kek.jp/belle/transparency`.

[69] A. Abashian *et al.* (Belle Collaboration), "The Belle detector", Nucl. Instrum. Methods Phys. Res. Sect. A **479**, 117 (2002).

[70] J. Brodzicka *et al.* (Belle Collaboration), "Physics achievements from the Belle experiment", Prog. Theor. Exp. Phys. **2012**, 04D001 (2012).

[71] G. Alimonti *et al.* (Belle Collaboration), "The BELLE silicon vertex detector", Nucl. Instrum. Methods, Phys. Res. Sect. A **453**, 71 (2000).

[72] Z. Natkaniec *et al.* (Belle Collaboration), "Status of the Belle silicon vertex detector", Nucl. Instrum. Methods Phys. Res. Sect. A **560**, 1 (2006).

[73] H. Hirano *et al.* (Belle Collaboration), "A high-resolution cylindrical drift chamber for the KEK B-factory", Nucl. Instrum. Methods Phys. Res. Sect. A **455**, 294 (2000).

[74] T. Iijima *et al.* (Belle Collaboration), "Aerogel Cherenkov counter for the BELLE detector", Nucl. Instrum. Methods Phys. Res. Sect. A **453**, 321 (2000).

[75] H. Kichimi *et al.* (Belle Collaboration), "The BELLE TOF system", Nucl. Instrum. Methods Phys. Res. Sect. A **453**, 315 (2000).

[76] K. Miyabayashi (Belle Collaboration), "Belle electromagnetic calorimeter", Nucl. Instrum. Methods Phys. Res. Sect. A **494**, 298 (2002).

[77] K. Ueno *et al.* (Belle Collaboration), "Detection of minimum-ionizing particles and nuclear counter effect with pure BGO and BSO crystals with photodiode readout", Nucl. Instrum. Methods Phys. Res. Sect. A **396**, 103 (1997).

[78] A. Abashian *et al.* (Belle Collaboration), "The K_L/μ detector subsystem for the BELLE experiment at the KEK B-factory", Nucl. Instrum. Methods Phys. Res. Sect. A **449**, 112 (2000).

[79] Y. Ushiroda *et al.* (Belle Collaboration), "Development of the central trigger system for the BELLE detector at the KEK B-factory", Nucl. Instrum. Methods Phys. Res. Sect. A **438**, 460 (1999).

[80] S. Y. Suzuki *et al.* (Belle Collaboration), "The BELLE DAQ system", Nucl. Instrum. Methods Phys. Res. Sect. A **453**, 440 (2000).

[81] `http://belle.kek.jp`.

[82] V. Chabaud *et al.*, “The DELPHI silicon strip microvertex detector with double sided readout”, Nucl. Instrum. Methods Phys. Res. Sect. A **368**, 314 (1996).

[83] Y. Fujita *et al.* (Belle Collaboration), “Test of charge-to-time conversion and multi-hit TDC technique for the BELLE CDC readout”, Nucl. Instrum. Methods Phys. Res. Sect. A **405**, 105 (1998).

[84] E. Nakano, “Belle PID”, Nucl. Instrum. Methods Phys. Res. Sect. A **494**, 402 (2002).

[85] W. R. Leo, “Techniques for Nuclear and Particle Physics Experiments”, Springer-Verlag (1987).

[86] B. Aubert *et al.* (BABAR Collaboration), “The BABAR detector”, Nucl. Instrum. Methods Phys. Res. Sec. A **479**, 1 (2002).

[87] T. Sjöstrand *et al.*, “High-energy-physics generation with PYTHIA 5.7 and JETSET 7.4”, Comput. Phys. Commun. **135**, 238 (2001).

[88] D. J. Lange, “The EvtGen particle decay simulation package”, Nucl. Instrum. Methods Phys. Res. Sect. A **462**, 152 (2001).

[89] R. Brun *et al.*, “GEANT 3.21”, `CERN Report DD/EE/84-1` (1984).

[90] I. Adachi *et al.*, “Computing System for the Belle Experiment”, `arXiv:physics/0306120` (2003).

[91] G. Majumder, “Uncertainty of Track Finding Efficiency with Embedded Tracks”, Belle Note 641 (2004).

[92] B. Bhuyan, “High P_T Tracking Efficiency Using Partially Reconstructed D^* Decays”, Belle Note 1165 (2010).

[93] H. Stöck, “Spin Formalism, Amplitudes and Line Shapes”, `http://www.physics.syr.edu/\~sblusk/Spin/CBX0330\_spin.ps` (2003).

[94] S. Chekanov *et al.* (ZEUS Collaboration), “Production of excited charm and charm-strange mesons at HERA”, Eur. Phys. J. C **60**, 25 (2009).

[95] J. Blatt and V. Weisskopf, “Theoretical Nuclear Physics”, Wiley (1952).

[96] F. Rademakers and R. Brun, “ROOT: An Object-Oriented Data Analysis Framework”, Linux Journal **51** (1998), `http://root.cern.ch`.

[97] W. Verkerke and D. Kirkby, "The RooFit toolkit for data modeling", arXiv:physics/0306116 (2003).

[98] W. Lavrijsen, "PyROOT", http://wlav.web.cern.ch/wlav/pyroot.

[99] http://www.python.org.

[100] F. James and M. Roos, "Minuit: A System for Function Minimization and Analysis of the Parameter Errors and Correlations", Comput. Phys. Commun. **10**, 343 (1975).

[101] F. James, "Statistical Methods in Experimental Physics", World Scientific (2006).

[102] F. Fang, "Study of $K_S \to \pi^+\pi^-$ Selection", Belle Note 323 (2000).

[103] G. Arfken and H. Weber, "Mathematical Methods for Physicists", Elsevier (2001).

[104] G. Breit and E. P. Wigner, "Capture of Slow Neutrons", Phys. Rev. **49**, 519 (1936).

[105] E. P. Wigner, "Higher Angular Momenta and Long Range Interaction in Resonance Reactions", Phys. Rev. **72**, 29 (1947).

[106] R. H. Dalitz and S. F. Tuan, "The Phenomenological Representation of $\overline{K}$-Nucleon Scattering and Reaction Amplitudes", Ann. Phys. **3**, 307 (1960).

[107] I. J. R. Aitchison, "The K-Matrix Formalism for Overlapping Resonances", Nucl. Phys. A**189**, 417 (1972).

[108] H. Frauenfelder and E. M. Henley, "Subatomic Physics", Prentice Hall (1991).

[109] G. Cowan, "Statistical Data Analysis", Oxford University Press (1998).

[110] L. Lyons, "Statistics for nuclear and particle physicists", Cambridge University Press (1986).

[111] S. Lee *et al.*, "Development of a New Analysis Software Framework for the SuperBelle Experiment", J. Korean Phys. Soc. **55**, 2082 (2010).

[112] S. Lee *et al.*, "A common real time framework for SuperKEKB and Hyper Suprime-Cam at Subaru telescope", J. Phys.: Conf. Ser. **219**, 022012 (2010).

[113] S. Lee *et al.*, “Development of High Level Trigger Software for Belle II at SuperKEKB”, J. Phys.: Conf. Ser. **331**, 022015 (2011).

[114] S. Lee *et al.*, “Belle-II High Level Trigger at SuperKEKB”, J. Phys.: Conf. Ser. **396**, 012029 (2012).

[115] T. Abe *et al.*, “Belle II Technical Design Report”, `arXiv:physics/1011.0352` (2010).

[116] A. Moll, “The Software Framework of the Belle II Experiment”, J. Phys.: Conf. Ser. **331**, 032024 (2011).

[117] T. Bray *et al.* (World Wide Web Consortium), “Extensible Markup Language (XML) 1.0”, W3C Recommendation (2008), `http://www.w3.org/TR/xml/`.

[118] `http://www.sgi.com/tech/stl/`.

[119] V. Cerf and R. Kahn, “A Protocol for Packet Network Intercommunication”, IEEE Trans. on Comms. **22**, 637 (1974).

[120] J. Postel, “Internet Protocol”, RFC, 791 (1981), `http://tools.ietf.org/html/rfc791`.

[121] P. Almquist, “Type of Service in the Internet Protocol Suite”, RFC, 1349 (1992), `http://tools.ietf.org/html/rfc1349`.

[122] K. Nichols *et al.*, “Definition of the Differentiated Services Field (DS Field) in the IPv4 and IPv6 Headers”, RFC, 2474 (1998), `http://tools.ietf.org/html/rfc2474`.

[123] `http://root.cern.ch/root/html534/TMessage`.

[124] B. Schäling, “The Boost C++ Libraries”, XML Press (2011).